Hochschule Geisenheim University

Smart Horticulture: Application of sensors and modelling to predict fruit growth, quality and storage behaviour of 'Braeburn' apples

Dissertation submitted in fulfilment of the requirements for the degree Doktor der Agrarwissenschaften- doctor scientiarum agriculturae (Dr. sc. agr.)

Submitted by
Konni Biegert

Born
January 1989

Place of birth
Göppingen, Germany

Ravensburg, September 2022

Chair of the Examination Board:
Prof. Dr. Manfred Stoll
First Reviewer:
Prof. Dr. Peter Braun
Second Reviewer:
Prof. Dr. Christian Zörb
Third Reviewer:
Prof. Dr. Luigi Manfrini
Examiner 1:
Prof. Dr. Judith Kreyenschmidt
Examiner 2:
Prof. Dr. Marianne Darbi

Submitted: September 30, 2022
Date of Defense: March 30, 2023

This thesis was accepted by Hochschule Geisenheim University as a dissertation for the award of the doctoral degree of Doktor der Agrarwissenschaften - doctor scientiarum agriculturae (Dr. sc. agr.). The reviewer of the academic degree is based on the institutional assignment of the second examiner, who is a member of the Faculty of Agricultural Sciences of University of Hohenheim.

Whence arises all that order and beauty we see in the world?

Isaac Newton

Contents

List of Figures

Abbreviations

AI artificial intelligence.

App application software.

CA controlled atmosphere.

DMC dry matter content.

e.g. for example.

GPS global positioning system.

ha hectar.

i.e. id est / that is.

ILM Institut für Lasertechnologien in der Medizin an der Universität Ulm.

kg kilogram.

KI künstliche Intelligenz.

LDA linear discriminant analyses.

LiDAR light detection and ranging.

LME linear mixed effects.

m meter.

NAI normalized anthocyanin index.

NDVI normalized difference vegetation index.

NIR near-infrared.

nm nanometer.

PLSR partial least square regression.

ROC receiver operating characteristic curves.

SSC soluble solids content.

t ton.

T-stage the developmental stage of the fruit after which only cell elongation occurs and the fruit stalk and stem form a T.

TS löslicher Trockensubstanz.

Vis visible.

Summary

Physiological storage disorders cause significant economic losses in a number of commercially important pome fruit varieties worldwide. Under the same storage conditions with the same cultivar, the incidence and frequency of disorders may vary in different years in a manner that must be explained by an interaction of pre-harvest and post-harvest factors. Major factors known to influence disorder incidence include annual weather pattern, management in the orchard, such as leaf-fruit ratio, calcium content of the fruit, harvest date and storage conditions. So far, the occurrence of the disorders cannot be predicted with certainty, and thus to adapt the management in the orchard or in the storage facility accordingly.

Analysis of large amounts of data using artificial intelligence (AI) offers new opportunities to link large data sets into a meaningful context. The aim of the present work is the small-scale and non-destructive monitoring of fruit development in orchards under the above mentioned management practices. AI prediction models were created for the cultivar 'Braeburn'. 'Braeburn' is most susceptible to physiological storage disorders which cause browning in the fruit tissue below the skin. With tent-like constructions over the fruit trees, in which the temperature was controlled during two fruit physiologically important periods (petal drop to T-stage, three weeks before harvest), the temperature influence on disorder incidence was investigated. To the best of our knowledge, this was the first time that different temperature profiles could be generated in the orchard for mature 'Braeburn' trees. Thereby a positive influence on the reduction of internal browning caused by warm night temperatures (>10°C) before harvest was observed. Overall, each trial year showed different occurrences of physiological disorders. Orchard management and weather conditions resulted in significantly different fruit growth patterns and optical non-destructive point spectroscopy. The bi-weekly spectroscopy measurements on the same fruit and subsequent use in partial least square regression (PLSR) models were tested for their informative value. Additionally, the future fruit state was predicted in models based on weather data. The statistical evaluation of three years of data showed that the number of destructive soluble solids content (SSC) samples required to be collected each year for the PLSR models with an acceptable error rate was 100. These samples in particular needed to include the range of low and high SSC values. An unbalanced laboratory error of 0.1-1.0 °Brix had no influence on the modeled SSC values. Compared to destructive SSC determination in the laboratory, SSC could be non-destructively determined with an average deviation of 0.5 °Brix. Field measurements after a rain event had no influence on visible spectral

indices. However, orchard covers such as rain protection over the fruit trees led to lower water absorption values at 975 nm.

The separation of data on a tree-sector level in this work was performed manually, but initial steps were taken to display fruit growth and spectroscopy data via GPS signal location within a map. The acquisition of small-scale data at the tree-sector level revealed significant differences for SSC, chlorophyll and anthocyanin indices as well as significant differences in the incidence of physiological disorders. In future research and modeling approaches the tree sector information should be taken into account, even if this is not yet feasible to implement in a completely automated system under the given circumstances. The prediction models for the development of physiological disorders (core browning, cavities) were able to predict with two years of data the development of the disorders in the storage and the fruit flesh firmness at harvest 90 % correctly. Further research using non-destructive fruit measurements in orchards and the influence of weather conditions will provide further insights into apple quality improvement.

Zusammenfassung

Physiologische Lagerkrankheiten verursachen weltweit beträchtliche wirtschaftliche Verluste bei einer Reihe von kommerziell wichtigen Kernobstsorten. Bei gleichen Lagerungsbedingungen bei derselben Sorte kann das Auftreten und die Häufigkeit der Krankheiten in verschiedenen Jahren in einer Weise variieren, die durch eine Interaktion von Vorernte- und Nacherntefaktoren erklärt werden muss. Wesentliche bekannte Einflussgrößen sind Jahreswetterverlauf, Management in der Obstanlage, wie z.B. Blatt-Frucht Verhältnis, Calciumgehalt in den Früchten sowie Erntetermin und Lagerungsbedingungen. Bislang kann das Auftreten der Krankheiten jedoch nicht sicher vorhergesagt werden, um dadurch das Management in der Obstanlage oder im Lager entsprechend anzupassen. Analysen großer Datenmengen mithilfe künstliche Intelligenz (KI) bieten neue Möglichkeiten unterschiedliche Datenarten und -sätze zu verknüpfen. Das Ziel der vorliegenden Arbeit ist die kleinräumig und nicht-destruktive Überwachung der Fruchtentwicklung in der Obstanlage mit den oben genannten Managementmaßnahmen. KI Prognosemodelle wurden für die Sorte 'Braeburn' erstellt. 'Braeburn' ist anfällig für physiologische Lagerkrankheiten, bei der im Fruchtfleisch oder unter der Schale Verbräunungen auftreten. Mit zeltartigen Umbauungen über den Obstbäumen wurde die Temperatur in zwei fruchtphysiologisch wichtigen Perioden (Blütenblattabfall bis T-Stadium, drei Wochen vor der Ernte) erhöht oder abgesenkt, um den Temperatureinfluss zu untersuchen. Unseres Wissens nach konnte dadurch zum ersten Mal in der Obst- anlage über ausgewachsenen Bäumen unterschiedliche Temperaturverläufe erzeugt werden. Dabei wurde ein positiver Einfluss auf die Reduzierung von inneren Verbräunungen durch warme Nachttemperaturen (>10°C) vor der Ernte festgestellt. Insgesamt zeigte jedes Versuchsjahr unterschiedliche Ausprägungen der physiologischen Fruchterkrankungen. Managementmaßnahmen und Witterungsbedingungen führten zu signifikant unterschiedlichen Fruchtwachstumsverläufen und optischer nicht-destruktiver Punktspektroskopie. Die zweiwöchentlich wiederholten Spektroskopiemessungen an den gleichen markierten Früchten und deren Weiterverarbeitung in PLSR Modellen wurden einerseits auf ihre Genauigkeit überprüft und zusätzlich mit Modellen und Wetterdaten deren zukünftige Zustände vorhergesagt. Die statistische Auswertung der dreijährigen Daten zur nötigen Probenanzahl und Fehler bei der destruktiven löslicher Trockensubstanz (TS) Analyse resultierte in Probenanzahlen von 100 Stück pro Jahr, die eine Bandbreite von niedrigen bis hohen TS Werten umfassen müssen. Ein unbalancierter Laborfehler von 0.1-1 °Brix hat keinen Einfluss auf die modellierten TS Werte. Im Vergleich zur destruktiven TS Bestimmung im Labor konnte die Spektroskopie die TS im

Mittel mit einer Abweichung von 0.5 °Brix bestimmen. Spektralmessungen in der Obstanlage nach einem Regenereignis führten dabei zu keiner Veränderung im sichtbaren Spektralbereich. Jedoch können Kulturabdeckungen wie z.B. Regenschutzfolien über den Obstbäume zu geringeren Wasserabsorptionswerten bei 975 nm führen.
Die Bereitststellung der Daten auf Baumsektor Ebene wurde in dieser Arbeit manuell durchgeführt. Jedoch wurden erste Schritte unternommen, um Fruchtwachstums- und Spektroskopiedaten per GPS Signal innerhalb einer Karte darzustellen. Die kleinräumige Datenaufnahme auf Baumsektor Ebene ergaben für TS, Chlorphyll und Anthocyan Indexberechnungen, sowie auch für physiologische Krankheiten deutliche Unterschiede. Bei zukünftigen Forschungsarbeiten und Entscheidungsmodellierungen sollte dies berücksichtigt werden, auch wenn dies unter den gegebenen Umständen noch nicht voll-automatisiert umsetzbar ist. Das Prognosemodell zur Entstehung von physiologischen Krankheiten (Kernhausbräune, Kavernen) konnte mit zweijährigen Daten die Entstehung der Lagerkrankheiten nach der Auslagerung und die Fruchtfleischfestigkeit zur Ernte in 90 % der Fälle richtig vorhersagen. Somit konnte gezeigt werden, dass eine kleinräumige Datenerhebung auf Baumsektor Ebene zur Prognose von physiologischen Lagerkrankheiten mithilfe KI Modellierungen angewendet werden kann. Weitere Forschungsarbeiten mit nicht-destruktiven Fruchtmessungen in der Obstanlage und dem Einfluss von Wetterbedingungen werden weitere Einblicke zur Qualitätsverbesserung von Äpfeln ermöglichen.

Author contributions

Chapter 2 is based on the following peer-reviewed publication:

Biegert, K., McCormick R. J., Zoth, M. and Braun P. (2021). A precision management approach to monitor apple fruit growth and quality. *Acta Hortic.*, (1314):447–454. `https://doi.org/10.17660/ActaHortic.2021.1314.55`

Konni Biegert: Conceptualization, Methodology, Investigation, Data Curation, Formal Analysis, Validation, Writing – Original Draft, Writing – Review & Editing.
Roy J. McCormick: Conceptualization, Investigation, Data Curation, Formal Analysis, Writing – Review & Editing.
Michael Zoth: Review & Editing.
Peter Braun: Supervision, Writing – Review & Editing.

Chapter 3 is based on the following peer-reviewed publication:

Biegert, K., Lohner S. A., McCormick R. J., Kienle, A. and Braun, P. (2021). Influence of precipitation on VIS/NIR spectra of 'Gala' apples. *Acta Hortic.*, (1327):669-676. `https://doi.org/10.17660/ActaHortic.2021.1327.88`

Konni Biegert: Conceptualization, Methodology, Investigation, Data Curation, Formal Analysis, Validation, Writing – Original Draft, Writing – Review & Editing.
Stefan A. Lohner: Conceptualization, Methodology, Investigation, Data Curation, Formal Analysis, Writing – Review & Editing.
Roy J. McCormick: Conceptualization, Investigation, Data Curation, Formal Analysis, Writing – Review & Editing.
Alwin Kienle: Supervision, Writing – Review Editing.
Peter Braun: Supervision, Writing – Review Editing.

Chapter 4 is based on the following peer-reviewed publication:

Biegert, K.[1], Stöckeler, D.[1], McCormick R. J. and Braun P. (2021). Modelling soluble solids content accumulation in 'Braeburn' apples. *Plants*, 10(2):302. `https://doi.org/10.3390/plants10020302`

[1] These authors contributed equally to this work.
Konni Biegert: Conceptualization, Methodology, Software, Validation, Investigation,

Data Curation, Writing Original Draft, Visualization, Project Administration.
Daniel Stöckeler: Methodology, Software, Validation, Formal Analysis, Investigation, Writing – Original Draft.
Roy J. McCormick: Conceptualization, Methodology, Software, Validation, Data Curation, Writing – Review & Editing, Supervision.
Peter Braun: Writing – Review & Editing, Supervision.

Chapter 5 is based on the following peer-reviewed publication:

McCormick R. J., Biegert, K. and Streif. J. (2021). Occurence of physiological browning disorders in stored 'Braeburn' apples as influenced by orchard and weather conditions. *Postharvest Biology and Technology*, 177:111534.
`https://doi.org/10.1016/j.postharvbio.2021.111534`

Roy J. McCormick: Investigation, Methodology, Project administration, Formal Analysis, Writing - original draft, Visualization.
Konni Biegert: Investigation, Methodology, Data Curation, Writing – Review & Editing, Formal Analysis.
Josef Streif: Conceptualization, Investigation, Methodology, Writing – Review & Editing.

Chapter 6 is based on the following peer-reviewed publication:

Osinenko, P.[1], Biegert, K.[1], McCormick, R.J., Göhrt, T., Devadze, G., Streif, J. and Streif, S. (2021). Application of non-destructive sensors and big data analysis to predict physiological storage disorders and fruit firmness in 'Braeburn' apples. *Computers and Electronics in Agriculture*, 183:106015.
`https://doi.org/10.1016/j.compag.2021.106015`
[1] These authors contributed equally to this work.

Pavel Osinenko: Methodology, Formal Analysis, Writing – original draft.
Konni Biegert: Investigation, Data Curation, Validation, Writing – Original Draft.
Roy J. McCormick: Project Administration, Validation, Methodology, Writing – Review & Editing.
Thomas Göhrt: Investigation, Formal Analysis, Software, Writing - Review & Editing.
Grigory Devadze: Investigation, Formal Analysis, Software, Writing – Review & Editing.
Josef Streif: Conceptualization, Methodology, Writing – Review & Editing.
Stefan Streif: Conceptualization, Methodology, Funding acquisition, Writing – Review & Editing.

Konni Biegert co-authered the following peer-reviewed publications:

Lohner, S. A., Biegert, K., Nothelfer, S., Hohmann, A., McCormick, R. J. and Kienle, A. (2021). Determining the optical properties of apple tissue and their dependence on physiological and morphological characteristics during maturation. Part 1: Spatial frequency domain imaging. *Postharvest Biology and Technology*, 181:111647.
`https://doi.org/10.1016/j.postharvbio.2021.111647`

Lohner, S. A., Biegert, K., Nothelfer, S., Hohmann, A., McCormick, R. J. and Kienle, A. (2021). Determining the optical properties of apple tissue and their dependence on physiological and morphological characteristics during fruit maturation. Part 2: Mie's theory. *Postharvest Biology and Technology*, 181:111652.
`https://doi.org/10.1016/j.postharvbio.2021.111652`

McCormick, R. and Biegert, K. (2021). Non-destructive Vis/NIR time-series to model apple fruit maturation on the tree. *Acta Hortic.*, (1311):131-140. `https://doi.org/10.17660/ActaHortic.2021.1311.17`

Lohner, S. A., Biegert, K., Hohmann, A., McCormick, R.J. and Kienle, A. (2022). Chlorophyll- and anthocyanin-rich cell organelles affect light scattering in apple skin. *Photochemical & Photobiological Sciences*, 21(2):261-373
`https://doi.org/10.1007/s43630-021-00164-1`

All authors gave final approval for publication.

1 General Introduction

Aim of the study

Physiological storage disorders (hereafter referred to as disorders) continue to cause significant fruit losses during apple fruit storage and during the post-storage shelf-life period. The underlying factors causing the development of disorders are partly understood, but vary with cultivar and within orchard, growing season and with management practices to an extent which cannot be explained by existing tools. The present study links pre-harvest management practices, in particular crop load, calcium sprays and seasonal weather conditions obtained by non-destructive sensor information with post-harvest (id est / that is (i.e.) post-storage) fruit grading results within a 'big data' modelling and classification process. The study involved a commercially important apple cultivar ('Braeburn'), susceptible for a range of disorders, in a novel 'big data' modelling approach to merge the complexity of fruit growth conditions and fruit production processes to the development of disorders.

The study applied optical sensors in a 'Braeburn' apple orchard to obtain non-destructive time-series data on an individual tree sector level during the fruit growth period. This digital time-series information together with the daily weather records was used in 'big data' analyses to predict the occurrence of physiological disorders and firmness to adjust management strategies or post-harvest fruit handling (see Figure 1.1).

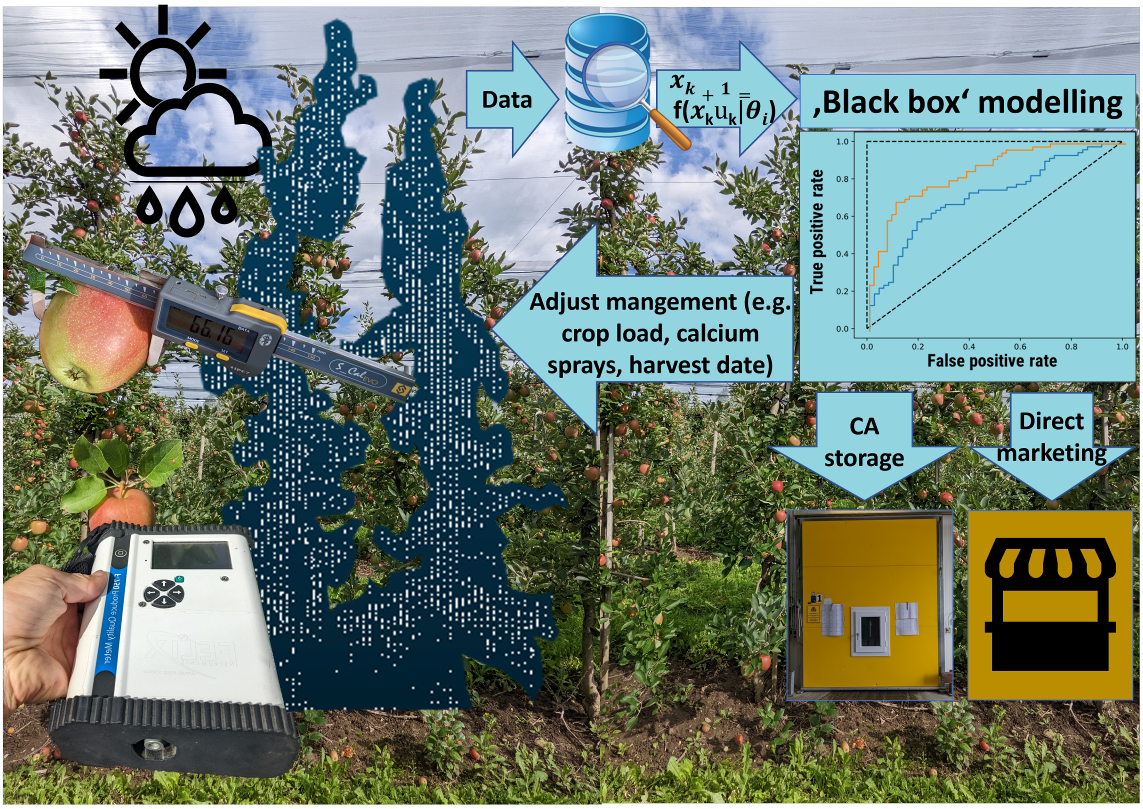

Figure 1.1: Graphical abstract of the study. Fruit growth and tree volume were monitored during the vegetation season with optical sensors. Sensor data, weather conditions and post-storage fruit quality data were saved on a tree sector level in a database. Data were post-processed through a 'black box' classifier to predict physiological storage disorders and fruit firmness after controlled atmosphere (CA) storage. The prediction result leads to a smart horticulture approach to adjust the management in the orchard and to optimise post-harvest handling of the fruit either for different storage types or direct marketing.

Introduction

Apples (*Malus* x *domestica* BORKH.) are the world's most important temperate tree fruit crop. The annual German production of pome fruit is approximately 1 million ton (t) (Faostat, 2022), whereas 24 kilogram (kg) were consumed in 2020/21 per capita per year (Ahrens, 2022). The main production areas are the "Altes Land" nearby Hamburg and the Lake Constance region in the Southwest of Germany (Garming et al., 2018). Commercial apple orchards are mainly grown as slender spindle trees with heights of up to 4 meter (m) with an average yield of some 30 t/hectar (ha). The majority of German apple production goes into controlled atmosphere (CA) storage to ensure fresh fruit is available in the market for up until approximately July the following year. On the one hand this provides local harvested produce for marketing over the whole year. On the other hand it helps to stabilize the market price. However, during and after storage in the shelf-life period in shops or at home, a range of different disorders can develop. The post-harvest losses for apples due to storage disorders are estimated at about 11 % by Lake Constance marketers (Thinnes, 2017, personal communication) or 5-25 % in the United Kingdom (Terry et al., 2011) for fruit not meeting the specifications. This is due to disorders, as well as including other quality issues such as low levels of fruit firmness, water content (for example (e.g.) shrivel) or the development of mealiness. The European Union's Farm to Fork strategy aims to halve food waste by the year 2030 and the application of digital techniques for a sustainable agriculture (Guyomard and Bureau, 2020) is seen as one important approach to help achieve this goal. The present study aims to provide an early prediction tool for the risk of disorder development based on non-destructive sensor data from the orchard in order to adapt the post-harvest storage and marketing and/or orchard management strategy.

Disorders are cultivar specific. 'Braeburn' apples obtain high flesh firmness values and have a high risk to develop internal disorders. Low gas exchange rates through cells which is associated with high firmness can induce oxygen deficiency and membrane break down. The brown color which is distinctive of internal disorders are caused by phenolic compounds (Franck et al., 2007). There are a range of different disorders (see Figure 1.2) which lead to, e.g. visible browning of the fruit skin (e.g. superficial scald) or disorders non-visible from the outside of the fruit such as internal browning around the core (core browning) or in the fruit flesh (e.g. flesh browning). Bitter pit is correlated with calcium deficiency (Saure, 1996) in the fruit and results in brown spots on the fruit skin and/or in the fruit flesh. When fruit tissues break down and lose moisture, internal cavities can form in the fruit flesh that often occur together with core or flesh internal browning. However, the consumer's preference and therefore the fruit-grower's choice to plant new cultivars that produce apples with high levels of fruit firmness and a crisp eating texture can also be associated with a higher risk of disorders.

Pre- and post-harvest factors influence the occurrence of apple fruit disorders. The main

Core browning with cavities

Superficial scald

Bitter pit

Figure 1.2: Examples of physiological disorders.

drivers in the orchard are an advanced maturity at harvest, light crop loads with unbalanced source-sink relationships of energy distribution or nutritional deficits such as calcium which is an integral part of cell wall stability and deficits in calcium can increase internal breakdown (Bangerth and Streif, 1972; Lau, 1998; Elgar et al., 1999; Ferguson et al., 1999). The gas exchange through cells, which is influenced by crop load, impacts on the development of disorders. However, they remain so far largely unexplained (Wünsche and Ferguson, 2010). Elgar et al. (1999) and Rogers (2014) state that the largest source of variation in disorder incidence are growing conditions (shoot growth, light availability and growing degree hours) which are all factors strongly dependent on seasonal weather conditions. Furthermore, incorrect cultivar-specific post-harvest handling and storage regimes contribute to the development of disorders (i.e. temperature and atmosphere settings, delayed or direct CA start) (Hatoum et al., 2016).

Manfrini et al. (2020) and Aggelopoulou et al. (2009) found a large spatial variability in sensor data obtained within orchards. Consequently, individual trees or smaller areas of land should be managed in a precision farming approach. Management practices adopted to target excessive variation can lead to cost savings, e.g. nitrogen fertilization savings of 38 % (Aggelopoulou et al., 2010) and opportunities to maintain and/or increase fruit yield and quality throughout the whole fruit production process. At present, fruit growing management mainly depends on decisions made at a farm-scale level. Experienced growers are capable of adjusting orchard machinery to match a batch of single trees. For example, with mechanical flower thinning in an orchard with alternate bearing trees, a good tractor driver can exclude trees with low flower intensity or only conduct root pruning in areas of stronger tree growth. These grower decisions are based on many years experience and background knowledge. So to say, a decision support model sits within a good grower's head. However, the area of land a single grower now has to manage has increased (Garming et al., 2018) and it is increasingly difficult or impossible to micro-manage large orchard areas to the same level as in the past. Furthermore, qualified specialist personnel for orchard management are increasingly difficult to find and this situation looks likely to continue into the future. Also, increasing official regulation requirements such as different distances to waterways (non-target areas) and non-target organisms for plant protection sprays as well as a growing number of plant protections spray registrations under an emergency rule and further regulations to protect the environment and consumer lead to a complicated situation for the grower to prevent mistakes. Therefore, orchard management operations can be supported by the development of decision support systems that take into account the changing official regulations during the vegetation period. Another driver towards a sensor based automation process (smart horticulture) is the high demand for manual labour in fruit growing. Apple production requires around 466 hours/ha (Verbiest et al., 2020) and due to rising costs with minimum wage salaries now at 12 €/hour (2022) excessive manual labor becomes unaffordable. The key to best management practice and economically well-positioned orchards that have low fruit losses, is orchard information, knowledge and advice.

Optical sensors

Within industrial production processes there are a range of sensor technologies available to monitor in real-time the production line or regulate machines. The application of sensors in this area is mainly within a controlled environment (e.g. even light conditions or exact driveways). However, there are commercially available sensors already in use in agricultural cropping. Harvesters (e.g. for hay or grain crops) are equipped with moisture and chlorophyll sensors (e.g. Yara N sensor) to monitor produce quality and nitrogen imbalances. Anyhow, within apple orchards the adoption of optical sensor technology is hampered by a range of factors. First of all, the target market in terms of size and financial investment in horticulture is much smaller compared to arable farming and many industrial production processes. Hence, sensor innovations have been deployed to a much lower extent. As compared to arable crops, a fruit tree is a large complex 3D structure with the marketable product (i.e the fruit) largely hidden by the foliage and branches. Also, optical recordings are required from both sides of the tree row and there are problems with back-lighting when viewing one tree side, especially under daylight conditions outside. To work around back-lighting, an artificial light source can be used after sunset (Anderson et al., 2021b). Additionally, a precise geo-location signal with a global positioning system (GPS) is required to map the sensor information. A geo-located tree growth or crop load or fruit quality map can be used in further decision support systems. Occlusion by the orchard trees themselves (Underwood et al., 2015) can hamper the adoption. With the detection of a single tree, there is an on-going challenge to link the sensor data to individual tree sectors (height) and combine two tree sides to one tree. In Southwest Germany apple production is under hail nets and this limits the use of un-manned aerial vehicles (drones) to capture sensor data with an overview flight.

A range of optical sensors (spectrometers) are available for use in orchards as non-destructive handheld proximal (point) devices that measure diffuse light reflection in the visible (Vis) and near-infrared (NIR) range from the fruit skin. The Vis spectra ranges from 400-750 nanometer (nm) and the NIR from 750-2500 nm. For handheld and low-cost devices only the short-wave NIR wavelength until 1100 nm are measured- the so called Hershel regions. Changes in fruit pigments such as chlorophyll, carotenoids, xanthophylls and anthocyanins can be monitored in the Vis range (Solovchenko et al., 2019). These plant pigments peak in different spectral ranges (Walsh et al., 2020) and can be distinguished through that. However, the pigment spectra overlap which hampers for example a clear separation of individual anthocyanins and carotenoids. Light interactions in the Hershel region in particular with the oxygen and hydrogen bonds are due to water and carbohydrates in the apple flesh. Further processing with destructive laboratory fruit samples to determine dry matter content (DMC) and soluble solids content (SSC) values and the use of PLSR models allows these fruit quality parameters to be tracked non-destructively in the orchard. At present the optical sensors used for fruit quality determination in the orchard do not separate light absorption and scattering effects. However, the in-field determination of quality attributes through non-destructive monitoring can aid growers in their decision making processes and further the understanding of fruit physiological processes that are important for the development of fruit quality. Consequently, robots or drones can use this information for targeted or precision machinery action or crop monitoring.

’Big data’ analyses

Digital data in our daily lives is now ubiquitous. The collection of data within a database and assembly of intelligent connections has resulted in ’big data’ analyses. ’Big data’ analyses should assess management complexity and raise economic value. The machine learning approach aids humans in processing of widely scattered data which seem to have no meaningful relationship and present new opportunities. Chi et al. (2016) defined five criteria essential to achieve effective ’big data’. Naturally, its the size of data (volume) and variety of data types such as images, field-based and longitudinal data (variety). The subsequent real-time processing (velocity) for decision support systems is another prerequisite. Furthermore, data should be reliable, unbiased and qualified to solve the problem (veracity). Valorization defines the ability to propagate knowledge. In various fields (banking, insurance, health care) ’big data’ analyses are already successfully applied. In contrast to orchard research, data points in insurances or banking are assembled automatically through other electronic processes. Up-to-date ’big data’ analyses have not been widely applied in agriculture, even less in horticulture (Kamilaris et al., 2017). In orchard systems there are technical challenges to save and store ’big data’ online at the time of data capture. On the one hand, the wireless data transfer in orchards is problematic or the sensors, e.g. a light detection and ranging (LiDAR) sensor gives out large quantities of data which cannot at present be cost-effectively saved and/or process the raw data by the sensor device in the orchard.

Hypotheses

The expression of physiological disorders that occur after storage of two seemingly identical lots of apples (same grower, cultivar, storage conditions and harvest date) can vary markedly every year. Therefore, the question arises what influence the annual weather conditions, especially changes in temperature, have on fruit quality formation, maturation processes and storage stability of the fruit. Important fruit quality and maturation processes were monitored in this work with sensors in different field experiments (harvest date, calcium sprays, crop load and temperature profiles) for the cultivar ’Braeburn’ which is known to be susceptible for a range of disorders. Due to the above mentioned constrains with the application of sensors in horticulture, the present study solely used a handheld spectrometer at the sunny side of apple fruit skin together with digital calipers.

The following hypotheses will be investigated:

1. Vis/NIR sensing can detect different management practices during fruit growth through known spectral indices such as normalized difference vegetation index (NDVI) and normalized anthocyanin index (NAI).

2. Rain events prior to an optical sensor measurement on dry fruit skin won't affect fruit absorption or scattering properties.

3. Warm air temperatures in the orchard after flowering till the T-stage and cool maturation conditions contribute to the development of disorders. The T-stage is defined as the developmental stage of the fruit after which only cell elongation occurs and the fruit stalk and stem form a T (T-stage). Warm temperatures will shorten the period from fruitset until the T-stage and result in fruitlets with fewer but larger cells which are more prone to breakdown during post-harvest storage. In contrast, warm air temperatures before harvest will lead to a more active cell defense that maintains higher energy levels against the formation of disorders.

4. Non-destructive hand-held sensors can provide SSC values through PLSR models at a comparable accuracy to destructive laboratory measurements and can be implemented for orchard determinations. The spectral range of the shortwave NIR regions can be used for SSC and DMC determinations using PLSR models.

5. Non-destructive Vis/NIR sensor data collected during fruit growth, weather records and treatment information can predict disorders after storage and firmness at harvest through 'big data' modelling.

Structure of the cumulative dissertation

The overall aims of this work were to investigate the explanatory power of longitudinal sensor data in the orchard in real-time, to link the interaction of pre-harvest seasonal and orchard factors to build a prediction tool for disorders and bring apple fruit production one step closer to smart horticulture farming. Smart farming in this context will enable a grower to use a decision support system based on sensor information from the orchard and thereafter conduct tasks site-specifically, i.e. decide on long-term storage type or direct marketing of fruit or adopt management strategies in the orchard (e.g. crop load, calcium sprays, harvest date). The thesis starts with an introduction of the research topic and continues with a series of chapters of already published articles in peer-reviewed, international, scientific journals. Chapters 2-4 concentrate on the explanatory power of time-series sensor data obtained by non-destructive orchard scanning. Chapter 5 describes the range of disorders obtained by different management practices in different years. The 6^{th} chapter shows the sensor and disorder information from chapter 2-5 as input into a 'black box' prediction. In the final chapter 7 the results of the theses are discussed.

The light propagation through apple fruit tissue with the separation of absorption and scattering properties were investigated together in a cooperative work with Stefan Lohner from the Institut für Lasertechnologien in der Medizin an der Universität Ulm

(ILM). These publications, see author contributions, focused on the technical setup and modeling of light through apple fruit tissue and were excluded from this thesis.

The specific aims of each chapter are summarised as:

Chapter 2

In this chapter data from one year (2018) are presented for chlorophyll (red edge), DMC and SSC obtained from the non-destructive spectral time-series collected from a 'Braeburn' orchard as well as fruit diameter growth per tree sector level. The general approach of 'big data' generation in the orchard and statistical constraints for the subsequent use of these data in 'black box' modelling and classification were discussed. Fruit diameter values showed a strong scatter starting from the end of July, similar to the DMC values. The spectral data showed a large variance depending on the time of season or storage. The apples from the bottom tree sector and also the light crop load had a significantly higher severity of bitter pit.

Chapter 3

In chapter 3, the effect of precipitation on spectral scans was examined in 2019 for apples grown under hail-netting or plastic sheet covers as data were obtained on a regular bi-weekly cycle on dry fruit skins, as well as after a rain event. Additionally, a combined data set from a handheld field spectrometer is compared to laboratory data obtained with an integrating sphere. The study showed that the absorption of apple fruit skin in the Vis and NIR wavelength range was not affected by rain events. However, fruit grown under hail-netting show consistently higher water absorption values throughout the study. Furthermore, the estimated water content obtained by the integrating sphere setup showed apples grown under hail-netting have 4-5 % higher values as compared to fruit covered by plastic sheets. However, the standard deviation of the spectral data was 4 % which relativize the explanatory power of these findings.

Chapter 4

In this chapter, in-depth statistical analyses of SSC data modelled from PLSR models were evaluated with regard to their explanatory power. Monte Carlo simulations were undertaken to investigate model transferability to different years, accuracy, sample size, seasonal variation and laboratory errors. Furthermore, a linear mixed effects (LME) model assessed different management practices for differences in SSC values between crop load, tree sector and calcium spraying. A multi-year PLSR model for SSC showed good results. However, independent yearly models performed best. The laboratory reference measurements of 100 samples was sufficient to develop the models. Sector position and crop load had a significant effect on the development of SCC in the orchard.

Chapter 5

Chapter 5 investigated the effect of crop load and air temperature during cell division for three weeks post-petalfall as well as before harvest on the incidence and severity of disorders. Plastic tents were built over trees in the orchard and equipped with heaters or cooling machines in order to obtain different temperature regimes. Data were assessed with receiver operating characteristic curves (ROC) and linear discriminant analyses (LDA) to predict with binary classifiers for disorder risk using pre-harvest factors. The three years of disorder data varied markedly over the experiments. Heavy crop loads and warm night temperatures (>10°C) prior harvest showed a reduced expression of disorders. ROC analyses showed a reasonable to good utility (78-90 % accuracy) for all treatments to predict disorders.

Chapter 6

Chapter 6 used optical sensor information for NDVI, NAI, DMC and SSC together with weather parameters as an input into a 'black box' classification process to predict disorder scores after long-term CA storage. The dataset was split into a training and validation set. For the fruit growing season 2016/17 and 2017/18 a prediction success for cavities and internal browning of 90 % on average was achieved. Also, a classifier trained to predict changes in fruit firmness prior harvest and over the harvest window obtained good correlation with measured results. A 'proof of concept' for this modelling and disorder classification approach was demonstrated. Fruit firmness along with SSC predictions can be used to help non-destructively determine the optimal harvest window for 'Braeburn' CA storage.

2

A precision management approach to monitor apple fruit growth and quality

K. Biegert, S. A. Lohner, R. J. McCormick, P. Braun

Acta Hortic. 1314 (2021)

A precision management approach to monitor apple fruit growth and quality

K. Biegert[1,a], R.J. McCormick[1], M. Zoth[1] and P. Braun[2]

[1]Kompetenzzentrum Obstbau-Bodensee, Ravensburg, Germany; [2]Geisenheim University, Department of Pomology, Geisenheim, Germany.

Abstract

The application of precision management sensing technologies in apple production is challenging as many of the key physiological processes that influence fruit quality occur within the fruit tissue and are masked from the outside by the fruit skin. We report results from a three-year project at the Kompetenzzentrum Obstbau-Bodensee in Southwest Germany to monitor 'Braeburn' apple fruit growth and quality using a precision management approach. Field time-series data were collected regularly with a standard type of hand-held spectrometer and a set of Bluetooth digital calipers from the same marked apples while growing on-tree. Data were collected from three tree sectors (bottom, middle and top, trees were ~3.8 m high) and different field treatments (e.g., calcium spraying and crop load). Fruit were placed in delayed CA storage for a period of ~5 months. After a shelf-life period all fruit were cut and assessed for internal physiological disorders. In 2018, fruit from the bottom tree sectors showed a higher disorder severity for bitter pit than those from the middle or top tree sectors. Total soluble solids content modelled from the spectral time-series data varied notably between measurement acquisitions, whereas chlorophyll (red edge) degradation and fruit diameter growth showed an overall smoother decline or increase, respectively. The results are discussed with some insights into the data management necessary for a precision orchard approach.

Keywords: 'Braeburn', physiological storage disorders, VIS/NIR, Big Data

INTRODUCTION

Key factors influencing the development of internal physiological storage disorders (PSD) in apple include the picking date, orchard management (e.g., crop load, calcium chloride spraying), storage conditions and regional climate additionally altered by seasonal changes. While physiological disorders arise mostly in storage or shelf-life, the main influencing factors occur during growth and development processes in the field. Often there can be marked differences in disorder incidence even at the orchard level between different lots of the same cultivar (Ford, 1979; Ferguson et al., 1999; Sams, 1999; Lammertyn et al., 2000; Hatoum et al., 2014). In general, more mature fruit, high CO_2 partial pressures in storage, light crop load, higher potassium-calcium ratios and cool preharvest temperatures result in a higher incidence of internal storage disorders (Streif and Kittemann, 2018; Watkins and Mattheis, 2019). For apple and pear production quantifying the pre- and postharvest factors that influence PSD and their interactions has proven to be more complex than expected (Verlinden et al., 2002; Franck et al., 2007; Hatoum et al., 2014) and requires further research.

Malus domestica 'Braeburn' and other recently developed apple cultivars with high flesh firmness values and low gas diffusivity (Ho et al., 2010) have an increased risk to develop PSD, especially during CA storage (Lammertyn et al., 2000). The fruit cellular defenses can be reduced by insufficient energy metabolism due to the above-mentioned processes. De-compartmentalization can occur and phenolic compounds oxidized by polyphenol oxidase result in brown tissue (Mayer, 2006). In addition, cavities can develop as

---

[a]E-mail: Konni.biegert@kob-bavendorf.de

Acta Hortic. 1314. ISHS 2021. DOI 10.17660/ActaHortic.2021.1314.55
Proc. International Symposium on Precision Management of Orchards and Vineyards
Eds.: R. Lo Bianco et al.

tissues dehydrate. Modern fruit sorting machines can detect PSD with non-destructive transmission spectroscopy before marketing. In 2016/2017, in the Lake Constance region of Southwest Germany substantial marketing losses occurred due to PSD in 'Braeburn'.

Non-destructive optical sensors for field applications are now available at reasonable prices and with relatively fast scanning times (Walsh, 2016). Optical spectroscopy is a non-destructive technique capable of repeated scanning of fruit within an orchard and to obtain a broad band of information from the VIS (visible)/NIR (near infrared) spectra. The NIR spectral signatures can be correlated with a partial least square regression (PLSR) model to chemical compounds such as soluble solids content (SSC) or to obtain information from the VIS spectra on plant pigments in the fruit skin. Known non-destructive indicators of fruit ripeness/quality in apple are SSC, chlorophyll degradation or anthocyanins in terms of red blush skin colour for higher quality (priced) fruit (McGlone et al., 2002; Merzlyak et al., 2003; Zude et al., 2006). Also, the VIS spectra can provide information about plant stress during ripening (Solovchenko et al., 2010).

The present study was part of the 'BigApple' project running from 2016 to 2019 (McCormick et al., 2017). The approach of the study was to obtain a 'Big Data' structure for field data as input (fruit growth, spectral indices, weather) and PSD scores after storage as output, using a black box artificial intelligence (AI) system analysis to predict PSD. Moreover, the study aimed to obtaining new information about fruit susceptibility to PSD from the fruit growth and spectral time-series data obtained at a small-scale orchard level.

The objectives of the present study were to 1) explain the 'Big Data' generation in the 'BigApple' project and 2) investigate if the fruit position on the tree has an influence on the severity of PSD.

MATERIALS AND METHODS

Experimental site

The study was performed at the Kompetenzzentrum Obstbau-Bodensee (KOB) in South-West Germany, 47.767137°N, 9.556544°E with an average annual rainfall of 691 mm, temperature of 8.4°C and 1758 h of sunshine. Research was undertaken on 'Braeburn' apple (clone Hillwell) grafted on M9 rootstock and planted in 2006. Trees were grown as slender spindles in a North-South row direction (3.20×0.80 m) with an approximate tree height of 3.80 m. Weather data were obtained from a weather station (Thiess, Germany) located 200 m from the trees. Results are presented for the season 2018/2019.

Study design

The field layout used a randomized design containing seven trees for each repetition and replicated three times per treatment. Each tree was separated into three sectors of 1.25 m tree height for bottom, middle and top and subsequently measured, harvested and stored sector-wise. A one-factorial experiment was established for crop load or calcium spraying. Three crop load levels of light (55%), standard (100%) or heavy (160%) were established by hand thinning after bloom (May 24 to June 2). In the calcium chloride experiment, sprays were applied on a weekly basis from July until harvest or not. Fruit were picked at an optimal harvest date as defined by the Streif-Index (Streif and Kittemann, 2018). The controlled atmosphere storage conditions were delayed for 21 days after harvest and set at 1 kPa O_2, 0.7 kPa CO_2 and 1°C for 139 days followed by a shelf-life period of 7 days at 20°C.

Fruit diameter and spectral reflectance

Fruit growth measurements were undertaken with a set of digital Bluetooth calipers (Sylvac, Crissier, CH) and captured on an Android smartphone app developed at the KOB at a marked, equatorial position on a biweekly basis.

A portable spectrometer with a spectral range of 310-1100 nm and a spectral sampling of 3 nm was used with daylight correction (F-750, Felix Instruments, Camas, USA). Single fruit were marked on the equatorial and sunny side of the fruit. Data were processed with software supplied with the instrument and a 'BigApple' PLSR reference model developed for SSC (n=362, 6 principal components, R^2=0.92; RMSEC/RMSECV = 0.48/0.49) and dry matter (DM) (n=329, 6 principal components, R^2=0.67; RMSEC/RMSECV=1.07/1.09) for the 2018/2019 season. Samples were scanned at 10, 20 and 30°C to help adjust for temperature effects in the NIR region. Changes in chlorophyll were followed as the red edge (RE) wavelength, calculated as the value where the second derivative between 680 and 700 nm was equal to zero.

Disorder assessments after storage

All fruit per tree and sector were cut after storage and a 7 days shelf-life period (~20°C), and visually assessed by trained staff for PSD (ordinal score 0 to 3 with 0.5 intermediate steps, where 0 = no symptoms and 3 = most severe. A severity index (0-100) was calculated as:

$$severity = \frac{\sum_{i\epsilon B}(n_i xi)x100}{N * 3}$$

where I = score, n_i = number of fruit with score i, B = $\{0,0.5,1,1.5,2,2.5,3\}$ and $N = \sum_{i\in B} n_i$.

Statistical analyses

Checking for homogeneity of variance and normal distribution was conducted with the Levene and Shapiro-Wilks tests. A one-way analysis of variance (ANOVA) was performed on the treatment groups and means were separated by Tukey's HSD post-hoc test for various fruit parameters at harvest. Significance was defined as $p<0.05$. If not stated otherwise the standard deviation (sd) is given in brackets. Analyses were performed using R version 3.5.1 (R Core Team, 2018) with the packages pwr for the power calculation and car for the ANOVA.

RESULTS AND DISCUSSION

'Big Data' approach

Data were recorded on a sector per tree level to obtain a 'Big Data' structure for subsequent black-box processing (Osinenko et al., 2021). To structure and handle field and storage data in a database a "unique fruit group" (UFG) structure was assigned where each UFG represented one tree and sector. A precondition for data modelling was time-series measurements for each device within a day on a consecutive sampling rhythm. Digital calipers connected to an app allowed real-time tracking and a delete function while measuring in the field. This measurement setup allowed fruit growth data for the 'BigApple' project to be collected from n=846 fruit in a few hours. However, spectral scanning was more time consuming, and only n=423 fruit data were obtained during one day for a feasible three-year research. During this work, efforts were made to upload the field data in real-time to a database.

In horticultural systems, variability is high (Aggelopoulou et al., 2010). Therefore, a high number of fruit determinations per sample and/or replications are generally needed which can be difficult with limited resources. Additionally, the selection of fruit samples is on a subjective basis, e.g., picking a sample for maturity testing can result in varying FF or SSC values depending on who took the sample. Moreover, spectral data varied strongly between sunny or shade sides of fruit (Zude et al., 2006; Betemps et al., 2012) and among sampling dates (Figure 1). In order to face these problems, a measurement protocol was set up to reduce data variability while sampling and subsequently reducing measurement errors. The protocol was partly described in the Materials and Methods section. On the other hand, with the UFG structure a 'Big Data' approach was possible and might help to overcome unknown treatment factors which could not be addressed within a traditional research framework (see further discussion about the UFG structure below).

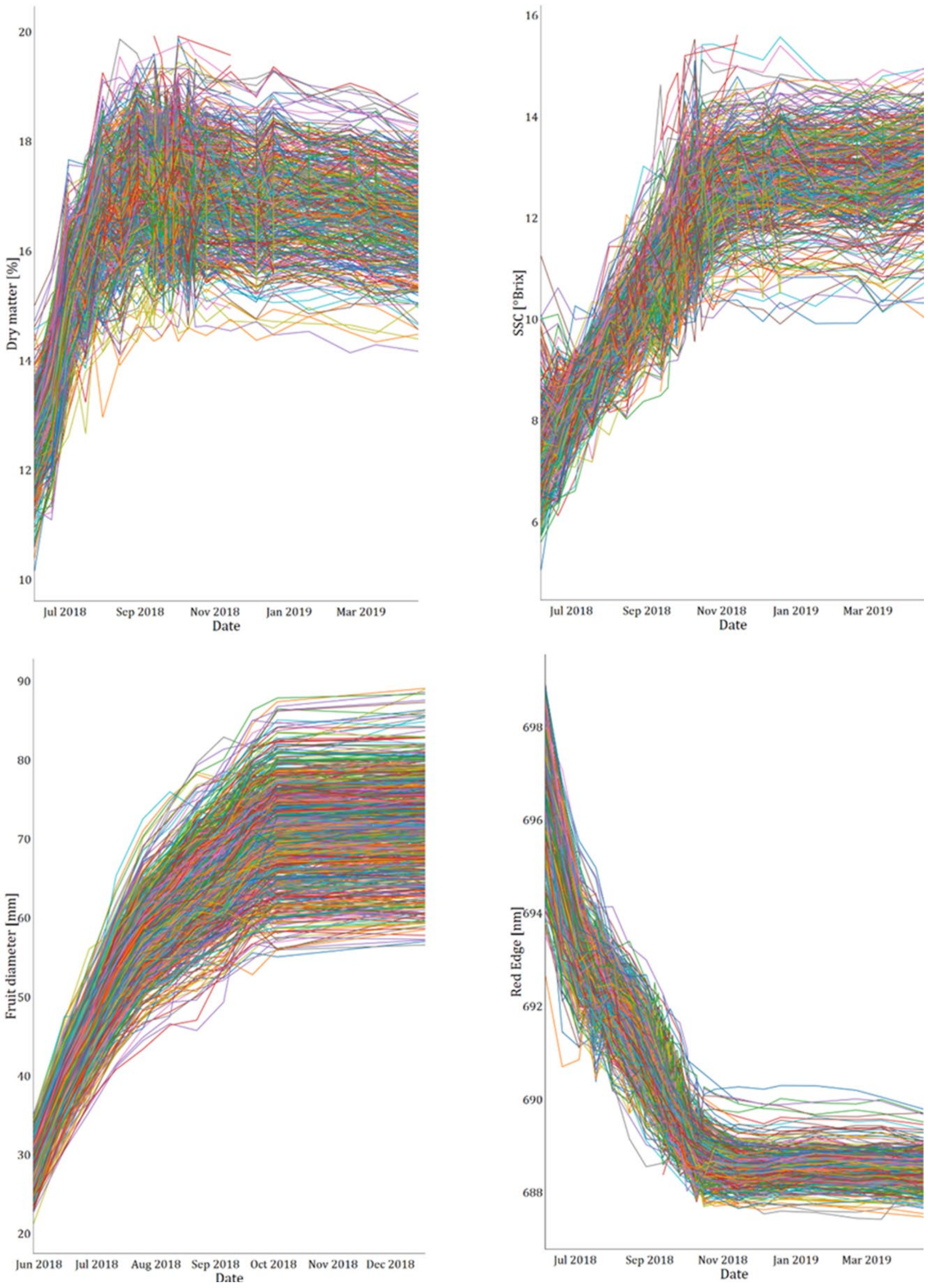

Figure 1. Spectral time-series for dry matter (top left), soluble solids content (SSC, top right) and red edge (bottom right) and fruit diameter (bottom left) data measured in the season 2018/2019. Each line represents individual fruit (*n*=423 for spectrometer; *n*=846 for caliper measurements). Fruit was harvested on 3 October 2018.

No other ‘Big Data’ study within our research question was found in the literature to be able to compare results with. However, it is known that constraints exist to link physiological disorders with standard statistical methods since the factors interact in a complex way (Lammertyn et al., 2000; Verlinden et al., 2002). Hence, these models could have a problem with over-fitting.

Statistical constraints

There is always the question on how much data to collect. Reinhart (2015) described that it is possible to miss real effects by not collecting enough data for further statistical analyses. However, statistical power is defined as the ability to detect true effects with a given experimental design and sample size. It is mainly determined by natural variability between subjects, sample size, effect size and measurement errors. Assuming independent, normally distributed observations, power analyses (with a preferred significance level of 0.05 and a power of 0.80) showed that a minimum sample size of n=29 is necessary to detect a conventional large effect size (0.5) for a t-test and n=144 for a three level ANOVA per group. The UFG structure in the present study contained one or two repeated measurements per device. With this structure a ‘Big Data’ modelling approach with numerous collections (information on PSD from one tree sector) containing always the same input data (e.g., VIS/NIR, fruit growth) was provided and “unimportant” information should get sorted out due to the numerous collections. Anyhow, the present research data were reviewed using standard statistical analyses with treatment means.

Time-series data for SSC, DM, RE and fruit growth (non-destructive)

Figure 1 shows the increase of SSC and DM during fruit maturation for single fruit (n=423). Single SSC values have a greater variance for the first measurement compared to DM in 2018. Additionally, there is a strong fluctuation across measurement dates for both DM and SSC in the field, whereas storage values seem to be more stable. The decrease in RE is overall smoother (Figure 1) and is towards harvest as expected (McGlone et al., 2002; Zude-Sasse et al., 2002; Merzlyak et al., 2003). We therefore expect that the oscillation seen in the SSC and DM values based on the NIR spectra is not due to mishandling the device in the field. Further research on the PLSR model needs to be undertaken, also with regard to temperature effects in the NIR region and differences in diurnal/seasonal fruit water content which also affects absorbance in the NIR region. Sample timing during a day should have no effect on RE (Zude-Sasse et al., 2002; Padilla et al., 2019).

The mean RE (s.d. in brackets) for standard crop load treatment was 689.3 (0.49) nm. No differences were found between crop load and calcium treatments. In general, RE values at harvest differ every season (data not shown).

The mean DM value for the standard crop load was 17.6 (0.81) % at harvest. There were no differences in DM among light, standard or heavy crop load. Calcium spraying resulted in a significant difference of DM content (Table 1). DM content with spraying was 17.4 (0.64) % compared to no spraying 16.6 (0.95) %.

Table 1. Results of one-way ANOVA for differences in treatment means at harvest in the season 2018/2019.

Parameter	Treatment	Levels	ANOVA
Dry matter	Calcium spraying	With, without	F(1.34)=9.20, p<0.01
Soluble solids content	Crop load	Light, standard, heavy	F(2.105)=6.05, p<0.001
Fruit diameter	Crop load	Light, standard, heavy	F(2.211)=80.46, p<0.001
Fruit diameter	Tree sector	Bottom, middle, top	F(2.836)=138.30, p<0.001

Assumptions of homogeneity and normality for SSC were slightly violated with p=0.09 and p=0.03, respectively. ANOVA showed a significant difference for SSC between crop load treatments. Post hoc comparisons using the Tukey HSD test indicated that the mean SSC values were significantly (p<0.001) different between light and heavy crop load with 12.3

(0.95) and 11.7 (0.60) °Brix, respectively. There was no difference in SSC for the calcium treatments.

Fruit diameter showed a highly significant difference among the crop load levels. Post hoc comparisons using the Tukey HSD showed that the mean between each treatment was significantly different for light 75.9 (5.19), standard 70.8 (5.22) and heavy crop load 65.1 (4.85) mm. No difference in fruit diameter for the calcium treatments were detected. Additionally, fruit diameter at harvest from all 'BigApple' treatments showed a significant difference in means between tree sectors of bottom 67.5 (5.53) mm, middle 69.5 (5.27) mm and top 74.6 (5.14) mm. Looking at the influence of the sector on spectral data, we also have a problem with homogeneity and normality.

The mean number of fruit per tree at harvest were 75 (24), 135 (21) and 219 (63) for light, standard, and heavy crop load, respectively.

Sector influence on physiological disorders

Every season showed different severity of PSD. The 2018 growing season at the KOB was unusually warm and dry. A high severity for bitter pit (Figure 2) and also some superficial scald was observed. Superficial scald is a non-typical PSD for 'Braeburn'. There is a positive correlation between shaded parts of the apple tree canopy and calcium related disorders (de Freitas and Pareek, 2019) which could be related to a decreased photosynthesis and a reduced transpiration rate from the bottom sector. Further, warm temperatures might have led to an inhibited translocation of important plant metabolites, such as SSC and DM, within different tree sectors and increased PSD susceptibility. The severity score data are strongly skewed to the right on the zero value (no PSD) which leads to a non-normal distribution. Therefore, no ANOVA is displayed.

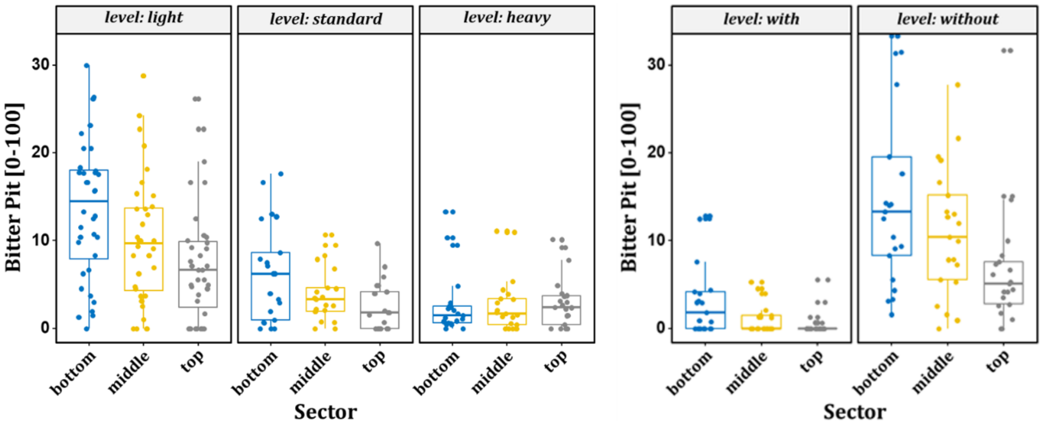

Figure 2. Bitter pit severity [0-100] for the crop load treatments (left) shown by crop load level and sector. Crop load treatments received good practice applications for calcium chloride spraying. Calcium treatments (right) with or without weekly sprays shown by sector.

CONCLUSIONS

The 'Big Data' approach resulted in a large data set with interesting side effects such as the sector influence on bitter pit in 2018. The sector influence on PSD occurrence and yield at harvest will be examined in future research. More research is needed regarding VIS/NIR prediction of soluble solids content and dry matter with PLSR field models to improve model reliability in the field. Given that the expression of PSD varies markedly each year and a high number of collections are needed to train AI models, a much longer period than three years is needed for a robust PSD prediction.

ACKNOWLEDGEMENTS

We would like to thank Daniel Stöckeler for statistical discussions and advice and Josef Streif for his enduring support to search for new ways to maintain fruit quality.

The project was supported by funds of the Federal Ministry of Food and Agriculture (BMEL) based on a decision of the Parliament of the Federal Republic of Germany via the Federal Office for Agriculture and Food (BLE) under the innovation support program.

Literature cited

Aggelopoulou, K.D., Wulfsohn, D., Fountas, S., Gemtos, T.A., Nanos, G.D., and Blackmore, S. (2010). Spatial variation in yield and quality in a small apple orchard. Precis. Agric. *11* (*5*), 538–556 https://doi.org/10.1007/s11119-009-9146-9.

Betemps, D.L., Fachinello, J.C., Galarça, S.P., Portela, N.M., Remorini, D., Massai, R., and Agati, G. (2012). Non-destructive evaluation of ripening and quality traits in apples using a multiparametric fluorescence sensor. J. Sci. Food Agric. *92* (*9*), 1855–1864 https://doi.org/10.1002/jsfa.5552. PubMed

de Freitas, S.T., and Pareek, S. (2019). Postharvest physiological disorders in fruits and vegetables. In Postharvest Physiological Disorders in Fruits and Vegetables, 1st edn, S.T. de Freitas, and S. Pareek, eds. (Boca Raton, Florida, USA: CRC Press), p.3–14 https://doi.org/10.1201/b22001.

Ferguson, I., Volz, R., and Woolf, A. (1999). Preharvest factors affecting physiological disorders of fruit. Postharvest Biol. Technol. *15* (*3*), 255–262 https://doi.org/10.1016/S0925-5214(98)00089-1.

Ford, E.M. (1979). Effect of post-blossom environmental conditions on fruit composition and quality of apple. Commun. Soil Sci. Plant Anal. *10* (*1-2*), 337–348 https://doi.org/10.1080/00103627909366899.

Franck, C., Lammertyn, J., Ho, Q.T., Verboven, P., Verlinden, B., and Nicolaï, B.M. (2007). Browning disorders in pear fruit. Postharvest Biol. Technol. *43* (*1*), 1–13 https://doi.org/10.1016/j.postharvbio.2006.08.008.

Hatoum, D., Buts, K., Hertog, M.L.A.T.M., Geeraerd, A.H., Schenk, A., Vercammen, J., and Nicolaï, B.M. (2014). Effects of pre- and postharvest factors on browning in Braeburn. HortScience *41*, 19–26 https://doi.org/10.17221/180/2013-HORTSCI.

Ho, Q.T., Verboven, P., Verlinden, B.E., Schenk, A., Delele, M.A., Rolletschek, H., Vercammen, J., and Nicolaï, B.M. (2010). Genotype effects on internal gas gradients in apple fruit. J. Exp. Bot. *61* (*10*), 2745–2755 https://doi.org/10.1093/jxb/erq108. PubMed

Lammertyn, J., Aerts, M., Verlinden, B.E., Schotsmans, W., and Nicolaï, B.M. (2000). Logistic regression analysis of factors influencing core breakdown in ‘Conference’ pears. Postharvest Biol. Technol. *20* (*1*), 25–37 https://doi.org/10.1016/S0925-5214(00)00114-9.

Mayer, A.M. (2006). Polyphenol oxidases in plants and fungi: going places? A review. Phytochemistry *67* (*21*), 2318–2331 https://doi.org/10.1016/j.phytochem.2006.08.006. PubMed

McCormick, R.J., Biegert, K., and Streif, J. (2017). Risk of ‘Braeburn’ browning disorder based on weather and orchard factors. Acta Hortic. (in press).

McGlone, A.V., Jordan, R.B., and Martinsen, P.J. (2002). Vis/NIR estimation at harvest of pre- and post-storage quality indices for "Royal Gala" apple. Postharvest Biol. Technol. *25* (*2*), 135–144 https://doi.org/10.1016/S0925-5214(01)00180-6.

Merzlyak, M.N., Solovchenko, A.E., and Gitelson, A.A. (2003). Reflectance spectral features and non-destructive estimation of chlorophyll, carotenoid and anthocyanin content in apple fruit. Postharvest Biol. Technol. *27* (*2*), 197–211 https://doi.org/10.1016/S0925-5214(02)00066-2.

Osinenko, P., Biegert, K., McCormick, R., Göhrt, T., Devadze, G., Streif, J., and Streif, S. (2021). Application of non-destructive sensors and big data analysis to predict physiological storage disorders and fruit firmness in ‘Braeburn’ apples. Computers and Electronics in Agriculture 183, 106015 https://doi.org/10.1016/j.compag.2021.106015.

Padilla, F.M., de Souza, R., Peña-Fleitas, M.T., Grasso, R., Gallardo, M., and Thompson, R.B. (2019). Influence of time of day on measurement with chlorophyll meters and canopy reflectance sensors of different crop N status. Precis. Agric. *20* (*6*), 1087–1106 https://doi.org/10.1007/s11119-019-09641-1.

R Core Team. (2018). A Language and Environment for Statistical Computing. www.R-project.org.

Reinhart, A. (2015). Statistics Done Wrong (San Francisco, CA, USA: William Pollock)

Sams, C.E. (1999). Preharvest factors affecting postharvest texture. Postharvest Biol. Technol. *15* (*3*), 249–254 https://doi.org/10.1016/S0925-5214(98)00098-2.

Solovchenko, A.E., Merzlyak, M.N., and Pogosyan, S.I. (2010). Light-induced decrease of reflectance provides an insight in the photoprotective mechanisms of ripening apple fruit. Plant Sci. *178* (*3*), 281–288 https://doi.org/10.1016/j.plantsci.2010.01.008.

Streif, J., and Kittemann, D. (2018). Fruchtqulität und Lagerung. In Lucas' Anleitung zum Obstbau, 33rd edn, M. Büchele, ed. (Stutgartt, Germany: Eugen Ulmer Verlag), p.393–435.

Verlinden, B.E., de Jager, A., Lammertyn, J., Schotsmans, W., and Nicolaï, B.M. (2002). PH-postharvest technology: effect of harvest and delaying controlled atmosphere storage conditions on core breakdown incidence in 'Conference' pears. Biosystems Eng. *83* (*3*), 339–347 https://doi.org/10.1006/bioe.2002.0127.

Walsh, K.B. (2016). The evolution of spectrophotometers used in fruit quality assessment. Acta Hortic. *1119*, 203–208 https://doi.org/10.17660/ActaHortic.2016.1119.28.

Watkins, C.B., and Mattheis, J.P. (2019). Apple. In postharvest physiological disorders in fruits and vegetables. In Postharvest Physiological Disorders in Fruits and Vegetables, 1st edn, S.T. de Freitas, and S. Pareek, eds. (Boca Raton, Florida, USA: CRC Press), p.165–206 https://doi.org/10.1201/b22001.

Zude, M., Herold, B., Roger, J.M., Bellon-Maurel, V., and Landahl, S. (2006). Non-destructive tests on the prediction of apple fruit flesh firmness and soluble solids content on tree and in shelf life. J. Food Eng. *77* (*2*), 254–260 https://doi.org/10.1016/j.jfoodeng.2005.06.027.

Zude-Sasse, M., Truppel, I., and Herold, B. (2002). An approach to non-destructive apple fruit chlorophyll determination. Postharvest Biol. Technol. *25* (*2*), 123–133 https://doi.org/10.1016/S0925-5214(01)00173-9.

3 Influence of precipitation on VIS/NIR spectra of ’Gala’ apples

K. Biegert, S. A. Lohner, R. J. McCormick, A. Kienle, P. Braun

Acta Hortic. 1327 (2021)

Influence of precipitation on Vis/NIR spectra of 'Gala' apples

K. Biegert[1,a], S.A. Lohner[2], R.J. McCormick[1], A. Kienle[2] and P. Braun[3]

[1]Kompetenzzentrum Obstbau Bodensee, Ravensburg, Germany; [2]Institut für Lasertechnologien in der Medizin und Meßtechnik an der Universität Ulm, Ulm, Germany; [3]Hochschule Geisenheim University, Institut für Obstbau, Geisenheim, Germany.

Abstract

Vis/NIR (visible/near infrared) scanning is a promising tool to obtain non-destructive information on apple fruit quality parameters. Changes in plant pigments like chlorophyll, anthocyanins and carotenoids can be followed in the Vis region during fruit growth. Soluble solids and dry matter content are obtained from partial least square regression models developed from the NIR spectra. However, the light absorption in the NIR wavelength range is particularly influenced by water and carbohydrates. This study investigates, if precipitation before field scanning can lead to changes in the NIR absorption. In Southwest Germany Vis/NIR orchard and lab scanning of 'Gala' apples were undertaken for seven weeks around harvest in 2019. Apples were either covered with hail net (standard orchard practice) or plastic sheet rain covers (RC). RC were installed to protect fruit from direct precipitation in order to reduce plant protection applications. The study showed no influence of precipitation on the Vis spectra. The NIR spectra revealed a 4-5% lower water concentration for the RC treatment in the lab, but no distinct effects for field scanning at 975 nm after rain events. Results from spectral indices and standard maturity testing during fruit ripening are shown.

Keywords: absorbance, scattering, fruit water content, field spectrometer, integrating sphere

INTRODUCTION

The optimum harvest date (OHD) determines fruit storability, quality and reduces post-harvest losses in apple production. The OHD is influenced among others by seasonal weather conditions, cultivar or crop load. A commonly used destructive maturity index to determine the OHD is the Streif index (SI) calculated from fruit firmness, soluble solids content (SSC) and a starch index (Streif and Kittemann, 2018). The SI is usually calculated for representative samples taken from a wider fruit growing region and are often not specific enough to determine individual block differences. Currently, Vis/NIR spectrometer scanning is being investigated to predict OHD non-destructively in the field and in particular for orchard lots on a small scale. A detailed OHD mapping could potentially be used in automated harvest machines. Suitable Vis/NIR spectrometers are available, but their field application is still at its beginning (Walsh et al., 2020). Reasonably priced spectrometers for the Vis/NIR range between 400 and 1200 nanometer (nm) with relatively fast processing for field use can be obtained. However, the lower cost devices offer only a limited spectral range or a partial least square regression (PLSR) model control which means that PLSR models are limited only to reference values obtained from the manufacturer. PLSR models using the shortwave NIR region can be built to predict apple SSC and dry matter content (DMC) (Zhang et al., 2019). The light absorption in the wavelength range around 980 nm can be attributed to the influence of water, which generally depends on the temperature and the concentration of other organic substances (Giangiacomo, 2006).

However, starch and firmness which are also input variables in the SI cannot yet be related to spectral information in the Vis/NIR wavelength. Additional fruit information from the Vis wavelength can be obtained from changes in the plant pigments using spectral indices

---

[a]E-mail: Konni.biegert@kob-bavendorf.de

Acta Hortic. 1327. ISHS 2021. DOI 10.17660/ActaHortic.2021.1327.88
Proc. IV International Symposium on Horticulture in Europe – SHE2021
Eds.: J.N. Wünsche and A. Milyaev

for chlorophyll, anthocyanin or carotenoids (Merzlyak et al., 2003).

Current research approaches for OHD predictions are based on autoregressive time series to model chlorophyll, anthocyanin, SSC and DMC changes from the beginning of the growing season together with weather data to predict future values (Osinenko et al., 2021). Other approaches to separate light absorption and scattering with more advanced technologies like spatial frequency domain imaging to separate structural and chemical characteristics are being followed (Lohner et al., 2019, 2021). These methods all aim to find a reliable link between the sensor information and non-destructive OHD predictions, fruit physiological responses related to changes in weather and orchard management factors.

Rainfall and subsequent uptake of water through the fruit skin might have an influence on the aforementioned results. In other words, sampling time in relation to rain events might influence the scan results. A possible influence of rain events on these apple Vis/NIR spectra has not been addressed before. Knoche (2014) explained the mechanism between rainfall and fruit cracking of soft fruit like cherries. Small micro cracks develop in the outer layers of the fruit during growth and can lead to a “zipper-type propagation” that increases the fruit’s water content after rain. The micro cracks are located only in the cuticula, and develop further into macro cracks in the epidermal cells, ultimately releasing cell contents into the apoplast (Grimm et al., 2019). It remains an open research question as to whether or not and to which extent apple fruit skin takes up water during growth. Lang (1990) suggested that water uptake through the skin has a marginal effect on apple fruit growth.

This work presents time-series data for spectral absorbance and scattering properties on ‘Gala’ apples grown under hail net (HN) and plastic sheet rain covers (RC) before harvest. We examined, if precipitation prior to a Vis/NIR sampling has an effect on the shortwave NIR absorption which is used further in PLSR models to predict SSC and DMC. In addition, we present the temporal development of Vis/NIR spectral and conventional harvest indices for ‘Gala’ apples in the season 2019.

MATERIALS AND METHODS

Study design

The study was performed in 2019 during the ‘Gala’ harvest season at the Kompetenzzentrum Obstbau Bodensse (KOB) in Southwest Germany (47.767212 N, 9.558757 E). Spectral Vis/NIR scans were taken on a weekly basis and additionally after heavy rain events for a period of four weeks prior to the first selective harvest and until the end of the harvest window. To exclude temperature effects on PLSR predictions the reference fruit in the lab were scanned at three different temperatures and the field scanning was always around mid-morning. The apple cultivar *Malus × domestica* ‘Gala’ (clone Simmons/Buckeye) was grafted on M9 rootstock and planted in 2017. Trees were grown as slender spindles in a North-South row direction (3.20×0.60 m). Temperature and rainfall data were obtained from a weather station some 100 m from the trial plots (Bavendorf location www.wetter-bw.de).

The trial plots were located in the 1.6 ha ‘Interreg’ model orchard to improve the integrated production toward a low-residue strategy (project “Modellanlage zur Weiterentwicklung des Integrierten Pflanzenschutzes”). A row of 54 ‘Gala’ trees was chosen at random in the middle of each of two blocks covered either with plastic sheet Rain Cover (RC) or Hail Net (HN). Within each respective row, 20 trees were hand thinned after June drop to approximately 50 fruit per tree. Thereof, 20 apples (10 on the east and 10 on the west side of the trees) in the middle sector of five trees were marked on the sun exposed fruit face for repeated Vis/NIR scanning. Ten comparable apples from the neighboring 15 trees in the rows were picked for weekly SI maturity tests (Streif and Kittemann, 2018) and six apples couriered for integrated sphere laboratory scanning (see below).

Vis/NIR spectral measurements

Repeated scans on tree were taken with a portable spectrometer (F-750, Felix Instruments, Camas, USA, spectral range of 310-1100 nm, spectral sampling of 3 nm, and daylight correction) from 20 apples per scanning date. The F-750 device does not provide the user with absolute absorbance. The software uses an internal daylight correction with shutter open and closed scan per fruit scan and therefore gives a relative value for the absorbance. In comparison to other spectral devices the absorbance pattern is the same, but negative (Donis-González et al., 2020). The mean of three scan repetitions per apple position were used. Water absorbance was derived at the wavelength value of 975 nm (close to the second overtone water absorbance peak). Pigment indices for a normalized difference anthocyanin index (NAI), a normalized difference vegetation index (NDVI) and a plant senescence reflection index (PSRI) were calculated from the following formulas:

$$NAI = \frac{(\mathrm{R780} - \mathrm{R549})}{(\mathrm{R780} + \mathrm{R549})}\quad NDVI = \frac{(\mathrm{R750} - \mathrm{R705})}{(\mathrm{R750} + \mathrm{R705})}\quad PSRI = \frac{(\mathrm{R678} - \mathrm{R501})}{\mathrm{R801}}$$

where R is the reflectance at the respective wavelength (Merzlyak et al., 2003; Zude, 2003).

In the laboratory, the light remission and transmission of different apple samples in the spectral range of 400-1600 nm were measured with an integrating sphere setup (Bergmann et al., 2020; Foschum et al., 2020). Subsequently, an evaluation algorithm based on Monte-Carlo simulations was used to determine the effective scattering coefficient μ_s and absorption coefficient μ_a. To estimate the water content of the samples, the ratio of their absorption coefficients relative to the absorption of deionized water at a wavelength of 975 nm (0.04485 mm^{-1}) was calculated (Hale and Querry, 1973). This procedure is based on the assumption that the absorption of water dominates in this wavelength range and that no other background absorbers are present.

RESULTS AND DISCUSSION

Laboratory results for fruit maturity

There was no clear difference for the SI before harvest for the two treatments (Figure 1). However, SSC was higher for the RC treatment, although it was expected that the RCs would have a higher shading effect on the trees resulting in a reduced SSC accumulation in the fruit. Elevated SSC values in the RC treatment might have an influence on the absorption at 975 nm (Giangiacomo, 2006). The laboratory reference values taken for SSC analysis were insufficient to build a suitable PLSR model. Therefore, no SSC predictions were made for the field scans. No difference in fruit size between RC and HN treatments was measured (data not shown).

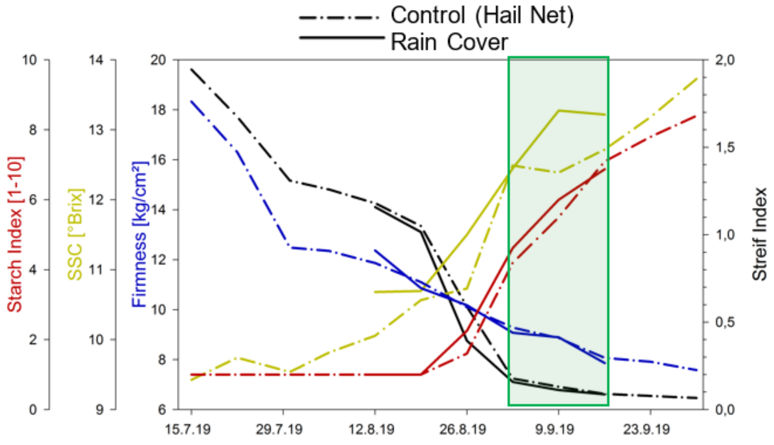

Figure 1. Mean maturity values (firmness, soluble solids content, starch index) for ‘Gala’ apples under hail net (dotted line) and rain cover (solid line). Harvest window defined by the Streif index was September 2 till 16 (shown as green box).

Spectral Vis/NIR measurements

From the Vis/NIR spectra, the NDVI, NAI and PSRI indices for chlorophyll, anthocyanin and chlorophyll / carotenoids, respectively are shown in Figure 2. Spectral scans taken in the present study show a high variability. Therefore, only the standard error was plotted.

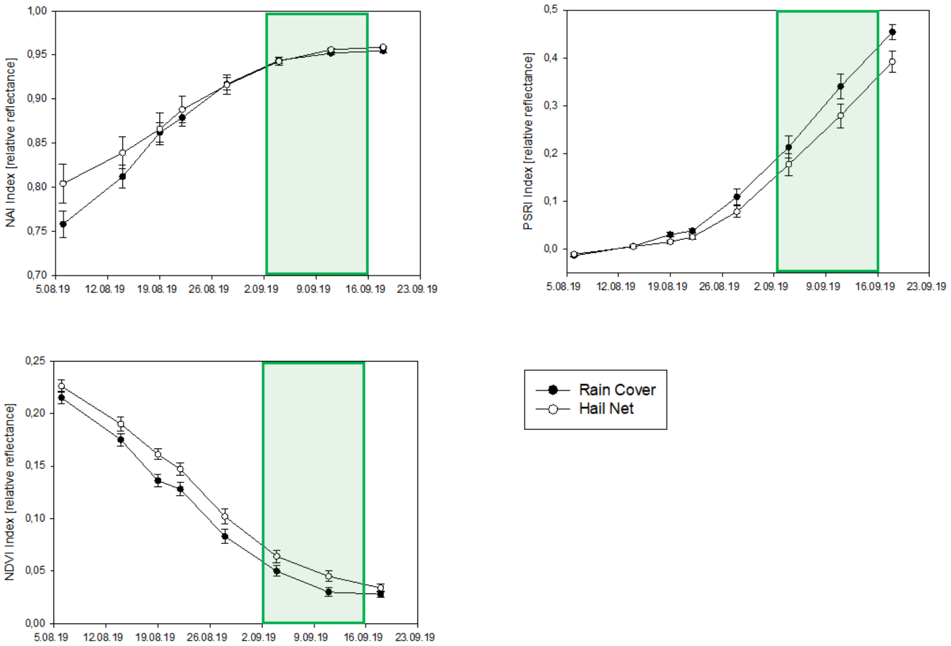

Figure 2. Repeated non-destructive field measurements on same marked apples calculated from normalized difference anthocyanin index (NAI), normalized difference vegetation index (NDVI) and plant senescence reflection index (PSRI) shown as mean ± standard error for the rain cover and hail net treatment. Harvest window defined by the Streif index is shown as green box.

Four weeks before harvest, the NAI values for the HN treatment were higher than for the RC, but at harvest no differences between treatments were found. High light levels and large daily temperature variations accelerate the built up of anthocyanins. On the other hand when night temperatures are warm or the difference between day and night temperatures is small, anthocyanins can decrease (Saure, 1990). It is assumed that light interception is lower and differences in temperature are smaller under the RC treatment (no data available). This could explain the NAI results long before harvest which was also observed in other years at harvest for both cover types (data not shown). However, it does not fit with the results just before and at harvest time. We assume that distinct temperature differences in the season 2019 enhanced the anthocyanin built up in the RC treatment (Figure 2).

The chlorophyll decrease, as shown by the NDVI, in Figure 2 for the two treatments is generally similar throughout the preharvest period with fruit from the RC treatment constantly having lower values.

The PSRI is sensitive to changes in both chlorophyll and carotenoid pigments. In bicolored cultivars like 'Gala', this index is additionally affected by the overlapping influence of anthocyanins. The PSRI shows a slowly increasing difference between the RC and HN treatments. Assuming that foliar pesticide applications could affect the fruit coloration, the time of spray applications was compared to the measured reflectance indexes. However, no such effects could be detected. Plant protection sprays against apple scab were applied before the rain events (5.08. scab, 13.08. leaf fertilizer and codling moth, 22.08. leaf fertilizer, codling moth and storage rots). Further information about precipitation amounts is given in Figure 3. In conclusion, pigment information alone is not a sufficient indicator for an OHD for apples. However, the time-series data for NAI and NDVI flatten around harvest for 'Gala'. As expected, there was no obvious difference for the different spectral indices in the Vis spectra region after rain events.

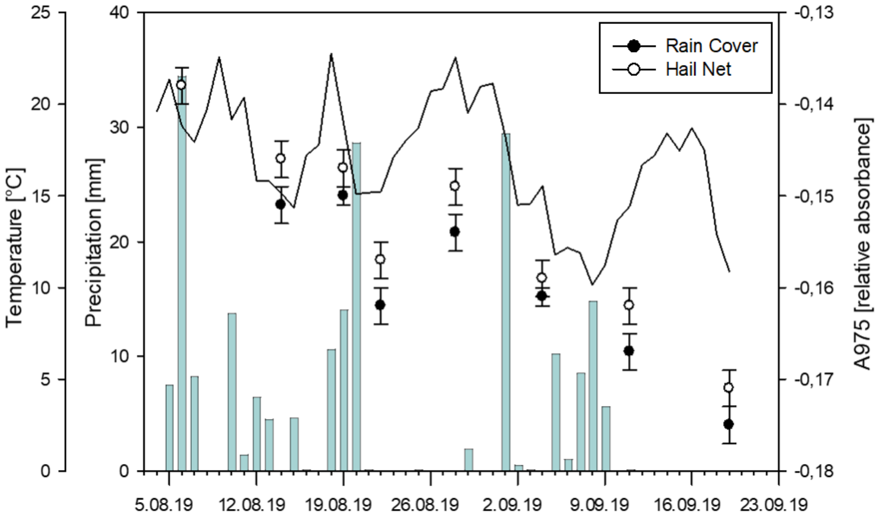

Figure 3. Daily mean air temperature (black line) and precipitation (turquoise bars) shown together with water absorbance at the 975 nm wavelength (dots) obtained with the F-750 field device for 'Gala' apples grown under plastic rain covers or hail net/control (mean ± standard error).

Water absorbance at 975 nm and the daily mean temperature and precipitation sum are shown in Figure 3. The first scans with the field device took place only minutes after a 30 mm rain event and showed no difference between the two treatments (06.08.19). Unlike the large variance for the spectral data, both treatments showed only a marginal difference after the first rain event. Also, there was no distinct effect observed for either the HN or RC fruit in the following scanning period after rain events. However, the RC treatment consistently revealed smaller absorbance values compared to HN fruit throughout the study. We hypothesize therefore that it is possible for apple fruit to take up small amounts of water from direct precipitation which leads to higher fruit water content. The calculated water content in Figure 4 with values around 100% or above (value on 15.07.19) is unrealistic and indicates that additional unknown absorbers like cellulose or sugars apparently affect the 975 nm scan absorbance. The amount of preharvest precipitation in August and September 2019 was 26% higher compared to the long-term station average. This wet weather pattern led to little difference in soil water availability between the HN and RC treatments. The precipitation run off from the plastic sheet RC, fell in the middle of the tractor driveway between the tree rows and was likely distributed laterally in the soil where it became available for the fruit trees. To ensure a similar water status, trees under RC and HN additionally received drip irrigation water throughout the study. For these reasons, the difference in water status between the two treatments was likely to be small.

Integrating sphere measurements in the laboratory for both RC and HN took place only on two sampling dates and a standard deviation of 4% was obtained for all samples. The estimated water content with the integrating sphere setup shows for apples grown under HN that the water content increased by 4-5% compared to fruit grown under the RC treatment (Figure 4). However, as described above, both HN and RC treatments received sufficient rain and drip irrigation water. Together with the high fruit variability this might explain why we found no clear treatment differences, at least with the laboratory scanning. The fruit scans taken in this study occurred mostly between 15 and 20°C and we conclude that no temperature effect altered the shortwave NIR spectra absorption. However, differences in the accumulation of SSC between the samples could have affected the NIR absorption. The apparent absorption spectra measured by the F-750 device are the result of both light scattering and absorbance effects. Additionally, scattering decreased during ripening. Within the limitations of the study methodology as discussed above we assume no direct effect of rain events on the Vis/NIR spectra. However, the consistent difference between the treatments might indicate that fruit can take up water through the apple skin. Further studies are needed to evaluate whether direct precipitation can lead to an increased apple fruit water content.

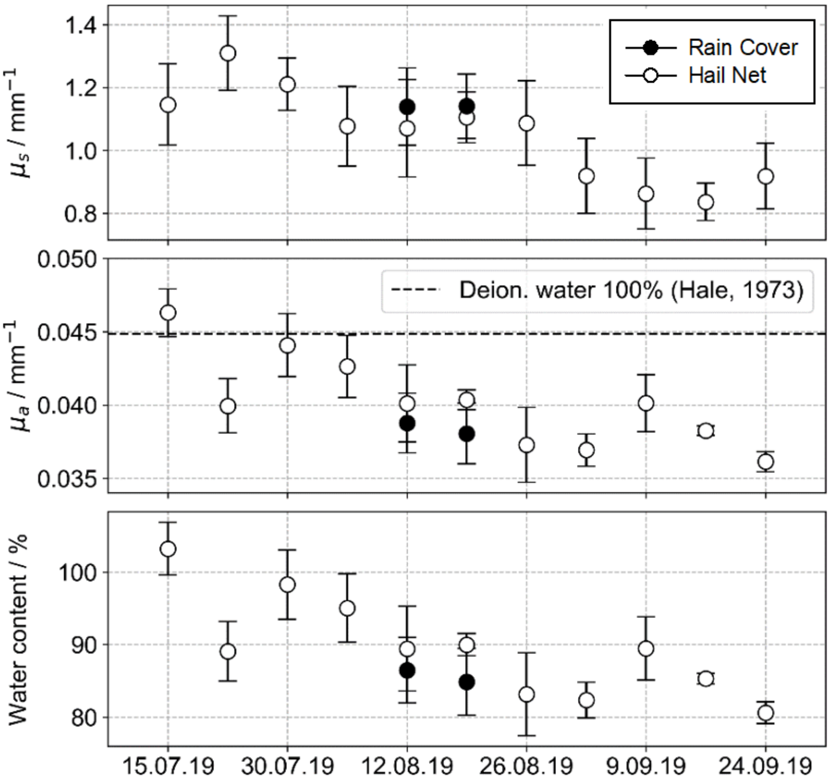

Figure 4. Effective scattering coefficient (top), absorption coefficient (middle) and estimated water content (bottom) at a wavelength of 975 nm measured in the laboratory with integrating sphere for ‘Gala’ apples grown under rain covers (black dot) or hail net (white dot). Shown is the scan mean and vertical bars as ± standard error, dashed line indicates absorption for deionized water at 975 nm.

CONCLUSIONS

1) Apple fruit scans directly after a rain event did not lead to an increase of water absorbance values for the HN and RC treatments.
2) Fruit grown under HN showed a consistently higher water absorbance for the field scans in comparison to fruit grown under RC.
3) Integrating sphere calculation in the laboratory on two occasions (no more data available) showed a 4-5% higher water content for HN fruit compared to RC (standard deviation per single fruit scan is higher than the difference in water

concentration in total). Therefore, no significance can be stated. However, the absorbance derived from the field scans is consistently higher, see (2). More research is needed.

4) Field and laboratory scans showed a similar decreasing course for absorbance values at 975 nm during maturation.
5) Spraying of plant protection products showed no effect on any of the spectral indices (PSRI, NDVI or NAI).

ACKNOWLEDGEMENTS

The project was supported by funds of the “Projektträger des BMWi ZIM Koooperationsprojekte im Rahmen des Programms Zentrales Innovationsprogramm Mittelstand” and undertaken within the orchard planted with funds from the European regional program “interreg Alpenrhein, Bodensee, Hochrhein”.

Literature cited

Bergmann, F., Foschum, F., Zuber, R., and Kienle, A. (2020). Precise determination of the optical properties of turbid media using an optimized integrating sphere and advanced Monte Carlo simulations. Part 2: experiments. Appl. Opt. *59* (*10*), 3216–3226 https://doi.org/10.1364/AO.385939. PubMed

Donis-González, I.R., Valero, C., Momin, M.A., Kaur, A., and C. Slaughter, D. (. (2020). Performance evaluation of two commercially available portable spectrometers to non-invasively determine table grape and peach quality attributes. Agron. *10*, 148 https://doi.org/10.3390/agronomy10010148.

Foschum, F., Bergmann, F., and Kienle, A. (2020). Precise determination of the optical properties of turbid media using an optimized integrating sphere and advanced Monte Carlo simulations. Part 1: theory. Appl. Opt. *59* (*10*), 3203–3215 https://doi.org/10.1364/AO.386011. PubMed

Giangiacomo, R. (2006). Study of water–sugar interactions at increasing sugar concentration by NIR spectroscopy. Food Chem. *96* (*3*), 371–379 https://doi.org/10.1016/j.foodchem.2005.02.051.

Grimm, E., Hahn, J., Pflugfelder, D., Schmidt, M.J., van Dusschoten, D., and Knoche, M. (2019). Localized bursting of mesocarp cells triggers catastrophic fruit cracking. Hortic. Res. *6* (*1*), 79 https://doi.org/10.1038/s41438-019-0161-3. PubMed

Hale, G.M., and Querry, M.R. (1973). Optical constants of water in the 200-nm to 200-μm wavelength region. Appl. Opt. *12* (*3*), 555–563 https://doi.org/10.1364/AO.12.000555. PubMed

Knoche, M. (2014). Water Uptake through the surface of fleshy soft fruit: barriers, mechanism, factors, and potential role in cracking. In Abiotic Stress Biology in Horticultural Plants, (Springer Japan), p.147–166 https://doi.org/10.1007/978-4-431-55251-2_11.

Lang, A. (1990). Xylem, phloem and transpiration flows in developing apple fruits. J. Exp. Bot. *41* (*6*), 645–651 https://doi.org/10.1093/jxb/41.6.645.

Lohner, S.A., Nothelfer, S., Hohmann, A., Foschum, F., Biegert, K., Prunier, C., McCormick, R., and Kienle, A. (2019). Spatial-frequency domain imaging for maturation determination of Elstar apples. In Imaging and Appl. Optics 2019 (COSI, IS, MATH, PcAOP), (Optical Soc. of Am.), p. ITh4B.6.

Lohner, S., Biegert, K., Nothelfer, S., Hohmann, A., McCormick, R.J., and Kienle, A. (2021). Determining the optical properties of apple tissue and their dependence on physiological and morphological characteristics during maturation. Part 1: spatial frequency domain imaging. Postharvest Biol. Technol. *181*, 111647.

Merzlyak, M.N., Solovchenko, A.E., and Gitelson, A.A. (2003). Reflectance spectral features and non-destructive estimation of chlorophyll, carotenoid and anthocyanin content in apple fruit. Postharvest Biol. Technol. *27* (*2*), 197–211 https://doi.org/10.1016/S0925-5214(02)00066-2.

Osinenko, P., Biegert, K., McCormick, R.J., Göhrt, T., Devadze, G., Streif, S., and Streif, S. (2021). Application of non-destructive sensors and big-data analysis to predict physiological storage disorders and fruit firmness in ‘Braeburn’ apples. Comp. and Elec. in Agric. *183*, 106015 https://doi.org/10.1016/j.compag.2021.106015.

Saure, M.C. (1990). External control of anthocyanin formation in apple. Sci. Hortic. (Amsterdam) *42* (*3*), 181–218 https://doi.org/10.1016/0304-4238(90)90082-P.

Streif, J., and Kittemann, D. (2018). Lucas’ Anleitung zum Obstbau (Ulmer Eugen Verlag), p.393–435.

Walsh, K.B., McGlone, V.A., and Han, D.H. (2020). The uses of near infra-red spectroscopy in postharvest decision support: a review. Postharvest Biol. Technol. *163*, 111139 https://doi.org/10.1016/j.postharvbio.2020.111139.

Zhang, Y., Nock, J.F., Shoffe, Y.A., and Watkins, C.B. (2019). Non-destructive prediction of soluble solids and dry matter contents in eight apple cultivars using near-infrared spectroscopy. Postharvest Biol. Technol. *151*, 111–118 https://doi.org/10.1016/j.postharvbio.2019.01.009.

Zude, M. (2003). Comparison of indices and multivariate models to non-destructively predict the fruit chlorophyll by means of visible spectrometry in apple fruit. Anal. Chim. Acta *481* (*1*), 119–126 https://doi.org/10.1016/S0003-2670(03)00070-9.

4 Modelling soluble solids content accumulation in 'Braeburn' Apples

K. Biegert, D. Stöckeler, R. J. McCormick, P. Braun

Plants 10 (2021)

plants

MDPI

Article

Modelling Soluble Solids Content Accumulation in 'Braeburn' Apples

Konni Biegert [1,*,†], Daniel Stöckeler [2,†], Roy J. McCormick [1] and Peter Braun [3]

[1] Kompetenzzentrum Obstbau Bodensee, Fachgebiet Ertragsphysiologie, 88213 Ravensburg, Germany; mccormick@kob-bavendorf.de
[2] TUM School of Life Sciences, Technische Universität München, 85354 Freising, Germany; d.stoeckeler@posteo.de
[3] Institut für Obstbau, Hochschule Geisenheim University, 65366 Geisenheim, Germany; peter.braun@hs-gm.de
* Correspondence: konni.biegert@kob-bavendorf.de; Tel.: +49-751-7903-343
† These authors contributed equally to this work.

check for updates

Citation: Biegert, K.; Stöckeler, D.; McCormick, R.J.; Braun, P. Modelling Soluble Solids Content Accumulation in 'Braeburn' Apples. *Plants* **2021**, *10*, 302. https://doi.org/10.3390/plants10020302

Academic Editor: Riccardo Lo Bianco
Received: 31 December 2020
Accepted: 1 February 2021
Published: 5 February 2021

Abstract: Optical sensor data can be used to determine changes in anthocyanins, chlorophyll and soluble solids content (SSC) in apple production. In this study, visible and near-infrared spectra (729 to 975 nm) were transformed to SSC values by advanced multivariate calibration models i.e., partial least square regression (PLSR) in order to test the substitution of destructive chemical analyses through non-destructive optical measurements. Spectral field scans were carried out from 2016 to 2018 on marked 'Braeburn' apples in Southwest Germany. The study combines an in-depth statistical analyses of longitudinal SSC values with horticultural knowledge to set guidelines for further applied use of SSC predictions in the orchard to gain insights into apple carbohydrate physiology. The PLSR models were investigated with respect to sample size, seasonal variation, laboratory errors and the explanatory power of PLSR models when applied to independent samples. As a result of Monte Carlo simulations, PLSR modelled SSC only depended to a minor extent on the absolute number and accuracy of the wet chemistry laboratory calibration measurements. The comparison between non-destructive SSC determinations in the orchard with standard destructive lab testing at harvest on an independent sample showed mean differences of 0.5% SSC over all study years. SSC modelling with longitudinal linear mixed-effect models linked high crop loads to lower SSC values at harvest and higher SSC values for fruit from the top part of a tree.

Keywords: Vis/NIR; repeated longitudinal measurements; apple maturation; precision horticulture

1. Introduction

In apple fruit production, tree physiological status, the farmer's management decisions in the orchard, together with environmental factors influence postharvest fruit quality and storage pack-out. More specifically, factors that affect fruit quality can include crop load [1,2], timing of harvest [3], application of calcium and potassium fertilizer [4,5], light distribution within the orchard and temperature during important growth periods [6,7] as well as single tree or tree sector physiology [3].

Many factors within apple fruit tissues (cells per apple, energy status, cell wall stability [8]) which can determine harvest date and storage pack-out cannot be seen from the outside of the fruit. Depending on the wavelength, optical sensors (visible (Vis) and near-infrared (NIR) point spectroscopy) can help to get a non-destructive view of the fruit from 1–2 cm under the skin [9]. These portable optical sensors are now relatively inexpensive and fast [10]. In addition, data handling and chemometric software are user friendly (own experience). Light reflectance from the fruit can be monitored in the field to give information about plant pigment development such as chlorophyll, anthocyanins and carotinoids in the Vis spectra [11]. In addition, partial least squares regression (PLSR) modelling for the NIR spectra can be used to estimate soluble solids content (SSC) and dry matter content [12–14]. Further information on fruit tissues can be obtained from the light scattering of cell walls and other cellular components using more advanced technologies like spatial frequency domain imaging [15,16]. However, the latter laboratory based technology is not available for applied field-sensing to separate the absorbance from the scattering coefficient. One of the advantages of non-destructive sensor technology is the possibility to gain a large data set on a small-orchard scale during fruit maturation and link these spectral data together with other temporal and orchard field data. Biological and spatial variation are typically high, even within a small-scale apple orchard [17,18]. Moreover, fruit should be harvested and managed according to orchard variation such as site and cropping history to maintain the best possible fruit quality after long-term controlled atmosphere storage [19].

The development of SSC in individual apples depends mainly on the light distribution within the planting system and the fruit to leaf ratio per tree [20]. Furthermore, SSC values vary between different fruit and even for the same measurement position [12,21]. However, spectral scanning allows a large sample size to be obtained relatively fast. These measurements could provide a feasible alternative in the practice to labour intensive and costly laboratory analyses to gain a better idea of the distribution in SSC values.

Furthermore, standard ANOVA analyses are used at a particular moment in time (mostly at harvest) to determine the SSC distribution. This approach overlooks SSC developement over the course of time [22]. In the case of repeated measurements in agriculture and horticulture, mixed-effects models show clear advantages with respect to missing or unbalanced observations and different or restricted measurement periods [23]. When modelling is based on repeated measurements during fruit development, the longitudinal structure results in linear mixed-effect (LME) models to describe time-dependent changes linked to treatment effects and physiological influences. This class of LME models is a flexible subset of (generalized) regression models and can be used to model growth patterns in horticulture [24,25] and other research areas such as physical anthropology [26], clinical biometry [27] or ecology [28]. Modelling apple growth with expolinear, Gompertz and logistic [29,30] functions and adapted von Bertalanffy models [31] is common but SSC accumulation has been less frequently modelled. This is gradually changing through the use of in-depth biochemical analyses and the use of optical handheld sensors. Vis/NIR point spectrometers allow for repeated non-destructive spectral scanning on the same fruit. In a further classification process, longitudinal Vis/NIR data can enable modelling and classification of optimal harvest dates [32,33].

The present study focuses on non-destructive and longitudinal SSC accumulation in fruit in the orchard and the practical application of the above outlined methodology to set guidelines for their broader use. The carbohydrate physiology i.e., SSC accumulation during apple ripening was monitored within the experimental field treatments, reviewed from a user perspective and a statistical viewpoint. The results of the study were based on a large data set of Vis/NIR scans obtained over three study years.

This study investigates in detail (1) the number of calibration samples needed for a robust SSC prediction, (2) the effects of laboratory errors in wet chemistry analyses on PLSR model results, (3) the reliability of modelled SSC values in the orchard in comparison to standard laboratory tests of an independent sample and (4) time-dependent treatment effects on longitudinal SSC accumulation.

2. Results

The apple cropping seasons of 2016, 2017 and 2018 in Southwest Germany were distinctively different. A very wet spring with a light frost event during bloom was recorded in 2016. In 2017, severe frosts occurred during bloom in many European horticulture regions. At the Kompetenzzentrum Obstbau Bodensee, the number of trees available for research studies was reduced to those protected with heaters in plastic tents. Furthermore, 2018 was a relatively hot and dry year with 398 mm of precipitation between April to October compared to 956 mm and 730 mm for the same periods of 2016 and 2017, respectively.

There were also clear differences between years in plant development for the growth stages (BBCH) flowering and fruit ripe for picking with differences of up to 12 days.

SSC accumulation derived from the yearly calibrated PLSR model (Section 2.1.1) (Figure 1a) and fruit diameter growth (Figure 1b) are plotted as days after full bloom (DAFB) over the three study years. Fruit diameter and SSC were monitored at the same measurement intervals and for the same fruit. Fruit growth will not be further discussed here and serves only as additional background information on orchard data variance. SSC increases over time following a linear trend. In general, these data indicate a continuous mean SSC accumulation until apple maturity which is consistent with biochemical fruit analyses. In 2017 around 120 DAFB, the within-fruit variability during the time-series data acquisition shows either that the same fruit accumulate and degrade SSC between the scanning intervals or that the measurement environment negatively affected data acquisition. In 2016 and 2017, SSC had approximately the same values at around 120 DAFB. For 2018 the highest SSC values for the three study years were observed. In order to obtain a higher time-series resolution and larger time-series data for improved modelling in [33], data acquisition took place on a daily basis for 120-180 DAFB and SSC scanning started at 50 DAFB in 2018.

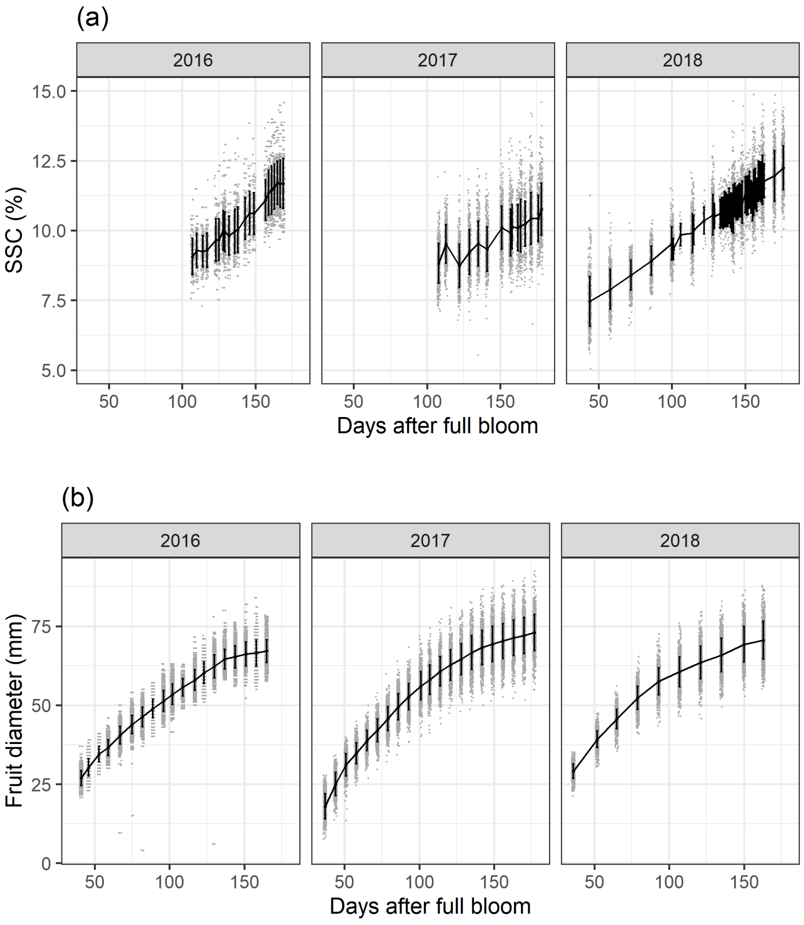

Figure 1. Soluble solids content (SSC) accumulation derived from the yearly calibrated (Section 2.1.1) partial least squares regression models (**a**) and fruit diameter growth (**b**) for the three study years and all treatments are shown. Mean values per measurement day are plotted as solid line, single values as grey dots and +/−standard deviations as black vertical bars.

2.1. PLSR Calibration Models

2.1.1. Multi-Year (2016–2018) Calibrated Model

The multi-year model was built with calibration data from all study years (2016–2018). The multi-year model was subsequently validated with either a multi-year or the respective yearly data set.The multi-year model results in a root mean square error of prediction (RMSEP) of 0.65% SSC (adjusted R^2 of 0.77) in 2016, 0.67% SSC in 2017 (adjusted R^2 of 0.72), and 0.54% SSC in 2018 (adjusted R^2 of 0.89) compared to 0.62% SSC (adjusted R^2 of 0.81) over all three years combined (Figure 2). A look at the RMSEP and the adjusted prediction R^2 is usually not sufficient to determine the presence of systematic errors in the PLSR model. Fitting a linear regression to the prediction values resulted in a slight deviation from a diagonal line indicating the presence of small but negligible systematic errors (bias). More specifically, the multi-year PLSR model possibly underestimates or overestimates the frequency of particularly low or high SSC values in 2017 and 2018. Residual plots (data not shown) suggest a slightly heteroscedastic structure. In terms of model performance over all years, the multi-year PLSR model appears to yield reasonable predictions with minor restrictions.

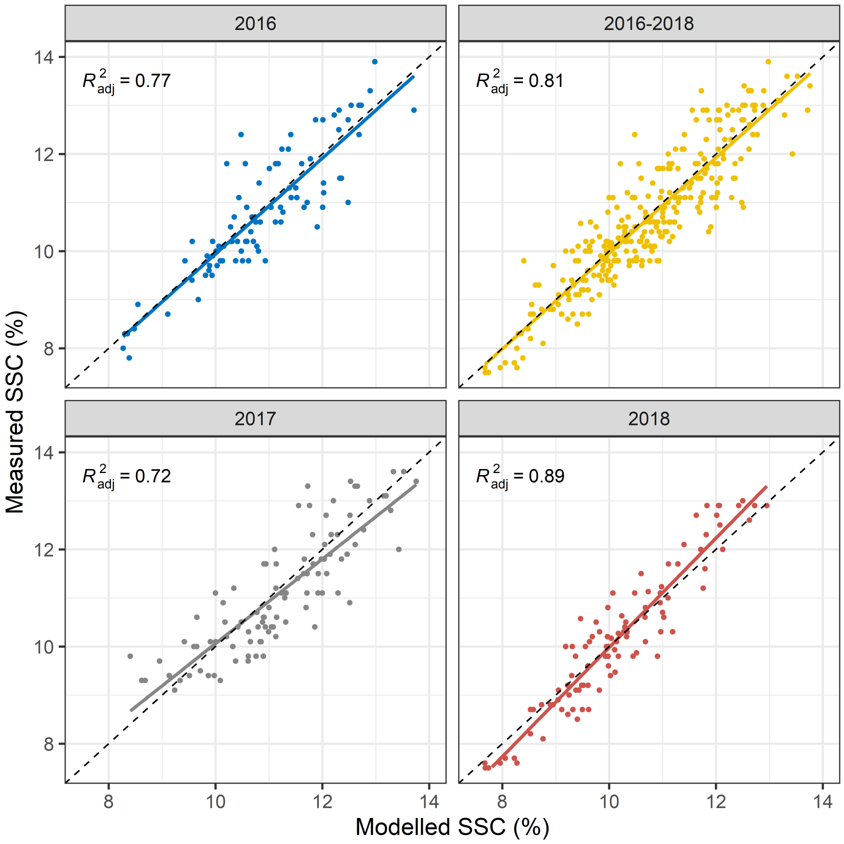

Figure 2. Regressions between laboratory measured and modelled % SSC. The calibration model was trained on 2016–2018 data. This model was thereafter evaluated with an independent validation data set for all years together and separately. Regression lines are plotted for each validation data set and adjusted prediction R^2 is displayed.

2.1.2. Year-Dependent Calibration Model Transfer to Other Years

Independent PLSR calibration models for each study year were calculated to check the transferability and adequacy of year-dependent PLSR model to other study years (500 observations in the calibration data set, 100 observations in the validation data set).

Results suggest that yearly calibrated models perform best for scans taken within the same year (Table 1).

Table 1. Root mean square error of prediction (RMSEP) of % soluble solids content (SSC) to test the transferability of calibration models after 500 Monte Carlo simulation runs per point (500 observations in each calibration data set, 100 observations in each validation data set. Mean and standard deviation (in brackets) for each point are shown.

Training Data Set	**Validation Data Set of Respective Years**			
	2016–2018	**2016**	**2017**	**2018**
2016–2018	0.65 (0.05)	0.68 (0.05)	0.68 (0.04)	0.57 (0.04)
2016	0.90 (0.16)	0.61 (0.05)	1.00 (0.30)	1.02 (0.21)
2017	0.83 (0.12)	0.95 (0.23)	0.57 (0.04)	0.90 (0.14)
2018	0.95 (0.10)	1.19 (0.20)	1.01 (0.08)	0.48 (0.03)

The multi-year PLSR model predictions (calibration data set) based on reference samples measured from all years in equal parts show a slight increase in the mean RMSEP values compared to the yearly calibrated prediction models. The calibration model based on 2016 data gives a RMSEP and standard deviation (sd) in bracket value of 0.61 (+/−0.05) % SSC for 2016 validation data compared to a RMSEP value of 0.68 (+/−0.05) % SSC for the multi-year model (2016–2018). In 2017 and 2018 similar results were obtained. Yet, all yearly calibrated models performed poorly in other years. Standard deviations were considerably higher when using validation data from years that were not part of the calibration data sets. This suggests two conclusions: first, yearly calibrated models tend to overfit the data and can hardly be used as general PLSR models. Second, as the range in SSC values in 2018 was wider than in 2016 or 2017, this increased range led to poor model performance for the 2016 and 2017 models which were not trained for particularly low or high SSC values.

2.2. Evaluation of the Training Data

2.2.1. Effect of Sample Sizes

To assess the effects of different calibration sample sizes, 500 repeated Monte Carlo simulation runs were performed. For each simulation run a stratified random sample with n = 20, 30, 40, 50, 75, 100, 125, 150, 175, 200, 300, 400 or 500 calibration measurements per year (corresponding to 60 to 1500 calibration measurements in total) was used as a calibration data set to calibrate a multi-year (2016–2018) PLSR model. The RMSEP was determined using a validation set with n = 200 observations for each year. The mean RMSEP of these Monte Carlo simulation runs and the standard deviations thereof are shown in Figure 3. PLSR models based only on 20 calibration scans per year show a mean RMSEP of 0.93 (+/−0.18 sd) % SSC in 2016, 0.91 (+/−0.17 sd) % SSC in 2017 and 0.95 (+/−0.28 sd) % SSC in 2018. PLSR models based on 100 calibration measurements per year result in a mean RMSEP of 0.70 (+/−0.06 sd) % SSC in 2016, 0.70 (+/−0.06 sd) % SSC in 2017 and 0.60 (+/−0.07 sd) % SSC in 2018. Based on 500 calibration measurements per year, a mean RMSEP of 0.67 (+/−0.05 sd) % SSC in 2016, 0.67 (+/−0.04 sd) % SSC in 2017 and 0.56 (+/−0.04 sd) % SSC in 2018 are obtained. As the 2018 calibration measurements include a higher proportion of scans taken during early fruit development, the larger range of SSC values available results in a supposedly lower RMSEP value. This fact, to a large extent, explains the apparent model improvement in 2018. Besides, the accuracy of laboratory calibration work may also have improved in the third year of the study. No differences in mean RMSEP values were detected for scans conducted at different temperatures in the laboratory with Monte Carlo simulation (∼10, 20 or 30 °C).

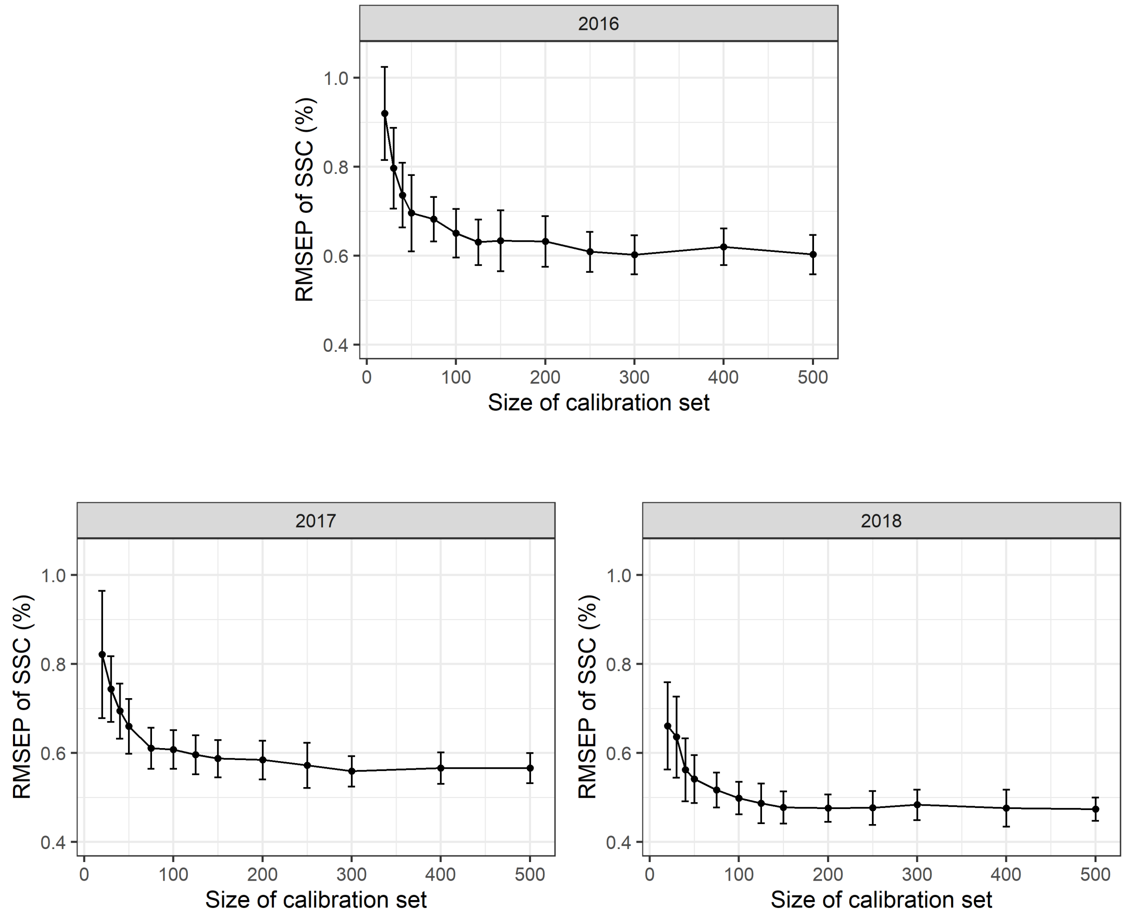

Figure 3. Root mean square error of prediction (RMSEP) in % soluble solids content (SSC) based on 2016, 2017 and 2018 partial least squares regression (PLSR) models to test the effect of reduced calibration sample sets. For each setting, 500 Monte Carlo simulation runs were performed. Mean and standard deviation for each point are shown and 500 observations in each calibration data set and 100 observations in each validation data set used.

2.2.2. Effect of the Data Range

To assess the prediction quality at certain SSC values the RMSEP was also determined with 500 repeated Monte Carlo simulation (1200 observations in the calibration data, 300 observations in the validation data set). The multi-year model (2016–2018) was split into values of <9, 9–10, 10–11, 11–12, 12–13 and >13% SSC and resulted in a RMSEP of 0.59 (+/−0.08 sd), 0.55 (+/−0.05 sd), 0.57 (+/−0.04 sd), 0.65 (+/−0.06 sd), 0.73 (+/−0.08 sd) and 0.82 (+/−0.09 sd) % SSC, respectively. The analysis of the mean RMSEP shows signs of heteroscedasticity with a worse PLSR prediction for lower and especially higher SSC values. However, there was a smaller calibration data set at the beginning and end of fruit ripening.

In all years, mean RMSEP values were very high for a low number of calibration values and decrease rapidly up to $n = 100$ reference values per year with only a slight additional improvement in model adequacy as shown in the RMSEP for $n > 100$ calibration values per year. Standard deviations for the RMSEP values are rather high for small calibration sets and decrease with increasing sample size. This suggests that model accuracy might appear high in some cases “by chance”. This has two implications: first, the number of calibration measurements can be limited to a rather small number of observations per year and a reduced number of calibration measurements can be used in future experiments. Second, a certain prediction error seems to be inevitable with a given PLSR model no matter how many calibration measurements are available.

2.2.3. Effect of Refractometer Errors

In this simulation procedure, additional normally distributed noise with a mean value of m = 0% SSC and standard deviations of s = 0, 0.1, 0.2, 0.3, 0.4, 0.5, 0.75, 1.0, 2.0% SSC was added to the laboratory reference values for each simulation run. The standard deviation of s = 0% SSC corresponds to the standard PLSR calibration model. All the simulation runs show highly robust PLSR models. Even moderate and substantial laboratory errors only increase the RMSEP values slightly (Figure 4). The RMSEP in 2016 increased from 0.67 (+/−0.05 sd) % SSC to 0.74 (+/−0.06 sd) % SSC with an additional laboratory error and a standard deviation of 2.0% SSC. The simulations show similar results for 2017 and 2018.

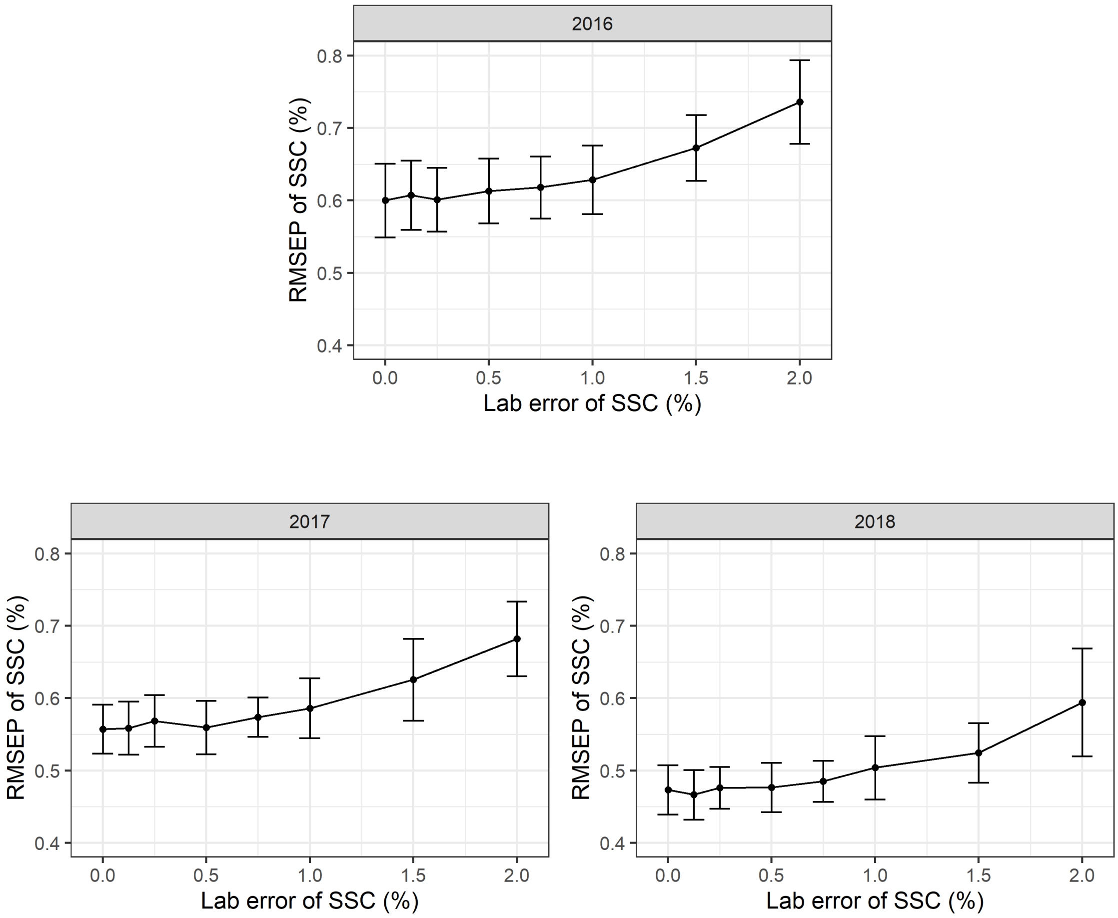

Figure 4. Root mean square error of prediction (RMSEP) in % soluble solids content (SSC) based on 2016, 2017 and 2018 partial least squares regression (PLSR) models to test for nonsystematic laboratory errors during wet chemistry analyses. For each setting, 500 Monte Carlo simulation runs were performed. Mean and standard deviation for each point are shown and 500 observations in each calibration data set and 100 observations in each validation data set used.

2.3. Use of LME Models to Describe SSC Accumulation

At any given time, the SSC values follow a linear trend with a normal distribution and a slight increase in variance during fruit development and maturation (Figure 1b). A breakdown by different orchard factors/experimental management treatments for tree sector, crop load, cell division temperature and calcium treatment for the 2018 season mainly suggests a clear effect of sector position, lower effects of crop load and temperature and no effect of calcium treatment (data not shown). These trends are consistent with the observations made for the 2016 and 2017 seasons. Three different models are considered to evaluate whether the specification of random effects and interaction terms yields a substantial improvement in model quality.

Model 1 is a fully-specified LME model with tree-specific and fruit-specific random intercepts, year, weeks after full bloom (WAFB), sector position, crop load, cell division temperature and calcium treatment as fixed effects and interactions between time and the above listed main effects. Model 1 is a fully-specified LME:

$$y_{ijk} = \beta_0 + u_{j,0} + u_{i,0} + \beta_1 t_k + u_{j,1} t_k + u_{i,1} t_k + \beta_X X_i + \beta_Y X_i t_k + e_{ijk} \tag{1}$$

with a population intercept β_0, a population parameter β_1 for modelling a time-dependent linear accumulation trend, a time-independent population parameter β_X for any other fixed effects such as treatment effects and sector position, a time-dependent parameter β_Y for these fixed effects, a random tree-specific intercept $u_{j,0}$ with $u_{j,0} \sim N(0, \sigma^2_{u_{j,0}})$, a random tree-specific slope $u_{j,1}$ with $u_{j,1} \sim N(0, \sigma^2_{u_{j,1}})$, a random fruit-specific intercept $u_{i,0} \sim N(0, \sigma^2_{u_{i,0}})$, a random fruit-specific slope $u_{i,1} \sim N(0, \sigma^2_{u_{i,1}})$ and a random error term $e_{ijk} \sim N(0, \sigma^2_e)$. Model 2 is nested in Model 1 without interaction terms ($\beta_Y = 0$):

$$y_{ijk} = \beta_0 + u_{j,0} + u_{i,0} + \beta_1 t_k + u_{j,1} t_k + u_{i,1} t_k + \beta_X X_i + e_{ijk} \tag{2}$$

Model 3 corresponds to a fully-specified linear regression model without random effects (with $u_{j,0} = u_{i,0} = u_{j,1} = u_{i,1} = 0$) and serves as a baseline model to compare the effects of the LME modelling. Model 3 is a standard linear regression model without random effects:

$$y_{ijk} = \beta_0 + \beta_1 t_k + \beta_X X_i + \beta_Y X_i t_k + e_{ijk} \tag{3}$$

The fixed time and treatment effects for any given fruit *i* from tree *j* were calculated as:

$$E(y_{ijk} | i, j) = \beta_0 + \beta_1 t_k + \beta_X X_i + \beta_Y X_i t_k \tag{4}$$

Using Akaike information criterion (AIC) and Bayesian information criterion (BIC) as indicators of goodness of fit, both LME models (Models 1–2) are clearly favourable over the standard linear regression (Model 3). Based on 17,004 observations, Model 1, 2 and 3 result in an AIC of 27,896, 29,154 and 35,708 and a BIC of 28,074, 29,255 and 35,871, respectively. The root mean square error (RMSE) was 0.48, 0.50 and 0.69% SSC for Model 1, 2 and 3, respectively. Further information about regression coefficients and time-dependent treatment effect of Model 1 can be obtained from Tables 2 and 3. Of these two mixed-effects models, Model 1 seems to give the best fit which suggests that the specification of interaction terms is appropriate to reflect the spatial and temporal dependencies between observations. Model 1 shows highly significant effects for year, WAFB, sector crop load and cell division temperature and their interactions. No significant effect is observed for the calcium treatments.

Table 2. Time-dependent treatment effects in 2017 on % soluble solids content (SSC) accumulation at different stages of fruit development given in days after full bloom (DAFB). The baseline configuration (Base) corresponds to fruit from the bottom sector of a tree with medium crop load without alterations of cell division temperature. Displayed effects are bottom, middle, top sectors and light, standard (stand.), heavy crop load and cold, ambient (amb.), warm cell division temperature treatments. SSC values of the respective effects need to be added or subtracted to the base value.

DAFB	**Base in % SSC**	**Sector**		**Crop Load**		**Temperature**	
		Middle	**Top**	**Light**	**Heavy**	**Cold**	**Warm**
40	5.54	0.21	0.53	0.02	−0.07	0.08	0.16
60	6.43	0.25	0.60	0.06	−0.09	0.05	0.13
80	7.31	0.30	0.67	0.11	−0.11	0.01	0.11
100	8.19	0.34	0.75	0.16	−0.13	−0.02	0.08
120	9.08	0.39	0.82	0.20	−0.15	−0.06	0.06
140	9.96	0.43	0.89	0.25	−0.17	−0.09	0.03

Table 3. SSC model simulations with a reduction of sample size and different measurement errors. Multi-year model (MYM) corresponds to a linear mixed-effect model with all data from 2016–2018 included (LME Model 1), Model A was reduced to samples from 100 trees of the MYM, Model B was reduced to 500 fruit samples of the MYM and Model C had an unbiased error of 1.0% SSC added to the MYM. The estimate % SSC (standard deviation) is stated with a significance code with *** <0.001, ** <0.01, * <0.05. The number of observations, different fruit and trees is shown.

	Multi-Year Model	**Model A**	**Model B**	**Model C**
Observations (N)	17,004	7457	6777	17,004
Fruit (N)	1274	540	500	1274
Trees (N)	237	100	211	237
Intercept	3.78 *** (0.084)	3.72 *** (0.115)	3.90 *** (0.127)	3.86 *** (0.157)
Year 2017	1.47 *** (0.096)	1.58 *** (0.136)	1.45 *** (0.148)	1.51 *** (0.183)
Year 2018	1.85 *** (0.081)	2.04 *** (0.114)	1.87 *** (0.125)	1.85 *** (0.150)
Week	0.31 *** (0.003)	0.31 *** (0.005)	0.31 *** (0.005)	0.31 *** (0.007)
Middle sector	0.11 * (0.054)	0.00 (0.078)	−0.03 (0.087)	0.01 (0.100)
Top sector	0.39 *** (0.054)	0.38 *** (0.078)	0.35 *** (0.089)	0.423 *** (0.101)
Cold temperature	0.15 (0.089)	−0.02 (0.126)	−0.03 (0.131)	−0.05 (0.152)
Warm temperature	0.21 ** (0.065)	0.15 (0.090)	0.26 ** (0.095)	0.09 (0.107)
Light crop load	−0.07 (0.064)	−0.05 (0.096)	−0.17 (0.094)	−0.11 (0.110)
Heavy crop load	−0.03 (0.069)	−0.11 (0.094)	−0.18 (0.101)	−0.01 (0.117)
Without calcium	0.17 (0.140)	0.00 (0.175)	0.43 (0.230)	0.03 (0.227)

The time-dependent effects of different treatment levels are displayed in Table 2. Fruit from the light crop load treatment show increasing SSC values throughout fruit development. At the end of cell division (∼40 DAFB), only small differences between different crop loads (range of 0.09% SSC between light and high crop load) and cell division temperature regimes (0.16% SSC between cold and warm temperatures) can be observed. Close to harvest (140 DAFB), relatively large differences in SSC can be seen between different levels of tree sector (range of 0.89% SSC between bottom and top sector) compared to only minor differences in SSC for different crop loads (range of 0.42% SSC between light and high crop load) and only negligible effects for different temperature regimes (range of 0.12% SSC).

2.4. Sensitivity Analysis of the Experimental Setup

Data collection in large orchard trial designs is labour and cost intensive. Therefore, it is of interest to investigate whether reduced sample sizes lead to different results. SSC values were derived from the multi-year PLSR calibration model based on laboratory reference measurements. The influence of reduced sample sizes and unbiased laboratory measurement errors of 1.0% SSC on research results was investigated with LME Model 1. Different simulation settings are presented in Table 3.

Three settings are discussed and the standard Model respectively altered: Model A shows the effects of a reduced number of trees (100 trees within three years, same number of fruit per tree). Model B is based on a reduced number of fruit (500 fruit within three years, same number of trees). While the first setting with less experimental trees makes if possible to have additional experiments in the same orchard block, the second setting reduces the number of working hours per tree. Additionally, Model C shows the effect of an increased but unbiased measurement error (additional white noise of 1.0% SSC) in the SSC measurements. As expected, Models A–C show increased standard deviations of all estimates compared to the multi-year SSC model due to a reduced sample size (for Models A and B) or an increased measurement error (Model C). In Model C, the cell division temperature and calcium treatment are not marked as "statistically significant" due to increased measurement errors. In most cases the effect of sample size remains comparable to the multi-year SSC model.

In summary, these simulations show the possibility of reduced sample sizes when the focus is on treatments with large effects. In order to detect small differences between different treatments, large sample sizes are still required, especially in the presence of measurement errors due to increased *t*-values of the estimates.

2.5. A Practical Comparison of Spectral and Conventional Laboratory Methods to Determine SSC at Harvest

Traditional destructive laboratory samples for SSC were taken at harvest from eight apples per tree sector, treatment (2 or 3× levels) and repetition (3×). At the same time, the last non-destructive scans in the orchard were taken from an independent batch of approx. seven apples, scanned and postprocessed with the yearly calibrated PLSR model. Mean destructive laboratory values for 2016, 2017, 2018 and all study years from 2016 to 2018 were 11.3, 11.1, 12.3 and 11.7% SSC, respectively (2016: +/−0.52 sd, $n = 63$; 2017: +/−0.55 sd, $n = 9$; 2018: +/−0.53 sd, $n = 50$). The non-destructive samples were 11.8, 10.7, 12.0 and also 11.7% SSC, respectively (2016: +/−0.85 sd, $n = 63$; 2017: +/−0.70 sd, $n = 27$; 2018: +/−0.56 sd, $n = 68$). There is a higher variance for the PLSR modelled SSC values as compared to the laboratory values. The mean difference of each treatment level for the two methods is 0.5% SSC for all study years. The obtained values from the two approaches were not biased.

3. Discussion

Varying weather conditions during the three study years resulted in different SSC values at harvest which is in accordance with the literature [34–36]. Using time-series data in the orchard offers the possibility to see a linear carbohydrate development in the form of SSC accumulation over time. For 2017, the severe frost year, the SSC increase showed a larger variance (Figure 1a), as was also seen for fruit growth (Figure 1b). Non-destructive technologies can provide researchers with new tools to study fruit physiology or offer the possibility to use these values in digital orchard management information systems to predict and manage fruit quality, as seen for fruit diameter [37]. The effects of field treatments and physiological differences were directly related to the developmental stage of the fruit. Differences in tree sector position and crop load [1,38] caused increasingly large differences in SSC during fruit development and negligible differences due to early season temperature (Δ 2 °C to ambient). Differences in sector position influence SSC early in the season whereas crop load effects increase steadily during fruit development.

Up until now the practical application of non-destructive scanning in apple research experiments has been restricted due to the intensive amount of laboratory work necessary to obtain reference samples and to the unknown precision of PLSR calibration models in the orchard. The results of the PLSR calibration only partially depend on the number and precision of the reference laboratory measurements. The results suggest that special emphasis should be placed on scanning fruit at low and high SSC values at the beginning and end of each season to cover a wider range of possible SSC values within a particular growing season. These results have some practical implications and suggest that even a considerably reduced sample size (100 samples) leads to comparable results, although the standard deviations of the estimates increase with reduced sample size. It suggests that repeated laboratory reference measurements of the same fruits to increase the accuracy of reference values lead to almost negligible improvements of the PLSR calibration models. These simulation results are consistent with standard results from statistical measurement error theory for response variables [39]. Moreover, in future experimental designs a reduced number of field scans would be sufficient to detect SSC differences between the treatments. A classical experimental field design with blocks and repetitions did not play a role in the LME modelling, which relaxes some limitations of the classical variance analysis framework and provides a more flexible way to adapt to temporal, spatial and tree-specific dependencies. A precision horticulture approach beyond research trials to monitor fruit SSC development on large sample numbers aligned to orchard structure should be possible.

The accuracy and robustness of the PLSR models was examined in great detail and only showed minor limitations to their broader use for our purposes. Yearly calibrated models cannot be generalised to other years, but multi-year models can be used for the same orchard and cultivar as was also seen in Peirs et al. (2003) [21]. The practical comparison between all laboratory based destructive measurements and the non-destructive orchard SSC data collection showed that the independent apple selection was unbiased and for the apple cultivar 'Braeburn' there was no difference between the two methods for determining SSC values at harvest in the orchard. In the future, however, new developments with model transfer methodology [40] together with neural networks or other 'big data' applications may facilitate the wider use of non-destructive sensor based SSC predictions for apples.

Our results may not be generalised to other apple cultivars or fruit species and to other sites or other climate regimes. However, since all effects are comparatively large and consistent with a literature review, additional measurements would probably confirm the overall effects. Analyses of dry matter content which can also be obtained by PLSR models were not considered in this study. As the number of non-destructive sensors available for horticultural practice and research is expected to increase in the coming years, longitudinal data will be available in ever greater quantities. The collaboration of horticultural science, computer science and statistics will avoid the collection of data as an end in itself and allow for new insights into currently hidden patterns of fruit physiology and development.

4. Materials and Methods

4.1. Experimental Setup

This research took place at the Kompetenzzentrum Obstbau-Bodensee (47°46′01.9″ N 9°33′23.3″ E) in the Lake Constance region of Southwest Germany using the apple cultivar 'Braeburn' *Malus domestica*. A randomised field design with treatments of crop load (light, standard, heavy), calcium spraying (with, without) and cell division temperature (ambient, $\Delta + 2$ and $\Delta - 2$ °C) were used. Each tree was divided into three sectors of ∼1.25 m height each for the bottom, middle and top. Apple phenological growth stages were recorded following the BBCH code scheme [41]. The experimental design (treatments and scanning number/frequency) varied during the different study years. For a detailed description of the field experiments see [33,42].

4.2. SSC Sampling

Around June drop, one representative fruit per tree and sector was selected, marked and repeatedly measured (scanned) until harvest. Fruit were scanned on the equatorial and sun side with a handheld portable Vis/NIR device (F-750, Felix Instruments, Camas, WA, USA). The device had a 3 nm spectral sampling over a 310–1100 nm spectral window, a spectral resolution of 8–13 nm and corrected each scan for background daylight. The spectral range of 729–975 nm was used in the PLSR models to predict SSC. Fruit were replaced by a similar nearby fruit, if the fruit was lost or was not representative.

Orchard sampling was performed weekly in 2016 between 15 August and 16 October for n = 198 fruit from n = 33 trees. A total of n = 3994 scans were performed. In 2017, sampling took place weekly between 3 August and 30 October for n = 603 fruit from n = 96 trees. A total of n = 5957 scans were made. In 2018, n = 473 fruit from n = 146 trees were measured biweekly between 6 June and 25 October. In total, n = 7087 scans were recorded. In 2018, data acquisition took place on a daily basis for 120–180 DAFB and SSC scanning started at 50 DAFB.

4.3. PLSR Models

Reference measurements combined both destructive wet chemistry results and non-destructive spectral scans. A sample of n = 30 reference fruit were taken regularly over the fruit development and maturation periods from nearby trees in the same block and around the same field at scanning time to ensure the transferability of the calibration model to the SSC of sampled fruit. In total, n = 599 fruit in 2016, n = 211 fruit in 2017 and n = 333 fruit in 2018 were selected. Non-destructive spectral reference measurements were performed at different temperatures (∼10, 20, 30 °C) to help adjust for temperature induced changes in hydrogen bonding [43]. The number of reference measurements is given as a total of n = 1639 observations in 2016 (529 observations at 10 °C, n = 583 observations at 20 °C, n = 527 observations at 30 °C), in 2017 n = 631 observations (210 observations at 10 °C, n = 211 observations at 20 °C, n = 210 observations at 30 °C) and in 2018 n = 984 observations (n = 328 observations at each temperature level). Destructive wet chemistry SSC measurements were obtained with a refractometer (Atago, Tokyo, Japan). PLSR models were postprocessed on a year- and site-specific basis.

The original models were built with the Felix model builder software (v1.3.0.177). Additional PLSR models were fitted using the R package pls [44]. Spectral data was transformed using second derivative spectra from 729 nm to 975 nm. The maximum number of principle components was set to 7 and the models were validated with leave-one-out cross validation methods. The reference data set was split into a calibration data set to train the PLSR model and a validation data set which was only used to test the prediction quality. A stratified random sample was drawn for each year to generate equal parts for all years. In total, n = 1200 observations were used as calibration data and n = 300 for validation data, if not stated otherwise. The RMSEP and adjusted prediction R^2 were used to describe the model performance and goodness of prediction. Reference measurements were taken as the longitudinal observations took place in the orchard. Therefore, we assume that the RMSEP for the validation data corresponds to the RMSEP of the SSC sampled fruit which could not be chemically analysed destructively due to the longitudinal structure of the study.

4.4. Monte Carlo Simulations

Monte Carlo simulations were used to assess PLSR model sensitivity to changes in input parameters and effects of sample size [45]. Measurement accuracy using standard laboratory analyses was simulated with repeated random samples. For simulations a modified and randomly sampled calibration set was generated without replacement. Reference measurements were split into a calibration data set with 1200 observations and a validation data set with 300 observations. The modified calibration sets were used in an automatic Monte Carlo simulation process to calculate the RMSEP and adjusted R^2 values for each setting. Each setting was repeated n = 100 times to calculate mean RMSEP values and standard deviations.

For sample size analyses, calibration sets with a reduced sample size were sampled for each year and all years combined. For laboratory errors, calibration sets were sampled for each year and all years combined. Laboratory errors were assumed to be unbiased and normally distributed. Additional normally distributed error terms (white noise) with different magnitudes were added afterwards.

4.5. Longitudinal LME Models

LME models (hierarchical regression models, nested linear models, multi-level regression models) are a subset of generalized regression methods to analyse repeated time-correlated and cluster-correlated observations [46]. DAFB and WAFB were used for time-dependent analyses in each year.

All time-correlated observations on a single fruit were part of a natural cluster of observations which shared the same fruit-specific and tree-specific characteristics. A hierarchical (nested) data structure was therefore applied. The LME model combined population-specific and subject-specific (spatial variation in the orchard) random effects.

The specification of the random effects needs special consideration as the longitudinal data structure makes two adaptions necessary: first, a random effect is given by a fruit-specific dependency as these observations are correlated over time (fruit-specific intercept and slope). Second, a random effect is necessary due to tree-specific dependency for all fruit from the same tree. Therefore, with respect to the natural dependency of observations from the same tree, a tree-specific intercept and slope were specified. Two random effects were modelled in addition to fixed effects which affect all fruit simultaneously. Details are specified in the previous sections. Modelling was done with the R package lme4 which provided various functions for fitting, analysing and evaluating mixed-effects models in a linear, generalised linear and nonlinear framework [47,48]. The restricted maximum likelihood method and full maximum likelihood method were used to estimate parameters. The R package lmerTest was used to approximate the degrees of freedom and calculate p-values for mixed-effects models using Satterthwaite's method [49]. Yet no emphasis is placed on the interpretation of these p-values, as there is an unresolved statistical discussion about their theoretical applicability [50]. Coefficients of fixed effects with a t-value (ratio of estimate and its standard deviation) of less than -2 or greater than 2 were considered statistically significant. Model choice was based on the AIC and the BIC both of which use the log-likelihood ratio and describe model quality by adjusting the goodness of fit with a penalization term for model complexity [51,52]. RMSEP was used to compare model predictions and observations.

4.6. Mann–Whitney–Wilcoxon Test

A Mann–Whitney–Wilcoxon test was conducted in R to compare the modelled SSC values from the field scans based on the PLSR modelsto destructively measured fruit in the laboratory. Refractometer values showed a normal distribution, whereas PLSR modelled SSC were not normally distributed and Mann–Whitney–Wilcoxon test was used. For the laboratory samples the top half of a fruit batch of eight apples was mixed in the laboratory with a conventional fruit blender.

5. Conclusions

In summary, the non-destructive temporal development of SSC accumulation could contribute new insights into apple fruit carbohydrate physiology. The present study linked an in-depth statistical analysis of large data sets with horticultural knowledge in order to test the application of 'Braeburn' SSC prediction models with a special focus on model transferability and accuracy.

- In terms of model performance over all years, the multi-year PLSR model appeared to be reasonable with minor restrictions for especially low and high SSC predictions. However, independent yearly calibration models performed best for the same year.
- A sample size of n = 100 fruit for a yearly PLSR model with a wide range of SSC values seems to be sufficient.
- Differences in sector position and crop load resulted in increasingly large differences in SSC during fruit development and offer the possibility for further physiological studies.

Author Contributions: Conceptualisation, K.B. and R.J.M.; methodology, R.J.M. and K.B. and D.S.; software, D.S. and R.J.M. and K.B.; validation, K.B. and D.S. and R.J.M.; formal analysis, D.S.; investigation, K.B. and R.J.M.; data curation, K.B. and R.J.M.; writing—original draft preparation, K.B. and D.S.; writing—review and editing, R.J.M. and P.B.; visualisation, K.B.; supervision, R.J.M. and P.B.; project administration, K.B.; funding acquisition, R.J.M. All authors have read and agreed to the published version of the manuscript.

Funding: This project was supported by the Federal Ministry of Food and Agriculture (BMEL) based on a decision of the Parliament of the Federal Republic of Germany via the Federal Office for Agriculture and Food (BLE) under the innovation support programme.

Data Availability Statement: All data reported here is available from the authors upon request.

Acknowledgments: We would like to thank the Kompetenzzentrum Obstbau-Bodensee orchard and lab staff and the yearly interns for extensive help in conducting this study and the ’BigApple’ project team.

Conflicts of Interest: The authors declare no conflict of interest. The funder had no role in the design of the study; in the collection, analyses, or interpretation of data; in the writing of the manuscript, or in the decision to publish the results.

Abbreviations

The following abbreviations are used in this manuscript:

AIC	Akaike information criterion
ANOVA	Analysis of variance
BIC	Bayesian information criterion
DAFB	Days after full bloom
LME model	Linear mixed-effects model
NIR	Near-infrared
PLSR	Partial least squares regression
RMSEP	Root-mean-square error of prediction
sd	Standard deviation
SSC	Soluble solids content
Vis	Visible
WAFB	Weeks after full bloom

References

1. Meland, M. Effects of different crop loads and thinning times on yield, fruit quality, and return bloom in Malus x domestica Borkh. ‘Elstar’. *J. Hortic. Sci. Biotechnol.* **2009**, *84*, 117–121. [CrossRef]
2. Yuri, J.; Talice, J.G.; Verdugo, J.; del Pozo, A. Responses of fruit growth, quality, and productivity to crop load in apple cv. Ultra Red Gala/MM111. *Sci. Hortic.* **2011**, *127*, 305–312. [CrossRef]
3. Ferguson, I.; Volz, R.; Woolf, A. Preharvest factors affecting physiological disorders of fruit. *Postharvest Biol. Technol.* **1999**, *15*, 255–262. [CrossRef]
4. Rabus, C.; Streif, J. Effect of various preharvest treatments on the development of internal browning in ‘Braeburn’ apples. *Acta Hortic.* **2000**, *518*, 151–157. [CrossRef]
5. Hatoum, D.; Buts, K.; Hertog, M.L.A.T.M.; Geeraerd, A.H.; Schenk, A.; Vercammen, J.; Nicolaï, B.M. Effects of pre- and postharvest factors on browning in Braeburn. *Hortic. Sci.* **2014**, *41*, 19–26. [CrossRef]
6. Ford, E.M. Effect of post-blossom environmental conditions on fruit composition and quality of apple. *Commun. Soil Sci. Plant Anal.* **1979**, *10*, 337–348. [CrossRef]
7. Warrington, I.; Fulton, T.; Halligan, E.; de Silva, H. Apple Fruit Growth and Maturity are Affected by Early Season Temperatures. *J. Am. Soc. Hortic. Sci.* **1999**, *124*, 468–477. [CrossRef]
8. Hatoum, D.; Hertog, M.L.A.T.M.; Geeraerd, A.H.; Nicolai, B.M. Effect of browning related pre- and postharvest factors on the ‘Braeburn’ apple metabolome during CA storage. *Postharvest Biol. Technol.* **2016**, *111*, 106–116. [CrossRef]
9. Seifert, B.; Zude, M.; Spinelli, L.; Torricelli, A. Optical properties of developing pip and stone fruit reveal underlying structural changes. *Physiol. Plant.* **2014**, *153*, 327–336. [CrossRef]
10. Walsh, K.B.; McGlone, V.A.; Han, D.H. The uses of near infra-red spectroscopy in postharvest decision support: A review. *Postharvest Biol. Technol.* **2020**, *163*, 111139. [CrossRef]
11. Beers, R.V.; Aernouts, B.; Watté, R.; Schenk, A.; Nicolaï, B.; Saeys, W. Effect of maturation on the bulk optical properties of apple skin and cortex in the 500–1850 nm wavelength range. *J. Food Eng.* **2017**, *214*, 79–89. [CrossRef]

12. Fan, S.; Zhang, B.; Li, J.; Huang, W.; Wang, C. Effect of spectrum measurement position variation on the robustness of NIR spectroscopy models for soluble solids content of apple. *Biosyst. Eng.* **2016**, *143*, 9–19. [CrossRef]
13. Abasi, S.; Minaei, S.; Jamshidi, B.; Fathi, D.; Khoshtaghaza, M.H. Rapid measurement of apple quality parameters using wavelet de-noising transform with Vis/NIR analysis. *Sci. Hortic.* **2019**, *252*, 7–13. [CrossRef]
14. Cozzolino, D.; Cynkar, W.U.; Shah, N.; Smith, P. Multivariate data analysis applied to spectroscopy: Potential application to juice and fruit quality. *Food Res. Int.* **2011**, *44*, 1888–1896. [CrossRef]
15. Zude-Sasse, M.; Hashim, N.; Hass, R.; Polley, N.; Regen, C. Validation study for measuring absorption and reduced scattering coefficients by means of laser-induced backscattering imaging. *Postharvest Biol. Technol.* **2019**, *153*, 161–168. [CrossRef]
16. Lohner, S.; Biegert, K.; Hohmann, A.; McCormick, R.; Kienle, A. Determining the optical properties of apple tissue and their dependence on physiological and morphological characteristics during maturation. Part 1: Spatial frequency domain imaging. *Postharvest Biol. Technol.* in press.
17. Aggelopoulou, K.D.; Wulfsohn, D.; Fountas, S.; Gemtos, T.A.; Nanos, G.D.; Blackmore, S. Spatial variation in yield and quality in a small apple orchard. *Precis. Agric.* **2009**, *11*, 538–556. [CrossRef]
18. Manfrini, L.; Grappadelli, L.C.; Morandi, B.; Losciale, P.; Taylor, J.A. Innovative approaches to orchard management: Assessing the variability in yield and maturity in a 'Gala' apple orchard using a simple management unit modeling approach. *Eur. J. Hortic. Sci.* **2020**, *85*, 211–218. [CrossRef]
19. Elgar, H.J.; Lallu, N.; Watkins, C.B. Harvest Date and Crop Load Effects on a Carbon Dioxide–related Storage Injury of 'Braeburn' Apple. *HortScience* **1999**, *34*, 305–309. [CrossRef]
20. Lordan, J.; Francescatto, P.; Dominguez, L.I.; Robinson, T.L. Long-term effects of tree density and tree shape on apple orchard performance, a 20 year study—Part 1, agronomic analysis. *Sci. Hortic.* **2018**, *238*, 303–317. [CrossRef]
21. Peirs, A.; Tirry, J.; Verlinden, B.; Darius, P.; Nicolai, B.M. Effect of biological variability on the robustness of NIR models for soluble solids content of apples. *Postharvest Biol. Technol.* **2003**, *28*, 269–280. [CrossRef]
22. Palmer, J.W.; Giuliani, R.; Adams, H.M. Effect of Crop Load on Fruiting and Leaf Photosynthesis of 'Braeburn'/M.26 Apple Trees. *Tree Physiol.* **1997**, *17*, 741–746. [CrossRef] [PubMed]
23. Gezan, S.A.; Carvalho, M. Analysis of Repeated Measures for the Biological and Agricultural Sciences. In *Applied Statistics in Agricultural, Biological, and Environmental Sciences*; American Society of Agronomy, Crop Science Society of America, and Soil Science Society of America, Inc.: Madison, WI, USA, 2018; pp. 279–297. [CrossRef]
24. Ketelaere, B.D.; Lammertyn, J.; Molenberghs, G.; Nicolai, B.; Baerdemaeker, J.D. Statistical models for analyzing repeated quality measurements of horticultural products. *Math. Biosci.* **2003**, *185*, 169–189. [CrossRef]
25. Godoy, C.; Monterubbianesi, G.; Tognetti, J. Analysis of highbush blueberry (Vaccinium corymbosum L.) fruit growth with exponential mixed models. *Sci. Hortic.* **2008**, *115*, 368–376. [CrossRef]
26. Johnson, W.; Balakrishna, N.; Griffiths, P.L. Modeling physical growth using mixed effects models. *Am. J. Phys. Anthropol.* **2012**, *150*, 58–67. [CrossRef] [PubMed]
27. Bastogne, T.; Samson, A.; Vallois, P.; Wantz-Mézières, S.; Pinel, S.; Bechet, D.; Barberi-Heyob, M. Phenomenological modeling of tumor diameter growth based on a mixed effects model. *J. Theor. Biol.* **2010**, *262*, 544–552. [CrossRef] [PubMed]
28. Weisberg, S.; Spangler, G.; Richmond, L.S. Mixed effects models for fish growth. *Can. J. Fish. Aquat. Sci.* **2010**, *67*, 269–277. [CrossRef]
29. Lakso, A.N.; Grappadelli, L.C.; Barnard, J.; Goffinet, M.C. An expolinear model of the growth pattern of the apple fruit. *J. Hortic. Sci.* **1995**, *70*, 389–394. [CrossRef]
30. Stanley, C.J.; Tustin, D.S.; Lupton, G.B.; Mcartney, S.; Cashmore, W.M.; Silva, H.N.D. Towards understanding the role of temperature in apple fruit growth responses in three geographical regions within New Zealand. *J. Hortic. Sci. Biotechnol.* **2000**, *75*, 413–422. [CrossRef]
31. Tijskens, L.M.M.; Unuk, T.; Okello, R.C.O.; Wubs, A.M.; Šuštar, V.; Šumak, D.; Schouten, R.E. From fruitlet to harvest: Modelling and predicting size and its distributions for tomato, apple and pepper fruit. *Sci. Hortic.* **2016**, *204*, 54–64. [CrossRef]
32. Herold, B.; Truppel, I.; Zude, M.; Geyer, M. Spectral Measurements on 'Elstar' Apples during Fruit Development on the Tree. *Biosyst. Eng.* **2005**, *91*, 173–182. [CrossRef]
33. Osinenko, P.; Biegert, K.; McCormick, R.J.; Göhrt, T.; Devadze, G.; Streif, S. Application of non-destructive sensors and big-data analysis to predict physiological storage disorders and fruit firmness in 'Braeburn' apples. *Comput. Electron. Agric.* **2021**, in press.
34. Sugiura, T.; Ogawa, H.; Fukuda, N.; Moriguchi, T. Changes in the taste and textural attributes of apples in response to climate change. *Sci. Rep.* **2013**, *3*. [CrossRef] [PubMed]
35. Warmund, M.R.; Starbuck, C.; Kadir, S. Changes in fruit quality parameters of 'Jonathan Rasa' and 'Delicious Flanagan' apples in response to elevated temperatures. *Trans. Kans. Acad. Sci.* **2007**, *110*, 259–267.[259:cifqpo]2.0.co;2. [CrossRef]
36. Toivonen, P.M.; Lannard, B. Dry matter content association with time of on-tree maturation, quality at harvest, and changes in quality after controlled atmosphere storage for 'Royal Gala' apples. *Can. J. Plant Sci.* **2020**, 1–9. [CrossRef]
37. Li, M.; Chen, M.; Zhang, Y.; Fu, C.; Xing, B.; Li, W.; Qian, J.; Li, S.; Wang, H.; Fan, X.; et al. Apple Fruit Diameter and Length Estimation by Using the Thermal and Sunshine Hours Approach and Its Application to the Digital Orchard Management Information System. *PLoS ONE* **2015**, *10*, e0120124. [CrossRef]
38. Anthony, B.; Serra, S.; Musacchi, S. Optimizing Crop Load for New Apple Cultivar: "WA38". *Agronomy* **2019**, *9*, 107. [CrossRef]
39. Sepanski, J.H. On a repeated-measurement model with errors in dependent variable. *Statistics* **2001**, *35*, 97–112. [CrossRef]

40. Mishra, P.; Roger, J.M.; Rutledge, D.N.; Woltering, E. Two standard-free approaches to correct for external influences on near-infrared spectra to make models widely applicable. *Postharvest Biol. Technol.* **2020**, *170*, 111326. [CrossRef]
41. Meier, U.; Graf, H.; Hack, H.; Hess, M.; Kennel, W.; Klose, R.; Mappes, D.; Seipp, D.; Stauss, R.; Streif, J.; et al. Phänologische Entwicklungsstadien des Kernobstes (Malus domestica Borkh. und Pyrus communis L.), des Steinobstes (Prunus-Arten), der Johannisbeere (Ribes-Arten) und der Erdbeere (Fragaria x ananassa Duch.). *Nachrichtenbl. Deut. Pflanzenschutzd.* **1994**, *46*, 141–153.
42. McCormick, R.J.; Biegert, K.; Streif, J. Occurrence of physiological browning disorders in stored 'Braeburn' apples as influenced by orchard and weather conditions. *Postharvest Biol. Technol.* **2021**, in press.
43. Golic, M.; Walsh, K.B. Robustness of calibration models based on near infrared spectroscopy for the in-line grading of stonefruit for total soluble solids content. *Anal. Chim. Acta* **2006**, *555*, 286–291. [CrossRef]
44. Mevik, B.H.; Wehrens, R. The pls Package: Principal Component and Partial Least Squares Regression in R. *J. Stat. Softw.* **2007**, *18*. [CrossRef]
45. Brodský, L.; Vašát, R.; Klement, A.; Zádorová, T.; Jakšík, O. Uncertainty propagation in VNIR reflectance spectroscopy soil organic carbon mapping. *Geoderma* **2013**, *199*, 54–63. [CrossRef]
46. Fitzmaurice, G.M.; Laird, N.M.; Ware, J.H. *Applied Longitudinal Analysis*; John Wiley & Sons, Inc.: Hoboken, NJ, USA, 2011. [CrossRef]
47. R Core Team. *R: A Language and Environment for Statistical Computing*; R Foundation for Statistical Computing: Vienna, Austria, 2019.
48. Bates, D.; Mächler, M.; Bolker, B.; Walker, S. Fitting Linear Mixed-Effects Models Using lme4. *J. Stat. Softw.* **2015**, *67*. [CrossRef]
49. Kuznetsova, A.; Brockhoff, P.B.; Christensen, R.H.B. lmerTest Package: Tests in Linear Mixed Effects Models. *J. Stat. Softw.* **2017**, *82*, 1–26. [CrossRef]
50. Luke, S.G. Evaluating significance in linear mixed-effects models in R. *Behav. Res. Methods* **2016**, *49*, 1494–1502. [CrossRef] [PubMed]
51. Akaike, H. Information Theory and an Extension of the Maximum Likelihood Principle. In *Springer Series in Statistics*; Springer: New York, NY, USA, 1998; pp. 199–213. [CrossRef]
52. Schwarz, G. Estimating the Dimension of a Model. *Ann. Stat.* **1978**, *6*, 461–464. [CrossRef]

5

Occurence of physiological browning disorders in stored ’Braeburn’ apples as influenced by orchard and weather conditions

R. J. McCormick, K. Biegert, J. Streif

Postharvest Biology and Technology 177 (2021)

Postharvest Biology and Technology 177 (2021) 111534

Contents lists available at ScienceDirect

Postharvest Biology and Technology

journal homepage: www.elsevier.com/locate/postharvbio

Occurrence of physiological browning disorders in stored ‘Braeburn’ apples as influenced by orchard and weather conditions

R.J. McCormick *, K. Biegert, J. Streif

Kompetenzzentrum Obstbau Bodensee, Ravensburg, Germany

ARTICLE INFO

Keywords:
Controlled atmosphere (CA) storage
Crop load
Internal browning disorders
Receiver operating characteristic (ROC)

ABSTRACT

Physiological storage disorders continue to cause sizable economic losses in a range of commercially important pomefruit cultivars. Given similar storage regimes, the incidence and severity of browning disorders in the apple cultivar ‘Braeburn’ can vary in different years in a way that can be explained by the interaction of preharvest seasonal and orchard factors. Over a three-year period (2016–2019) at the Kompetenzzentrum Obstbau Bodensee (KOB) in Southwest Germany a range of orchard and storage treatments were conducted for: air temperature during cell division for three weeks post petalfall or during four weeks preharvest, and crop load. Following controlled atmosphere (CA) storage, the disorder incidence for internal browning and cavity formation varied markedly over the three different growing seasons. Crop load treatments strongly influenced the expression of browning disorders in all years. Differences in air temperatures (△ +/- 2 °C compared to ambient) during the cell division period showed little effect on browning incidence. Warm night temperatures (>10 °C) prior to harvest can reduce internal browning in ‘Braeburn’ apples during CA storage and shelf-life.

1. Introduction

Physiological browning disorders in the apple cultivar ‘Braeburn’ can occur in the orchard but mostly symptoms develop during postharvest handling and controlled atmosphere (CA) storage. Much of the variation in the occurrence of internal browning symptoms is due to preharvest factors as similar fruit handling and storage conditions often result in very different outcomes (Lau, 1998; Elgar et al., 1999; Watkins and Mattheis, 2019).

A conceptual understanding of browning development in ‘Braeburn’ is supported by recent work to identify genetic biomarkers (Mellidou et al., 2014; Rudell et al., 2017) and technological advances with the non-destructive 3D microstructural analysis of whole fruit (Janssen et al., 2020). The genetic findings link changes in energy and lipid related genes with the spatial and temporal development of browning symptoms in fruit tissues. Furthermore, ‘Braeburn’ is an apple cultivar with a high resistance to gas exchange, the fruit skin has a low permeance for O_2 (Rajapakse et al., 1990) and the cellular microstructure is dense with narrow connecting pores especially within the inner cortex / core tissues (Dražeta et al., 2004; Herremans et al., 2013; Janssen et al., 2020). Taken together these research findings are consistent with a model of browning development where failures in the functioning and/or structure of cell membranes occur when respiration processes either do not provide enough energy to maintain cellular defences / homeostasis or products such as CO_2 accumulate to damage cells. When cell integrity is lost, cell contents mix, enzymatic oxidation browning occurs, cells can die and cavities can form when cell fluids are lost to surrounding tissues (Herremans et al., 2014). Variation in the cellular microstructure can explain the pattern of browning symptoms. Browning develops in ‘hotspots’ that often stay localised when surrounding tissues allow for better gas exchange (Herremans et al., 2014). The management strategy of delayed-CA storage is very effective at controlling browning disorders in ‘Braeburn’. Fruit have a higher energy status after a three week period in air storage and begin to better tolerate low temperature CA conditions (Saquet et al., 2003). In addition, apples in air storage can show increases in intercellular volume (Ruess and Stösser, 1993) and these changes could also help fruit adapt to CA conditions by increasing gas exchange within the cortex and core tissues.

Nevertheless, many questions remain about how environmental and orchard factors affect fruit during growth and development on the tree to influence the susceptibility and expression of browning disorders during postharvest handling and storage. Approaches to predict ‘Braeburn’ browning disorder risk have often included air temperature data, e.g. growing degree day (GDD) models as a number of workers have

---

* Corresponding author.
E-mail address: mccormick@kob-bavendorf.de (R.J. McCormick).

https://doi.org/10.1016/j.postharvbio.2021.111534
Received 15 September 2020; Received in revised form 11 March 2021; Accepted 16 March 2021

identified cool growing seasons as a higher risk for browning (Lau, 1998; Volz et al., 2000); with some data to suggest that low temperatures in the 30 d preharvest period are correlated with a higher browning risk (Volz et al., 2000).

Fruit growth is affected by orchard temperature. Air temperatures during the spring post bloom period (primarily involving cell division in the young fruitlets) and in the autumn preharvest harvest period (fruit maturation and ripening) are known to influence fruit growth and development in a different way compared to temperatures during the summer. Air temperatures in the post bloom and preharvest periods can affect the potential fruit size and the rate of fruit maturation (Warrington et al., 1999) and the incidence of internal browning in `Braeburn' (Volz et al., 2000).

Light crop loads are a well-known risk factor for a range of postharvest disorders including internal browning in 'Braeburn' however, there is very little literature to understand the physiological basis on how crop load affects final fruit quality following postharvest storage (Ferguson et al., 1999; Wünsche and Ferguson, 2005). Calcium spray treatments in the orchard strongly affect the incidence of bitter pit. However, the effects on 'Braeburn' browning susceptibility are reported as protective (Rabus and Streif, 2000) or less well correlated (Elgar et al., 1999). Furthermore, while late harvests are generally associated with a higher risk of browning susceptibility this is not always the case (Lau, 1998).

From 2016–2019, a research project to encourage the use of digital technologies in the horticultural sector was undertaken at the Kompetenzzentrum Obstbau Bodensee (KOB) in Southwest Germany. The project focused on the prediction of storage disorder risk using a data based classification methodology (Osinenko et al., 2021). The experimental design enabled the linkage between a number of preharvest physiological processes and the occurrence of internal browning disorders during storage to be investigated. Specifically, the following hypotheses were tested: 1) Warm conditions during the three week post-bloom cell division period will predispose 'Braeburn' apples to postharvest internal browning; 2) Warm conditions during the four week pre-harvest period will reduce postharvest internal browning; 3) High crop loads will reduce postharvest browning incidence/severity when preharvest air temperatures in the orchard vary.

2. Materials and methods

2.1. *Orchard treatments*

Field experiments involving orchard day/night temperatures and crop load treatments were conducted at the KOB (Table 1). Treatments involved either two or three levels and were replicated three or four times in a randomised design using seven trees per plot. Experiments in all years used the same block of 'Braeburn' apple trees at the KOB (planted in 2006, 3.2 by 0.8 m spacing, 3.8 m in height). Tree canopies were divided into three sectors; top (1/3), middle (1/3) and bottom (1/3) to obtain data on the disorder incidence with regard to fruit position within the tree canopy.

All apples from a specific tree-sector and storage condition represented one storage sample (Table 1). Each sample was harvested, stored and assessed separately excluding 2016, here trees were harvested as total apples per sector within a repetition (Table 1).

2.1.1. *Cell division temperature treatments*

Air temperature treatments were conducted in spring in all three experimental years for three weeks post petalfall. There were three treatment levels (warm +2 °C compared to ambient, ambient or cold -2 °C compared to ambient). Treatments were replicated three times and conducted in plastic greenhouse tents built over the plots in the orchard using either small 2.4 kW domestic fan heaters placed on the ground or 3.0 kW cooling machines (Riedel, Kulmbach, Germany) mounted at the top of the tents covering the trees. The ambient control trees were covered in hail netting to adjust for the light reduction caused by the plastic sheeting and were not in a tent. Temperature difference controllers (HTronic TDR 2004, Hirschau, Germany) were used to control the heaters or cooling machines and `ibutton' temperature dataloggers (Measurement Systems Ltd, Newbury, UK) placed at three heights within the tree canopies in each plot to record the temperature hourly. Cooling treatments were most effective during the night to maintain the intended -2 °C difference compared to ambient but were not effective when the sun shone brightly where the tents had to be opened and vented to maintain temperatures closer to ambient conditions. In 2017, a damaging late spring frost (-4.5 °C) occurred during full flowering. The

Table 1

Overview of the field and storage experiments* conducted on 'Braeburn' trees at the Kompetenzzentrum für Obstbau Bodensee (KOB) from 2016 to 2019.

Year	Orchard Experiment	Levels	Repetitions	Crop load	Mean fruit no. / storage sample	Storage	Data
2016/17	Temp. cell division post petalfall	cold (-2 °C) ambient warm (+2 °C)	3x	standard	57	Delayed-CA or direct-CA for 5 months	Pooled per sector per plot
	Crop load	light standard heavy	3x	light standard heavy	56		
	Temp. preharvest >10 °C day and night	ambient warm	1x	standard	25		Pooled per sector per tree
2017/18	Crop load nested within Temp. cell division post petalfall	cold (-2 °C) ambient warm (+2 °C)	3x	light standard heavy	19		
2018/19	Temp. cell division post petalfall	cold (-2 °C) ambient warm (+2 °C)	3x	standard	20	Delayed-CA for 5 and 7 months	
	Crop load	light standard heavy	3x	light standard heavy	25		
	Temp. preharvest >10 °C night temperature	ambient warm	4x	light standard heavy	21		

* Temperature cell division treatments conducted for 3 weeks post petalfall. Temperature preharvest treatments conducted for 4 weeks preharvest. Crop load treatments of approximately 50 % / 100 % / 180 % of a standard crop load. In 2017/18 (due to spring frost / limited tree availability) in the temperature cell division experiment and in the 2018/19 temperature preharvest experiment, crop load treatments were nested within the temperature plots.

cell division temperature treatment trees at the KOB were able to be protected with plastic sheeting and heated.

Temperature data were used to calculate growing degree hours (GDH) by subtracting a base temperature of 10 °C (as used by Lau, 1998; Volz et al., 2000) from the mean hourly air temperature and summing (e.g. 3 °C above the base temperature for 1 h gives 3 GDHs). Hourly temperatures of 10 °C or less were set to zero.

2.1.2. *Preharvest temperature treatments*

Preharvest air temperature experiments during the final four weeks preharvest involved warm and ambient treatment levels only. In 2016, a small plastic greenhouse was built over one plot of seven trees and the air temperature maintained at >10 °C during the day and night up until harvest. In the frost year (2017/18) additional `Braeburn’ trees without frost damage were found on a commercial orchard at Kippenhausen some 25 km away from the KOB and eight experimental plots of four trees were established with five different timings of the warm periods, two levels of crop load (light or standard) and one replication (Table 2). Plastic greenhouse tents were built over the plots and heated (>10 °C) from the late afternoon until early morning.

In 2018/19, a replicated (4x) preharvest experiment was conducted at the KOB. Plots of seven trees were either heated in plastic greenhouse tents to maintain >10 °C at night or kept at ambient under one layer of hail net. In addition, three levels of crop load were nested within each temperature plot (crop load details follow below in section 2.1.3). Tents were opened in the morning and closed at night. Large roof windows were designed to maximise the amount of daylight reaching the trees and also to allow any daytime rainfall to wet the trees. Ambient plots were covered with hail netting to try and maintain similar lighting conditions over all plots.

In all study years, temperature dataloggers were placed at three heights with the tree canopies to record the temperature each hour and data used to calculate GDHs.

2.1.3. *Crop load treatments*

At the KOB in each experimental year, three levels of crop load were established as light, standard or heavy, corresponding to approximately 50 %, 100 % or 180 % of a standard crop load, respectively (Table 1). Fruit numbers varied slightly each year due to differences in natural fruit-set, frost event and tree canopy growth. Hand thinning treatments were conducted during flowering and after June drop to establish the final crop load some 12 weeks preharvest. When bloom intensity was very heavy (2016/17), early flower cluster thinning was conducted to space clusters out at 10, 20 or 30 cm with additional hand thinning of fruitlets conducted directly after June drop. In the frost year (2017/18) with limited tree availability, crop load treatments were nested within the cell division temperature plots. In this year little hand thinning was required as in each plot of seven trees there were either two or three trees with a light, standard or heavy crop load. However due to the frost the fruit distribution over the tree was uneven with more fruit at the top and less at the bottom.

Table 2
Preharvest air temperature treatments conduced at Kippenhausen in 2017/18. Harvest date 18 October, N = approximately 200 fruit assessed per plot (4 trees).

Temp. treatment, Crop load level	Warm phase preharvest temp. treatments ~ >10 °C for 10 nights			Mean core-browning % incidence (severity index)
	16–26 Sep.	26 Sep.–06 Oct.	06–17 Oct.	
ambient, light	–	–	–	63 % (18)
ambient, standard	–	–	–	55 % (12)
warm phase1, standard	X	–	–	41 % (9)
warm phase2, standard	X	X		38 % (8)
warm phase3, light	X	X	X	27 % (7)
warm phase3, standard	X	X	X	13 % (3)
warm phase4, standard	–	X	X	12 % (3)
warm phase5, standard	–	–	X	17 % (4)

In the Kippenhausen orchard preharvest experiment, mature `Braeburn’ trees (3.1 by 0.9 m spacing, 3.5 m in height) were hand thinned some 5 weeks prior to harvest to two levels of crop load as light (50 %) or standard (100 %).

In 2018/19 sufficient trees were available for all experiments so in addition to a crop load experiment, three levels of crop load were nested within the preharvest temperature experiment plots.

2.2. *Harvesting and postharvest CA storage conditions*

Standard apple maturity tests for fruit firmness (FF N), starch staining pattern index (scale 1–10) and soluble solids content (SSC %) were used to calculate a harvest index [FF/(SSC x starch)] and set a harvest window following the usual commercial practice in Southwest Germany (Streif and Kittemann, 2018). At-harvest maturity data (three repetitions of eight fruit) from 2016 to 2018 are shown in Table 3. At-harvest, all fruit from trees were picked separately by sector. Immediately after harvest, the ‘Braeburn’ fruit were sorted (very small fruit <60 mm removed) and randomly allocated into storage treatments. In 2016 and 2017 fruit were placed in CA for five months in either a storage condition intended to reduce ’Braeburn’ browning disorder (BBD) by low CO_2 concentrations (1 °C, 21 d delayed-CA establishment, 1 kPa O_2, <0.7 kPa CO_2) or a storage condition intended to induce BBD symptoms (1 °C, direct-CA, 2.0 kPa O_2 and 2.3 kPa CO_2). In 2018, all fruit were stored in delayed-CA as given above and removed from storage after five and seven months.

2.3. *Assessments at storage removal*

At storage out-turn, fruit samples (Table 1) were kept at room temperature for 7 d and then all fruit (>10,000 in each study year) were individually assessed by trained staff for external disorders (bitter pit, CO_2 damage, superficial scald) and by cutting for internal disorders (core browning, flesh browning, cavities, bitter pit). For assessments in 2016, fruit samples were pooled together from each treatment repetition per sector. In 2017 and 2018 fruit were assessed separately for each tree and sector. All disorders were scored on the same 0–3 scale (in 0.5 steps), where 0 = no symptoms and 3 = most severe symptoms. Apples with only slight symptoms (i.e. scores of 1 and below) would most likely be acceptable for consumers. Incidence was calculated as the total number of fruit with a score ≥ 0.5 divided by the total fruit number expressed as a percentage. A disorder severity index (0–100) was calculated where i = disorder score as either 0, 0.5, 1, 1.5, 2, 2.5, 3, n_i = number of fruit with score i and N = total number of fruit assessed.

$$Severity\ Index = \frac{\sum_{i=0}^{i=3} (n_i\ x\ i)\ x\ 100}{N * 3}$$

2.4. *Statistics and data analysis*

The disorder score data obtained after storage and shelf-life are shown as the mean percentage incidence and mean severity index (0–100) with the standard deviation (sd).

The core browning data from the crop load and temperature experiments (cell division and preharvest) were analysed further using box-plots and receiver operating characteristic (ROC) curves calculated with the software package ‘pROC’ available for R (Robin et al., 2011). ROC curve analyses are used in many medical fields to assess the performance

Table 3
Full bloom and harvest dates and at-harvest maturity parameters of fruit firmness (FF), soluble solids content (SCC), starch pattern index and harvest index [FF/(SSC x starch)] for experiments on 'Braeburn' apples in 2016 to 2018.

Year	Full Bloom	Location	Experiment	Harvest date	FF (N)	SSC (%)	Starch (1–10)	Harvest Index**
2016 /17	30. Apr	KOB	Crop load*	16/17. Oct	108	11.3	3.3	0.29
2017 /18	18. Apr		Crop load*	17. Oct	96	11.2	5.6	0.16
2018 /19	23. Apr		Crop load*	03. Oct	97	12.1	3.3	0.25
2017 /18	21. Apr	Kippen-hausen	Temp. preharvest	18. Oct	89	11.2	5.6	0.14

* Values for the middle sector of standard crop load trees. Other maturity tests taken on same day showed similar values regardless of crop load / tree sector / temperature cell division treatment.

** Harvest index FF units as kg/cm^2.

of biomarkers as binary classifiers to predict disease risk. In postharvest biology, ROC curves have found application in fruit sorting when VIS/NIR non-destructive equipped graders are used to assess internal fruit quality (Walsh et al., 2020). And recently, Leisso et al. (2019) used ROC curves to assess the influence of preharvest factors like GDD, chilling hours and other fruit quality parameters as binary classifiers to predict the risk of disorders developing in 'Honeycrisp' apples. Here we have followed a similar approach.

As a non-parametric assessment of binary classifier performance ROC curves are much less demanding for the assumptions of data normality, equal variance and balanced datasets as required for statistical methods based on probability distributions with deviations from a mean or variance value. ROC curves are commonly based on the frequencies with which a classifier produces true positives (TP = fruit with disorder), true negatives (TN = sound fruit), false positives (FP = sound fruit classed as disordered) and false negatives (FN = disordered fruit classed as sound) as shown as an example in Fig. 1.

In all the ROC curves given below, the y-axis shows the true positive percentage (also known as sensitivity) = TP/(TP + FN) with the false positive percentage (1-specificity) = 1-(TN/ (TN + FP)) on the x-axis. The area under the curve (AUC) is shown in plots, as it is an important measure of classifier performance. When the AUC is close to 50 %, the classifier has no power to discriminate between sound and disordered fruit, while AUC values of ~ 75 % and above show good utility, with a perfect classifier having an AUC value of 100 %. The 'pROC' software package allowed 95 % confidence intervals (CIs) for the AUC to be calculated using 2000 stratified bootstrapping resamplings, these CIs are displayed in the plots as a shaded area. The CIs show the range of values the AUC would take if the experiment was repeated many times under identical conditions, but note also these CIs are not appropriate when the same classifier is applied in other situations. In addition, the 'pROC' software can calculate an optimal balance of true positive and false positive percentages and give the corresponding threshold value of the classifier. However, this threshold value may not always be appropriate in a practical sense i.e. when the negative cost of FNs is high and results in product rejection by a customer / end consumer.

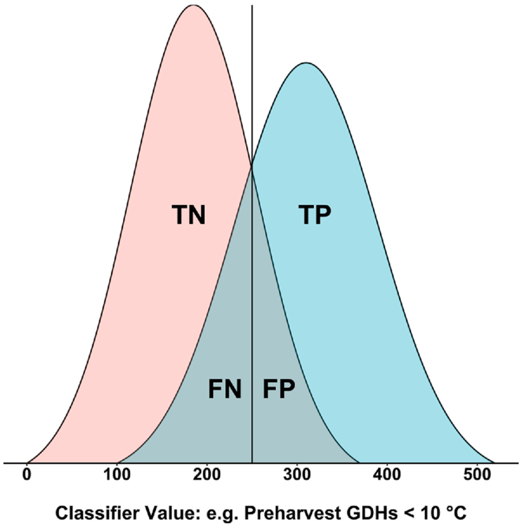

Fig. 1. Theoretical distributions for sound fruit (TN = true negative) and disordered fruit (TP = true positive) separated by a binary classifier (vertical line) at a cut-off value of ~ 250 growing degree hours < 10 °C in the preharvest period. TN values on the right of the cut-off become false positives (FP) and TP values on the left become false negatives (FN).

ROC curve analyses with data combined from all years were conducted for three different classifiers of core browning incidence and severity: 1) GDH > 10 °C for the cell division treatments (data as means per plot per sector); 2) GDH < 10 °C for the preharvest treatments (data as means per plot per sector per tree); 3) crop load, as the percentage of a standard full crop load per tree sector (100 %) (data for all years as means per plot per sector except 2017/18 as means per plot per sector per tree as crop load treatments were nested within the cell division temperature plots). The mean core browning data from each storage sample were subjectively allocated into two binary categories as either high or no / low incidence and severity. To achieve binary categories for the ROC curve analysis a subjective cut-off value of 30 was used for the severity index to separate the samples when incidence was high in 2016/17 and when severity was much lower in 2017/18 and 2018/19, a 30 % incidence threshold was used. Fruit below this 30 % threshold had very slight symptoms (very low severity). The boxplots summarise the binary distributions but do not show *p* values as most of these data were skewed i.e. non-normal.

Multivariate linear discriminant analysis (LDA) to classify fruit into binary classes as either no / low browning or high browning (using the incidence and severity cut-off values as explained above) was conducted for preharvest GDH < 10 °C and crop load data as predictor variables. LDA models were built for each year separately and combined for all years (N = 84, 96, 335 for 2016/17, 2017/18 and 2018/19, respectively). Models used the crop load data per plot per sector per tree and the temperature values for each plot per sector. The GDH < 10 °C data for 2017/18 and 2018/19 were able to be separated into two variables and entered in the LDA models as GDH < 10 °C during the last 10 d preharvest and GDH < 10 °C during the 11–20 d preharvest period. GDH < 10 °C data in the 2016/17 LDA model could not be separated into two variables as it was collinear. GDH < 10 °C data from the earlier 21–30 d preharvest period contained too many zero values and could not be used in the LDA models. The GDH < 10 °C and crop load predictor data were non-normal bi-modal or skewed distributions and were forced into normal distributions by using transformations from the 'bestNormalize' package in R. These data were then mean centred ($\mu = 0$) and scaled (sd $=$ 1) and split into a training (80 %) and test data set (20 %) for input into LDA using the 'Mass' package in R. The LDA model performance to predict the test data was assessed from the % of correctly classified samples and the AUC values from a ROC curve. The sign and the absolute size of the linear coefficients can show the contribution and relative importance of each predictor variable in the LDA model. When LDA is used for a binary classification, the linear discriminant has one dimension only.

3. Results and discussion

3.1. *Occurrence of browning disorders during the three experimental years*

The incidence of internal browning disorders varied greatly over the three study years (Table 4). The 2016/17 season was a severe internal browning year for 'Braeburn' with a mean core browning incidence (severity) of 58 % (16) and 82 % (31) over all field treatments in delayed-CA and direct-CA, respectively. The mean incidence (severity) of cavities was 9 % (2) and 33 % (9) over all field treatments in delayed-CA and direct-CA, respectively. The incidence of flesh browning was close to zero.

In 2017/18, the severe frost event at the KOB during flowering strongly affected the incidence of storage disorders. Apples in direct-CA were extremely susceptible to external CO_2 damage (bronzed areas on the fruit skin, mostly sunken with irregular shaped edges) with a high incidence (31 %) over all treatments, while fruit in delayed-CA showed no incidence (Table 4). Frosts during bloom can lower the apples' tolerance for stress factors like high CO_2, low O_2 or low temperatures (Little and Holmes, 2000). Furthermore, an assessment of internal browning symptoms for the direct-CA storage samples was not possible. Core and flesh browning symptoms could not be clearly separated as internal CO_2 damage (browning with numerous large cavities) was also present in the majority of samples. Thus, only data for the delayed-CA storage samples from 2017/18 are presented. At the KOB, the incidence (severity) of core browning, flesh browning and cavities over all field treatments was 37 % (12), 4 % (2) and 3 % (1), respectively and for the Kippenhausen orchard, symptoms were broadly similar to the KOB with 33 % (8), 7 % (2) and 0 % (0), respectively (Table 4).

In 2018/19 all fruit were stored in delayed-CA storage and removed at five and seven months. The incidence (severity) of core browning over all treatments was 5 % (1) and 24 % (6) at the first and second storage removals, respectively. There was no incidence of flesh browning or cavities. 2018/19 was a bitter pit and superficial scald year (Table 4). Our observations of fruit industry pack-outs for 'Braeburn' over numerous years together with our storage results in this three year study suggest seasons with a high incidence of bitter pit are in general not severe internal browning years and vice versa.

Over the three experimental seasons at the KOB, neither different harvest timings nor calcium spray treatments conducted in the same orchard block in adjacent plots and stored under the same CA conditions showed any clear effects on the postharvest browning disorders (details and results not given).

3.2. *Cell division temperature experiments*

The spring temperature field treatments aimed to influence growth processes occurring during cell division and it was difficult to maintain the intended temperatures. During the warmest parts of the day there were clear temperature gradients between the top and bottom of the trees within both the warm and cold treatments. During the day, the desired temperature differences ($\triangle$ +/- 2 °C) to the ambient air temperatures were mostly not achieved and conditions in the plastic tents were too warm when the sun shone strongly around the middle of the day. However, at night there were minimal temperature gradients and the desired temperature differentials were generally well maintained. In each of the three study years, when the tents were removed after the three week post petal fall treatment period, there was a mean fruit diameter of 20 mm in the ambient treatment and mean diameters of +/- 2 mm for the warm and cold treatments, respectively. Apple fruit are known to grow (expand) mostly at night (Lang, 1990) when leaf transpiration is at a minimum, so we assume that the night temperatures were mainly responsible for these initial differences in fruit diameter. After the treatments were removed and all plots experienced ambient conditions until harvest, the cold treated fruit showed a higher relative growth rate for around five weeks and reached a similar mean fruit size as the ambient treated fruit but never exceeded it. The warm treated

Table 4

Mean incidence and severity (over all field treatments) of storage disorders in 'Braeburn' apples after seven day shelf-life following direct-CA or delayed-CA from the Kompetenzzentrum Obstbau Bodensee (KOB) and Kippenhausen orchards over three different years.

Year	Storage Duration	Orchard	Symptom	Delayed-CA		Direct-CA	
				Incidence (%)	Severity (1–100)	Incidence (%)	Severity (1–100)
2016/17	5 months	KOB	Core browning	58	16	82	31
			Flesh browning	0	0	0	0
			Cavities	9	2	33	9
2017/18		Both orchards	External CO_2	0	0	31	17
		KOB	Core browning	37	12	n.a.	
			Flesh browning	4	2		
			Cavities	3	1		
		Kippenhausen	Core browning	33	8		
			Flesh browning	7	2		
			Cavities	0	0		
2018/19		KOB	Core browning	5	1	No Direct CA storage	
			Flesh browning	0	0		
			Cavities	0	0		
			Bitter pit	22	9		
			Superficial scald	8	2		
	7 months		Core browning	24	6		
			Flesh browning	0	0		
			Cavities	0	0		
			Bitter pit	16	6		
			Superficial scald	28	8		

fruit maintained the initial difference of approximately 10 % larger fruit size over the ambient fruit until harvest. Our growth rate data are exactly in line with those described by Warrington et al. (1999) working with temperature treatments applied during cell division to potted apple trees in growth chambers and then moved outside to ambient conditions. However, unlike Warrington et al. (1999) we found no differences between treatments for fruit maturity at harvest (harvest index).

In 2016/17 and 2018/19 all trees in the cell division temperature plots were hand-thinned to a standard crop load. In 2017/18, three levels of crop load were nested within each temperature treatment plot. These crop load differences were established early during bloom and adjusted slightly by hand thinning when the plastic tents were removed. We did not determine the internal cell structure at-harvest for possible differences in cell size, cell number or intercellular space (porosity). How apple fruit growth is influenced by the interaction of orchard air temperatures and differences in crop load is by no means clear and it is an ongoing research question (Malladi, 2020). Unpublished work suggests higher temperatures during cell division result in the fruit completing a set number of cell division cycles in a shorter time, thus allowing the fruit more time on the tree until harvest to grow larger, compared to fruit growing under cooler temperatures which take longer to complete the same number of cell divisions and are smaller at-harvest (Hirst, 2016). While differences in crop load and timing of when the final crop load is established on the tree will result in fruit having differences in carbohydrate supply, with the final fruit size due largely to differences in cell numbers (Hirst, 2016).

We can find no literature on how spring air temperatures or changes in crop load during fruit development can influence the intercellular space of apples at-harvest and subsequently how the intercellular space may change during postharvest handling and CA storage. However, work by Ruess and Stösser (1993) determined changes in the intercellular volume for five apple cultivars (not including 'Braeburn') from two weeks after full bloom until harvest and during 20 weeks cool storage in air. All fruit were sourced from the same orchard site and trees were controlled for a similar crop load (standard for each cultivar). Results (common for all tested cultivars) showed that the intercellular space did not develop to any large extent until after cell division was completed some four to six weeks after full bloom. For a specific cultivar larger fruit (with a lower specific gravity) showed a higher intercellular volume. Thus, we have reasonable grounds to conclude our experimental cell division temperature treatments produced three distinct groups of fruit (each with very different growth rates and final mean fruit size) that would all have important differences in cellular structure at-harvest and different gas exchange characteristics during postharvest storage. In particular, for the 2017/18 season when fruit development in the orchard was influenced by both temperature treatments and differences in crop loads that were established very early during bloom.

Fig. 2A shows a box plot with all available data combined from all three experimental seasons for the two classes of high or no / low browning versus GDH > 10 °C during the three week spring post bloom period. The box plot shows a slightly higher median value of 2957 GDH > 10 °C for no / low browning compared to 2762 for high browning. When all these data are analysed as a ROC curve there is no utility for GDHs during the spring postbloom period to predict core browning (either high severity or high incidence) with an overall AUC value of 56.7 % (Fig. 2B). Conducting analyses separately for each year showed very similar AUC values. In summary, we have no evidence that spring temperatures can influence browning disorders during storage and our initial hypothesis that warm temperatures (within the range of $\triangle$ +/- 2 °C) after bloom during cell division result in browning disorders should be rejected.

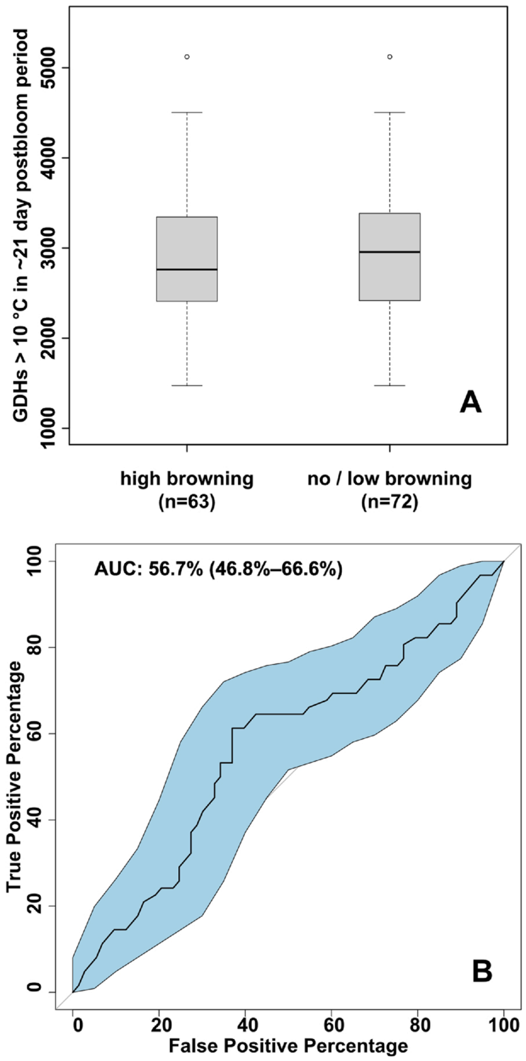

Fig. 2. A) Boxplot of high or no / low core browning in 'Braeburn' apples after five or seven months controlled atmosphere (CA) storage versus growing degree hours (GDH) >10 °C in the three week postbloom period. Number of samples = 135 (54, 27, 54 for 2016/17, 2017/18, 2018/19, respectively). B) The corresponding receiver operating characteristic (ROC) curve for GDHs >10 °C in the three week postbloom period to predict core browning in 'Braeburn' apples. All available data from all three experimental years are combined in one ROC curve. Shaded area is the 95 % CI for the ROC curve (N = 135).

3.3. *Temperature pre-harvest experiments*

The preharvest temperature experiment in 2016/17 had a very pronounced effect on core browning. Trees maintained at >10 °C in the four week preharvest period had very low core browning with a mean incidence (severity) of 6 % (2) from both storage conditions compared to fruit from trees at ambient conditions with 56 % (18).

In the Kippenhausen orchard preharvest temperature experiment in 2017/18, eight experimental treatments were established on 'Braeburn' trees (Table 2). The trends in mean core browning incidence (severity) for each treatment are given in Table 2. Warm treatments closer to harvest appear more effective at reducing core browning.

2018/19 was not a severe browning year (Table 4). However, the 2018/19 results are in line with the other two seasons. The first storage removal shows core browning incidence (severity) for all the warm treatments of 1 % (0) regardless of crop load (Table 5). At the second storage removal warm treatments show approximately half the incidence (severity) compared to the fruit from ambient conditions.

Table 5

Incidence and severity of core browning and the starch pattern index at-harvest after five and seven months delayed-CA storage for the temperature preharvest experiment in 2018/19 at the Kompetenzzentrum Obstbau Bodensee (KOB).

Storage	Treatment		Core browning				Starch pattern index*	
			incidence		severity			
	Temp.	Crop load	%	(sd)	0–100	(sd)	1–10	(sd)
5 months	ambient	heavy	0	(0.0)	0	(0.0)	2.5	(0.3)
	ambient	standard	3	(6.3)	1	(1.1)	3.2	(0.3)
	ambient	light	13	(5.4)	2	(1.1)	3.1	(0.2)
	warm	heavy	0	(0.5)	0	(0.1)	2.9	(0.6)
	warm	standard	1	(1.4)	0	(0.3)	4.2	(0.7)
	warm	light	1	(1.4)	0	(0.2)	3.5	(0.7)
7 months	ambient	heavy	0	(0.3)	0	(0.1)	2.5	(0.3)
	ambient	standard	10	(14.0)	2	(2.9)	3.2	(0.3)
	ambient	light	39	(8.0)	9	(1.5)	3.1	(0.2)
	warm	heavy	0	(0.3)	0	(0.1)	2.9	(0.6)
	warm	standard	4	(8.0)	1	(1.2)	4.2	(0.7)
	warm	light	22	(5.2)	4	(1.2)	3.5	(0.7)

* Starch pattern index, 1 = black, 10 = clear, at-harvest (10 Oct.), middle tree sector, Number of samples = 3.

Fig. 3A shows a box plot with all available data combined from all three experimental seasons for the two classes of high or no / low core browning incidence versus GDHs <10 °C during the four week preharvest. The corresponding ROC curve (Fig. 3B) shows a good utility to predict core browning incidence with a AUC value of 78.6 %. The ROC curve suggests a threshold value of 266 GDHs <10 °C during the 4 week preharvest period shown as the point on the ROC curve and the dotted horizonal line in the box plot. Over the three study years, warm preharvest conditions are protective for core browning in ‘Braeburn’ and confirm our initial hypothesis.

We know of no other literature where preharvest temperature treatments have been conducted on ‘Braeburn’ in regard to postharvest disorders. However, our results are in agreement with the GDD observations from a range of workers (Lau, 1998; Volz et al., 2000) that link ‘Braeburn’ browning incidence to cool preharvest conditions, in particular during the last 30 d preharvest as recorded by Volz et al. (2000). We also note that for the apple cultivar ‘Fuji’, cooler growing conditions during fruit maturation are associated with a higher incidence of watercore, commonly understood as a disturbance in carbohydrate uploading into the fruit (Ferguson et al., 1999).

Our results from three consecutive seasons show strong evidence that temperature conditions very close to harvest can influence browning susceptibility, but without further experimental data we cannot explain a possible mechanism, however, we can share some ideas.

Apples in the warm preharvest treatment in 2016 show a trend for higher starch degradation at-harvest with a starch pattern index of 4.1, a FF of 99 N and a SSC of 10.5 % compared to 3.5, 103 N and 10.6 %, in ambient conditions, respectively. In 2018, warm preharvest treatments also show a similar trend for higher starch degradation (Table 5), with a mean starch pattern index of 3.6, a FF of 92 N and a SSC of 11.5 % compared to 2.9, 93 N and 11.3 %, in ambient conditions, respectively. No maturity data for the different treatment levels are available from the Kippenhausen study in 2017. In summary, warm preharvest treated fruit compared to ambient fruit appear slightly more mature with an altered carbohydrate status i.e. more starch conversion but similar or slightly raised SSC. But these trends do not fit well with the literature and our experience where starch clearing and maturation is higher under cooler conditions (Smith et al., 1979; Sperling et al., 2017). The apparent higher starch conversion in the warm treated plots may be due to a smaller day night temperature difference and lower starch accumulation in the fruit (Toivonen, 2019). These aspects of carbohydrate metabolism require closer study during fruit maturation, in particular given that autumn temperatures are now in general warmer and diurnal temperature differences often less marked than were usual in the past. Fruit continue to upload carbohydrates while on the tree. Carbohydrate uploading via the apoplast is the most important pathway for sugars during the final stages of apple maturation and is an energy intensive process (Zhang et al., 2004). Fruit growth (expansion) is largely driven by osmotic pressure created by sugar accumulation in the vacuoles (Malladi, 2020) and largely occurs at night (Lang, 1990). After the first experimental year, the preharvest warming treatments were applied at night only to coincide with when cell expansion was mostly taking place. Thus, fruit from the preharvest warming treatments may have also had an altered energy / carbohydrate status at-harvest due to differences in uploading processes and these effects could be protective against browning occurring during postharvest handling and storage. However, fruit growth also involves dynamic ongoing changes in particular with the intercellular volume both on and off the tree (Ruess and Stösser, 1993). Such internal structural changes within the fruit will affect gas exchange, these changes could be protective or not in regard to browning disorders. Fruit diameter growth was measured in this study but did not show any differences between preharvest temperature treatments. Measuring fruit diameter only will underestimate fruit growth during final maturation (Malladi, 2020), thus we cannot exclude that there may have been treatment differences in fruit length or growth expansion in and around the fruit shoulders of the calyx or stem ends.

Some other environmental factors that could have influenced the fruits’ susceptibility to browning during final maturation were not controlled for in our experimental setup. Rainfall occurring in the days immediately preharvest is a factor now known to affect internal browning incidence in some of the more recent apple cultivars with a very firm fruit flesh texture (Johnston, 2018). The experimental tents used in the study were fitted with large roof windows to be open during the day to maximise photosynthesis and carbohydrate supply from the leaves and also to allow any daytime rainfall to wet the trees and fruit. But even so the tent treatments very likely reduced the amount of free moisture on the fruit skin from dew or fog (common in autumn in this growing region) with the warm treated fruit being somewhat drier overnight compared to ambient conditions, although we did not specifically determine this. It is possible for apple fruit to uptake water osmotically through the skin (Lang, 1990) and as the skin of ‘Braeburn’ apples is the major barrier to gas exchange, any change in skin permeance could also have affected browning susceptibility.

Experiments were intended to test our hypothesis that warm preharvest conditions will reduce postharvest browning and also provide some data as to when warming (time before harvest) was most effective. The results show that preharvest conditions can markedly change browning disorder incidence with evidence that conditions directly before harvest (within the last 11 days) can be effective.

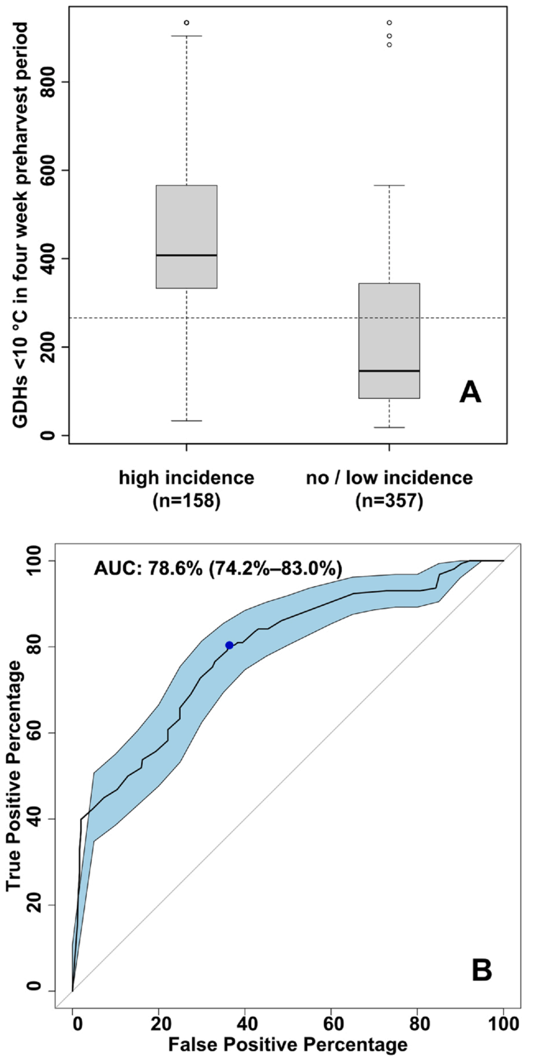

Fig. 3. A) Boxplot of high or no / low core browning incidence in ‘Braeburn’ apples after five or seven months controlled atmosphere (CA) storage versus growing degree hours (GDH) <10 °C in the four week preharvest period. Number of samples = 515 (84, 96, 335 for 2016/17, 2017/18, 2018/19, respectively). B) Corresponding receiver operating characteristic (ROC) curve for GDHs <10 °C in the four week preharvest period to predict core browning incidence in ‘Braeburn’. All available data are combined in one ROC curve for all three experimental seasons. The optimal threshold from the ROC curve of 266 GDHs <10 °C is shown as the point (x = 36, y = 80) and as a dotted horizontal line in the box plot. Shaded area is the 95 % CI for the ROC curve. N = 515.

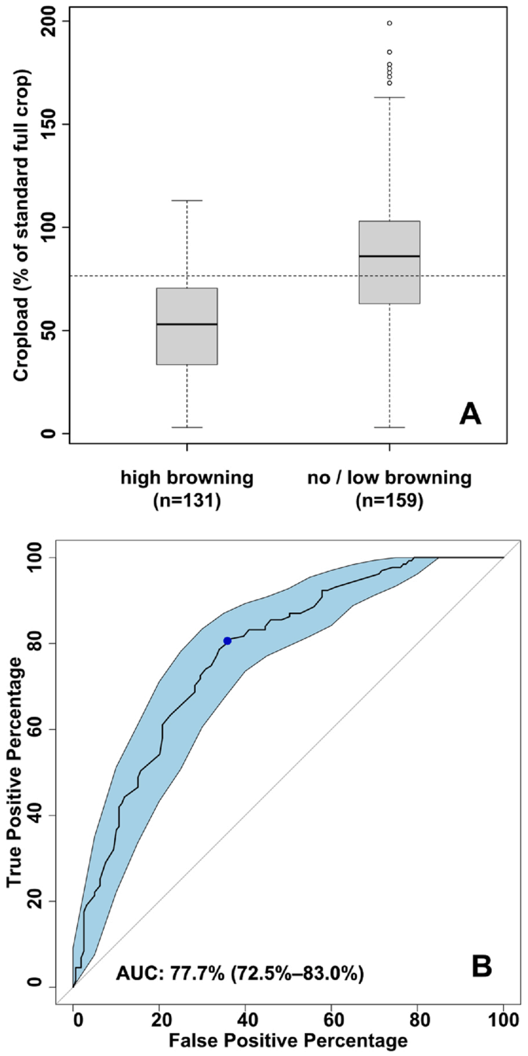

Fig. 4. A) Boxplot of high or no / low core browning in ‘Braeburn’ apples after five and seven months controlled atmosphere (CA) storage versus crop load as a % of a standard full crop (100 %). Number of samples = 290 (54, 182, 54 for 2016/17, 2017/18, 2018/19, respectively). B) Corresponding receiver operating characteristic (ROC) curve for crop load to predict core browning in ‘Braeburn’ apples. All available data are combined in one ROC curve for all three experimental seasons. The optimal threshold from the ROC curve of 76.5 % of a standard crop load is shown as the point (x = 36, y = 81) and as a dotted horizontal line in the box plot. Shaded area is the 95 % CI for the ROC curve. N = 290.

3.4. *Crop load experiments*

Fig. 4A shows a box plot with all available data combined from all three experimental seasons for the two classes of high or no / low core browning versus crop load as a % of a standard full crop (100 %). The corresponding ROC curve (Fig. 4B) shows a reasonable utility to predict core browning incidence with a AUC value of 77.7 %. The ROC curve suggests a threshold value of 76.5 % of a standard crop load shown as the point on the ROC curve and the dotted horizonal line in the box plot.

In 2018/19, the clear protective effect of crop load treatments nested within the temperature preharvest treatments to reduce the incidence and severity of core browning can be seen in Table 5. At the first storage removal, fruit from the ambient heavy and standard treatments show either no or a very low core browning. The ambient light crop load treatment shows a higher but still relatively low incidence (severity) of 13 % (2). At the second storage removal core browning in all treatments is higher overall but the disorder pattern is similar to the first removal with a clear influence of crop load. Heavy crop loads are totally protective and show very low (no) symptoms.

As other reviewers have noted, the effects of crop load on postharvest behaviour of apple in regard to gas exchange disorders, remain largely unexplained (Ferguson et al., 1999; Wünsche and Ferguson, 2005). With the exception of calcium physiology there is very little relevant literature to help link crop load effects on postharvest behaviour. We can find only two papers that are partially relevant, both deal with carbohydrate metabolism and do not address other aspects that could affect gas exchange within the fruit such as skin characteristics, cell size, number or intercellular structure. Klages et al. (2001) could explain fruit size differences in 'Braeburn' apple between high and light crop load trees based on differences in the carbohydrate supply from the leaves or within high crop load trees by sink activity and Palmer et al. (2013) studied the crop load effects of 'Scifresh' apples on carbohydrate accumulation. However, neither of these two studies included any postharvest assessments.

In all study years, the heavy crop load treatments consistently reduced core browning when compared to standard or light treatments and our initial hypothesis that the protective effect of crop load could be maintained when preharvest temperatures varied was confirmed.

3.5. Multivariate analysis of preharvest GDH < 10 °C and crop load to predict core browning

The multivariate LDA model for the KOB 2016/17 data showed an accuracy of 88 % to correctly classify the test data set and a very high ROC curve AUC value of 92 % (ROC curve not given). The model coefficients were -0.19, and +1.07 for crop load and GDH < 10 °C, respectively. The relatively small coefficient for crop load is due to the fact that all trees in the preharvest plots in 2016/17 carried a similar standard crop load and the dominant effect on the model was due to GDH < 10 °C.

The multivariate LDA model for Kippenhausen in 2017/18 showed an accuracy of 89 % and a high ROC curve AUC value of 90 % for the test data set. The linear discriminant coefficients show the model was most influenced by the GDH < 10 °C (value of -1.12) during the 0–10 d preharvest period while the influence of crop load (+0.32) and GDH < 10 °C (-0.31) during the 11–20 d preharvest period had similar magnitude but opposite signs.

The multivariate LDA preharvest model for the KOB in 2018/19 showed an accuracy of 83 % and a high ROC curve AUC value of 83 % when applied to classify the test data set. The model coefficients were +0.99, -0.13 and -0.42 for crop load, GDH < 10 °C in the 0–10 d and 11–20 d preharvest periods, respectively. Crop load had the most effect on the model but GDH < 10 °C also contributed, but mostly from the 11–20 d preharvest period as it was colder than in the 10 d period immediately preharvest.

The multivariate LDA model for all years showed an accuracy of 83 % to correctly classify the test data set with a ROC curve AUC value of 87 %. The model coefficients were +0.48, -1.28 and +0.32 for crop load, GDH < 10 °C in the 0–10 d and 11–20 d preharvest periods, respectively. The LDA model for all years was mostly influenced by the GDH < 10 °C during the 0–10 d preharvest period. A better understanding of the relative contribution of cool preharvest temperatures and crop load and their interactions on browning will require more experimental data from a year with a high browning incidence / severity.

4. Conclusions

In each study year, the cell division temperature treatments effectively produced three distinct populations of fruit each with different size profiles and growths rates and presumably these apples all had a range of different internal tissue structures / porosity at-harvest. However, the field data we were able to collect over the three seasons does not support a strong effect (if any) of post bloom temperatures (△ of +/- 2 °C from ambient) during cell division on internal browning incidence in 'Braeburn' apples. In contrast, preharvest temperature conditions of > 10 °C during the last four weeks preharvest can markedly influence the development of internal browning. Further studies are necessary in the preharvest period to try and untangle the effects of temperature on carbohydrate uploading into the fruit, fruit growth and expansion (ideally including non-destructive determination of porosity) and to explore these processes in relation to the stage and rate of fruit maturation and ripening. In all study years, the high crop load treatments consistently reduced core browning when compared to standard or light treatments. How crop load affects postharvest browning behaviour is not as yet clearly explained.

ROC curve analyses are a useful methodology to form stronger links between preharvest factors and the postharvest behaviour of fruit. The crop load carried by the tree, the timing of thinning operations in relation to fruit development together with the decision of when to harvest the apples are factors under grower control that can be managed to help reduce disorders in CA storage. In addition, a better understanding of the preharvest temperature effects on browning susceptibility has the potential to allow the duration of CA stored 'Braeburn' to be optimised.

CRediT authorship contribution statement

R.J. McCormick: Investigation, Methodology, Project administration, Formal analysis, Writing - original draft, Visualization. **K. Biegert:** Investigation, Methodology, Data curation, Writing - review & editing, Formal analysis. **J. Streif:** Conceptualization, Investigation, Methodology, Writing - review & editing.

Declaration of Competing Interest

The authors declare that they have no known competing financial interests or personal relationships that could have appeared to influence the work reported in this paper.

Acknowledgements

The 'BigApple' project was supported by funds of the Federal Ministry of Food and Agriculture (BMEL) based on a decision of the Parliament of the Federal Republic of Germany via the Federal Office for Agriculture and Food (BLE) under the innovation support programme. We gratefully acknowledge our 'BigApple' project partners who all contributed to the successful completion of this project. We thank Paul Figel Refrigeration for technical assistance with the cooling machines and temperature controllers in the orchard, Erich Röhrenbach and the Marktgemeinschaft Bodenseeobst (MaBo) for access to the orchard at Kippenhausen and our KOB work colleagues for help in the field and lab and all the students who undertook internships at the KOB over this time.

References

Dražeta, L., Lang, A., Hall, A., Volz, R., Jameson, P., 2004. Air volume measurement of 'Braeburn' apple fruit. J. Exp. Bot. 55, 1061–1069. https://doi.org/10.1093/jxb/erh118.

Elgar, H., Lallu, N., Watkins, C., 1999. Harvest date and crop load effects on a carbon dioxide–related storage injury of 'Braeburn' apple. HortScience 34, 305–309. https://doi.org/10.21273/hortsci.34.2.305.

Ferguson, I., Volz, R., Woolf, A., 1999. Preharvest factors affecting physiological disorders of fruit. Postharvest Biol. Technol. 15, 255–262. https://doi.org/10.1016/s0925-5214(98)00089-1.

Herremans, E., Verboven, P., Bongaers, E., Estrade, P., Verlinden, B., Wevers, M., Hertog, M., Nicolai, B., 2013. Characterisation of 'Braeburn' browning disorder by means of X-ray micro-CT. Postharvest Biol. Technol. 75, 114–124. https://doi.org/10.1016/j.postharvbio.2012.08.008.

Herremans, E., Verboven, P., Defraeye, T., Rogge, S., Ho, Q., Hertog, M., Verlinden, B., Bongaers, E., Wevers, M., Nicolai, B., 2014. X-ray CT for quantitative food microstructure engineering: the apple case. Nucl. Instrum. Methods Phys. Res. B 324, 88–94. https://doi.org/10.1016/j.nimb.2013.07.035.

Hirst, P., 2016. private communication.

Janssen, S., Verboven, P., Nugraha, B., Wang, Z., Boone, M., Josipovic, I., Nicolaï, B., 2020. 3d pore structure analysis of intact 'Braeburn' apples using x-ray micro-CT. Postharvest Biol. Technol. 159, 111014 https://doi.org/10.1016/j.postharvbio.2019.111014.

Johnston, J., 2018. private communication.

Klages, K., Donnison, H., Wünsche, J., Boldingh, H., 2001. Diurnal changes in non-structural carbohydrates in leaves, phloem exudate and fruit in 'Braeburn' apple. Funct. Plant Biol. 28, 131–139. https://doi.org/10.1071/pp00077.

Lang, A., 1990. Xylem, phloem and transpiration flows in developing apple fruits. J. Exp. Bot. 41, 645–651. https://doi.org/10.1093/jxb/41.6.645.

Lau, O., 1998. Effect of growing season, harvest maturity, waxing, low O_2 and elevated CO2 on flesh browning disorders in 'Braeburn' apples. Postharvest Biol. Technol. 14, 131–141. https://doi.org/10.1016/s0925-5214(98)00035-0.

Leisso, R., Hanrahan, I., Mattheis, J., 2019. Assessing preharvest field temperature and at-harvest fruit quality for prediction of soft scald risk of 'Honeycrisp' apple fruit during cold storage. HortScience 54, 910–915. https://doi.org/10.21273/HORTSCI13558-18.

Little, C., Holmes, R., 2000. Storage Technology for Apple and Pears: a Guide to Production Postharvest Treatment and Storage of Pome Fruit in Australia. Department of Natural Resources and Environment, Victoria, Australia.

Malladi, A., 2020. Molecular physiology of fruit growth in apple. Hortic. Rev. (Am Soc Hortic Sci) 47, 1–42. https://doi.org/10.1002/9781119625407.ch1.

Mellidou, I., Buts, K., Hatoum, D., Ho, Q., Johnston, J., Watkins, C., Schaffer, R., Gapper, N., Giovannoni, J., Rudell, D., Hertog, M., Nicolai, B.M., 2014. Transcriptomic events associated with internal browning of apple during postharvest storage. BMC Plant Biol. 14, 328–344. https://doi.org/10.1186/s12870-014-0328-x.

Osinenko, P., Biegert, K., McCormick, R.J., Göhrt, T., Devadze, G., Streif, J., Streif, S., 2021. Application of non-destructive sensors and big-data analysis to predict physiological storage disorders and fruit firmness in' Braeburn' apples. Comput. Electron. Agric. https://doi.org/10.1016/j.compag.2021.106015.

Palmer, J., Diack, R., Johnston, J., Boldingh, H., 2013. Manipulation of fruit dry matter accumulation and fruit size in 'Scifresh' apple through alteration of the carbon supply, and its relationship with apoplastic sugar composition. J. Hortic. Sci. Biotechnol. 88, 483–489. https://doi.org/10.1080/14620316.2013.11512995.

Rabus, C., Streif, J., 2000. Effect of various preharvest treatments on the development of internal browning in 'Braeburn' apples. Acta Hortic. 518, 151–157. https://doi.org/10.17660/actahortic.2000.518.20.

Rajapakse, N., Banks, N., Hewett, E., Cleland, D., 1990. Development of oxygen concentration gradients in flesh tissues of bulky plant organs. J. Am. Soc. Hortic. Sci. 115, 793–797. https://doi.org/10.21273/jashs.115.5.793.

Robin, X., Turck, N., Hainard, A., Tiberti, N., Lisacek, F., Sanchez, J., Müller, M., 2011. pROC: an open-source package for R and S+ to analyze and compare ROC curves. BMC Bioinformatics 12, 77. https://doi.org/10.1186/1471-2105-12-77.

Rudell, D., Leisso, R., Mattheis, J., Giovannoni, J., Gapper, N., Nicolai, B., Watkins, C., Johnston, J., Hertog, M., Schaffer, R., 2017. Gene expression monitoring for risk assessment of apple and pear fruit storage stress and physiological disorders. URL: http://www.freepatentsonline.com/y2017/0260586.html. US Patent Application No. US20170260586(A1).

Ruess, F., Stösser, R., 1993. Untersuchungen über das interzellularsystem bei apfelfrüchten mit methoden der digitalen bildverarbeitung. Gartenbauwissenschaft 58, 197–205.

Saquet, A., Streif, J., Bangerth, F., 2003. Reducing internal browning disorders in' Braeburn' apples by delayed controlled atmosphere storage and some related physiological and biochemical changes. Acta Hortic. 628, 453–458. https://doi.org/10.17660/actahortic.2003.628.57.

Smith, R., Lougheed, E., Franklin, E., McMillan, I., 1979. The starch iodine test for determining stage of maturation in apples. Can. J. Plant Sci. 59, 725–735. https://doi.org/10.4141/cjps79-113.

Sperling, O., Silva, L., Tixier, A., Theroux-Rancourt, G., Zwieniecki, M., 2017. Temperature gradients assist carbohydrate allocation within trees. Sci. Rep. 7, 1–10. https://doi.org/10.1038/s41598-017-03608-w.

Streif, J., Kittemann, D., 2018. Fruchtqualität, Ernte und Lagerung, chapter 14. In: Büchele, M. (Ed.), Lucas 'Anleitung zum Obstbau. Verlag Eugen Ulmer, Stuttgart, DE, pp. 393–435.

Toivonen, P., 2019. Relation between preharvest conditions, harvest maturity and postharvest performance of apples. Acta Hortic. 1256, 469–480. https://doi.org/10.17660/actahortic.2019.1256.67.

Volz, R., Oliver, M., Legg, S., Stanley, J., Morgan, C., Bradley, A., Pidakala, P., 2000. Prediction of BBD (HR99P11.05). Technical Report No 2001/160. HortResearch Report to ENZA (NZ) International, 21 pp..

Walsh, K., McGlone, V., Han, D., 2020. The uses of near infra-red spectroscopy in postharvest decision support: a review. Postharvest Biol. Technol. 163, 111139 https://doi.org/10.1016/j.postharvbio.2020.111139.

Warrington, I., Fulton, T., Halligan, E., De Silva, H., 1999. Apple fruit growth and maturity are affected by early season temperatures. J. Am. Soc. Hortic. Sci. 124, 468–477. https://doi.org/10.21273/jashs.124.5.468.

Watkins, C., Mattheis, J., 2019. Apple, chapter 8. In: de Freitas, S.T., Pareek, S. (Eds.), Postharvest Physiological Disorders in Fruits and Vegetables. CRC Press, Boca Raton, FL, USA, pp. 165–206.

Wünsche, J., Ferguson, I., 2005. Crop load interactions in apple. Hort. Rev. 31, 231–290. https://doi.org/10.1002/9780470650882.ch5.

Zhang, L.Y., Peng, Y.B., Pelleschi-Travier, S., Fan, Y., Lu, Y.F., Lu, Y.M., Gao, X.P., Shen, Y., Delrot, S., Zhang, D.P., 2004. Evidence for apoplasmic phloem unloading in developing apple fruit. Plant Physiol. 135, 574–586. https://doi.org/10.1104/pp.103.036632.

6

Application of non-destructive sensors and ’big data’ analysis to predict physiological storage disorders and fruit firmness in Braeburn apples

P. Osinenko, K. Biegert, R. J. McCormick, T. Göhrt, G. Devadze, J. Streif, S. Streif

Computers and Electronics in Agriculture 183 (2021)

Computers and Electronics in Agriculture 183 (2021) 106015

Contents lists available at ScienceDirect

Computers and Electronics in Agriculture

journal homepage: www.elsevier.com/locate/compag

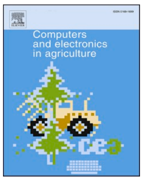

Original papers

Application of non-destructive sensors and big data analysis to predict physiological storage disorders and fruit firmness in 'Braeburn' apples

Pavel Osinenko [a,1,2], Konni Biegert [b,2], Roy J. McCormick [b], Thomas Göhrt [a], Grigory Devadze [a], Josef Streif [b], Stefan Streif [a,*]

[a] *Technische Universität Chemnitz, Automatic Control and System Dynamics Laboratory, Reichenhainer Str. 70, 09107 Chemnitz, Germany*
[b] *Kompetenzzentrum Obstbau Bodensee, Schuhmacherhof 6, 88213 Ravensburg, Germany*

ARTICLE INFO

Keywords:
Orchard management
Modeling
Classification
Fruit quality
Spectral indices
Recurrent neural networks

ABSTRACT

Physiological storage disorders affect a range of commercially important pomefruit and result in fruit losses and wastage of resources. Disorders can develop during and/or after storage and symptoms are strongly influenced by the growing environment and orchard management. Furthermore, fruit which receive similar orchard management and storage can vary greatly in disorder incidence and severity. Biological systems are complex and simple cause-and-effect approaches have not up until now resulted in robust methods to predict disorder risk. Reliable predictions are needed by fruit industries worldwide to better manage fruit production processes, to determine optimal harvest dates and long-term storage regimes. The current work proposes a new methodological approach to model 'Braeburn' apple disorder risk. Autoregressive time series (ARX) models via model identification techniques for chlorophyll, anthocyanins, soluble solids and dry matter content were obtained from weather conditions and different orchard management treatments and then served as input into a classifier for internal browning, cavities and fruit firmness after long-term controlled atmosphere storage. The classification results for internal browning disorder show a 90% agreement between two separate years and for fruit firmness an 80% success rate was obtained by training the classifier with two years of data.

1. Introduction

1.1. *Physiological storage disorders in apple production*

Pomefruit industries worldwide continue to suffer unexpected postharvest losses due to the development of physiological storage disorders (simply referred to as disorders in the text below) such as core browning, flesh browning, lens shaped cavities in the fruit flesh, bitter pit and superficial scald (Watkins and Mattheis, 2019). Disorder symptoms typically develop during and/or after storage. In controlled atmosphere (CA) stored 'Braeburn' apples, internal browning symptoms typically develop during and/or after storage and can intensify as storage duration increases (Hatoum et al., 2014; Elgar et al., 1999; Ford, 1979; Ferguson et al., 1999).

Prior studies have identified the orchard as the greatest source of variation in disorder incidence (Elgar et al., 1998; Rogers, 2014). Preharvest factors that are known to influence the development of disorders in apple include advanced fruit maturity at-harvest, light croploads, high fruit potassium-calcium mineral ratios and seasonal weather conditions. Incorrect cultivar-specific postharvest handling and storage regimes also contribute to the development of disorders (Elgar et al., 1998; Clark and Burmeister, 1999; Hatoum et al., 2016). Studies have attempted to link the risk of disorder development with multiple pre- and postharvest factors using logistic regression analysis (Verlinden et al., 2002; Lammertyn et al., 2000). Other studies using growing degree days have tried to find an influence of temperature or determine a threshold temperature summation for disorder risk (Rogers, 2014; Moggia et al., 2015; Lau, 1998). Given the general lack of discriminatory power with existing postharvest disorder prediction models, Konopacki and Tijskens (2005) explored a conceptual model of disorder development based on fundamental enzyme kinetics. This method seems feasible but requires the use of non-destructive big data with repeated measurements on the same fruit.

An understanding of the primary biological processes linked to

---

* Corresponding author.
E-mail address: stefan.streif@etit.tu-chemnitz.de (S. Streif).

[1] Currently at Skolkovo Institute of Science and Technology, Moscow, Russia.

[2] The first two authors contributed equally.

https://doi.org/10.1016/j.compag.2021.106015
Received 27 July 2020; Received in revised form 20 November 2020; Accepted 22 January 2021

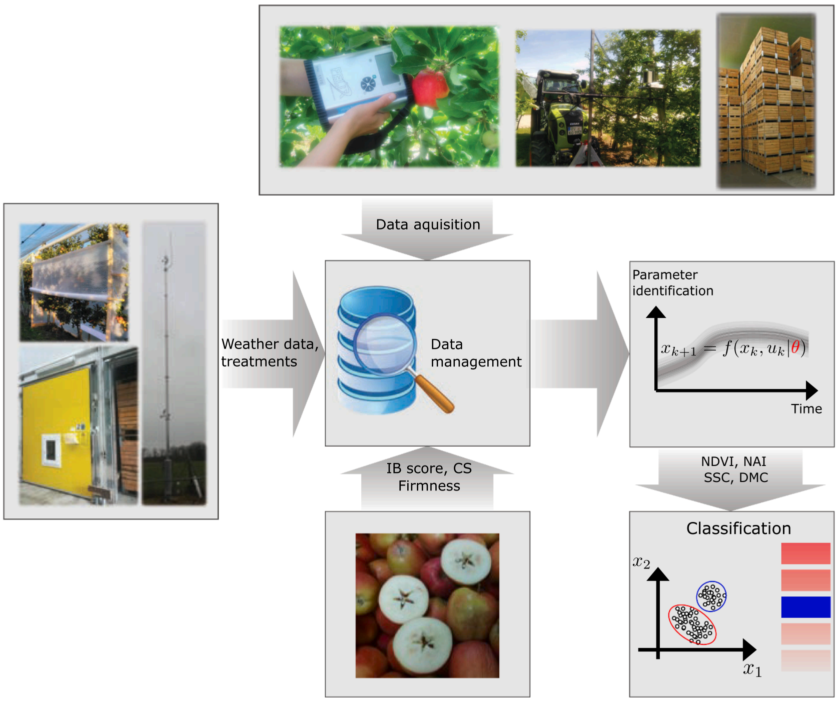

Fig. 1. Flowchart of the suggested methodology in the project (IB- Internal browning, CS- Cavities score, NDVI- Normalized difference vegetation index, NAI- Normalized anthocyanin index, SSC- Soluble solids content, DMC- Dry matter content).

disorder development is increasing rapidly. In particular, how ripening and senescence processes are connected with stress reactions when fruit are stored under low temperatures, low O_2 and/or high CO_2 (Watkins and Mattheis, 2019). At the biochemical level, markers have been identified in pears to predict the risk of disorder development under high CO_2 conditions (Deuchande et al., 2017). There is an improved understanding of the molecular networks associated with chilling injury (e.g. superficial scald) in apples (Honaas et al., 2019) and there is a better basic knowledge of how fruit respond to low O_2 conditions (Cukrov, 2018). A consortium of researchers has filed for a US patent for a diagnostic tool to predict the risk of storage disorders in apples and pears based on a large group of pomefruit genes identified as biomarkers in fruit samples taken at-harvest or in the period shortly after (Rudell et al., 2017). Such biomarker tools are currently unavailable for use in fruit industries and their efficacy under practical conditions has yet to be fully tested. Quantifying the interaction of all possible pre- and postharvest factors in disorder incidence and severity has up until now proven notoriously difficult for fruit researchers and industry managers to develop and apply a robust method of disorder prediction.

1.2. *Application of non-destructive sensors in apple production*

Non-destructive sensors used to obtain repeated measurements on the same fruit lot can contribute to a big data base containing potentially relevant information for use in fruit quality prediction models. Future data generation technologies will need to be fitted on-tractor and capture data during standard orchard maintenance operations to ensure fruit growers adopt any new technology. To establish a harvest schedule for an apple orchard or production area, time-consuming and labour-intensive destructive tests of fruit quality and maturity development are generally required. Suitable sensors could replace these destructive quality tests and the data evaluated with big data methods to allow for precision farming.

Vis (visible)/NIR (near infrared) spectroscopy in the Vis wavelength region can provide information on plant pigments in the apple skin such as chlorophyll, anthocyanins and carotenoids (Walsh et al., 2020). The shortwave NIR region spectra can be correlated with wet chemistry analyses and partial least square regression (PLSR) models to predict soluble solids content (SSC) and dry matter content (DMC) (Walsh et al., 2020). Changes in plant pigments, SSC and DMC can be correlated with fruit maturity, but these data alone are insufficient to determine a harvest window. Time-series data and system-theoretical methods as presented in this study might help overcome these limitations.

Other relevant factors that influence quality in fruit production include the light and fruit distribution within the tree canopy and need to be in an optimal balance for efficient photosynthesis rates and assimilate distribution to produce fruit with good internal quality characteristics and external appearance such as high blush color. With LiDAR (light detection and ranging) sensors a 2 or 3D point cloud of an apple tree can provide information on the leaf area (Sanz et al., 2013; Selbeck et al., 2013), tree height, stem position and canopy volume (Tsoulias et al., 2019).

Furthermore cropload is an important factor to determine fruit quality and fruit growth monitoring is an indirect measure since light croploads lead to a larger sized fruit. Inexpensive self-built dendrometers (Morandi et al., 2007) or hand measurements with digital calipers (see Fig. 1) were other approaches tested in the present study.

1.3. *Contribution and approach of this work*

In pomefruit, the biological processes that result in physiological storage disorders are complex and currently are not fully understood in sufficient detail to allow for reliable predictions and to avoid sizeable fruit losses that can occur in some growing seasons. In this study (see Fig. 1), the commercially important apple cultivar ‘Braeburn’ was monitored for three years and various data from non-destructive sensors along with weather data were collected and stored in a central data-management facility. Ultimately, only Vis/NIR sensing data together

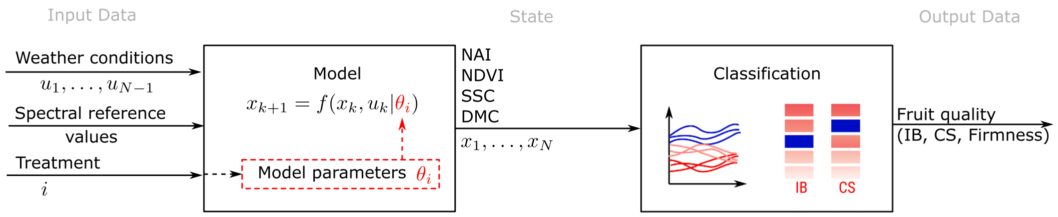

Fig. 2. Functional diagram of the approach (NAI- Normalized anthocyanin index, NDVI- Normalized difference vegetation index, SSC- Soluble solids content, DMC-Dry matter content, IB- Internal browning, CS- Cavities score).

Table 1
Naming convention to code the field treatments as unique fruit group (UFG).

Season	Orchard treatments						
	Temperature cell division	Temperature preharvest	Cropload	Harvest Date	Calcium	Tree sector	UFG*
2016/2017	C,A,W	A,W	L,S,H	E,O	W,O	B,M,T	264
2017/2018	C,A,W_1	A,W_1	L,S,H_1	NA	W,O_2	B,M,T	708
2018/2019	C,A,W	A,W_1	L,S,H	E,O,L	W,O	B,M,T	1812

Temperature cell division: cold (C), ambient (A), warm (W).
Temperature preharvest: ambient (A), warm (W).
Calcium: common practice with (W), without (O).
Cropload: heavy (H), standard (S), light (L).
Harvest date: early (E), optimum (O), late (L).
Tree sector: bottom (B), middle (M), top (T).
NA (Not available).

Subscript 1: two-factorial field design with treatments temperature and cropload for the same trees.
Subscript 2: treatments calcium with a light cropload.
* Number of unique fruit group (UFG) information (on sector per tree basis).

with weather and orchard/storage treatment information served as input into several dynamic parametric models. The use of relatively simple and fast devices was a key decision as the dynamic parametric models predict best when only a few parameters of apple development are used as input data. Apple parameters in the present study were: color pigments (chlorophyll, anthocyanins), SSC and DMC. Orchard treatments altered the air temperature during important physiological growth phases and also included calcium spraying, different croploads, harvest dates and storage conditions. Fruit quality information was obtained with standard destructive tests for fruit firmness, SSC and starch index to determine harvest dates. The combination of non-destructive sensor data along with the ARX modeling and classification is the major contribution of the current work.

2. Materials and methods

The methodical approach is summarized in Section 2.2. In this work ‘Braeburn’ is used as a model pomefruit cultivar for a big data analysis to predict disorder risk based on experimental orchard and storage data for the severity of internal browning, cavities score and fruit firmness after storage. Post storage predictions are used as a backward prediction to adapt the harvest window to the current seasonal conditions for fruit intended to be placed in long-term CA storage. The development of anthocyanin, chlorophyll, SSC and DMC is used in ARX models. In this process, weather time-series data and orchard treatment information were used as inputs. Repeated orchard Vis/NIR scanning and PLSR models only provided reference values for the ARX models. The idea is that a disseminator (like a consultant) can obtain Vis/NIR scans once or twice in the growing season to check for ARX model correctness. Then, the modelled factors were plugged into a classification algorithm to predict the disorders scores and also fruit firmness after storage and shelf-life (see Section 2.3). The overall setup is illustrated in Fig. 2.

2.1. *Experimental field setup*

The study was conducted from 2016 to 2019 at the Kompetenzzentrum Obstbau Bodensee in Southwest Germany (47.767137 N, 9.556544 E) with *Malus domestica* ‘Braeburn’ apple trees planted in 2006 as slender spindles on M9 rootstock with a row spacing of 3.20 x 0.80 m. The randomized one-factorial study design was used with seven trees per plot and three repetitions (see Table 1). Due to a severe frost event during bloom in 2017, field treatments were conducted on a limited number of trees in a two-factorial design. Average climatic conditions were 8.4 °C, 691 mm of rainfall and 1758 total sunshine hours.

To obtain more data on the influence of temperature within each season, different temperature treatments were applied in spring for three weeks immediately following flowering or preharvest. Here, plots of trees (covered by plastic thermofoil) were either heated or cooled in spring to maintain a 2 °C difference in air temperature compared with ambient (untreated control) trees or night temperatures maintained above 10 °C in the period immediately before harvest (McCormick et al., 2021). The night temperature of 10 °C was selected as it is often used as a threshold in biological growth models (Moggia et al., 2015). In the cropload treatments, trees were thinned to levels of 50%, 100% or 180% of a standard tree yield. In addition, trees were harvested either ‘early’, ‘optimum’ or ‘late’ within a harvest window based on the industry standard destructive harvest-index (Streif, 1996). After June drop, trees were sprayed weekly or not with calcium chloride (5 kg/ha).

Trees were separated into three equal sectors (1.25 m) to obtain data with regard to fruit position (height) inside the tree canopy. Measurements were organized in a unique fruit group (UFG) structure to allow for data modeling and classification. Here, apples from a specific tree-sector and storage condition represented one UFG and consisted of ~ 20 fruit. The UFG apples were subsequently, harvested, stored and assessed separately excluding 2016, here trees were harvested as total apples per sector within a repetition. UFGs within a specific treatment level received a standard level for all other treatments, e.g. trees with a cold temperature post flowering treatment received ambient preharvest temperatures, a standard cropload, an optimum harvest date and no calcium spray treatment.

Fruit were stored for five months under two storage conditions (McCormick et al., 2021), one storage condition was intended to induce disorders symptoms (direct CA and high CO_2) and one storage condition to avoid disorders (delayed CA and low CO_2). At storage removal fruit were kept for a 7 d shelf-life at room temperature and then each fruit was visually assessed by a small team of trained assessors for external disorders (i.e. bitter pit, CO_2 damage, scald) and by cutting for internal disorders (i.e. flesh browning, core browning, bitter pit). In the present study only disorder assessments for internal browning (IB) and cavities score (CS) were considered. Apples were ranked from 0 to 3 with 0.5 increments, where 0 = no symptoms and 3 = most severe. Mean disorder values were used in the classification.

From after June drop until harvest fruit growth measurements were taken with a set of digital Bluetooth calipers (Sylvac, Crissier, CH) and reflectance spectra (Vis/NIR) were collected using a portable hand-held spectrometer (F-750 Produce Quality Meter, Felix Instruments, Camas, USA). Measurements were done regularly (each week in 2016 and fortnightly in other years) from the same marked apples per season. The Vis/NIR data were subsequently used in autoregressive models with exogenous inputs, denoted by ARX (see Section 2.2). The Vis/NIR device used background light corrected scans in the range from 400 to 1100 nm with a spectral sampling of 3 nm. Spectra were used to calculate two pigment reflectance indices: a normalized difference vegetation index (NDVI) for chlorophyll and a normalized anthocyanin index (NAI).

$$\mathrm{NDVI} = \frac{(R750 - R705)}{(R750 + R705)}, \mathrm{NAI} = \frac{(R780 - R549)}{(R780 + R549)} \tag{1}$$

Using the methodology and software supplied with the spectrometer (F-750 Modelbuilder v1.3.0177) PLSR models for SSC and DMC were built each season using independent wet chemistry reference samples (~400) taken regularly during the scanning period from comparative trees within the same orchard block. Each year new PLSR models were built with an independent reference set (Biegert et al., 2021). Reference samples were scanned at approximately 10, 20 and 30 °C to help the models adjust for temperature effects. The models used 6 principle components with R^2 and RMSECV values of 83–92% and 0.49–0.61 for SSC and 67–90% and 0.51–1.09 for DMC, respectively.

Flesh firmness (N/cm^2) was measured at-harvest and at storage removal plus a 7 d shelf-life using a fruit texture analyzer (Güss, Strand, South Africa) fitted with a 11 mm probe.

2.2. *Model identification*

The apple fruit factors (NAI, NDVI, DMC and SSC) were modeled depending on the integral daytime and nighttime temperature, humidity, precipitation and a global radiation integral index obtained from a weather station (Thiess, Germany) located 300 m from the trees. The ARX modelling structure should a) offer a real-time approach to predict apple factors for the next day and b) only use several seasonal Vis/NIR spectrometer measurements to avoid a farmer from regularly having to scan the orchard. NAI, NDVI, DMC and SSC were available as mean values for each respective UFG. Both input (weather conditions) and output data (apple factors) were given as time series with a sampling time of one day. At the modeling stage, a total of 84 UFG for 2016 and 192 UFG for 2017 were considered. Due to difficult weather conditions in 2017 only 9 UFG were used. The models were then established per treatment pattern, i.e. a collection of UFGs that had the same treatment to achieve abstraction from a concrete tree and to consider only the average apple factors within a UFG depending on weather and treatment (see Table 1).

The modeling was done using ARX-structures of the following type:

$$\widehat{x}_{k+1} = \theta_A^\top v_{k,l,m} \tag{2}$$

where

$$v_{k,I,J}^\top = \begin{pmatrix} -x_k & -x_{k-1} & \cdots & -x_{k-l} & u_k^\top & \cdots & u_{k-m}^\top \end{pmatrix}^\top$$

Here, $x_k \in \mathbb{R}, u_k \in \mathbb{R}^4$ denote the vectors of apple factor and inputs at day k respectively, θ_A is the parameter vector, l, m denotes the order of the model respective to the apple factor and input. The estimation of θ_A was done by solving the following least squares problem:

$$\min_{\theta_A} \| \sum_{i=1}^{N-1} x_{i+1} - \theta_A^\top v_{i,l,m} \|^2,$$

where N is the number of available data of the corresponding output. The model (2) was used to predict the time series of the apple factor based on the initial value of the time series and the input data. The obtained models were analyzed for the normalized root mean square error (NRMSE) of the prediction as well as confidence intervals of its parameters. The NRMSE here serves as a measure for accuracy of the prediction and was calculated as follows:

$$\mathrm{RMSE} = \sqrt{\frac{\sum_{i=2}^{N} (\widehat{x}_i - x_i)^2}{N}},$$

$$\mathrm{NRMSE} = \frac{\mathrm{RMSE}}{x_{max} - x_{min}},$$

where x_{max} is the maximal value and x_{min} is the minimal value of the respective apple factors. The confidence intervals were calculated for each model parameter in each treatment pattern using the t-distribution with significance of 95%.

The resulting models were then used in the classification routine according to the principle depicted in Fig. 2. The respective methodology is described in the next section.

2.3. *Classification*

In general, it was assumed that the IB and CS depend on the apple factors. The apple factors in this study (NAI, NDVI, DMC and SSC) comprised multiple parameters and multivariate time series (MTS) that had to be addressed. This is a problem of finding a classification function f_c, to predict which MTS class a test sample would fall into, based on a training set, denoted by $\mathcal{M}$, of the initial MTS treatment pattern, whose class membership is known a priori (the so called supervised learning setting). The MTS classification problem is a notoriously difficult task requiring a certain level of pre-processing, feature extraction and segmentation techniques (Wang et al., 2016; Gorecki and Luczak, 2014; Kadous and Sammut, 2005; Baydogan and Runger, Mar 2015; Spiegel et al., 2011). Recently, deep learning techniques have yielded good results in overcoming these issues in regard to MTS classification. In this work, the approach selected for the MTS classifier was based on the methodology of Karim et al. (2018). In MTS via deep learning, the long short-term memory (LTSM) recurrent neural networks (RNN) are typically used. Basic RNNs are capable of obtaining the temporal factor during learning by investigating the direct connections between the layers. At the time t the update of some hidden vector h is read as:

$$\mathrm{h_t} = \tanh(Wh_{t-1} + Ix_t).$$

It is also useful to stack the RNNs in order to maintain the deeper learning by using the hidden vector as an input to the next RNN to obtain the following update rule:

$$\mathrm{h_t^l} = \tanh\left(Wh_{t-1}^l + Ih_t^{l-1}\right).$$

An LSTM RNN consists of a hidden vector h and a memory vector m. The hidden vector controls the state updates and the memory vector the outputs at each time step respectively.

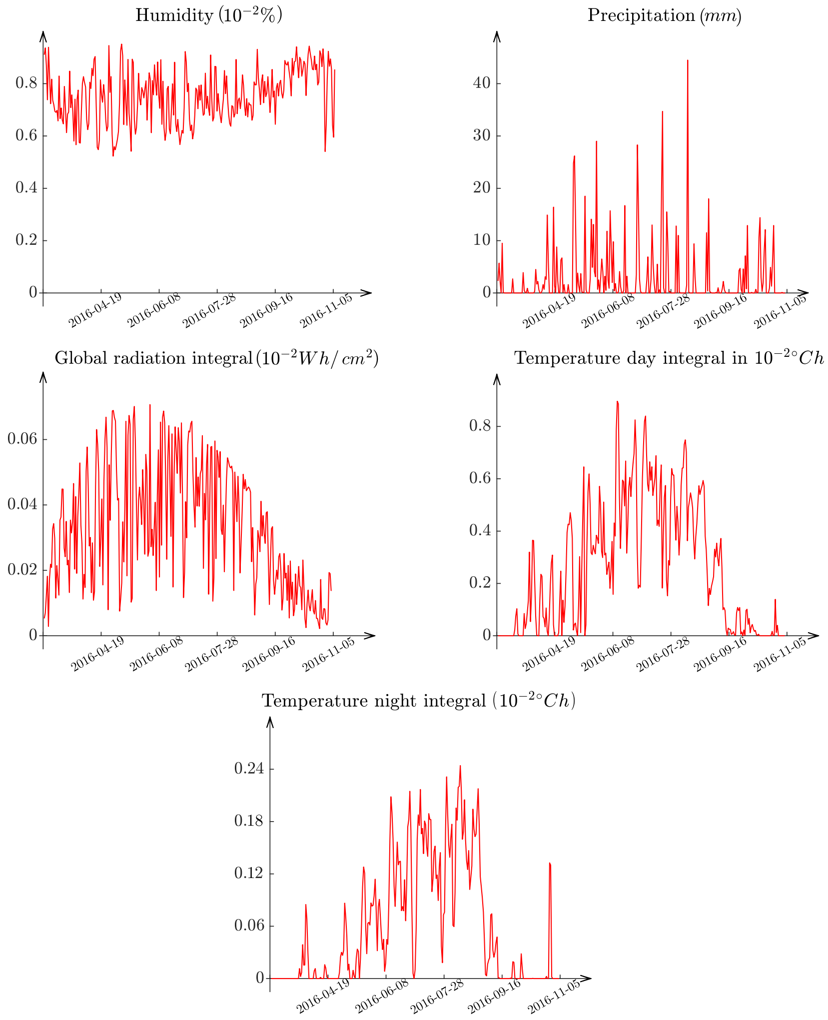

Fig. 3. Input data used in the current study.

$$
\begin{aligned}
g^u &= \mathrm{sgd}(W^u h_{t-1} + I^u x_t)\\
g^f &= \mathrm{sgd}\left(W^f h_{t-1} + I^f x_t\right)\\
g^o &= \mathrm{sgd}(W^o h_{t-1} + I^o x_t)\\
g^c &= \tanh(W^c h_{t-1} + I^c x_t)\\
m_t &= g^f \odot m_{t-1} + g^u \odot g^c\\
h_t &= \tanh(g^o \odot m_t)
\end{aligned}
$$

where sgd is the sigmoid function and $\odot$ is the element-wise matrix multiplication. The recurrent weight matrices are W^u, W^f, W^o, W^c. According to Bahdanau et al. (2014), LTSMs can learn temporal dependencies. In order to achieve the ability of learning the long-term temporal dependencies the so-called attention mechanism has been proposed in Bahdanau et al. (2014). The prediction y is made using the hidden state h and the weight matrix W:

$$y_t = \mathrm{softmax}(Wh_{t-1}).$$

where for any $x \in \mathbb{R}^n$ and $\mathrm{softmax}(x)_i := \frac{e^{x_i}}{\sum_{i=1}^{n} e^{x_i}}$ for $i = 1, \ldots, n$ is the normalized exponential function.

3. Results and discussion

3.1. Modeling apple factors

For better numerical performance, the input data for modeling were normalized to have approximately the same scale. The input data are depicted in Fig. 3.

The ARX-models for each apple parameter were computed. One particular example for a UFG from 2016 is depicted in Fig. 4.

Table 2 shows the mean NRMSE over all treatment patterns separated by years.

In each treatment pattern, the mean and standard deviation as well as the confidence intervals were calculated. In Fig. 5, particular examples of the model parameters with the respective confidence intervals are shown (the complete set of parameters and respective confidence intervals is available in the supplementary material). The middle red line shows the mean value, the boxes show the standard deviation and the whiskers correspond to the confidence intervals. If the confidence interval contains 0, the respective parameter may be seen as non-significant and thus may be dropped in the modeling in order to reduce the complexity of the ARX-models.

The constructed models were then used as input for classification as

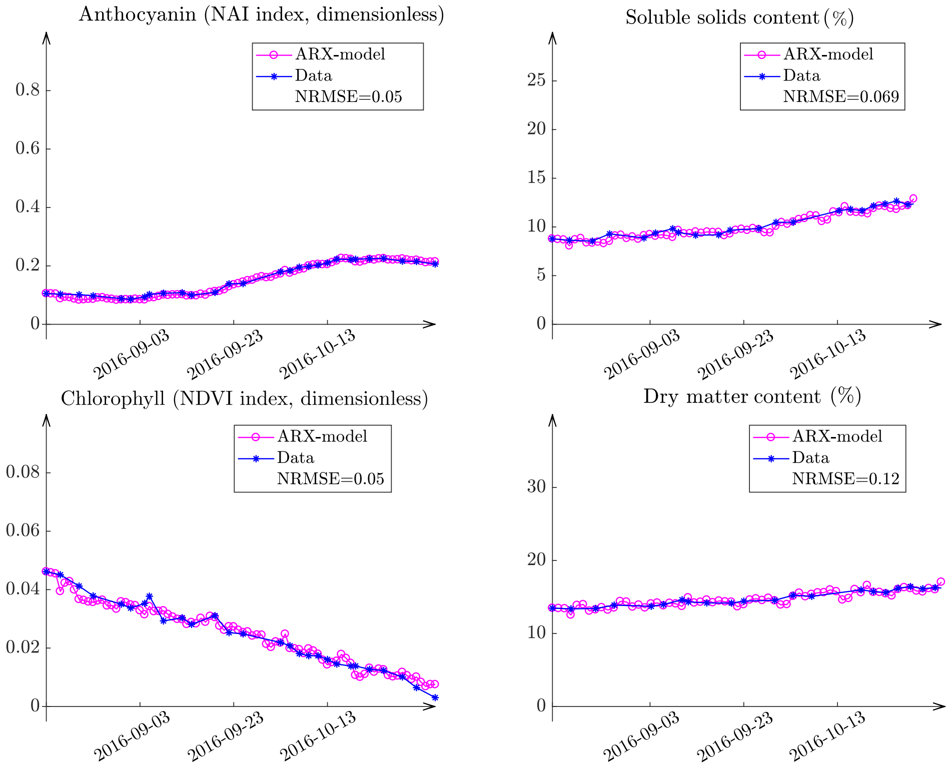

Fig. 4. Comparison of model against the data for one particular UFG (NDVI- Normalized difference vegetation index, NAI- Normalized anthocyanin index).

Table 2
NRMSE of the models of the apple factors (NAI- Normalized anthocyanin index, SSC- Soluble solids content, NDVI- Normalized difference vegetation index, DMC- Dry matter content).

Parameter	Mean 2016	Mean 2017
NAI	0.082	0.139
SSC	0.110	0.256
NDVI	0.100	0.100
DMC	0.202	0.399

functionally shown in Fig. 2. The respective results are presented in the next section.

3.2. *Apple disorder classification*

Based on the data set, the following MTS classification problem was defined:

- The development of NAI, NDVI, DMC and SSC were described by $4 \times T$ MTS
- For each MTS, a class membership was given by the following characteristic of the IB score and CS:
  - Internal browning score (binary classification):

$$Class\left(MTS_i\right) = \begin{cases} 0, & \text{if } \overline{IB} \leq 0.9 \\ 1, & \text{else} \end{cases}$$

  - Cavities score (binary classification):

$$Class\left(MTS_i\right) = \begin{cases} 0, & \text{if } \overline{CS} \leq 0.2 \\ 1, & \text{else} \end{cases}$$

  - Internal browning score (three class classification):

$$Class\left(MTS_i\right) = \begin{cases} 0, & \text{if } \overline{IB} \leq 0.4 \\ 1, & \text{if } 0.4 < \overline{IB} \leq 1 \\ 2, & \text{if } 1 < \overline{IB} \end{cases}$$

  - Cavities score (three class classification):

$$Class\left(MTS_i\right) = \begin{cases} 0, & \text{if } \overline{CS} \leq 0.2 \\ 1, & \text{if } 0.2 < \overline{CS} \leq 0.4 \\ 2, & \text{if } 0.4 < \overline{CS} \end{cases}$$

  - Firmness (two class classification):

$$Class\left(MTS_i\right) = \begin{cases} 0, & \text{if } \overline{FM} \leq 85 \\ 1, & \text{if } 85 < \overline{FM} \end{cases}$$

  - Firmness (three class classification):

$$Class\left(MTS_i\right) = \begin{cases} 0, & \text{if } \overline{FM} \leq 85 \\ 1, & \text{if } 85 < \overline{FM} \leq 95 \\ 2, & \text{if } 95 < \overline{FM} \end{cases}$$

The results of the algorithms are reported in Tables 3–5 for the IB index, CS index and firmness, respectively, for different sizes of randomly sampled training and test sets. Different sizes of the training sets were generated and the algorithms were applied 30 times. The first number shows the average classification error rate and the second

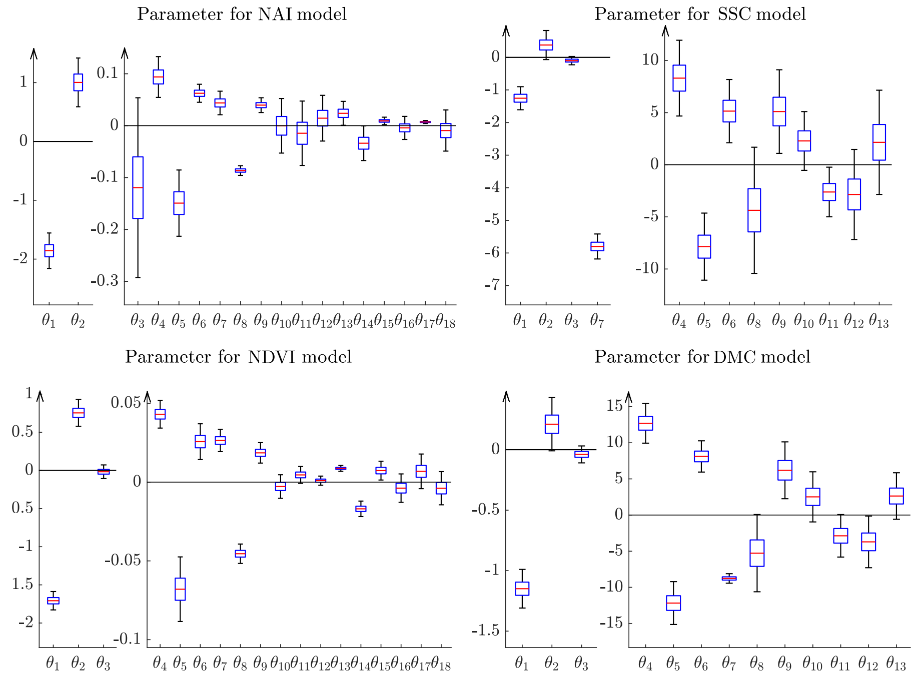

Fig. 5. Example of ARX-model parameters for one UFG (UFG- Unique fruit group, NAI- Normalized anthocyanin index, SSC- Soluble solids content, NDVI- Normalized difference vegetation index, DMC- Dry matter content).

Table 3
Classification results: Internal browning score.

Training set split ratio	$C = 2$	$C = 3$
50%	0.204 (0.038)	0.275 (0.051)
60%	0.186 (0.040)	0.244 (0.062)
70%	0.181 (0.037)	0.225 (0.073)
80%	0.161 (0.064)	0.211 (0.082)

Table 4
Classification results: Cavities score.

Training set split ratio	$C = 2$	$C = 3$
50%	0.290 (0.074)	0.241 (0.070)
60%	0.242 (0.043)	0.252 (0.073)
70%	0.223 (0.065)	0.243 (0.083)
80%	0.197 (0.090)	0.232 (0.080)

Table 5
Classification results: Firmness.

Training set split ratio	$C = 2$	$C = 3$
50%	0.280 (0.054)	0.285 (0.074)
60%	0.232 (0.043)	0.243 (0.075)
70%	0.224 (0.060)	0.230 (0.083)
80%	0.172 (0.080)	0.210 (0.081)

number (in parentheses) shows its standard deviation.

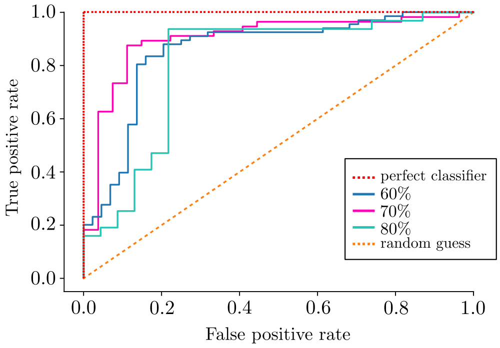

Fig. 6. ROC curve for the Internal Browning classifier.

These results show that, on average, the classifier is capable of "guessing" the IB score, CS and firmness in approximately 4 of 5 cases. In comparison, a simple random guess would on average yield a 50% success rate for a binary classification and 25% for a quaternary classification. In order to support this statement consider Fig. 6 which represents the receiver operator characteristic (ROC) curves of the binary browning score classifier, which is essentially the relationship between the false positive rate and the true positive rate. Here, "false positive" means the classifier predicts a good IB score, but is in fact bad (please keep in mind, here we are considering a binary classification). The orange and red lines represent the random choice and perfect classifier, respectively, whereas other lines represent the ROC curves for different split ratios. As one can see the lines are close to the perfect classifier. The 70% split model is the closest to the left top edge of the figure, which means that the model has the most predictive power and is robust against false positives. In this regard, the obtained results show a substantial advantage. In particular, the internal browning disorder show a 90% agreement between two separate years. However, the computed classifiers obviously have limitations and renewed training is required in future to achieve wider applicability and classification quality. The purpose of this study was to suggest and demonstrate a new methodology, based on big data analysis and classification, for IB, CS

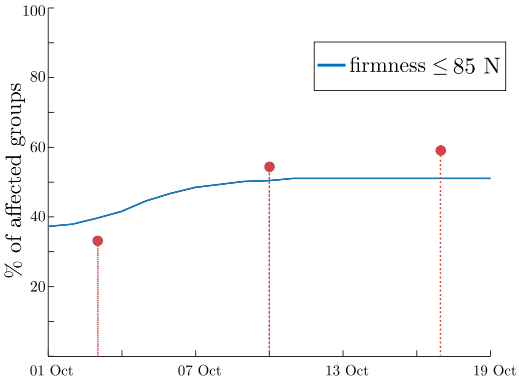

Fig. 7. Changes over the ‘Braeburn’ harvest window for the predicted number of UFGs (%) with an expected post storage fruit firmness of ⩽85 N (UFG-Unique fruit group).

and firmness prediction. It may be utilized in the apple orchard based on the algorithms developed and the non-destructive sensors described in Section 2.1.

The classifier was trained for the time series data for the seasons 2016/17 and 2017/18. The results for the ratio of the UFGs which show a post-storage fruit firmness value below 85 N are given in Fig. 7 where the blue line is the prediction and the red dots are the true values for the three different harvest dates.

One may see that the prediction captures the reality well and can be used for a backwards harvest date prediction. As time passes, the % of affected groups with an expected fruit firmness of ⩽85 N after storage is increasing from around 38% at 01 October to 50% around 08 October. The optimum timing to start the ‘Braeburn’ apple harvest (also dependant on other factors like suitable colour development) is predicted to be within this time window.

4. Conclusion

In the work presented, ‘Braeburn’ is used as model for a big data analysis to predict disorder risk based on experimental data for the severity of IB, CS and fruit firmness after storage. Post-storage predictions of disorder risk and expected fruit firmness can also be used to adapt the harvest window to the current seasonal conditions for fruit intended to be placed in long-term CA storage.

This work considered a new systematic approach to predict apple storage disorders using non-destructive sensors, parameter identification and classification algorithms. Preliminary results of modeling of various apple parameters are presented, in particular:

- Development of NAI, NDVI, DMC and SSC indices depending on weather conditions and orchard treatment;
- Prediction of fruit quality and firmness via the above factors using classification methods.

The suggested approach seeks to overcome limitations of the existing models for disorder prediction. The work suggests a possible basis for quality maximization in apple production after long-term CA storage. The results of modeling show a good fitting accuracy on average, whereas the classification algorithm demonstrated an 80% success rate on average to predict the IB, CS and fruit firmness. The ‘proof of concept’ given can be considered generic and applicable to a range of other disorders/situations depending on the availability of suitable input data.

CRediT authorship contribution statement

Pavel Osinenko: Methodology, Formal analysis, Writing - original draft. **Konni Biegert:** Investigation, Data curation, Validation, Writing - original draft. **Roy J. McCormick:** Project administration, Validation, Methodology, Writing - review & editing. **Thomas Göhrt:** Investigation, Formal analysis, Software, Writing - review & editing. **Grigory Devadze:** Investigation, Formal analysis, Software, Writing - review & editing. **Josef Streif:** Conceptualization, Methodology, Writing - review & editing. **Stefan Streif:** Conceptualization, Methodology, Funding acquisition, Writing - review & editing.

Declaration of Competing Interest

The authors declare that they have no known competing financial interests or personal relationships that could have appeared to influence the work reported in this paper.

Acknowledgments

This project was supported by the Federal Ministry of Food and Agriculture (BMEL) based on a decision of the Parliament of the Federal Republic of Germany via the Federal Office for Agriculture and Food (BLE) under the innovation support programme. We would like to thank the KOB orchard and lab staff for extensive help in conducting this study and the ‘BigApple’ project team.

Appendix A. Supplementary material

Supplementary data associated with this article can be found, in the online version, at https://doi.org/10.1016/j.compag.2021.106015.

References

Bahdanau, D., Cho, K., Bengio, Y., 2014. Neural machine translation by jointly learning to align and translate. arXiv preprint arXiv:1409.0473.
Baydogan, M.G., Runger, G., Mar 2015. Learning a symbolic representation for multivariate time series classification. Data Min. Knowl. Disc. 29 (2), 400–422.
Biegert, K., Stöckeler, D., McCormick, R.J., Braun, P., 2021. Modelling soluble solids content accumulation in ’Braeburn’ apples. Plants 10(2), 302. MDPI AG. Retrieved from https://doi.org/10.3390/plants10020302.
Clark, C., Burmeister, D., 1999. Magnetic resonance imaging of browning development in ‘Braeburn’ apple during controlled-atmosphere storage under high CO2. HortScience 34 (5), 915–919.
Cukrov, D., 2018. Progress toward understanding the molecular basis of fruit response to hypoxia. Plants 7 (4), 78.
Deuchande, T., Larrigaudière, C., Guterres, U., Carvalho, S.M., Vasconcelos, M.W., 2017. Biochemical markers to predict internal browning disorders in ‘Rocha’ pear during storage under high CO2. J. Sci. Food Agric. 97 (11), 3603–3612.
Elgar, H., Burmeister, D., Watkins, C., 1998. Storage and handling effects on a CO2-related internal browning disorder of ‘Braeburn’ apples. HortScience 33 (4), 719–722.
Elgar, H., Lallu, N., Watkins, C., 1999. Harvest date and crop load effects on a carbon dioxide–related storage injury of ‘Braeburn’ apple. HortScience 34 (2), 305–309.
Ferguson, I., Volz, R., Woolf, A., 1999. Preharvest factors affecting physiological disorders of fruit. Postharvest Biol. Technol. 15 (3), 255–262.
Ford, E.M., 1979. Effect of post-blossom environmental conditions on fruit composition and quality of apple. Commun. Soil Sci. Plant Anal. 10 (1–2), 337–348.
Gorecki, T., Luczak, M., 2014. Multivariate time series classification with parametric derivative dynamic time warping. Expert Syst. Appl. 42 (5), 2305–2312.
Hatoum, D., Buts, K., Hertog, M.L.A.T.M., Geeraerd, A.H., Schenk, A., Vercammen, J., Nicolaï, B.M., 2014. Effects of pre- and postharvest factors on browning in ‘Braeburn’. Horticult. Sci. 41, 19–26.
Hatoum, D., Hertog, M.L.A.T.M., Geeraerd, A.H., Nicolai, B.M., 2016. Effect of browning related pre- and postharvest factors on the ‘Braeburn’ apple metabolome during CA storage. Postharvest Biol. Technol. 111, 106–116.
Honaas, L.A., Hargarten, H.L., Ficklin, S.P., Hadish, J.A., Wafula, E., dePamphilis, C.W., Mattheis, J.P., Rudell, D.R., 2019. Co-expression networks provide insights into molecular mechanisms of postharvest temperature modulation of apple fruit to reduce superficial scald. Postharvest Biol. Technol. 149, 27–41.
Kadous, M.W., Sammut, C., 2005. Classification of multivariate time series and structured data using constructive induction. Mach. Learn. 58 (2), 179–216.
Karim, F., Majumdar, S., Darabi, H., Harford, S., 2018. Multivariate LSTM-FCNs for time series classification. Neural Netw. 116.
Konopacki, P., Tijskens, L., 2005. Benefits of fundamental modelling-the case of physiological disorders. Acta Horticult. 674, 157–163.
Lammertyn, J., Aerts, M., Verlinden, B.E., Schotsmans, W., Nicolaï, B.M., 2000. Logistic regression analysis of factors influencing core breakdown in ‘Conference’ pears. Postharvest Biol. Technol. 20 (1), 25–37.

Lau, O.L., 1998. Effect of growing season, harvest maturity, waxing, low O2 and elevated CO2 on flesh browning disorders in 'Braeburn' apples. Postharvest Biol. Technol. 14 (2), 131–141.

McCormick, R.J., Biegert, K., Streif, J., 2021. Occurrence of physiological browning disorders in stored 'Braeburn' apples as influenced by orchard and weather conditions. Preprints 2021. https://doi.org/10.20944/preprints202102.0584.v1.

Moggia, C., Pereira, M., Yuri, J.A., Torres, C.A., Hernández, O., Icaza, M.G., Lobos, G.A., 2015. Preharvest factors that affect the development of internal browning in apples cv. 'Cripp's Pink': Six-years compiled data. Postharvest Biol. Technol. 101, 49–57.

Morandi, B., Manfrini, L., Zibordi, M., Noferini, M., Fiori, G., Grappadelli, L.C., 2007. A low-cost device for accurate and continuous measurements of fruit diameter. HortScience 42 (6), 1380–1382.

Rogers, G., 2014. Managing the risk of flesh browning for 'Cripps Pink' apples using a climate model. Horticulture Australia Ltd.. https://www.horticulture.com.au/globalassets/laserfiche/assets/project-reports/ap08004/ap08004-final-report-complete.pdf.

Rudell, D., Leisso, R., Mattheis, J., Giovannoni, J., Gapper, N., Nicolai, B., Watkins, C., Johnston, J., Hertog, M., Schaffer, R., September 2017. Gene expression monitoring for risk assessment of apple and pear fruit storage stress and physiological disorders. URL http://www.freepatentsonline.com/y2017/0260586.html.

Sanz, R., Rosell, J.R., Llorens, J., Gil, E., Planas, S., 2013. Relationship between tree row LIDAR-volume and leaf area density for fruit orchards and vineyards obtained with a LIDAR 3D dynamic measurement system. Agric. For. Meteorol. 171–172, 153–162.

Selbeck, J., Pforte, F., Dworak, V., 2013. Vergleich zweier optischer Techniken zur automatischen Abschätzung der Blattfläche auf Baumebene. In: Clasen, M., Kersebaum, C.K., Meyer-Aurich, A., Theuvsen, B. (Eds.), Massendatenmanagement in der Agrar- und Ernährungswirtschaft - Erhebung - Verarbeitung - Nutzung. Gesellschaft für Informatik e.V, Bonn, pp. 319–322.

Spiegel, S., Gaebler, J., Lommatzsch, A., De Luca, E., Albayrak, S., 2011. Pattern recognition and classification for multivariate time series. In: Proceedings of the fifth international workshop on knowledge discovery from sensor data. ACM, pp. 34–42.

Streif, J., 1996. Optimum harvest date for different apple cultivars in the 'Bodensee' area. In: de Jager, A., Johnson, D., Hohn, E. (Eds.), COST 94. The postharvest treatment of fruit and vegetables: Determination and prediction of optimum harvest date of apples and pears. ECSC-EC-EAEC, Brussels, pp. 15–20.

Tsoulias, N., Paraforos, D.S., Fountas, S., Zude-Sasse, M., 2019. Estimating canopy parameters based on the stem position in apple trees using a 2D LiDAR. Agronomy 9 (11), 740.

Verlinden, B.E., de Jager, A., Lammertyn, J., Schotsmans, W., Nicolai, B.M., 2002. Effect of harvest and delaying controlled atmosphere storage conditions on core breakdown incidence in 'Conference' pears. Biosyst. Eng. 83, 339–348.

Walsh, K.B., Blasco, J., Zude-Sasse, M., Sun, X., 2020. Visible-NIR 'point' spectroscopy in postharvest fruit and vegetable assessment: The science behind three decades of commercial use. Postharvest Biol. Technol. 168, 111246.

Wang, L., Wang, Z., Liu, S., 2016. An effective multivariate time series classification approach using echo state network and adaptive differential evolution algorithm. Expert Syst. Appl. 43, 237–249.

Watkins, C.B., Mattheis, J.P., 2019. Postharvest physiological disorders in fruits and vegetables. Innovations in postharvest technology series, vol. 1. CRC Press. pp. 165–206 (ch. Section II Temperate Fruits 8: Apple) doi:10.1201/b22001.

7 General Discussion

Discussion

Physiological disorders during the three study years

The three study years from 2016 - 2019 resulted in distinctively different expressions of disorders in each year. The first season showed a high incidence of core browning. The second season took place after a severe frost event resulting in a light crop load which produced high numbers of cavities and browning disorders in the direct CA storage regime. Optimal storage conditions for the cultivar 'Braeburn' are delayed CA conditions for up to three weeks with solely cooling the fruit. However, the present study split fruit from the same tree sector into direct and delayed CA storage conditions since growers occasionally have to mix different cultivars together in one CA storage room. In the third year, superficial scald and bitter pit were the dominant disorders observed after CA storage and shelf-life of the apples.

Varying orchard management factors affected the incidence and severity of disorders to a great extent. Light crop loads consistently produced higher disorders as was also found by Elgar et al. (1999) while disorders from different calcium and harvest date treatments showed yearly differences in their expression as was also found by Rabus and Streif (2000), Hatoum et al. (2014) and Buts et al. (2015).

This work achieved 15 different air temperature conditions through building plastic greenhouse tents over trees in the orchard. However, establishing different temperature regimes in an orchard situation is technically challenging. This was especially true for the orchard cooling treatments. A re-construction of the tents with additional roof top windows after the first study year was needed in order to provide more ventilation during the warm sunny periods of the day. The tents required manual opening and closing of the windows during the day as cloud conditions changed to prevent excessive temperature overshoot. Energy consumption of heaters and cooling machines could at times exceed the available power supply and the defrosting cycle of cooling machines reduced the effective cooling capacity of the tent treatments. Lau (1998) in British Columbia showed that apples grown in three cool growing seasons (<1300 degree-days >10°C) had a higher susceptibility for disorders. We could show that warm night temperatures (>10 °C) prior to harvest resulted in a lower incidence of disorders. In contrast, negligible effects could be detected of Δ+/- 2 °C to ambient conditions during the physiological important post-bloom period until T-stage phase (chapter 5). Therefore our hypothesis was rejected that post-bloom temperatures of Δ+/-2 °C have an effect on the occurrence of disorders in 'Braeburn' apples under Lake Constance growing conditions. However, the programmed temperature change of Δ+/- 2 °C might not have been sufficient to produce physiological effects. Another factor was that Δ+/- 2 °C was not maintained during sunny days due to reduced cooling supply. However, the Δ+/- 2 °C was kept at night, but night temperatures might have been compensated in the physiological tree status by the lack of cooler temperatures (i.e. difference to ambient temperature conditions) during the day. Further experiments in this context should try to induces stronger temperature differences during the day. In general, the above mentioned limitations out-weighted the advantages of conducting research on mature apple trees planted in orchard soil to gain 'big data' within a triennial research. 'Big data' analyses need large data sets to achieve enough training data. As shown above disorders are highly dependent on weather conditions and many years of data acquisition in different growing conditions are therefore required for a reasonable prediction result for different types of disorders.

Fruit Vis/NIR sensor information

The present work monitored the growth of marked apples on the trees with repeated spectral scans from after June drop until harvest. Scans were taken only in the centre of an easy to reach apple, which was the side of the apple exposed to the sun. A single scan position was used to avoid turning the apple and risk detaching it from the tree. While fruit quality parameters vary around a fruit, a study conducted on pears found comparable SSC values at multiple spectral scan positions on the same fruit when compared to one scan position and with a difference of Δ0.7 % SSC obtained between non-destructive and destructive measurements (Cruz et al., 2021).

During the study period, disorder incidence and/or severity varied greatly. In the orchard, different fruit growth rates were measured each year as affected by the prevailing seasonal weather conditions and orchard experimental treatments (i.e post-bloom temperatures, crop load, harvest date). For the three study years, in total a combination of 41 experimental treatments, three orchard replications and three tree sectors were monitored for the fruit spectral properties and diameter growth. Differences in management practices were related to different Vis/NIR spectral time-series data. In each study year, heavy crop load treatments maintained the highest NDVI values at harvest compared to trees with a standard or light crop load. Additionally, fruit positioned at the bottom tree sector consistently showed slightly higher NDVI values. Furthermore, in every year, NDVI values after June started from a different point and showed a near linear decrease until harvest. In contrast, NAI values decreased till mid of August, followed by a strong increase until harvest. For NAI, the lowest values were always in the bottom tree sector (Schuler, 2022). In storage, spectral absorption indices from the Vis spectrum and fruit diameter showed no distinct development (chapter 2).

Information about fruit water content can be found in the shortwave NIR region. Additional water absorption bands are situated further in the NIR region (Rubo and Zinkernagel, 2022) but these longer wavelength bands could not to be measured with the spectrometer used in this study. The spectrometer can only give fruit skin and tissue information from approximately 1-2 cm beneath the skin due to light intensity and cultivar-specific tissue structure of the hand-held spectrometer (Lohner, 2020, personal communication). In chapter 3 we presented time-series Vis/NIR data of fruit covered with plastic sheet rain covers or hail nets (standard production practice). Measurements directly after a rain event on a dry fruit skin resulted in no differences for the spectral indices obtained from the Vis range. Although no differences were measured after a rain event, fruit grown under rain covers showed reduced absorption values at 975 nm throughout the study. Calcium transport into the fruit after calcium chloride spraying is possible through lenticels and cracks in the cuticle (Harker and Ferguson, 1988) and the water content of fruit might therefore be affected from the rain covers preventing direct wetting of the fruit from precipitation.

The diffuse reflection from apples in the shortwave NIR spectral region is affected in particular by the oxygen and hydrogen bonds found in water and carbohydrate molecules. PLSR models use this spectral information to non-destructively predict DMC and SSC values in the orchard. However, these models have to be trained with orchard and seasonally specific destructive laboratory measurements which have to be additionally scanned at different temperature regimes in order to compensate the temperature effect in the NIR region. Chapter 4 showed that SSC can be reliably detected with non-destructive multi-year PLSR models for a specific orchard as was also shown by Peirs et al. (2003), if the SSC values in the laboratory and orchard were in a standard distributional range. Also, different seasons produced different SSC values as was also observed by Sugiura et al. (2013). Differences in the SSC accumulation from the different post-bloom temperature treatments were negligible.

Precision farming to obtain small-scale orchard data

We could show that the tree sector had a significant effect on the development of SSC (chapter 4). Furthermore, tree sectors (chapter 2) and single trees developed differences in disorder incidence and/or severity even within the same treatment repetition. Given this amount of variation in disorder expression coming from the orchard, future decision support systems should focus on developing a precise tree sector map of obtained field data and link these field data to post-storage fruit quality grading results. The present study only achieved this with manual data acquisition and manual data labeling linked to specific tree sectors. Up until the time of writing this text, the connection of pre- and post-harvest data on a tree sector basis is an unresolved research issue with no practical solution to effectively link fruit quality storage outcomes with the orchard trees. Praat et al. (2003) reported similar results for kiwifruit. In the future, it is questionable whether tree sector information can be mapped due to technical restrictions, the main one being that apples are currently commercially picked into large bins containing 300 kgs of fruit mixed from a number of trees. But, we could show that there are fruit quality differences between fruit from different tree sectors with tree heights of 3,80 m (planting distance 0.80 x 3.20 m). A transitional solution for a precision farming would be an online decision support system where data is neither saved nor connected to other sources and are processed online on the tractor and decisions are applied immediately. With this, a precise GPS location is needlessly and an online tool with immediate calculations of these data can be used to control one dimensional tasks such as pesticide spray adjustments. However, this solution would only be sufficient for less complex tasks where the connection to post-harvest grading results is not needed and therefore is not an adequate solution for this work.

Smart farming with systems control and regulation

The 'big data' analyses with two-year's of data resulted in an acceptable prediction value of 90 % correct predictions of disorders through a 'black box' modelling and classification approach. As the name indicates, 'black box' classification provides a researcher with no causal information about the relationship between the data in-feed and output. Depending on data sources (biased or not), the amount of data in a 'black box' classification and prediction approach is fully dependent on the type of data used. However, chapter 6 provided a 'proof of concept' and claimed that this approach might be reasonable. The model and classifier contained treatment information (e.g. light, standard and heavy crop load levels) as input factors. As explained above, these data sets were obtained using as wide a range of management methods that possibly affected changes in fruit growth and development, e.g. fruit sizing. As shown in chapters 2 and 4 crop load treatments especially had a consistent and marked effect on the development of disorders over all study years. Also, the post-bloom temperature treatments affected fruit sizing from the T stage up until harvest. Spectral data showed a large variance for individual scans taken during fruit growth. These spectral data trends were consistent over all study years for sectors and treatments, i.e. crop load. In general, variability of fruit quality parameters is high (Peirs et al., 2003). Future work should focus on the development of non-destructive leaf-fruit ratio or crop load information linked to the tree volume in order to use this in future modelling approaches which is missing up to date.

Modelling of fruit properties

The present study combined different modelling approaches to investigate the explanatory power of longitudinal sensor data and derive prediction models. Orchard data was modelled with Monte Carlo simulations, ROC plots, ARX models and 'black box' modelling. As a 'proof of concept' these approaches were sufficient as was shown in chapters 4-6. Here it was possible to form stronger links between pre-harvest factors and the post-harvest fruit quality as has not been done up to date in other 'big data' analyses for apple disorders. Given the availability of large data sets, there are other possible approaches to investigate fruit quality for example artificial training data produced from Monte Carlo simulations (produced without field labour, only modelled). Monte Carlo simulations for SSC supported PLSR modelling as a reliable non-destructive output measure (chapter 4). Also, the modelling approach to predict post-harvest fruit firmness resulted in a good agreement with the destructive measurements. However, any disorder or fruit firmness model classifier needs to be robust in terms of usage with new data from different sources, orchards and seasonal conditions. This is especially challenging during this time as climate warming is resulting in growing conditions that are unfamiliar and different to our previous growing experience. However, technical advances like AI for real-time fruit detection and orchard fruit load estimation are under current development (Koirala et al., 2019). Also work to model tree fruit bearing capacity for precision fruit thinning is proceeding quickly (Penzel, 2022). Models are clearly trying to reflect the real world but are built based only on the available data. The challenge for smart horticulture in the future is the development of robust models which reflect the real world best.

Implications on practical research

The broad practical expectation underlying the present work was to generate an application to track fruit quality within the apple supply chain. Within the scope of the project work a wireless smartphone application software (App) was developed to connect with digital calipers. The App enabled fruit diameter measurements to be easily linked to treatment codes and GPS location in order to map the growth of a tagged fruit in the orchard. Immediate access to the data within the App meant the user could check and correct any errors. However, in the end these growth data were not able to be used in the 'big data' classifier due to unresolved communication issues with the data-bank server.

Another study outcome was that rain events had no effect on the Vis wavelength spectra and orchard scanning could be repeated on a regular basis. Zude-Sasse et al. (2002) reported that fruit temperature had no effect on the spectral reflection in the 600-750 nm range. Furthermore, non-destructive SSC data modelling resulted in a reasonable goodness of fit and robustness (R^2 of $\sim$75% and RMSE of $\sim$0.6%) with a handheld orchard spectrometer. Although we could show that yearly models performed best, multi-year models also achieved reasonable and comparable predictions.

Research experience with non-destructive spectral and laboratory reference measurements to determine fruit quality parameters is developing rapidly. Progress with spectral modelling and the use of extremely large data sets collected from orchards is helping and will help in the near future to extend the application of these methods in fruit growing industries (Mishra and Woltering, 2021; Anderson et al., 2021b). Modern apple packing houses are now equipped with Vis/NIR non-destructive grading machines. These machines generate 'big data' as every apple is scanned which potentially generates 'big data'. However, in this study considerable efforts were made to access commercial fruit grader data sets for our research fruit and link this spectral grader data with the spectral time-series scans and other data obtained in the orchard. Unfortunately, technical difficulties did not allow to obtain individual fruit spectra from these commercial machines. The individual apple spectra were mostly not saved. Up to date, the connection between pre- and post-harvest fruit data on a commercial scale is hampered by limited data storage, the associated costs of this and missing interfaces to exchange data between different sources. However, with increasing availability of 'big data' in apple growing, fruit quality models that are robust for differences in orchard location and growing seasons can be developed for use within the fruit quality chain. These developments will be assisted by decreasing costs for real-time data storage, processing and transmission of fruit quality data from all points within the apple production chain.

A research approach based on the use of 'big data' is not as dependent on a classical experimental layout to achieve reliable predictions assuming one has access to sufficient 'big data'. Anderson et al. (2021a) recently demonstrated this principle using a large data set of orchard scans and a neural network classifier working to predict DMC of mango. In our work, albeit with much smaller data sets, we demonstrated the same trend with the prediction of SSC in apple (chapter 4). Although the amount of data collected were insufficient to build robust prediction models across different seasons, locations and cultivars, the use of spectral time-series scanning was an important step towards achieving 'big data' in apple fruit quality research. We demonstrated a 'proof of concept' for 'big data' modelling in order to predict physiological disorders after harvest and fruit firmness at harvest.

Investigations with other optical sensors such as LiDAR and hyperspectral imaging didn't lead to usable research data or practical outcomes. Analysis of the LiDAR data proved to be too technically demanding for the project consortium and the hyperspectral camera lacked sufficient resolution and was unsuitable for use outdoors under strong daylight conditions. However, in future research both these technologies will very likely be increasingly used to monitor orchard tree and fruit growth. In a recent study, a LiDAR sensor was able to distinguish between leaves and tree branches and measure fruit diameter growth (Tsoulias et al., 2020). Especially for plant protection sprays, LiDAR sensors can potentially reduce pesticide usage by 25-45 % with improved application targeting in orchards with variable tree canopies (Solanelles et al., 2006). However, Verbiest et al. (2020) showed that in horticulture there are almost no existing fully automated control and regulation production processes which are economical viable despite a considerable research effort.

Outlook

Presumably, the wide range of 'Braeburn' fruit grown in the research trial plots, all with measurable differences in growth rates, spectral time-series and final fruit size, had differences in internal tissue structure (i.e cell size and number and differences in intercellular porosity). Future experimental work in the orchard on carbohydrate modelling can be supported by non-destructive DMC and SSC data to better understand tree and fruit physiological processes as fruit with a higher energy status can maintain itself better when placed under storage stress (Saquet et al., 2003). Wünsche and Lakso (2000) clearly formulated that there are only "two possible means to improve crop performance: increase total dry matter yield and/or increase the magnitude of partitioning of dry matter toward the fruits". Light spectra contain multiple information dimensions. When separated, the scattering and absorption coefficients in light spectra contain information about the fruit chemical composition and tissue structure (Stefan A. Lohner and Konni Biegert and Steffen Nothelfer and Ansgar Hohmann and Roy McCormick and Alwin Kienle, 2021; Lohner et al., 2021, 2022; Wang et al., 2020). Zerbini (2006) considered the effective scattering coefficient as fundamental property of fruit tissue as compared to standard diffuse reflectance spectra. The scattering coefficient can be directly related to tissue structure and fruit firmness and also used to detect internal browning for example in pears (Zerbini, 2006). In the current work efforts were initiated to measure the effective scattering and absorption coefficients on apples still attached to the tree in the orchard. While our cooperative work with the ILM in Ulm made very considerable progress in this direction (Stefan A. Lohner and Konni Biegert and Steffen Nothelfer and Ansgar Hohmann and Roy McCormick and Alwin Kienle, 2021; Lohner et al., 2021, 2022) the technical challenges for field scanning were too high and these techniques remain laboratory based. Without further technical advances for optical monitoring of fruit growth to obtain non-destructive estimates of fruit porosity or fruit firmness (chapter 6) one other possible research direction is enhanced carbohydrate modelling. Using non-destructive DMC and SSC data together with different field treatments (e.g. temperature sums, crop load, harvest date, calcium sprays) and scanning from different positions within the tree canopy there is potential to gain further insights into carbohydrate partitioning and fruit development.

The adoption of sensor technologies in fruit growing is dependent on many factors. An outlook for future productions systems will probably require the tree architecture to be simplified, i.e. to change from 3D to 2D tree canopy systems where fruit, leaves and branches are less overlapping. To achieve an economical advantage, orchard driveways will need to be narrower than the current 3.0-3.5m driveway. Jackson and Palmer (1972) cited in Tustin et al. (2022) showed that the interception of light is dependent on the cropping latitude of the world and commercial apple orchards with a row width of 50 cm were recently established in New Zealand (Tustin et al., 2022). The second step towards an economical feasible adoption process is the combination of sensing tasks. For example, a LiDAR sensor fitted on an orchard sprayer to improve pesticide applications can potentially calculate a fruit:leaf ratio per tree. However, to digitally record the 3D structure of a standard spindle apple tree requires that two different row scans are merged. In addition, LiDAR data need to be processed in real-time in the orchard for subsequent machinery tasks which will need further technical development to be feasible. In addition, it is assumed that problems associated with wireless data transmission in orchards with poor GPS signal reception or other mobile signals can be resolved in the near future with additional GPS base stations per farm. In the end, the orchard should be robot-ready to accomplish manual intensive tasks, but tree physiology and therefore yield and economical behavior must be targeted as well.

Conclusion

An experienced fruit grower having observed multiple seasons is capable of adjusting orchard management strategies according to fruit growth, historical data and can automatically adapt his ’eyes’ to differing environmental light conditions. On the other hand, humans are also error prone and subjective judgements can lead to poor crop estimates, e.g. assessment of thinning efficacy when fruitlets are small. Also, increasing official regulations and farm sizes are forcing growers to use electronic field data management tools or decision support systems to deal with the data inflow. Other not to be underestimated factors are the high manual labor input in fruit growing with increasing wage costs and the decreasing availability of skilled or trained workers. These trends are driving fruit growers into further mechanization. The present study focused on the prediction of disorders with optical sensors. Up until now, the causal factors and multi-factorial interaction of these factors, especially the influence of changing weather conditions that leads to the formation of disorders, are not fully understood. The present study showed that optical Vis/NIR sensor information from the orchard can be linked to different management and environmental factors. Furthermore DMC, SSC, and spectral indices for chlorophyll, anthocyanins and carotenoids showed differences within a tree sector. A precise decision support system is required in order to treat tree sectors according to their physiological status in the pre- and post-harvest period. However, within the current study data labelling on a tree sector level was undertaken manually. The link between pre-harvest fruit growing factors of crop load, picking date and calcium sprays to post-harvest disorders led within a ’big data’ analyses to reasonable prediction rates. However, in tree physiology there are no clear simple correlations at hand to improve fruit quality by enhancing or decreasing only one factor. In contrast, annual field crops like corn can be fertilized with nitrogen based on non-destructively obtained chlorophyll values. This leads to increased yields, but in apple production inappropriate fertilization will increase shoot growth and leaf area which negatively affects fruit quality. Therefore smart farming should consist of different sensor data which can detect the tree and fruit physiology. Further research is necessary to use non-destructive sensor data in the orchard in order to collect physiological important information (e.g. fruit-leave ratio). Future orchards to implement sensor technologies within an automated platform should have a 2D orchard tree structure where leaves and fruit can be distinguished easily. Associated therewith is a better understanding of interception of light and carbohydrate distribution within the tree. Further research with large data sets is required to achieve robust 'big data' models for smart horticulture systems in the future.

Bibliography

Aggelopoulou, K., Pateras, D., Fountas, S., Gemtos, T., and Nanos, G. (2010). Soil spatial variability and site-specific fertilization maps in an apple orchard. *Precision Agriculture*, 12(1):118–129.

Aggelopoulou, K. D., Wulfsohn, D., Fountas, S., Gemtos, T. A., Nanos, G. D., and Blackmore, S. (2009). Spatial variation in yield and quality in a small apple orchard. *Precision Agriculture*, 11(5):538–556.

Ahrens, S. (2022). Pro-Kopf-Konsum von Obst in Deutschland nach Art bis 2020/21. Technical report, de.statista.

Anderson, N., Walsh, K., Flynn, J., and Walsh, J. (2021a). Achieving robustness across season, location and cultivar for a NIRS model for intact mango fruit dry matter content. II. local PLS and nonlinear models. *Postharvest Biology and Technology*, 171:111358.

Anderson, N., Walsh, K., and Wulfsohn, D. (2021b). Technologies for forecasting tree fruit load and harvest timing—from ground, sky and time. *Agronomy*, 11(7):1409.

Bangerth, F. and Streif, J. (1972). Factors affecting the aroma quality of apple fruits. *Acta Horticulturae*, 97(466):29–30.

Buts, K., Hertog, M. L. A. T. M., Nicolaï, B. M., and Carpentier, S. (2015). In Search of Biomarkers for Browning in Apple: a Proteomics Approach. *Acta Horticulturae*, (1079):107–113.

Chi, M., Plaza, A., Benediktsson, J., Sun, Z., Shen, J., and Zhu, Y. (2016). Big data for remote sensing: Challenges and opportunities. *Proceedings of the IEEE*, 104(11):2207–2219.

Cruz, S., Guerra, R., Brazio, A., Cavaco, A., Antunes, D., and Passos, D. (2021). Nondestructive simultaneous prediction of internal browning disorder and quality attributes in ‘Rocha’ pear (Pyrus communis l.) using VIS-NIR spectroscopy. *Postharvest Biology and Technology*, 179:111562.

Elgar, H. J., Lallu, N., and Watkins, C. B. (1999). Harvest date and crop load effects on a carbon dioxide–related storage injury of `Braeburn' apple. *HortScience*, 34(2):305–309.

Faostat (2022). Faostat database. Online.

Ferguson, I., Volz, R., and Woolf, A. (1999). Preharvest factors affecting physiological disorders of fruit. *Postharvest Biology and Technology*, 15(3):255–262.

Franck, C., Lammertyn, J., Ho, Q. T., Verboven, P., Verlinden, B., and Nicolaï, B. M. (2007). Browning disorders in pear fruit. *Postharvest Biology and Technology*, 43(1):1–13.

Garming, H., Dirksmeyer, W., and Bork, L. (2018). Entwicklungen des Obstbaus in Deutschland von 2005 bis 2017: Obstarten, Anbauregionen, Betriebsstrukturen und Handel. techreport 100, Johann Heinrich von Thünen Institut.

Guyomard, H. and Bureau, J.-C. (2020). Research for AGRI Committee - The Green Deal and the CAP: policy implications to adapt farming practices and to preserve the EU's natural resources. *Policy Department for Structural and Cohesion Policies.*

Harker, F. and Ferguson, I. (1988). Transport of calcium across cuticles isolated from apple fruit. *Scientia Horticulturae*, 36(3-4):205–217.

Hatoum, D., Buts, K., Hertog, M. L. A. T. M., Geeraerd, A. H., Schenk, A., Vercammen, J., and Nicolaï, B. M. (2014). Effects of pre- and postharvest factors on browning in Braeburn. *Horticultural Science*, 41:19–26.

Hatoum, D., Hertog, M. L. A. T. M., Geeraerd, A. H., and Nicolai, B. M. (2016). Effect of browning related pre- and postharvest factors on the 'Braeburn' apple metabolome during CA storage. *Postharvest Biology and Technology*, 111:106–116.

Kamilaris, A., Kartakoullis, A., and Prenafeta-Boldú, F. (2017). A review on the practice of big data analysis in agriculture. *Computers and Electronics in Agriculture*, 143:23–37.

Koirala, A., Walsh, K., Wang, Z., and Mccarthy, C. (2019). Deep learning for real-time fruit detection and orchard fruit load estimation: benchmarking of 'MangoYOLO'. *Precision Agriculture*, 20(6):1107–1135.

Lau, O. L. (1998). Effect of growing season, harvest maturity, waxing, low O2 and elevated CO2 on flesh browning disorders in \`Braeburn' apples. *Postharvest Biology and Technology*, 14(2):131–141.

Lohner, S. A., Biegert, K., Hohmann, A., McCormick, R., and Kienle, A. (2022). Chlorophyll- and anthocyanin-rich cell organelles affect light scattering in apple skin. *Photochemical & Photobiological Sciences*, 21(2):261–273.

Lohner, S. A., Biegert, K., Nothelfer, S., Hohmann, A., McCormick, R., and Kienle, A. (2021). Determining the optical properties of apple tissue and their dependence on physiological and morphological characteristics during maturation. Part 1: Spatial frequency domain imaging. *Postharvest Biology and Technology*, 181:111647.

Manfrini, L., Grappadelli, L. C., Morandi, B., Losciale, P., and Taylor, J. A. (2020). Innovative approaches to orchard management: assessing the variability in yield and maturity in a ‘Gala’ apple orchard using a simple management unit modeling approach. *European Journal of Horticultural Science*, 85(4):211–218.

Mishra, P. and Woltering, E. (2021). Handling batch-to-batch variability in portable spectroscopy of fresh fruit with minimal parameter adjustment. *Analytica Chimica Acta*, 1177:338771.

Peirs, A., Tirry, J., Verlinden, B., Darius, P., and Nicolaı, B. M. (2003). Effect of biological variability on the robustness of NIR models for soluble solids content of apples. *Postharvest Biology and Technology*, 28(2):269–280.

Penzel, M. (2022). *Sensor-based determination of the fruit bearing capacity in Malus x domestica BORKH. aimed at precise crop load management.* PhD thesis, Technische Universität Berlin.

Praat, J.-P., Bollen, F., Gillgren, D., Taylor, J., Mowat, A., and Amos, N. (2003). Using supply chain information: Mapping pipfruit and kiwifruit quality. *Acta Horticulturae*, (604):377–385.

Rabus, C. and Streif, J. (2000). Effect of various preharvest treatments on the development of internal browning in ‘Braeburn’ apples. *Acta Hortic.*, 518:151–157.

Rogers, G. (2014). Managing the risk of flesh browning for ’Cripps Pink’ apples using a climate model. *Horticulture Australia Ltd.*

Rubo, S. and Zinkernagel, J. (2022). Exploring hyperspectral reflectance indices for the estimation of water and nitrogen status of spinach. *Biosystems Engineering*, 214:58–71.

Saquet, A. A., Streif, J., and Bangerth, F. (2003). Reducing internal browning disorders in 'Braeburn' apples by delayed controlled atmosphere storage and some related physiological and biochemical changes. *Acta Horticulturae*, (628):453–458.

Saure, M. (1996). Reassessment of the role of calcium in development of bitter pit in apple. *Functional Plant Biology*, 23(3):237.

Schuler, J. A. (2022). Einfluss von Managementmaßnahmen und Witterung auf Spektraldaten im Feld bei der Apfelsorte ’Braeburn’. Master’s thesis, Universität Hohenheim.

Solanelles, F., Escolà, A., Planas, S., Rosell, J., Camp, F., and Gràcia, F. (2006). An electronic control system for pesticide application proportional to the canopy width of tree crops. *Biosystems Engineering*, 95(4):473–481.

Solovchenko, A. E., Yahia, E. M., and Chen, C. (2019). *Pigments*, chapter 11, pages 225–252. Elsevier.

Stefan A. Lohner and Konni Biegert and Steffen Nothelfer and Ansgar Hohmann and Roy McCormick and Alwin Kienle, t. . D. (2021). *Postharvest Biology and Technology*, 181:111652.

Sugiura, T., Ogawa, H., Fukuda, N., and Moriguchi, T. (2013). Changes in the taste and textural attributes of apples in response to climate change. *Scientific Reports*, 3(1).

Terry, P., Terry, J., and Wolk, A. (2011). Fruit and vegetable consumption in the prevention of cancer: an update. *Journal of Internal Medicine*, 250(4):280–290.

Tsoulias, N., Paraforos, D. S., Xanthopoulos, G., and Zude-Sasse, M. (2020). Apple Shape Detection Based on Geometric and Radiometric Features Using a LiDAR Laser Scanner. *Remote Sensing*, 12(15):2481.

Tustin, D., Breen, K., and van Hooijdonk, B. (2022). Light utilisation, leaf canopy properties and fruiting responses of narrow-row, planar cordon apple orchard planting systems—a study of the productivity of apple. *Scientia Horticulturae*, 294:110778.

Underwood, J., Jagbrant, G., Nieto, J., and Sukkarieh, S. (2015). Lidar-based tree recognition and platform localization in orchards. *Journal of Field Robotics*, 32(8):1056–1074.

Verbiest, R., Ruysen, K., Vanwalleghem, T., Demeester, E., and Kellens, K. (2020). Automation and robotics in the cultivation of pome fruit: Where do we stand today? *Journal of Field Robotics*, 38(4):513–531.

Walsh, K. B., Blasco, J., Zude-Sasse, M., and Sun, X. (2020). Visible-NIR 'point' spectroscopy in postharvest fruit and vegetable assessment: The science behind three decades of commercial use. *Postharvest Biology and Technology*, 168:111246.

Wang, Z., Beers, R. V., Aernouts, B., Watt, R., Verboven, P., Nicolaï, B., and Saeys, W. (2020). Microstructure affects light scattering in apples. *Postharvest Biology and Technology*, 159:110996.

Wünsche, J. N. and Ferguson, I. B. (2010). Crop load interactions in apple. In *Horticultural Reviews*, pages 231–290. John Wiley & Sons, Inc.

Wünsche, J. N. and Lakso, A. N. (2000). Apple tree physiology- implications for orchard and tree management. In *The compact fruit tree*, volume 33, pages 82–88, Nelson Research Center, Motueka, New Zealand; Geneva, New York, USA; Napier, New Zealand.

Zerbini, P. E. (2006). Emerging technologies for non-destructive quality evalution of fruit. *Journal of Fruit and Ornamental Plant Research*, 41(2):11–22.

Zude-Sasse, M., Truppel, I., and Herold, B. (2002). An approach to non-destructive apple fruit chlorophyll determination. *Postharvest Biology and Technology*, 25(2):123–133.

Appendix

7.1 Supplementary publications from author contributions

Lohner, S. A., Biegert, K., Nothelfer, S., Hohmann, A., McCormick, R. J. and Kienle, A. (2021). Determining the optical properties of apple tissue and their dependence on physiological and morphological characteristics during maturation. Part 1: Spatial frequency domain imaging. *Postharvest Biology and Technology*, 181:111647.
`https://doi.org/10.1016/j.postharvbio.2021.111647`

Lohner, S. A., Biegert, K., Nothelfer, S., Hohmann, A., McCormick, R. J. and Kienle, A. (2021). Determining the optical properties of apple tissue and their dependence on physiological and morphological characteristics during fruit maturation. Part 2: Mie's theory. *Postharvest Biology and Technology*, 181:111652.
`https://doi.org/10.1016/j.postharvbio.2021.111652`

McCormick, R. and Biegert, K. (2021). Non-destructive Vis/NIR time-series to model apple fruit maturation on the tree. *Acta Hortic.*, (1311):131-140. `https://doi.org/10.17660/ActaHortic.2021.1311.17`

Lohner, S. A., Biegert, K., Hohmann, A., McCormick, R.J. and Kienle, A. (2022). Chlorophyll- and anthocyanin-rich cell organelles affect light scattering in apple skin. *Photochemical & Photobiological Sciences*, 21(2):261-373
`https://doi.org/10.1007/s43630-021-00164-1`

Postharvest Biology and Technology 181 (2021) 111647

Contents lists available at ScienceDirect

Postharvest Biology and Technology

journal homepage: www.elsevier.com/locate/postharvbio

Determining the optical properties of apple tissue and their dependence on physiological and morphological characteristics during maturation. Part 1: Spatial frequency domain imaging

Stefan A. Lohner [a],*, Konni Biegert [b], Steffen Nothelfer [a], Ansgar Hohmann [a], Roy McCormick [b], Alwin Kienle [a]

[a] *Institut für Lasertechnologien in der Medizin und Meßtechnik an der Universität Ulm, Helmholtzstr. 12, D-89081 Ulm, Germany*
[b] *Kompetenzzentrum Obstbau Bodensee, Schuhmacherhof 6, D-88213 Ravensburg, Germany*

ARTICLE INFO

Keywords:
Spatial frequency domain imaging
Scattering
Absorption
Apple maturation
Starch degradation

ABSTRACT

Relying on the optical properties of apple tissue for nondestructive quality or maturity prediction requires a detailed understanding of the dependence on its structure and ongoing physiological processes. In this study, a multispectral spatial frequency domain imaging (SFDI) setup was used to investigate local changes in the effective scattering coefficient μ_s' and absorption coefficient μ_a related to vascular bundles or heterogeneous starch distribution. Weekly measurements during the maturation period for the cultivars 'Elstar', 'Gala', 'Jonagold', and 'Braeburn' allowed further study of how different ripening processes affect the scattering and absorption properties. The results show both a characteristic location-dependent decrease of μ_s' between the cortex and core region of up to 30 % and an additional temporal decrease of up to 35 % during maturation. The absolute changes depended strongly on the respective cultivar. In general, transport structures such as vascular bundles led to a local decrease of μ_s' in combination with an increased absorption in the spectral regions that can be attributed to water and chlorophyll *b*. To our knowledge, it was demonstrated for the first time that the presence of starch granules in the cortex of immature apples had a significant effect on μ_s', associated with an increase of up to 60 %. Based on the temporal development of μ_a, the buildup and degradation of important plant pigments in the cortex during the maturation period could be traced. At a wavelength of 656 nm, a decrease in chlorophyll content and at 447 nm, an increase in carotenoid content was observed upon reaching ripeness. Thus, SFDI proved capable of providing deeper insight into the heterogeneous optical properties of apple tissue and linking these properties to physiological variables. Part 2 of this study investigates the observed effects from a theoretical point of view based on a Mie model considering microstructural properties.

1. Introduction

The demand and acceptance of optical measurement methods for applications to assess the properties and quality of products in the field of agricultural technologies is constantly growing. In particular, this is the case for apples (*Malus domestica* Borkh.), as one of the most consumed fresh fruit. However, as a central question in this context, it is important to understand to what extent optical parameters are related to certain physiological and morphological characteristics. For example, predicting the harvest date for optimal medium- to long-term storage, a very current research question, requires a deeper understanding of the processes that occur during fruit maturation. In this regard, many conventional approaches have been able to establish correlations of spectral information obtained from VIS or NIR spectroscopy with various chemical (e.g., soluble solids and chlorophyll content) or structural properties (e.g., firmness) using chemometric modelling techniques (Zude-Sasse et al., 2002; Zude et al., 2006; Sánchez et al., 2003; Qing et al., 2008). However, such models are not readily comparable because of different experimental setups or algorithms. The regression models are often not robust when applied to samples from different cultivars or from different years (McCormick and Biegert, 2019). To overcome these limitations, current research is increasingly oriented toward the development of measurement techniques that account for light propagation in biological tissue based on physical

---

* Corresponding author.
E-mail address: stefan.lohner@ilm-ulm.de (S.A. Lohner).

https://doi.org/10.1016/j.postharvbio.2021.111647
Received 1 April 2021; Received in revised form 30 June 2021; Accepted 3 July 2021

models. Although these require different assumptions and approximations, the resulting quantitative parameters are generally independent of the particular measurement technique or the specific experimental setup. The descriptions by the absorption coefficient μ_a, the scattering coefficient μ_s, and the anisotropy factor g, the latter often combined to define the effective scattering coefficient $\mu_s' = (1-g)\,\mu_s$, have proven to be suitable to describe and compare physiological changes during fruit maturation (Lu et al., 2020). While μ_a provides information about chemical constituents of the tissue (e.g., water, chlorophyll, carotenoids), μ_s' is related to its structural properties (e.g., porosity, scattering particles). Despite the numerous chemical constituents, such as water or pigments, characteristic absorption bands can be identified quite easily in most cases and can be used, for example, to estimate their volume concentration. In contrast, when investigating the scattering properties, the concrete influence of structural elements such as intercellular space, starch granules, chloroplasts or cell walls usually remains unclear.

A variety of measurement techniques and the associated evaluation algorithms have been developed and applied in recent years to study the optical properties of apples and other fruits. Important examples include integrating sphere setups (Van Beers et al., 2017; Wei et al., 2020), time-resolved spectroscopy (Cubeddu et al., 2001; Rizzolo et al., 2010, 2014; Vanoli et al., 2020), and spatially resolved spectroscopy (Nguyen Do Trong et al., 2014; Van Beers et al., 2015; Sun et al., 2016). Although their basic findings are largely in agreement, a rather strong variation in absolute scattering and absorption properties is observed in the overarching comparison. This includes results from different cultivars, at different dates during maturation or storage, and last but not least, comparison of measurements at different locations of the same apple. For these reasons, the study of temporal and spatial changes in μ_s' and μ_a is of great interest to better understand the relationships with underlying morphological and physiological properties. For this purpose, spatial frequency domain imaging (SFDI) or modulated imaging has proven to be a suitable technique for rapid and non-destructive determination of the optical properties (Cuccia et al., 2009; Hu et al., 2016). In this method, stripe patterns, which are usually sinusoidally modulated in one lateral direction, are irradiated obliquely onto the sample surface and the diffusely reflected light, which consists of modified stripes having the same stripe distance, is measured with a camera chip. From the change in amplitude and phase between the irradiated and detected signal, recorded at different stripe distances i.e., spatial frequencies, the optical properties of the sample can be determined spatially resolved with the aid of a suitable light propagation model. The separation of scattering and absorption offers great advantages for quantitative imaging and is successfully used e.g., in metrology or medical technology (Gioux et al., 2019). In the agricultural sector, one of the first applications was the detection of localized damage or bruises (Anderson et al., 2007; Lu and Lu, 2019), while more recent studies have increasingly focused on the measurement of whole apples and the development of two-layer evaluation algorithms (Hu et al., 2019, 2020).

The aim of this work was the spatially resolved determination of the optical properties of the core and cortex tissue of the apple cultivars ‘Elstar’, ‘Gala’, ‘Jonagold’, and ‘Braeburn’ with a multispectral SFDI setup. Special attention was paid to local changes of μ_s' and μ_a, e.g., related to heterogeneous starch distribution or vascular bundles. In addition, the temporal development of the scattering and absorption properties was investigated in more detail by means of weekly measurements during the maturation period.

2. Materials and methods

2.1. SFDI setup

A sketch of the SFDI setup used in this research is shown in Fig. 1(A). It consists of a projection unit based on a digital micro mirror device (DLP LightCrafter 6500, Texas Instruments, USA) in combination with a LED light source, and a cooled sCMOS camera (Zyla 4.2 sCMOS, Andor, UK). The DLP projects sinusoidal intensity patterns under an oblique angle of $\Theta = 35^\circ$ onto the sample. The self-configured light source provides subsequent illumination based on eight switchable LEDs (XLamp XP-E and XQ-E series, Cree, USA and LUXEON SunPlus series, Lumileds, USA) with peak emission at 447 nm, 471 nm, 521 nm, 619 nm, 656 nm, 718 nm, 845 nm, and 945 nm, each with a narrow bandwidth of approximately 10 nm. The diffuse reflected light from a 20 mm × 20 mm region of the illuminated sample is captured by a vertically attached sCMOS chip with a numerical detection aperture of approximately 0.08.

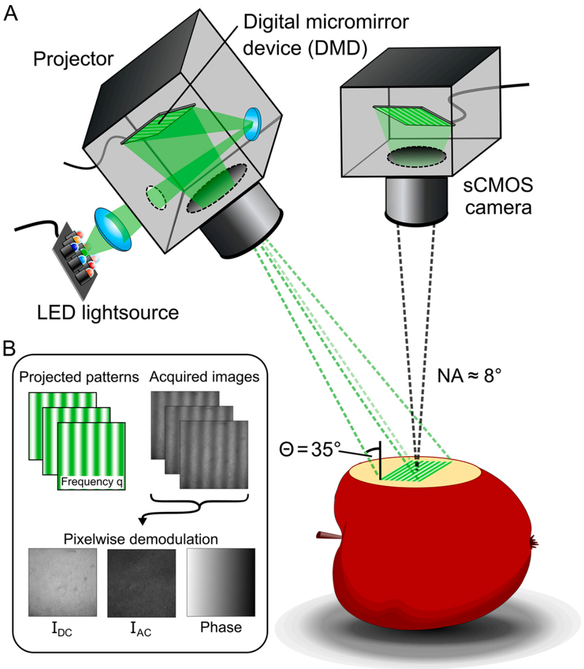

Fig. 1. Schematic drawing of (A) the spatial frequency domain imaging (SFDI) setup consisting of a sCMOS camera and a projector unit coupled to a tunable LED light source. Sinusoidal intensity patterns with spatial frequencies up to 0.5 mm^{-1} are projected obliquely onto a cut apple sample. In (B), the pixel-wise demodulation of the acquired images for a spatial frequency q is shown as an example, from which the offset I_{DC}, the modulation amplitude I_{AC}, and the phase are obtained.

The system has to be calibrated once by measuring a calibration pattern in different orientations and heights within a measuring volume of 20 mm × 20 mm × 20 mm, which is limited by the projector optics and camera focus depth. A pinhole-model based calibration algorithm is used to fully characterize the system by means of its extrinsic parameters (e.g., coordinates of camera and projector in world coordinates) and intrinsic parameters (e.g., respective principal points, focal lengths, lens distortions) as presented in Zhang (2000) and Chen et al. (2009). This knowledge allows calculation of pre-distored images on the one hand, which form, once projected, a nearly perfect homogeneous sine pattern on a fixed calibration plane at the center of the measuring volume. On the other hand, camera distortion is considered by use of a correction algorithm, which is applied directly after acquiring the raw images. In the actual measurement, seven different spatial frequencies between 0 mm^{-1} and 0.5 mm^{-1} are projected with three phase shifts of 0, $2\pi/3$, and $4\pi/3$, respectively, and the diffuse reflection is acquired in each case. The exposure time is typically 20 ms for one image, resulting in a total measuring time of approximately 450 ms for a complete sequence of 22 patterns (21 phase patterns + 1 dark pattern) at one wavelength. Thus, the multi-spectral data acquisition takes less than 5 s in total. Finally, a pixel-wise demodulation algorithm provides for each spatial frequency q the modulation amplitude I_{AC} (alternating component, AC), the offset I_{DC}

(direct component, DC), and the phase, as shown in Fig. 1(B).

2.1.1. Data post-processing and evaluation

After completion of the measurements, the raw data is post-processed before the actual evaluation. In a first step, inhomogeneities of the incident light intensity as well as the modulation transfer function (MTF) of the optical system are corrected. For a direct approach, a phantom with known reflectance $R_{SFD,ref}$ is measured at the same position as the samples within the measuring volume. The absolute spatial frequency domain (SFD) reflectance for a series of n different spatial frequencies q is then calculated as

$$R_{\mathrm{SFD}}(q) = \begin{cases} \sum_{i}^{n} \left(\frac{I_{\mathrm{DC}}(q_i)}{I_{\mathrm{DC,ref}}(q_i)} R_{\mathrm{SFD,ref}}(0) \right) \Big/ n & q = 0 \\ \frac{I_{\mathrm{AC}}(q)}{I_{\mathrm{AC,ref}}(q)} R_{\mathrm{SFD,ref}}(q) & q \neq 0, \end{cases} \tag{1}$$

where for the frequency $q = 0$, corresponding to homogeneous illumination, the average of the DC images of all measured frequencies was taken. However, this method is only applicable, if the reference phantom and the sample surface are perfectly flat and lie exactly in the same plane. In general, however, the samples often have irregular shapes with a displaced or tilted surface relative to the reference plane. These deviations can lead to large errors in both the absolute R_{SFD} and the local spatial frequency, which are crucial for the following quantitative evaluation (Bodenschatz et al., 2014, 2015). To overcome this limitation, a new referencing method was developed for almost arbitrarily shaped objects. With the phase image obtained from the demodulation and the initial calibration, a triangulation algorithm can be used to assign each pixel a unique position in a coordinate system defined by the reference plane. Based on this 3D model and the coordinates of the projector and camera, which are also known from calibration, geometric calculations provide for each pixel the height offset relative to the reference plane, the angle of incidence and detection, and the surface normal vector. After measuring the reference intensity phantom at different positions within the entire measuring volume, a 3D-interpolation algorithm provides the appropriate intensity value for each pixel based on its known position within the reference grid. Similarly, the individual spatial frequency can be corrected by taking into account the height and tilt angle of the sample surface relative to the reference plane for which the frequency projection was calculated.

To model light propagation in turbid media, an analytical solution of the radiative transfer equation for semi-infinite media and oblique projection of sinusoidal intensity patterns was used (Liemert and Kienle, 2012a, 2012b, 2013). To distinguish between volume scattering and surface scattering, the model was extended by introducing a surface roughness parameter, which is presented in more detail in Section 3.1.2. The extended model was subsequently applied to the post-processed data using a nonlinear least squares algorithm with a computational accuracy of order $N = 11$, resulting in μ_a, μ_s', and the surface roughness parameter r_s for each pixel. To reduce the evaluation time and the amount of data, a 16×16 binning was generally used, which results in a sufficient resolution of 300 µm × 300 µm.

Specifically for apple tissue, the refractive index and anisotropy factor are not precisely known and must be estimated for evaluation. Since water is by far the dominant component of apple tissue, it is assumed that its refractive index also largely corresponds to the refractive index of water (Hale and Querry, 1973). In Van Beers et al. (2017) and Saeys et al. (2008), a wavelength-independent constant of 0.04 was added to the refractive index of water, giving an exemplary value of 1.37 at a wavelength of 650 nm. This approach is also adopted in this work. A uniform value of 0.9 was assumed for the anisotropy factor g for apple tissue, since forward scattering usually predominates in biological tissue. This assumption is also in agreement with experimental results, Van Beers et al. (2017) for example determined values in the range of 0.93 at a wavelength of 800 nm for the cortex tissue of different apple cultivars.

2.2. Fruit samples

2.2.1. Cultivars and origin

Fruit samples were taken from the Kompetenzzentrum Obstbau-Bodensee (KOB) research orchard (47°46′01.8″N 9°33′30.3″E) in the season 2019. The cultivars were *Malus domestica* ‘Gala’ (Simmons/Buckeye), ‘Elstar’ (P.C.P.), ‘Jonagold’ (Novajo), and ‘Braeburn’ (Hillwell) planted in 2017, 2012, 2012, and 2016 respectively. The trees were planted as slender spindles in a north-south row orientation and hand thinned to a defined cropload per tree. Trees carried a full crop, except ‘Gala’. This selection of cultivars covered the early to late harvest season with different ripening characteristics. In the present study, for each cultivar, 20 similar trees (growth and hand thinned after June drop to the same cropload) were selected and grouped into four lots of five trees. At each sampling time 16 fruit were picked from different tree lots to ensure the reduction in cropload over all trees was minimal, as a strong reduction in cropload is known to influence the rate of fruit maturation. Individual fruit at each sampling time were used as repetitions.

2.2.2. Sample preparation and Streif index

Fruit samples were taken in the middle tree sector weekly after June drop until two weeks after the optimal harvest date for long term-storage. The optimal harvest date was selected based on the Streif index (SI) commonly used in the fruit industry according to long-term experience (Streif, 1996). Six apples were sent by refrigerated overnight express to the SFDI laboratory and ten fruit remained at the KOB for a SI test. The SI was calculated with mean values for each fruit lot according to

$$\mathrm{SI} = \frac{\mathrm{FF}}{\mathrm{SSC} \cdot \mathrm{SPI}} \tag{2}$$

with fruit firmness (FF), soluble solids content (SSC), and starch pattern index (SPI). FF was determined with either an 8 mm (for small immature apples) or an 11 mm probe (Fruit Texture Analyzer, Güss, South Africa), SSC with a portable refractometer (PR-1, Atago, Japan) on both sun and the shade sides of each apple. Juice samples for SSC determination were taken with a micropipette directly from the FF probe hole on each side of the fruit. The SPI was visually assessed from one fruit half with an ordinal score from 1 (all starch) to 10 (no starch).

In preparation for the SFDI measurements, a thin section of skin and underlying tissue approximately 3 mm thick was cut with a sharp slicer to expose the cortex tissue. The apple tissue was then carefully wiped to avoid reflections from small juice droplets and measured immediately before oxidative tissue browning could occur. To measure the entire transverse section, apples were cut along the equator to fully expose the cortex and core tissue. If necessary, multiple measurements were taken after moving the apple slightly in the transverse direction to cover the entire surface.

A basic classification of apple fruit is shown in Fig. 2. Internally, the tissue consists of capillary tissue (hereafter core) surrounded by the floral tube or hypanthium (hereafter cortex). Both are separated by the core line (MacDaniels, 1940). The chemical and structural properties of both tissue types are highly associated with a complex transport system for water-soluble substances and gases. In particular, the intercellular space plays an important role in the exchange of oxygen and carbon dioxide resulting in a porous structure, while various types of embedded

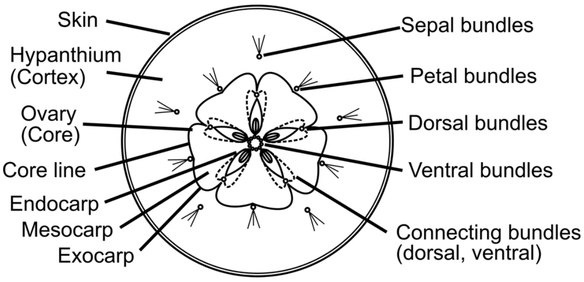

Fig. 2. Schematic morphology of apple fruit in transverse section (adapted from MacDaniels (1940)).

capillary bundles supply the cells with water, minerals, and sugar (Herremans et al., 2015).

3. Results and discussion

3.1. Validation of the SFDI setup

3.1.1. Determining the optical properties of intralipid phantoms

The SFDI setup was validated with four different phantoms based on 10 % intralipid (Fresenius Kabi, Austria) diluted with purified water to fat concentrations of 1.55 % (S1), 1.25 % (S2), 0.93 % (S3), and 0.55 % (S4). In addition, iron gall ink (4001 blue-black, Pelikan, Switzerland) was added at concentrations of 0.18 % (S1), 0.12 % (S2), 0.06 % (S3), and 0.02 % (S4) to achieve different absorption levels. Reference measurements were made with an integrating sphere setup recently described in Foschum et al. (2020) and Bergmann et al. (2020). Each sample was measured within two different glass cuvettes consisting of a spacer ring of 2 mm and 3 mm thickness, respectively, between two N-BK7 glass slides (34-427, Edmund Optics, USA). For the evaluation, the refractive index of water and an anisotropy factor of $g = 0.7$ were assumed for the samples, while the known thickness and refractive index of the glass slides were also taken into account. The resulting μ_s' and μ_a of the samples were calculated as the arithmetic mean of four measurements each. Subsequently, the samples were put in a beaker, measured with the SFDI setup and evaluated under the same assumption for the refractive index and anisotropy factor. In this case, μ_s' and μ_a were averaged over all pixels. Fig. 3 shows the results of both measurement methods in comparison. The SFD measurements generally show good agreement with a mean relative deviation of 4 % for μ_s' and 11 % for μ_a. Particularly for the low absorption range ($\mu_a < 0.01\ \mathrm{mm}^{-1}$), larger deviations in the resulting absorption properties become apparent.

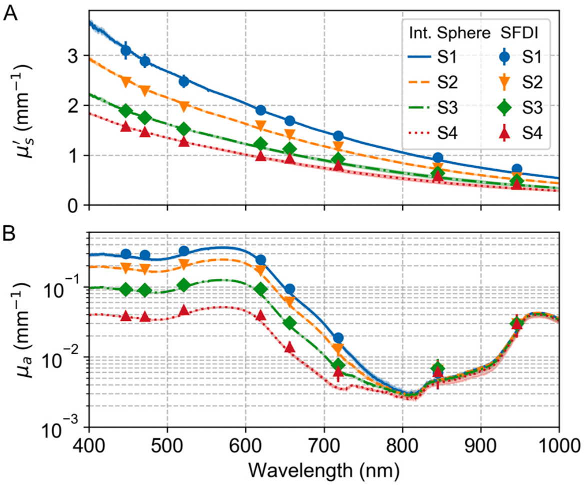

Fig. 3. Comparison of (A) the effective scattering coefficient μ_s' and (B) the absorption coefficient μ_a of four samples (S1-S4) with different intralipid and ink concentrations. The error bars indicate the standard deviation, for the integrating sphere based on four measurement repetitions and for SFDI based on averaging the optical properties over the entire image area.

3.1.2. Consideration of surface roughness

Especially for biological samples with typical irregular surface, the extension of the analytical model presented in Nothelfer et al. (2018) with a distinction between volume scattering and surface scattering proved to be useful. To illustrate the influence of surface roughness, Fig. 4(A) shows an example of the measured R_{SFD} for the cortex of typical apple fruit (black dots) and the results of two nonlinear least-square fits, on the one hand considering an extended model with surface scattering parameter r_s (orange markers) and on the other hand with the original model (blue markers). The measured R_{SFD} was averaged over all pixels in both cases. The bottom plot in Fig. 4(A) shows the relative deviation $\delta R_{SFD,fit}$ between the measurement and the two different models. Obviously, the extended model considering r_s achieves a much smaller deviation being below 1 % compared to the model neglecting surface

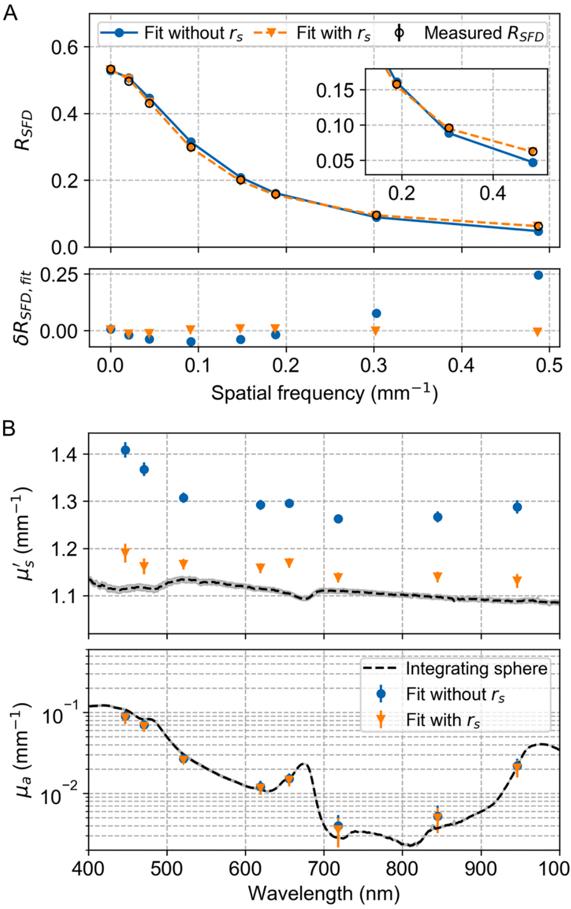

Fig. 4. Comparison of (A) the measured R_{SFD} reflectance of apple tissue and (B) the results of a model-based nonlinear least squares fit with and without consideration of the surface roughness parameter r_s. In (B), an integrating sphere measurement of the same apple cortex sample is shown as a reference. The error bars and colored shadows indicate the standard deviation, for the integrating sphere based on four measurement repetitions and for SFDI based on averaging the optical properties over the entire image area.

scattering, with deviations up to 25 % in the high spatial frequency regime. The obtained μ_s' and μ_a for both fit models are shown in Fig. 4(B). To validate the determined values for μ_s', the same sample was examined using an integrating sphere setup. For this purpose, a 2 mm thick slice of the exact same apple sample was cut and measured between two glass slides. The resulting spectrally resolved μ_s' and μ_a are shown as black lines in Fig. 4(B). The gray shadow shows the standard deviation from four independent measurements of the sample, which was measured twice on one side toward the integrating sphere and twice after turning over. To strongly suppress the surface effects, the sample of apple tissue was pressed between two glass slides, and the interface between the tissue and glass filled sufficiently with escaping juice by itself. The resulting μ_s' and μ_a therefore are not influenced by the surface scattering of the apple sample (we note that the glass slides were considered in the evaluation of the integrating sphere measurements). The comparison with the SFDI results shows a clear overestimation of μ_s' when r_s is neglected (blue dots). In contrast, when surface roughness is taken into account (orange dots), the results agree well with the integrating sphere measurements with a mean value found of $r_s = 2.6(1)$ %. This approach guaranteed a relative mean deviation between the SFDI and integrating sphere method of 6 %. As expected, μ_a remains almost unchanged for the two models with different surface roughness. The relative mean deviation of μ_a when comparing SFDI and integrating sphere measurements was 19 %.

3.2. Spatially resolved optical properties of apple tissue

To determine the spatially resolved optical properties, different ‘Braeburn’ apples were selected 25 weeks after full bloom, bisected along the equator, and measured at different positions between the core and skin using the SFDI setup. Fig. 5 shows the resulting scattering and absorption properties and, in the left column, the corresponding RGB image of each view. The results were averaged over three measurement repetitions without moving the sample. Comparing the bulk scattering properties at a wavelength of 845 nm, a spatial variation of μ_s' between 0.6 mm^{-1} and 1.4 mm^{-1} is noticed, with a tendency to increase from the core in Fig. 5(A) to the skin in Fig. 5(D). The core line and the petal bundle in Fig. 5(A) are clearly visible due to a local decrease of μ_s' relative to the surrounding area of about 0.2 mm^{-1}. A similar decrease also occurs for the dorsal bundle in Fig. 5(B) and the sepal bundles in Fig. 5(C) and Fig. 5(D). Marked increases in μ_s' occur near the endocarp in Fig. 5(B) and are particularly evident in the outer cortex in Fig. 5(D). Overall, μ_s' varies strongly depending on the local structural properties. The surface scattering parameter r_s, on the other hand, seems to depend only to a small extent on these structures, with mean values between 0.04 ± 0.02 (Fig. 5(D)) and 0.05 ± 0.02 (Fig. 5(A)). However, in Fig. 5 (A), there is a significant change in surface texture that highlights the core line. The r_s values and their changes are probably also related to water, which accumulates to varying degrees on the surface during the measurement and influences the total reflection.

The corresponding absorption properties were investigated at two characteristic wavelengths of 656 nm and 945 nm. As known from previous work, these spectral regimes are mainly related to the presence of chlorophyll *b* and water, respectively (Merzlyak and Solovchenko, 2002; Hale and Querry, 1973). Considering μ_a at 656 nm, increases above 0.04 mm^{-1} are observed mainly near the endocarp (Fig. 5(A,B)) and towards the skin (Fig. 5(D)). In contrast, the cortex shows less pronounced absorption, which is below 0.01 mm^{-1}. All types of capillary bundles show a locally strongly limited increase of μ_a combined with a radial decrease within a few millimeters of the surrounding tissue. In the

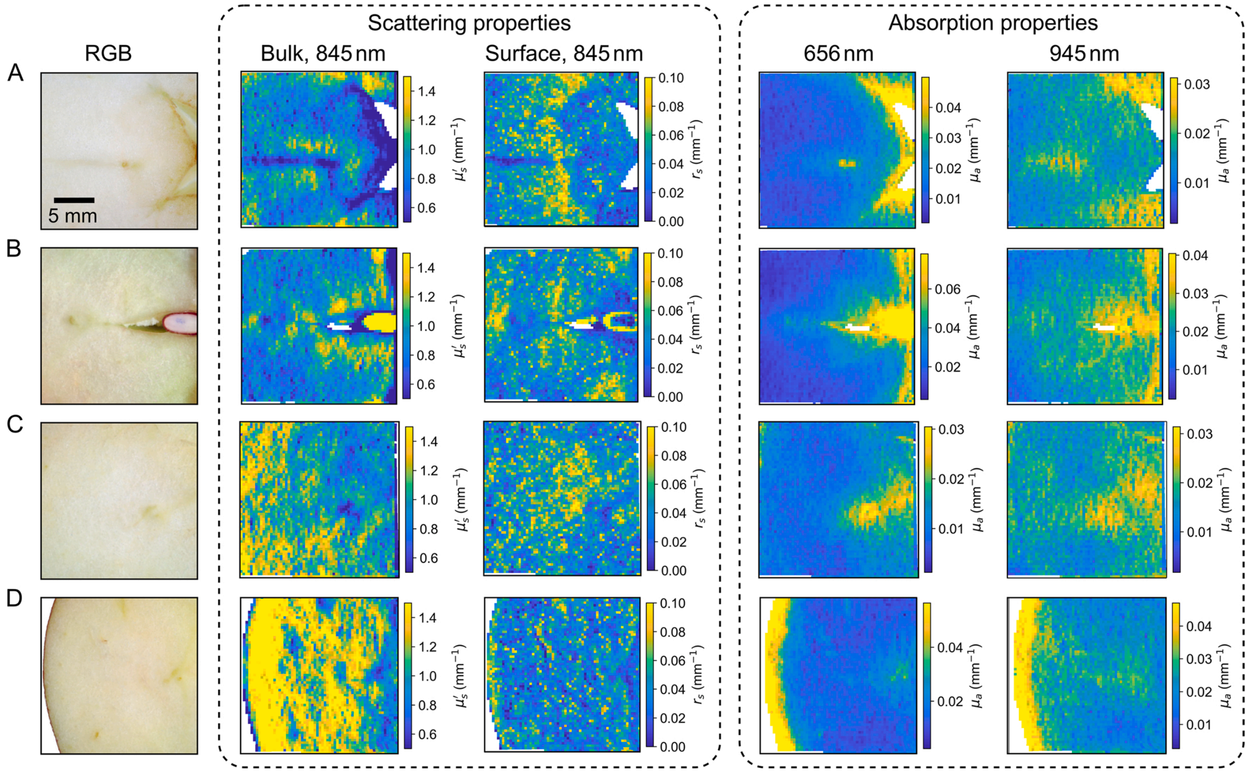

Fig. 5. Spatially resolved bulk effective scattering coefficient (μ_s'), surface scattering parameter (r_s), and absorption coefficient (μ_a) measured at four positions (A-D) of different ‘Braeburn’ apples bisected along the equator. Each measurement was averaged over three measurement repetitions performed without moving the sample.

case of the petal bundle in Fig. 5(B), a fan-shaped decrease in μ_a, starting at the endocarp and moving outward, can be seen. The corresponding measurements at 945 nm show a similar but overall more homogeneous distribution. A striking feature is the spatial offset of the absorption maxima in the comparison of both wavelengths, which is clearly observed near the petal bundle in Fig. 5(A). The radial decrease of μ_a around the bundles also covers a larger area. Taking all measurements into account, μ_a at a wavelength of 945 nm is approximately between 0.01 mm^{-1} and 0.04 mm^{-1}.

To our knowledge, this was the first time that the optical properties of apple tissue could be determined at a sufficiently high resolution to identify characteristic morphological features. Based on SFDI measurements of mature ‘Golden Delicious’ apples, Hu et al. (2020) recently observed an averaged μ_a of about 0.02 mm^{-1} at 650 nm and μ_s' between 1.0 mm^{-1} and 1.5 mm^{-1} at 850 nm for the cortex tissue, which agrees well with the present results. Although Hu et al. (2015) observed generally lower absolute values when examining ‘Redstar’ apples with an average μ_a of 0.007 mm^{-1} and μ_s' of 0.6 mm^{-1} at 630 nm, they also noted a pronounced inhomogeneity of the optical properties. Our results also show broad agreement when compared with previous non-spatially resolved measurements reported by other researchers. For example, based on measurements with an integrating sphere setup, Van Beers et al. (2017) reported the following optical properties for the cortex of ‘Braeburn’ apples with a comparable stage of maturity: $\mu_a = 0.014\ \mathrm{mm}^{-1}$ at 656 nm, $\mu_a = 0.012\ \mathrm{mm}^{-1}$ at 945 nm and $\mu_s' = 1.1\ \mathrm{mm}^{-1}$ at 850 nm. However, the magnitude of the results is also consistent with other work on different apple cultivars in storage (Cen et al., 2013; Rizzolo et al., 2010; Vanoli et al., 2020).

Since water and chlorophyll *b* are known absorbers in apple tissue, the interpretation of the absorption characteristics is quite straightforward. The local distribution of these main absorbers is relatively uniform and changes continuously between the skin, core, and capillary bundles. In contrast, the scattering properties show a much larger location-dependent variance, which, consequently indicates a very heterogeneous structure. This could be due to the relationship between μ_s' and many different structural and cellular components. In various studies, researchers have suggested that in particular cell walls, the intercellular space (gas pores) as well as starch granules, vacuoles, chloroplasts or other organelles have an influence on μ_s' (Van Beers et al., 2017; Vanoli et al., 2009; Cen et al., 2013). However, since there is usually not enough quantitative information about all these properties simultaneously, often only qualitative conclusions can be drawn by combining different indications. Thus, based on a statistical analysis of spatially resolved spectroscopy measurements, Wang et al. (2020) demonstrated a close correlation between μ_s', porosity, and pore surface density and a subordinate influence of cell properties. By a simplified description of scattering, which is mainly defined by the fraction of refractive index boundaries per volume element, a strong influence of the interfaces between aqueous cells ($n \approx 1.33$) and pores filled with gas ($n \approx 1.0$) on the light propagation seems plausible. In contrast, most cell components and the cell walls differ only slightly in their refractive index, which is evident, for example, in phase-contrast tomography measurements of apple cells (Verboven et al., 2008). From an experimental point of view, the intercellular space of apples has recently been studied by several researchers based on X-ray micro-computed tomography (micro-CT) (Janssen et al., 2020; Herremans et al., 2015), who observed a strong radial dependence of both the porosity and spherical equivalent diameter of the gas pores. They determined porosity by image post-processing, which exploits the high contrast between cells and intercellular spaces by additional segmentation, filtering and thresholding of the micro-CT data. Based on the resulting binary images, the volume fraction of both components and thus the porosity can be calculated. While the porosity increased from typically 10 % near the core to 30 % at the cortex, the mean pore diameter increased from 100 μm near the core to 300 μm at the cortex. Considering Mie’s theory describing light scattering from spherical particles in a surrounding medium, the changing porosity and broad size distribution of the gas pores could explain the observed positive gradient of μ_s' between the core and the outer cortex. Therefore, in Part 2 of this work, a theoretical estimation of the local change of μ_s' based on a Mie model considering the mentioned microstructural properties follows.

3.3. *Starch granules influence light scattering*

Within the scope of this work, emphasis was placed on investigating the influence of starch on the scattering properties of apple tissue. The starch content of unripe apples is known to reach up to 50 % of the apple dry weight and thus represents an important component especially during maturation and ripening (Stevenson et al., 2006). Starch accumulates in the form of spherical granules in specific storage organs of the cells, such as chloroplasts or amyloplasts (Gaweda and Ben, 2010). These granules have a dense, semi-crystalline structure with mean diameters of about 9 μm and are insoluble in water (Oates, 1997; Stevenson et al., 2006; Carrín et al., 2004). Their refractive index can be assumed to be in the range of 1.50 to 1.54 based on literature data on the granules of other starchy plants (Wolf et al., 1962; Borch et al., 1972). Starch content of apple fruit typically reaches its maximum about 21 weeks after full bloom with the highest concentrations in the cortex and lower concentrations near the core (Brookfield et al., 1997). During the following period of starch degradation, the granules are hydrolyzed by metabolic enzymes into various kinds of soluble sugars (Oates, 1997). Normally, hydrolysis is first completed near the core and therefore appears to spread from the center (Doerflinger et al., 2015). Although hydrolysis is assumed to start at the same time throughout the apple, its duration locally depends strongly on the initial content, granule size, and degradation rate in the particular part of the fruit (Doerflinger et al., 2015; Brookfield et al., 1997). As a result, the starch distribution in apple tissue can vary greatly during maturation. While some fruit zones have a very high starch content, this may already be completely degraded in other areas at the same time.

The spatially resolved measurement technique was applied to investigate the influence of the starch content onto the optical properties. Different ‘Braeburn’ and ‘Elstar’ apples were selected 23 weeks after full bloom at an advanced stage of starch degradation. Each apple was cut transversely along the equator into two equal halves. The first half was immediately coated with iodine solution to stain the fruit zones with high starch content, analogous to the conventional determination of the starch pattern index (SPI). After a few minutes, the resulting staining pattern revealed suitable measuring positions where significant differences in starch content could be observed. The second half of the same apple was then measured with the SFDI setup at each of the regions corresponding to the stained opposite part without further treatment. Subsequently, the second half of the apple was also coated with iodine solution and the respective staining patterns were photographed with a single-lens reflex camera (SLR) for later comparison, in exactly the same perspective as in the previous SFDI measurements. Fig. 6(A-C) shows both the recorded starch patterns (top row) and the corresponding μ_s' maps measured at a wavelength of 845 nm. Each measurement was averaged over three measurement repetitions without moving the sample. For quantitative comparison, a zone with high starch content (lined frame) and a zone with almost completed starch degradation (dashed frame) with a size of 5.5 mm × 5.5 mm were selected for each measurement. The corresponding μ_s' and μ_a values were averaged in each of these zones, and their spectra are shown in Fig. 6(D) with the respective standard deviations indicated, taking into account error propagation. In all three cases, the difference in μ_s' between the two zones was around 0.4 mm^{-1}, which corresponds to almost 60 %. No characteristic change in the spectral shape of μ_s' was observed, but rather an offset. At the same time, μ_a remained essentially unchanged when comparing the two zones.

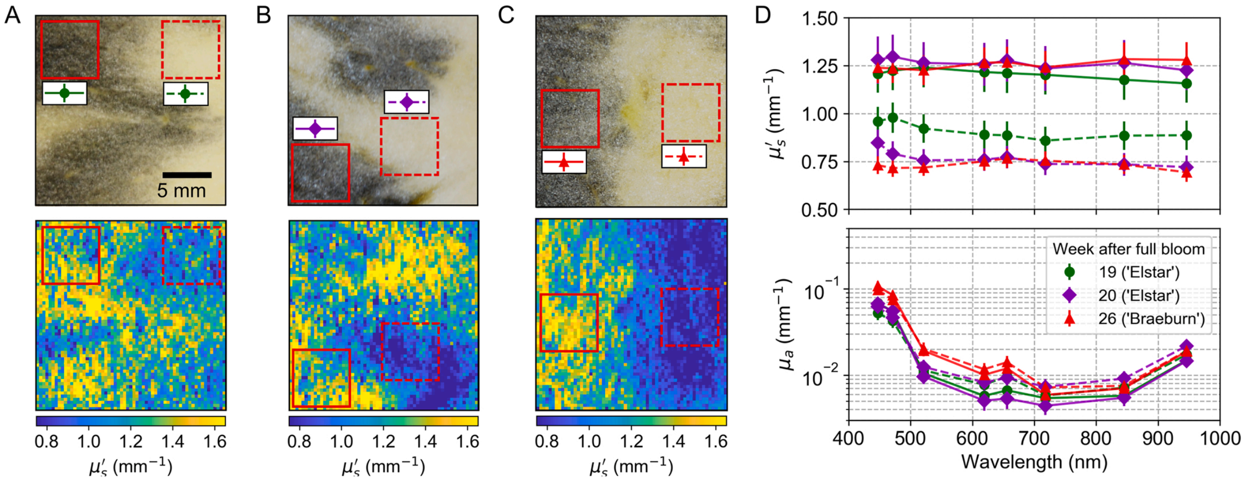

Fig. 6. (A-C) Comparison of starch patterns (top row) for different cortex samples (‘Elstar’ and ‘Braeburn’) and the corresponding μ_s' maps (bottom row) measured at a wavelength of 845 nm before the sample was treated with iodine solution. Each measurement was averaged over three measurement repetitions without moving the sample. In (D), the spectrally resolved μ_s' and μ_a averaged within different tissue zones with either high starch content (dark stained zones, marked with lined frames) or nearly completed starch degradation (unstained zones, marked with dashed frames) are shown. The error bars indicate the standard deviations obtained from averaging over the marked zones.

Overall, the results indicate a direct and considerable influence of the starch granules on the scattering properties. However, it must be taken into account that other cellular and structural characteristics may also change, e.g., with progress of starch degradation. No information was found on the extent to which porosity might be locally related to the progress of starch degradation. In addition, the starch staining pattern only allows a qualitative assessment of starch content and does not allow conclusions to be drawn about absolute concentrations. However, assuming that the granules are in an aqueous environment within the cell, a significant difference in refractive indices can be assumed. This, together with the temporarily high weight fraction of starch granules in the total dry weight, could explain the observed effects. A more accurate estimate, based on Mie’s theory considering the concentrations and granule diameters reported in the literature, will be investigated in Part 2 of this work.

3.4. Scattering and absorption profiles reveal characteristics of transport structures

Both the scattering and absorption properties investigated so far show a pronounced radial dependence. As already noted, on a structural level this can be related to both the intercellular space and the starch distribution. On the chemical level, characteristic changes in water content or plant pigments can also be expected. The radial changes in scattering and absorption properties are examined in more detail below using ‘Braeburn’ apple, harvested 26 weeks after full bloom. Measurements of the skin area with the outer cortex and inner cortex were carried out successively. The two measurements could then be accurately aligned by comparing the topography of an appropriately chosen overlapping area, determined by triangulation. Using the combined maps, the radial profiles of μ_s' and μ_a were finally calculated by averaging the optical properties between the skin and the core line within a 2 mm wide region. Fig. 7(A) shows the RGB image of the examined apple tissue, with the radial profile shown as a black dashed line. At a distance of 14 mm from the skin, approximately in the center of the marked area, a petal cluster is visible as a greenish spot. Fig. 7(B) shows the corresponding μ_s' profiles, again measured at wavelengths of 656 nm and 945 nm. As previously observed, μ_s' shows an almost linear decrease from values between 1.5 mm^{-1} at the skin to 0.6 mm^{-1} at the inner cortex. Beyond 20 mm from the skin, μ_s' tends to increase slightly over the last few millimeters toward the core region. At a distance of about 12.5 mm from the skin, both scattering profiles show a dip with a modulation depth of about 35 %, apparently related to the petal bundle. Furthermore, the nearly identical shape of the profiles at different wavelengths indicates that μ_s' does not have a pronounced spectral dependence and thus the main scatterers are large compared to the wavelength used. In contrast, the corresponding absorption profiles in Fig. 7(C) show a clear difference between the two wavelengths. After a strong decrease near the skin, the μ_a profiles hardly change toward the outer cortex, reaching values of 0.015 mm^{-1} at 656 nm and 0.022 mm^{-1} at 945 nm. It should be noted that the applied semi-infinite model leads to errors especially near the apple skin, which will be examined in more detail later. Towards the petal bundle, a slight increase followed by a subsequent absorption peak is observed in each case. At 656 nm, the absorption maximum occurs at a distance of 14 mm from the skin. In contrast, the rather flat absorption maximum at 945 nm occurs at a distance of 11 mm from the skin, offset by about 3 mm relative to the chlorophyll maximum seen at 656 nm, and increases again within a few millimeters after reaching the minimum absorption at a distance of about 16 mm. In both cases, the μ_a profiles increase continuously between 0.01 mm^{-1} and 0.04 mm^{-1} toward the core region.

Overall, it appears that the petal bundle at the core line separates the cortex from the core tissue, which differ in their structural properties as well as in their water and chlorophyll content. Similarly, Janssen et al. (2020) reported low mechanical connectivity between these regions based on micro-CT measurements. Since vascular bundles and the core line are composed of rather dense tissue with lower porosity, our observations of a decrease in μ_s' assuming comparable pore sizes seem to be in agreement with Janssen et al. (2020) and Verboven et al. (2008). Further, good agreement of the radial progression of μ_s' is particularly evident when compared with the porosity profile reported in Dražeta et al. (2004), since both profiles were measured in comparable orientation near a petal bundle. Considering $\mu_a = 0.03$ mm^{-1} for pure water at 945 nm (black dashed line in Fig. 7(C)), the spectral bandwidth of the LED, and neglecting other background absorbers, the measured μ_a profile allows a rough estimate of the absolute water volume content. It ranges from about 50 % in the inner cortex to 80 % in the outer cortex, which seems generally reasonable and further illustrates the influence of the petal bundle on the water balance in cortex tissue. In addition, the offset between maximum water and chlorophyll absorption may

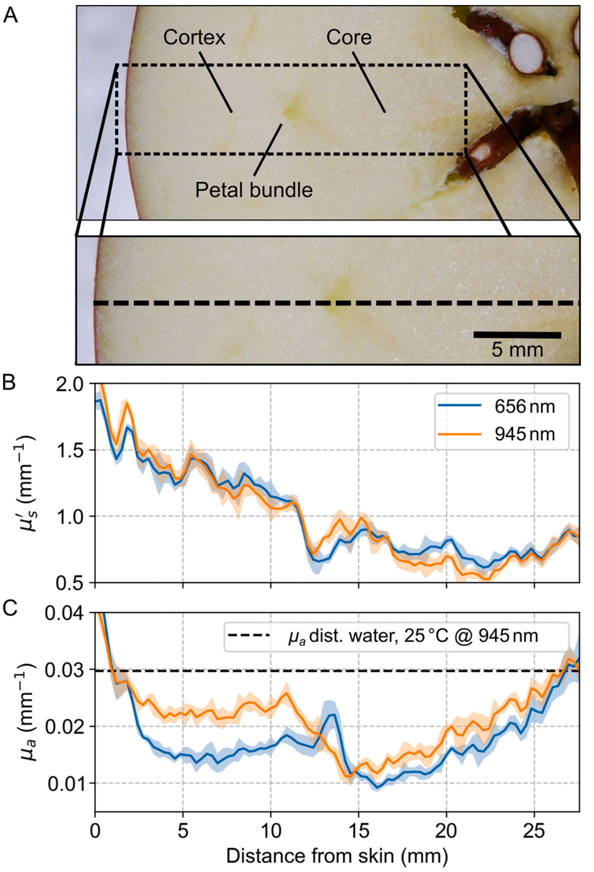

Fig. 7. (A) RGB image of an equatorially sliced 'Braeburn' apple with a petal bundle (greenish spot) at a distance of 14 mm from the skin. The black dotted line in the magnified image marks the position of the profile. The corresponding radial profiles of (B) μ_s' and (C) μ_a were determined at wavelengths of 656 nm and 945 nm averaged over a range of 2 mm, respectively, based on two complementary measurement positions with three measurement repetitions each. The colored shadows show the standard deviation within the 2 mm profile range. For comparison, the black dashed line in (C) marks the expected absorbance of dist. water at 945 nm considering the spectral bandwidth of the LED.

indicate a collateral-type petal bundle. In this case, the vessels for the transport of water and minerals (xylem) on one side and for the transport of soluble organic compounds metabolized during photosynthesis (phloem) on the other side are separated (Verboven et al., 2008; Herremans et al., 2015). Interestingly, μ_s' shows a local minimum exactly at the border between these two tissue types.

3.5. Temporal evolution of scattering and absorption profiles

Since optical sensors for the determination of optical properties are usually designed for measurements on intact apples, the outer cortex tissue in particular plays an important role in the investigation of light propagation, taking into account the wavelength and thus the penetration depth. It is known from previous studies, for example, that the tissue under the skin in particular has a high chlorophyll content, which is degraded during maturation. To investigate this in more detail, the temporal changes in the absorption and scattering profiles of the outer cortex were examined. The cultivar 'Jonagold' was selected as an example for the study, and the profiles of six apples were measured weekly according to the procedure presented in Section 3.4. A single measurement of the outer cortex region was performed in each case, allowing the outer 16 mm of tissue to be recorded on average. The scattering profiles in Fig. 8(A) show the temporal evolution of μ_s' measured at a wavelength of 850 nm.

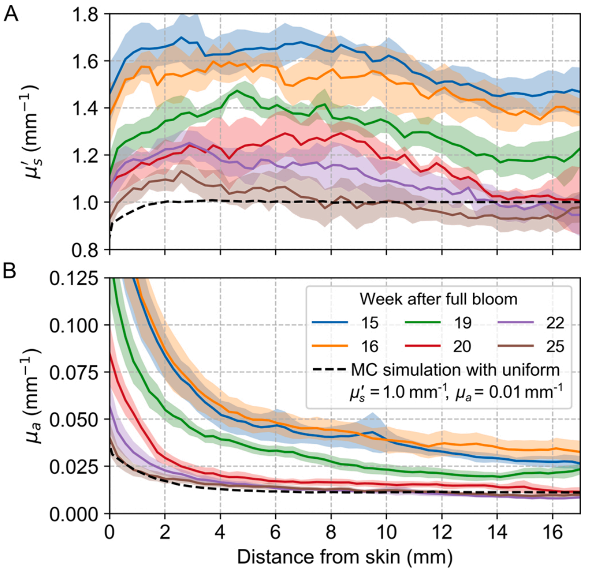

Fig. 8. Temporal evolution of radial line profiles for (A) μ_s' at a wavelength of 850 nm and (B) μ_a at a wavelength of 656 nm measured on 'Jonagold' apples during maturation. The colored shadows indicate the resulting standard deviations for a weekly sample set of six apples with one measurement each. The dashed lines show the optical properties obtained for simulated SFDI data for a sample with comparable geometry but homogeneous μ_s' and μ_a. Especially within the first 2 mm from the skin, boundary effects lead to deviations.

In general, the μ_s' profiles initially show a slight increase starting from the skin to a maximum reached approximately within the outer 5–10 mm of the cortex. Thereafter, a decrease is consistently observed toward the inner cortex. The lateral modulation of the profile is least pronounced at the beginning and end of the maturation period, at about 15 %, and most pronounced 20 weeks after full bloom, at 25 %. At the same time, an absolute decrease in the scattering profiles is observed from week to week, which means that the mean μ_s' decreases by almost 40 % during maturation. The absorption profiles in Fig. 8(B) were evaluated at a wavelength of 656 nm to draw conclusions about chlorophyll content. All profiles show an almost exponential decrease of μ_a from the outer to the inner cortex. The weekly decrease is very uniform and shows no pronounced location dependence, with an overall decrease by a factor of 3 during the studied period. However, it is noticeable that the degradation rate varies, in particular a very strong decrease was observed between week 19 and week 20 after full bloom, whereas no change is visible between week 15 and 16.

Since the evaluation is based on a semi-infinite model, it was expected that the skin area would exhibit artifacts due to the tissue-air boundary. To investigate the extent of this effect, a Monte Carlo simulation of the SFDI measurements was performed. For this, a hemisphere with comparable geometry but homogeneous optical properties (μ_s' = 1.0 mm^{-1} and $\mu_a = 0.01$ mm^{-1}) was assumed. Comparable to the experiment, the air-tissue boundaries were each aligned perpendicular to the sinusoidal patterns. In contrast to a parallel alignment, the boundary effects can be further minimized in this way. After evaluation of the simulated data with the same semi-infinite model as before, the black dotted profiles shown in Fig. 8(A and B) resulted. While optical properties were correctly determined at distances from the skin greater than about 2 mm, significant deviations are observed near the skin. The scattering properties are systematically under-determined in the boundary zone, which explains the corresponding decrease in the apple measurements near the skin. Absorption, on the other hand, is overestimated by the semi-infinite model, resulting in an incorrect μ_a within the first 3 mm. In particular, for week 25 after full bloom, the measured absorption profile agrees very well with the simulation, so an absorption gradient is no longer detectable in this case. This means that in the ripe apple, the low chlorophyll content in the outer cortex is relatively homogeneously distributed.

Overall, the results show that there is a very heterogeneous change in optical properties in the radial direction, especially during maturation. In the outer 1.5 cm of the cortex, a variation of μ_s' by up to 30 % and μ_a in the case of chlorophyll concentration even by up to 80 % relative to the skin area could be detected. This is relevant because typically the average penetration depths of optical measuring methods are exactly in this range of up to 1.5 cm (Lammertyn et al., 2000; Seifert et al., 2015). Depending on the wavelength and the depth sensitivity of the respective method, a considerable deviation of the results obtained with different devices can be expected. Also Vanoli et al. (2020) observed these differences, for example, when comparing measurements on the same apples with spatially-resolved and time-resolved spectroscopy. Overall, the results also allow conclusions to be drawn about different physiological processes. The very similar relative decrease in μ_a from week to week compared for all distances to the skin indicates that the rate of chlorophyll degradation depends primarily on the corresponding concentration. At the same time, it was also observed that the largest change occurs in a relatively short period of 2 weeks after about 19 weeks after full bloom. The scattering profiles show features that can be attributed to structural changes. Particularly at week 25 after full bloom, when starch degradation was complete, μ_s' showed a relatively flat curve. This is probably mainly due to changes in porosity as reported by Janssen et al. (2020) and Herremans et al. (2013). Much larger differences between the outer and inner cortex were observed in the weeks prior to this, most noticeably 20 weeks after full bloom, when starch degradation was about half complete. In this case, the larger gradient in the μ_s' profiles could be related to an additional influence of the different starch content of inner and outer cortex.

3.6. *Temporal evolution of the cortex mean optical properties*

The optical properties are now compared for each of the four cultivars. Six apples were measured weekly with the SFDI setup on the sun exposed and shaded sides after cutting off the skin and the outer tissue layer with a maximum thickness of about 4 mm. The resulting μ_s' and μ_a were first averaged over the measured area and over both sides of each apple. Then, taking into account error propagation, the results for each cultivar were also averaged over all apples per week and referred to as mean optical properties in the following discussion.

In a first step, the optical properties at particularly important wavelengths were considered. Fig. 9(A) shows the temporal evolution of μ_s' at 845 nm and μ_a at 447 nm, 656 nm, and 945 nm. Weekly examinations began 12 weeks after full bloom with ‘Elstar’ and ‘Gala’, two early maturing cultivars. Their initial μ_s' in Fig. 9(A) were the highest at 1.6 mm^{-1} and 1.7 mm^{-1}, respectively. No significant change was observed in the first four weeks, only in the following six weeks was a decrease detected, here μ_s' decreased to 1.25 mm^{-1} for ‘Elstar’ and 1.1 mm^{-1} for ‘Gala’. This corresponds to an overall decrease of 25 % and 35 %, respectively. ‘Jonagold’ is a medium-early maturing cultivar that was examined starting 15 weeks after full bloom. In this case, a pronounced steady decrease in μ_s' was observed from 1.43 mm^{-1} to 0.91 mm^{-1}, also corresponding to a change of 35 %. ‘Braeburn’, a late-maturing cultivar, was examined from week 18 after full bloom. In this case, μ_s' increased to 1.22 mm^{-1} in the first three weeks, followed by a slight decrease to 1.00 mm^{-1} within eight weeks. With a change of less than 20 %, the decrease was detectable but least pronounced. For all four cultivars, measurements were made up to four weeks after the optimal harvest date for long-term storage, which was determined using the Streif index shown in Fig. 9(E). The Streif indices at harvest were 0.44 for ‘Elstar’, 0.21 for ‘Gala’, 0.08 for ‘Jonagold’, and 0.30 for ‘Braeburn’. Due to changing climatic conditions fruit were mature for harvest earlier than indicated by the long term SI values. The harvest dates determined according to these indices are marked by arrows in Fig. 9(A).

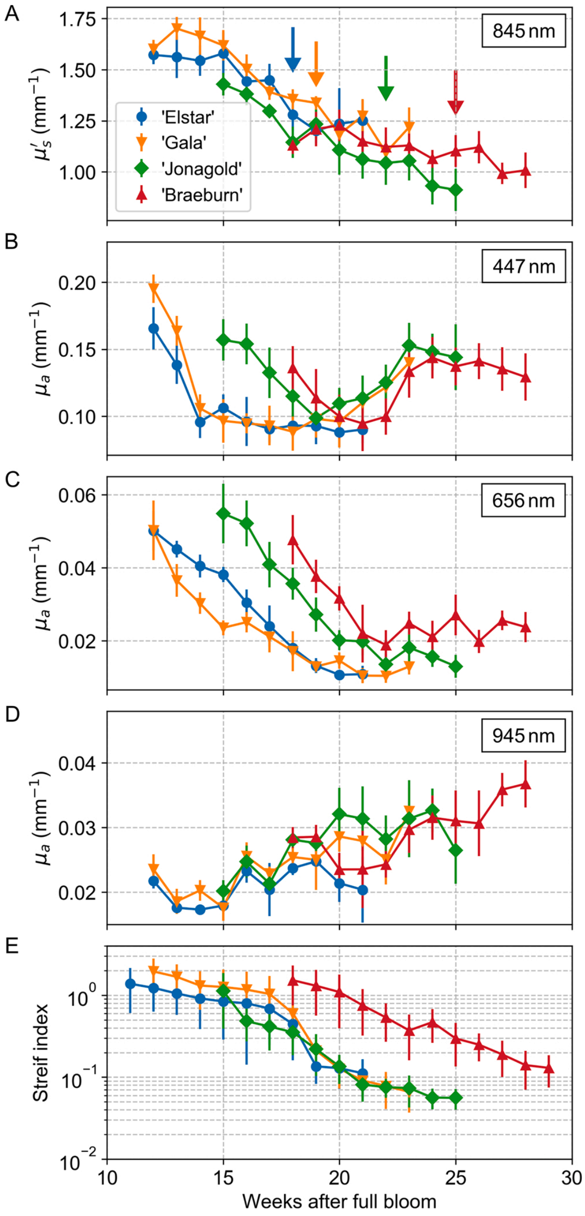

Fig. 9. Temporal evolution of mean (A) μ_s' at 845 nm, (B) μ_a at 447 nm, (C) μ_a at 656 nm, and (D) μ_a at 945 nm of apple cortex compared for all four cultivars during maturation. Error bars indicate the resulting standard deviations for a weekly sample set of six apples with two measurements each. The colored arrows in (A) mark the recommended harvest dates for each cultivar, which were determined based on the Streif indices shown in (E).

The cultivars show characteristic differences with regard to their absorption properties. In addition to chlorophyll and water, which have already been discussed, carotenoids in particular are known to play an important role in maturing apple tissue. In general, they are assigned to absorption characteristics in the range below 500 nm, Merzlyak et al. (2003) specifically mentioned 425 nm, 455 nm, and 480 nm. Thus, μ_a at 447 nm, as shown in Fig. 9(B), can be associated with carotenoid content in apple tissue. All cultivars showed a significant decrease in μ_a during the first four weeks after the start of the study, most pronounced for 'Gala' between 0.20 mm^{-1} and 0.10 mm^{-1}. From week 23 after full bloom, 'Gala', 'Jonagold', and 'Braeburn' showed a rapid increase in absorption up to 0.15 mm^{-1}, corresponding to an increase of 50 %. A slight decrease during the last weeks was observed especially for 'Braeburn'. At 656 nm in Fig. 9(C), all cultivars show a fairly uniform decrease in μ_a from 0.06 mm^{-1} to 0.02 mm^{-1}. More or less after the harvest date, no significant changes are seen. In Fig. 9(D), μ_a at 945 nm shows a continuous increase from 0.02 mm^{-1} to 0.035 mm^{-1}. Since water is one of the main absorbers in this spectral region, the temporal change in μ_a indicates an increase in water content per volume. However, μ_a exceeds the absorption of 0.03 mm^{-1} that would have been expected for distilled water, especially in the case of 'Braeburn'. This circumstance could be explained, for example, by the influence of additional background absorbers.

An overview of the spectrally resolved representation of the mean optical properties is shown in Fig. 10. For clarity, the values are given only for every second week. As observed in previous measurements, μ_s' shows no significant spectral dependence, neither for the different cultivars nor for the different weeks. The weekly change is also approximately the same for all wavelengths. The absorption properties hardly

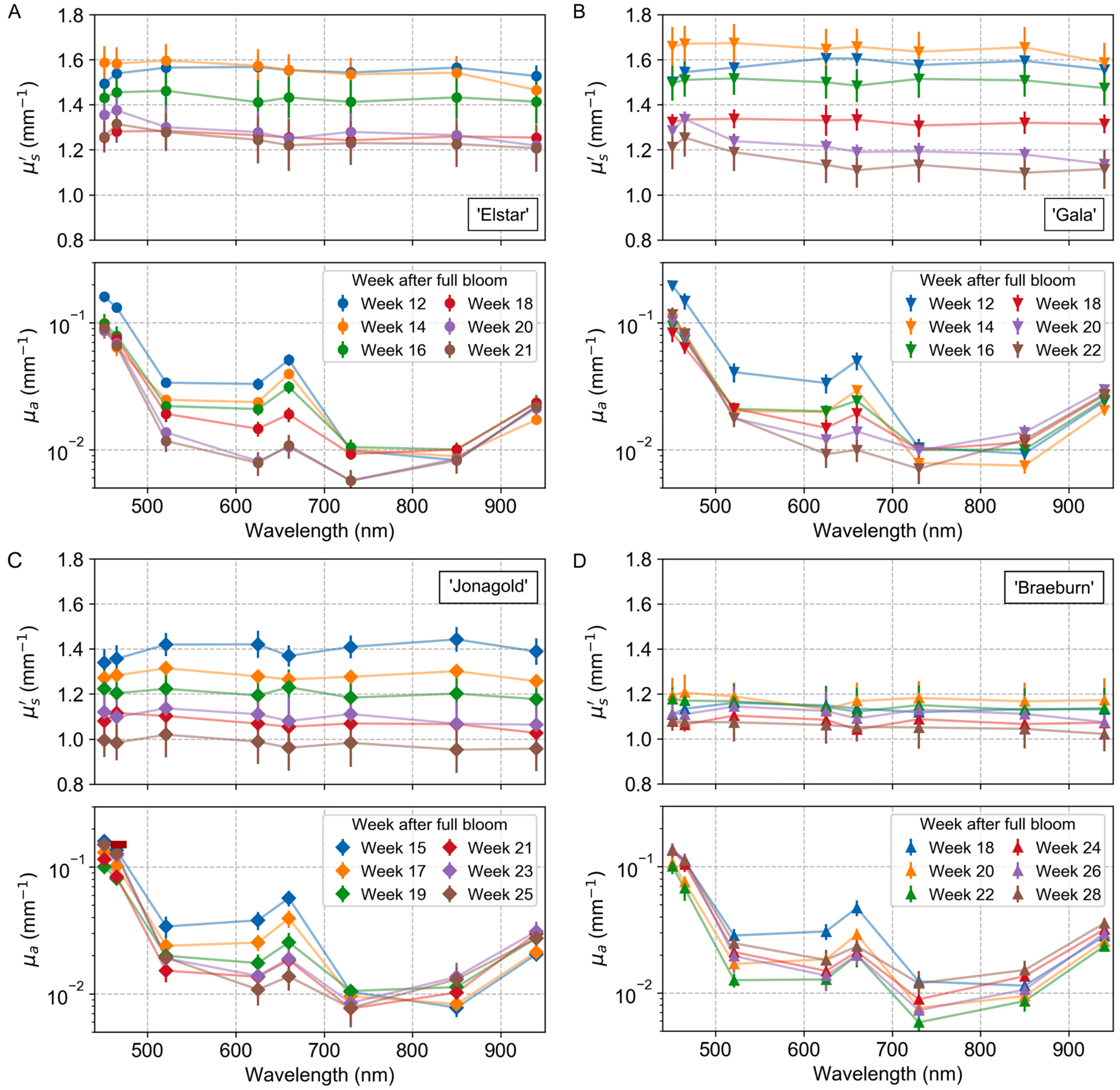

Fig. 10. Temporal evolution of spectrally resolved μ_s' and μ_a for the cortex of (A) 'Elstar', (B) 'Gala', (C) 'Jonagold', and (D) 'Braeburn'. The respective harvest date was determined by the Streif index at week 18 ('Elstar'), week 19 ('Gala'), week 22 ('Jonagold'), and week 25 ('Braeburn') after full bloom. Error bars indicate the resulting standard deviations for a weekly sample set of six apples with two measurements each.

show major difference in comparison for all four cultivars. The highest μ_a is at 447 nm, followed by two maxima at 656 nm and 945 nm, which can be assigned to carotenoids, chlorophyll *b*, and water, respectively. The most significant temporal changes occur at 619 nm and 656 nm and are therefore related to the general decline of chlorophylls during maturation.

In summary, the results show the temporal development of the optical properties, which are directly related to physiological processes - for example, the buildup and degradation of important plant pigments can be traced on the basis of the measurement results. In addition, significant cultivar-dependent differences were demonstrated for structural properties over a very long period of fruit development. In particular, with respect to chlorophyll decrease, researchers have frequently shown similar results for intact apple (Zude-Sasse et al., 2002; Merzlyak et al., 2003; McGlone et al., 2002), with the skin typically contributing by far the largest proportion of total chlorophyll content. With respect to the cortex, Van Beers et al. (2017) reported a decrease in μ_a at 680 nm from 0.06 mm^{-1} to 0.02 mm^{-1} based on integrating sphere measurements, which was attributed to chlorophyll *a* degradation. When comparing the results with our μ_a at 656 nm, it must be taken into account that they examined a deeper layer of the cortex, with consequently lower chlorophyll content. Also, during this study, the absorption peak of chlorophyll *a* at 680 nm could not be resolved due to the fixed wavelengths. However, a relative decrease of μ_a by a factor of 3 was found to be consistent for chlorophyll *a* and chlorophyll *b* considering both studies. This seems to confirm the observation of Merzlyak et al. (2003), who reported a constant ratio of chlorophyll *a* and chlorophyll *b* absorption for several cultivars. Ampomah-Dwamena et al. (2012) also found a general decrease in chlorophyll *a* and chlorophyll *b* concentrations in the cortex, while the ratio of initial and final concentrations depended strongly on the particular apple genotype. Regarding the temporal evolution of carotenoids, Ampomah-Dwamena et al. (2012) reported a decrease in their concentration in the cortex during maturation, followed by an increase during ripening. This was confirmed by the results for all cultivars in our study, except for ‘Elstar’. One explanation for this effect could be the involvement of several carotenoid compounds with similar absorption profiles. In particular, Ampomah-Dwamena et al. (2012) reported a high lutein content in the cortex of ‘Royal Gala’ at early fruit stages, which then decreased during maturation, followed by an accumulation of violaxanthin and neoxanthin during ripening. However, the predominant compounds and their proportions differed to a large extent in the different apple genotypes studied. The higher μ_a at 447 nm compared to 656 nm further indicates a predominant influence of carotenoids in apple cortex compared to chlorophyll, which is in agreement with Delgado-Pelayo et al. (2014). Lastly, the increase of μ_a at 945 nm remains to be discussed, which is probably related to the water content of the tissue. In this context, the water-containing vacuoles play an important role, as they can occupy up to 90 % of the cell volume in ripe apples and also have a considerable sugar content (Yamaki and Ino, 1992; Shiratake and Martinoia, 2007). The influence of different types of sugars on water absorption was studied, for example, by Giangiacomo (2006) using NIR spectroscopy. A significant increase in water absorption at 1928 nm is reported, most likely due to the increase in H-bonds and the ”structure breaking effect” when sugar molecules are added. It is likely that this effect could also be responsible for the increase in μ_a at 945 nm observed in this work. A similar interpretation can be made of the results of Wei et al. (2020), who recently reported a high correlation between μ_a at a wavelength of 980 nm and sucrose content, measured with an integrating sphere on stored ‘Fuji’ apples.

In contrast to the absorption properties, the temporal evolution of μ_s' of apple tissue during maturation has been investigated in only a few studies. Van Beers et al. (2017) reported a decrease from 1.3 mm^{-1} to 0.9 mm^{-1} for ‘Braeburn’ and two other cultivars based on integrating sphere measurements at a wavelength of 850 nm, but no characteristic differences were observed when comparing between different cultivars. For ‘Elstar’ apples, Seifert et al. (2015) demonstrated a decrease from 1.80 mm^{-1} to 1.55 mm^{-1} with time-resolved measurements at a wavelength of 850 nm. They mentioned a low dependence of μ_s' on wavelength and thus a flat spectral curve, which is in agreement with our findings. Other researchers focused on the study of μ_s' during storage, for example, Cen et al. (2013) noted a significant decrease during 30 d storage at 20 °C and Wei et al. (2020) during 150 d at, both, 0 °C and 20 °C. In contrast to our results during maturation, other researchers observed a significant increase in μ_s' during storage and fruit softening, as recently reported by Vanoli et al. (2020) or Rowe et al. (2014). Overall, the temporal evolution of μ_s' under defined conditions during maturation and storage shows reproducible results, but cannot in all cases be clearly attributed to specific components or structural properties of the apple tissue. Rather, it must be assumed that it is influenced by many parameters simultaneously and to varying degrees, as will be examined in more detail in Part 2 of this paper using Mie’s theory.

4. Conclusions

Based on SFDI measurements, high-resolution μ_s', μ_a, and r_s maps revealed considerable heterogeneity in the absorption and scattering properties of different types of apple tissue during maturation. Morphological features could be clearly visualized by their optical properties, e.g. the core line and vascular bundles cause local decreases in μ_s'. In contrast, μ_a maps at 656 nm and 945 nm indicate an overall homogeneous distribution of the main absorbers chlorophyll *b* and water, with characteristic increases in the cortex tissue under the skin, near vascular bundles, and near the core. There was a general tendency for μ_s' to increase from the core toward the skin by up to 30 %. This appears to be closely related to the radial-dependent properties of the intercellular space. Tissue with a high starch content has about 60 % higher μ_s' compared to tissue with low starch content. However, increases in μ_s' could not be fully attributed to the starch granules, although their size, concentration, and refractive index suggest it. The temporal decrease in μ_s' during maturation was up to 35 %, depending on the cultivar and also appeared to be related to changes in intercellular space and starch content. Lastly, the temporal evolution of μ_a during maturation indicated a decrease in chlorophyll *b* content at 656 nm and a sharp increase in carotenoid content at 447 nm just before ripening. However, the important question why μ_s' can increase during apple storage remains unresolved. Additional experimental approaches using micro-CT or phase contrast measurements may provide answers. Further theoretical considerations of the specific scattering components of apple tissue based on Mie’s theory are the subject of Part 2 of this study.

Credit author statement

Stefan A. Lohner: Conceptualization, Methodology, Investigation, Data Curation, Formal analysis, Validation, Writing – Original Draft, Writing – Review & Editing.

Konni Biegert: Conceptualization, Investigation, Project administration, Resources, Data Curation, Formal analysis, Writing – Original Draft, Writing – Review & Editing.

Steffen Nothelfer: Investigation, Software, Validation, Writing – Review & Editing.

Ansgar Hohmann: Investigation, Project administration, Writing – Review & Editing.

Roy McCormick: Investigation, Resources, Formal analysis, Writing – Review & Editing.

Alwin Kienle: Supervision, Writing – Review & Editing.

Conflict of interest

The authors declare no conflict of interest.

Acknowledgements

This research was funded in part by ‘Zentrales Innovationsprogramm Mittelstand’ (ZIM) of the ‘Bundesministerium für Wirtschaft und Energie’ (BMWi).

References

Ampomah-Dwamena, C., Dejnoprat, S., Lewis, D., Sutherland, P., Volz, R.K., Allan, A.C., 2012. Metabolic and gene expression analysis of apple (Malus × domestica) carotenogenesis. J. Exp. Bot. 63 (12), 4497–4511. https://doi.org/10.1093/jxb/ers134.

Anderson, E.R., Cuccia, D.J., Durkin, A.J., 2007. Detection of bruises on golden delicious apples using spatial- frequency-domain imaging. In: Vo-Dinh, T., Grundfest, W.S., Benaron, D.A., Cohn, G.E., Raghavachari, R. (Eds.), Adv. Biomed. Clin. Diagnostic Syst. V, p. 64301O. https://doi.org/10.1117/12.717608.

Bergmann, F., Foschum, F., Zuber, R., Kienle, A., 2020. Precise determination of the optical properties of turbid media using an optimized integrating sphere and advanced Monte Carlo simulations. Part 2: experiments. Appl. Opt. 59 (10), 3216. https://doi.org/10.1364/AO.385939.

Bodenschatz, N., Brandes, A., Liemert, A., Kienle, A., 2014. Sources of errors in spatial frequency domain imaging of scattering media. J. Biomed. Opt. 19 (7), 071405. https://doi.org/10.1117/1.JBO.19.7.071405.

Bodenschatz, N., Krauter, P., Nothelfer, S., Foschum, F., Bergmann, F., Liemert, A., Kienle, A., 2015. Detecting structural information of scatterers using spatial frequency domain imaging. J. Biomed. Opt. 20 (11), 116006. https://doi.org/10.1117/1.JBO.20.11.116006.

Borch, J., Sarko, A., Marchessault, R., 1972. Light scattering analysis of starch granules. J. Colloid Interface Sci. 41 (3), 574–587. https://doi.org/10.1016/0021-9797(72)90379-7.

Brookfield, P., Murphy, P., Harker, R., MacRae, E., 1997. Starch degradation and starch pattern indices; interpretation and relationship to maturity. Postharvest Biol. Technol. 11 (1), 23–30. https://doi.org/10.1016/S0925-5214(97)01416-6.

Carrín, M.E., Ceci, L.N., Lozano, J.E., 2004. Characterization of starch in apple juice and its degradation by amylases. Food Chem. 87 (2), 173–178. https://doi.org/10.1016/j.foodchem.2003.10.032.

Cen, H., Lu, R., Mendoza, F., Beaudry, R.M., 2013. Relationship of the optical absorption and scattering properties with mechanical and structural properties of apple tissue. Postharvest Biol. Technol. 85, 30–38. https://doi.org/10.1016/j.postharvbio.2013.04.014.

Chen, X., Xi, J., Jin, Y., Sun, J., 2009. Accurate calibration for a camera-projector measurement system based on structured light projection. Opt. Lasers Eng. 47 (3-4), 310–319. https://doi.org/10.1016/j.optlaseng.2007.12.001.

Cubeddu, R., D’Andrea, C., Pifferi, A., Taroni, P., Torricelli, A., Valentini, G., Ruiz-Altisent, M., Valero, C., Ortiz, C., Dover, C., Johnson, D., 2001. Time-resolved reflectance spectroscopy applied to the nondestructive monitoring of the internal optical properties in apples. Appl. Spectrosc. 55 (10), 1368–1374. https://doi.org/10.1366/0003702011953496.

Cuccia, D.J., Bevilacqua, F., Durkin, A.J., Ayers, F.R., Tromberg, B.J., 2009. Quantitation and mapping of tissue optical properties using modulated imaging. J. Biomed. Opt. 14 (2), 024012. https://doi.org/10.1117/1.3088140.

Delgado-Pelayo, R., Gallardo-Guerrero, L., Hornero-Méndez, D., 2014. Chlorophyll and carotenoid pigments in the peel and flesh of commercial apple fruit varieties. Food Res. Int. 65 (PB), 272–281. https://doi.org/10.1016/j.foodres.2014.03.025.

Doerflinger, F.C., Miller, W.B., Nock, J.F., Watkins, C.B., 2015. Variations in zonal fruit starch concentrations of apples - a developmental phenomenon or an indication of ripening? Hortic. Res. 2 (1), 15047. https://doi.org/10.1038/hortres.2015.47.

Dražeta, L., Lang, A., Hall, A.J., Volz, R.K., Jameson, P.E., 2004. Air volume measurement of ’Braeburn’ apple fruit. J. Exp. Bot. 55 (399), 1061–1069. https://doi.org/10.1093/jxb/erh118.

Foschum, F., Bergmann, F., Kienle, A., 2020. Precise determination of the optical properties of turbid media using an optimized integrating sphere and advanced Monte Carlo simulations. Part 1: theory. Appl. Opt. 59 (10), 3203. https://doi.org/10.1364/AO.386011.

Gaweda, M., Ben, J., 2010. Dynamics of changes of starch and its components in fruitlets and maturing ‘Jonagold’ and ‘Gala Must’ apples. J. Fruit Ornam. Plant Res. 18 (2), 109–119.

Giangiacomo, R., 2006. Study of water-sugar interactions at increasing sugar concentration by NIR spectroscopy. Food Chem. 96 (3), 371–379. https://doi.org/10.1016/j.foodchem.2005.02.051.

Gioux, S., Mazhar, A., Cuccia, D.J., 2019. Spatial frequency domain imaging in 2019: principles, applications, and perspectives. J. Biomed. Opt. 24 (07), 1. https://doi.org/10.1117/1.JBO.24.7.071613.

Hale, G.M., Querry, M.R., 1973. Optical constants of water in the 200-nm to 200-μm wavelength region. Appl. Opt. 12 (3), 555. https://doi.org/10.1364/AO.12.000555.

Herremans, E., Verboven, P., Bongaers, E., Estrade, P., Verlinden, B.E., Wevers, M., Hertog, M.L., Nicolaï, B.M., 2013. Characterisation of ’Braeburn’ browning disorder by means of X-ray micro-CT. Postharvest Biol. Technol. 75, 114–124. https://doi.org/10.1016/j.postharvbio.2012.08.008.

Herremans, E., Verboven, P., Hertog, M.L.A.T.M., Cantre, D., van Dael, M., De Schryver, T., Van Hoorebeke, L., Nicolaï, B.M., 2015. Spatial development of transport structures in apple (Malus × domestica Borkh.) fruit. Front. Plant Sci. 6, 1–14. https://doi.org/10.3389/fpls.2015.00679.

Hu, D., Fu, X., He, X., Ying, Y., 2016. Noncontact and wide-field characterization of the absorption and scattering properties of apple fruit using spatial-frequency domain imaging. Sci. Rep. 6 (1), 37920. https://doi.org/10.1038/srep37920.

Hu, D., Fu, X.P., Wang, A.C., Ying, Y.B., 2015. Measurement methods for optical absorption and scattering properties of fruits and vegetables. Trans. ASABE 58 (5), 1387–1401. https://doi.org/10.13031/trans.58.11103.

Hu, D., Lu, R., Ying, Y., 2020. Spatial-frequency domain imaging coupled with frequency optimization for estimating optical properties of two-layered food and agricultural products. J. Food Eng. 277, 109909. https://doi.org/10.1016/j.jfoodeng.2020.109909.

Hu, D., Lu, R., Ying, Y., Fu, X., 2019. A stepwise method for estimating optical properties of two-layer turbid media from spatial-frequency domain reflectance. Opt. Express 27 (2), 1124. https://doi.org/10.1364/OE.27.001124.

Janssen, S., Verboven, P., Nugraha, B., Wang, Z., Boone, M., Josipovic, I., Nicolaï, B.M., 2020. 3D pore structure analysis of intact ’Braeburn’ apples using X-ray micro-CT. Postharvest Biol. Technol. 159, 111014. https://doi.org/10.1016/j.postharvbio.2019.111014.

Lammertyn, J., Peirs, A., De Baerdemaeker, J., Nicolaï, B., 2000. Light penetration properties of NIR radiation in fruit with respect to non-destructive quality assessment. Postharvest Biol. Technol. 18 (2), 121–132. https://doi.org/10.1016/S0925-5214(99)00071-X.

Liemert, A., Kienle, A., 2012a. Analytical approach for solving the radiative transfer equation in two-dimensional layered media. J. Quant. Spectrosc. Radiat. Transf. 113 (7), 559–564. https://doi.org/10.1016/j.jqsrt.2012.01.013.

Liemert, A., Kienle, A., 2012b. Spatially modulated light source obliquely incident on a semi-infinite scattering medium. Opt. Lett. 37 (19), 4158. https://doi.org/10.1364/OL.37.004158.

Liemert, A., Kienle, A., 2013. Exact and efficient solution of the radiative transport equation for the semi-infinite medium. Sci. Rep. 3 (1), 2018. https://doi.org/10.1038/srep02018.

Lu, R., Van Beers, R., Saeys, W., Li, C., Cen, H., 2020. Measurement of optical properties of fruits and vegetables: A review. Postharvest Biol. Technol. 159, 111003. https://doi.org/10.1016/j.postharvbio.2019.111003.

Lu, Y., Lu, R., 2019. Structured-illumination reflectance imaging for the detection of defects in fruit: analysis of resolution, contrast and depth-resolving features. Biosyst. Eng. 180, 1–15. https://doi.org/10.1016/j.biosystemseng.2019.01.014.

MacDaniels, L.H., 1940. The morphology of the apple and other pome fruits. Mem. Cornell Agric. Exp. Stn. 230, 32 pp.

McCormick, R., Biegert, K., 2019. Monitoring the growth and maturation of apple fruit on the tree with handheld Vis/NIR devices. NIR News 30 (1), 12–15. https://doi.org/10.1177/0960336018814147.

McGlone, V., Jordan, R.B., Martinsen, P.J., 2002. Vis/NIR estimation at harvest of pre- and post-storage quality indices for ’Royal Gala’ apple. Postharvest Biol. Technol. 25 (2), 135–144. https://doi.org/10.1016/S0925-5214(01)00180-6.

Merzlyak, M.N., Solovchenko, A.E., 2002. Photostability of pigments in ripening apple fruit: a possible photoprotective role of carotenoids during plant senescence. Plant Sci. 163 (4), 881–888. https://doi.org/10.1016/S0168-9452(02)00241-8.

Merzlyak, M.N., Solovchenko, A.E., Gitelson, A.A., 2003. Reflectance spectral features and non-destructive estimation of chlorophyll, carotenoid and anthocyanin content in apple fruit. Postharvest Biol. Technol. 27 (2), 197–211. https://doi.org/10.1016/S0925-5214(02)00066-2.

Nguyen Do Trong, N., Erkinbaev, C., Tsuta, M., De Baerdemaeker, J., Nicolaï, B., Saeys, W., 2014. Spatially resolved diffuse reflectance in the visible and near-infrared wavelength range for non-destructive quality assessment of ’Braeburn’ apples. Postharvest Biol. Technol. 91, 39–48. https://doi.org/10.1016/j.postharvbio.2013.12.004.

Nothelfer, S., Bergmann, F., Liemert, A., Reitzle, D., Kienle, A., 2018. Spatial frequency domain imaging using an analytical model for separation of surface and volume scattering. J. Biomed. Opt. 24 (07), 1. https://doi.org/10.1117/1.JBO.24.7.071604.

Oates, C.G., 1997. Towards an understanding of starch granule structure and hydrolysis. Trends Food Sci. Technol. 8 (11), 375–382. https://doi.org/10.1016/S0924-2244(97)01090-X.

Qing, Z., Ji, B., Zude, M., 2008. Non-destructive analyses of apple quality parameters by means of laser-induced light backscattering imaging. Postharvest Biol. Technol. 48 (2), 215–222. https://doi.org/10.1016/j.postharvbio.2007.10.004.

Rizzolo, A., Vanoli, M., Bianchi, G., Zanella, A., Grassi, M., Torricelli, A., Spinelli, L., 2014. Relationship between texture sensory profiles and optical properties measured by time-resolved reflectance spectroscopy during post-storage shelf life of ’Braeburn’ apples. J. Hortic. Res. 22 (1), 113–121. https://doi.org/10.2478/johr-2014-0014.

Rizzolo, A., Vanoli, M., Spinelli, L., Torricelli, A., 2010. Sensory characteristics, quality and optical properties measured by time-resolved reflectance spectroscopy in stored apples. Postharvest Biol. Technol. 58 (1), 1–12. https://doi.org/10.1016/j.postharvbio.2010.05.003.

Rowe, P.I., Künnemeyer, R., McGlone, A., Talele, S., Martinsen, P., Seelye, R., 2014. Relationship between tissue firmness and optical properties of ’Royal Gala’ apples from 400 to 1050nm. Postharvest Biol. Technol. 94, 89–96. https://doi.org/10.1016/j.postharvbio.2014.03.007.

Saeys, W., Velazco-Roa, M.A., Thennadil, S.N., Ramon, H., Nicolaï, B.M., 2008. Optical properties of apple skin and flesh in the wavelength range from 350 to 2200 nm. Appl. Opt. 47 (7), 908. https://doi.org/10.1364/AO.47.000908.

Sánchez, N.H., Lurol, S., Roger, J.M., Bellon-Maurel, V., 2003. Robustness of models based on NIR spectra for sugar content prediction in apples. J. Near Infrared Spectrosc. 11 (2), 97–107. https://doi.org/10.1255/jnirs.358.

Seifert, B., Zude, M., Spinelli, L., Torricelli, A., 2015. Optical properties of developing pip and stone fruit reveal underlying structural changes. Physiol. Plant. 153 (2), 327–336. https://doi.org/10.1111/ppl.12232.

Shiratake, K., Martinoia, E., 2007. Transporters in fruit vacuoles. Plant Biotechnol. 24 (1), 127–133. https://doi.org/10.5511/plantbiotechnology.24.127.

Stevenson, D., Domoto, P., Jane, J., 2006. Structures and functional properties of apple (Malus domestica Borkh) fruit starch. Carbohydr. Polym. 63 (3), 432–441. https://doi.org/10.1016/j.carbpol.2005.10.009.

Streif, J., 1996. Optimum harvest date for different apple cultivars in the Bodensee area. In: de Jager, A., Johnson, D., E.H (Eds.), COST 94. postharvest Treat. fruit Veg. Determ. Predict. Optim. Harvest date apples pears, pp. 15–20.

Sun, J., Künnemeyer, R., McGlone, A., Rowe, P., 2016. Multispectral scattering imaging and NIR interactance for apple firmness predictions. Postharvest Biol. Technol. 119, 58–68. https://doi.org/10.1016/j.postharvbio.2016.04.019.

Van Beers, R., Aernouts, B., León Gutiérrez, L., Erkinbaev, C., Rutten, K., Schenk, A., Nicolaï, B., Saeys, W., 2015. Optimal illumination-detection distance and detector size for predicting Braeburn apple maturity from Vis/NIR laser reflectance measurements. Food Bioprocess Technol. 8 (10), 2123–2136. https://doi.org/10.1007/s11947-015-1562-4.

Van Beers, R., Aernouts, B., Watté, R., Schenk, A., Nicolaï, B., Saeys, W., 2017. Effect of maturation on the bulk optical properties of apple skin and cortex in the 500-1850 nm wavelength range. J. Food Eng. 214, 79–89. https://doi.org/10.1016/j.jfoodeng.2017.06.013.

Vanoli, M., Van Beers, R., Sadar, N., Rizzolo, A., Buccheri, M., Grassi, M., Lovati, F., Nicolaï, B., Aernouts, B., Watté, R., Torricelli, A., Spinelli, L., Saeys, W., Zanella, A., 2020. Time- and spatially-resolved spectroscopy to determine the bulk optical properties of 'Braeburn' apples after ripening in shelf life. Postharvest Biol. Technol. 168, 111233. https://doi.org/10.1016/j.postharvbio.2020.111233.

Vanoli, M., Zerbini, P.E., Spinelli, L., Torricelli, A., Rizzolo, A., 2009. Polyuronide content and correlation to optical properties measured by time-resolved reflectance spectroscopy in 'Jonagored' apples stored in normal and controlled atmosphere. Food Chem. 115 (4), 1450–1457. https://doi.org/10.1016/j.foodchem.2009.01.081.

Verboven, P., Kerckhofs, G., Mebatsion, H.K., Ho, Q.T., Temst, K., Wevers, M., Cloetens, P., Nicolaï, B.M., 2008. Three-dimensional gas exchange pathways in pome fruit characterized by synchrotron X-Ray computed tomography. Plant Physiol. 147 (2), 518–527. https://doi.org/10.1104/pp.108.118935.

Wang, Z., Van Beers, R., Aernouts, B., Watté, R., Verboven, P., Nicolaï, B., Saeys, W., 2020. Microstructure affects light scattering in apples. Postharvest Biol. Technol. 159, 110996. https://doi.org/10.1016/j.postharvbio.2019.110996.

Wei, K., Ma, C., Sun, K., Liu, Q., Zhao, N., Sun, Y., Tu, K., Pan, L., 2020. Relationship between optical properties and soluble sugar contents of apple flesh during storage. Postharvest Biol. Technol. 159 (1), 111021. https://doi.org/10.1016/j.postharvbio.2019.111021.

Wolf, M., Ruggles, V.J., MacMasters, M.M., 1962. Refractive indices of wheat starch granules at various moisture levels determined with an interference microscope. Biochim. Biophys. Acta 57 (1), 135–142. https://doi.org/10.1016/0006-3002(62)91089-2.

Yamaki, S., Ino, M., 1992. Alteration of cellular compartmentation and membrane permeability to sugars in immature and mature apple fruit. J. Am. Soc. Hortic. Sci. 117 (6), 951–954. https://doi.org/10.21273/JASHS.117.6.951.

Zhang, Z., 2000. A flexible new technique for camera calibration. IEEE Trans. Pattern Anal. Mach. Intell. 22 (11), 1330–1334. https://doi.org/10.1109/34.888718.

Zude, M., Herold, B., Roger, J.M., Bellon-Maurel, V., Landahl, S., 2006. Non-destructive tests on the prediction of apple fruit flesh firmness and soluble solids content on tree and in shelf life. J. Food Eng. 77 (2), 254–260. https://doi.org/10.1016/j.jfoodeng.2005.06.027.

Zude-Sasse, M., Truppel, I., Herold, B., 2002. An approach to non-destructive apple fruit chlorophyll determination. Postharvest Biol. Technol. 25 (2), 123–133. https://doi.org/10.1016/S0925-5214(01)00173-9.

Postharvest Biology and Technology 181 (2021) 111652

Contents lists available at ScienceDirect

Postharvest Biology and Technology

journal homepage: www.elsevier.com/locate/postharvbio

Determining the optical properties of apple tissue and their dependence on physiological and morphological characteristics during fruit maturation. Part 2: Mie's theory

Stefan A. Lohner [a,*], Konni Biegert [b], Steffen Nothelfer [a], Ansgar Hohmann [a], Roy McCormick [b], Alwin Kienle [a]

[a] *Institut für Lasertechnologien in der Medizin und Meßtechnik an der Universität Ulm, Helmholtzstr. 12, D-89081 Ulm, Germany*
[b] *Kompetenzzentrum Obstbau Bodensee, Schuhmacherhof 6, D-88213 Ravensburg, Germany*

ARTICLE INFO

Keywords:
Mie's theory
Scattering
Intercellular space
Starch degradation
Cell walls

ABSTRACT

Mie's theory was used to develop a theoretical model to describe light propagation in apple tissue based on its microstructural properties. Taking into account the size distributions and volume fractions of intercellular space and starch granules, which are known in detail from previous studies, the model predicted a decrease in the effective scattering coefficient μ_s' of about 30 % during maturation. For the lateral change of μ_s' within a ripe apple, the model predicted an increase up to 35 % from core to skin. In both cases, the relative changes agree well with the experimental results obtained with spatial frequency domain imaging (SFDI) and an integrating sphere setup. Based on the model, at least 70 % of total μ_s' is attributable to intercellular space, which accordingly plays a dominant role in the temporal and lateral change of scattering. Using an extended Mie model for layered particles assuming a dense cell structure, a negligible effect on μ_s' was observed for the cell wall. However, for cells separated from the surrounding tissue by a narrow air gap (e.g. dissolution of the middle lamella), μ_s' was 20 % higher than for cells theoretically isolated in air. Lastly, it was shown that an increase in soluble solids content (SSC) during maturation by up to 15 % and the associated higher refractive index in the cells led to an increase in μ_s' by about 3–5 % compared to the case without considering SSC. Overall, the application of Mie's theory proved suitable to investigate the influence of different morphological structures on light scattering in apple tissue.

1. Introduction

Despite numerous studies focused on determining the optical properties of agricultural products, the exact influence of individual morphological components at the microscopic level is still largely unknown. However, a deeper understanding of light propagation in different types of biological tissue is crucial for the future development of innovative optical measurement methods and applications. In recent years, this has led to an increase in using physics-based models for data analysis. The radiative transfer equation (RTE) provides a comprehensive theoretical approach to describe the propagation of light in scattering media and to obtain quantitative and thus comparable parameters. Besides the absorption coefficient μ_a, the scattering coefficient μ_s, and the anisotropy factor g derived from the phase function $P(\theta)$, the effective scattering coefficient defined according to $\mu_s' = (1-g)\mu_s$ is an important quantity to characterize the optical properties of fruit. In general, μ_a can be related to the chemical and μ_s' to the structural properties of the tissue. Various analytical solutions of the RTE can be found for simple and regular geometries. For example, a multilayer semi-infinite model allows, under certain conditions, the fast and accurate determination of the optical properties by solving the inverse problem based on measured data (Liemert and Kienle, 2012b, 2013; Liemert et al., 2017). The diffusion equation is also frequently used as an approximation of the RTE, but its validity is much more limited (Farrell et al., 1992). For complex geometries, numerical methods such as the Monte Carlo method are used to solve the RTE. The optical properties are then determined by a statistical simulation of scattering and absorption events for numerous light paths in the scattering medium. However, this requires a detailed knowledge of the structure and geometry of the individual components and their refractive indices, from which the scattering coefficient, the phase function, and the absorption coefficient can be calculated. In the case of biological tissue, these usually have to be determined empirically. If the

---

[*] Corresponding author.
E-mail address: stefan.lohner@ilm-ulm.de (S.A. Lohner).

https://doi.org/10.1016/j.postharvbio.2021.111652
Received 1 April 2021; Received in revised form 6 July 2021; Accepted 8 July 2021

scattering medium can be described as a suspension of regular spheres or cylinders in a surrounding medium, Mie type theories are applicable. As an analytical solution of the fundamental Maxwell equations, they provide exact results for particles with arbitrary size-to-wavelength ratios and refractive indices. This also explains their great importance and widespread use in various fields of application, e.g. atmospheric research, material sciences, graphics, and biology (Jackèl and Walter, 1997; Frisvad et al., 2007; Ulicný, 1992). However, the extent to which Mie's solution is applicable to model a particular type of scattering medium requires a profound knowledge of its microstructural properties. Extensive information is available for apple fruit (*Malus domestica* Borkh.), whose morphological and histological properties have recently received much attention through measurement techniques such as scanning electron microscopy (SEM) or X-ray computed microtomography (micro-CT) (Lapsley et al., 1992; Herremans et al., 2013; Janssen et al., 2020). In this context, experimental findings indicate that the structure of apple tissue is mainly characterized by the cell organelles, cell walls, and intercellular space. However, the question remains open to what extent these individual microscopic components interact with light and thus influence the optical properties of apple tissue during maturation and storage.

From an experimental point of view, extensive studies on the optical properties of apple tissue are available. Using various time-, spatially-, and spatial frequency-resolved techniques, a characteristic decrease in μ_s' was observed during maturation (Van Beers et al., 2017; Seifert et al., 2015; Lohner et al., 2021), while an increase in μ_s' was partially observed during storage (Vanoli et al., 2020; Rowe et al., 2014). Spatially resolved scattering property studies showed a high degree of heterogeneity with a tendency for μ_s' to increase from the core to the skin (Lohner et al., 2021). As part of a correlation analysis, Wang et al. (2020) suggested that the intercellular space has a major influence on the scattering properties, while the shape, size, and components of the individual cells play a minor role. Additional influences of the starch granules or the cell walls are often discussed and first experimental evidence has been provided (Lohner et al., 2021), but a doubtless separation of the different effects has not yet been achieved. On the theoretical side, there have been few attempts to directly simulate the optical properties of apples. Basic studies based on the Monte Carlo method investigated for example, the penetration depth of light at different wavelengths or the influence of the skin to determine the optical properties of apple tissue (Vaudelle and L'Huillier, 2015; Askoura et al., 2015; Qin and Lu, 2009). Mie's solution has mostly been used to roughly characterize the average size of the involved scatterers by assuming a power-law function for the spectral dependence of μ_s' (Seifert et al., 2015; Vanoli et al., 2011; Saeys et al., 2010).

The aim of this work was to develop a polydisperse Mie model to describe light scattering in apple tissue with realistic assumptions for its microstructure. Using the size distribution and volume content of air pores and starch granules known from literature, the associated temporal and lateral change of μ_s' can be simulated and compared with results from spatial frequency domain imaging (SFDI) and an integrating sphere setup. Another objective was to estimate how the change in the relative refractive index, e.g. by increasing soluble solids content (SSC) during maturation, affects scattering. Lastly, the extension of Mie's theory to layered particles should provide an approach to investigate the influence of cell walls on the scattering properties for different cell configurations. In particular, to clarify whether changes in cell walls may be associated with an increase in μ_s' during storage.

2. Theory

2.1. Mie solution for spherical particles

The Mie solution to Maxwell's equations (also called Lorenz–Mie theory) describes the electromagnetic scattering by single homogeneous and isotropic spheres in a surrounding medium. The results are characterized by the size parameter $x = \pi d/\lambda$, which is the ratio between sphere diameter d and light wavelength λ, and the ratio m between the complex refractive index n_{sph} of the sphere and the real refractive index n_{med} of the surrounding non-absorbing medium

$$m = \frac{n_{\text{sph}}}{n_{\text{med}}}. \tag{1}$$

In addition to this basic model, numerous extensions have been published which consider, e.g. an absorbing surrounding or layered spheres (Mundy et al., 1974; Kai et al., 1994). Advantageously, numerous fast and efficient implementations are available for these extended solutions, which have been used in the context of this work (Bohren and Huffman, 1983; van de Hulst, 1957; Wiscombe, 1980; Schäfer et al., 2012; Schäfer, 2016). Most often, a vector harmonic approach based on spherical Bessel functions is used to compute the far-field solution of a given configuration, providing, e.g. the scattering cross section C_{sca}, the absorption cross section C_{abs}, and the extinction cross section C_{ext}, which are linked via

$$C_{\text{ext}} = C_{\text{sca}} + C_{\text{abs}}. \tag{2}$$

Mie's solution further provides the phase function $P(\theta, \phi)$, which describes the dependence of the scattered light intensity in spherical coordinates, and the anisotropy factor g, which takes on values between -1 (backward scattering) and $+1$ (forward scattering) (Bohren and Huffman, 1983). For rotationally symmetric particles, the phase function $P(\theta)$ depends only on the scattering angle θ and is normalized so that

$$\int_0^\pi P(\theta)\sin(\theta)d\theta = 1. \tag{3}$$

If a medium consists of several spheres of the same type, the scattering coefficient μ_s and the absorption coefficient μ_a can be calculated by scaling with respect to their particle density ρ_N (particles per unit volume) as

$$\mu_{s/a} = \rho_N C_{\text{sca/abs}}. \tag{4}$$

The scattering coefficient and the anisotropy factor can be combined to yield the effective scattering coefficient $\mu_s' = \mu_s\,(1-g)$.

2.1.1. Polydisperse particles

Real systems usually consist of particles with different diameters, which are subject to a characteristic size distribution. In the case of a normal distribution, it can be defined by specifying a mean particle size μ and the standard deviation σ. In naturally formed systems, the log-normal distribution

$$f_N(r) = \frac{1}{r\,s\sqrt{2\pi}}\ \exp\left[\frac{-(\ln r - m)^2}{2s^2}\right], \quad \text{for} \quad r > 0, \tag{5}$$

with particle radius r and

$$m = \ln\left(\frac{\mu^2}{\sqrt{\mu^2+\sigma^2}}\right) \quad \text{and} \quad s = \sqrt{\ln\left(1+\frac{\sigma^2}{\mu^2}\right)}, \tag{6}$$

plays a particularly important role for describing the size distribution of biological tissue such as cells or colloids (Koch, 1966; Hergert and Wriedt, 2012). Since Mie's solution can only be applied for discrete particle sizes, a discretization of the size distribution is necessary. The distribution is divided into i intervals with a mean radius r_i and the distribution function $f_N(r)$ is normalized such that

$$f_v = \sum_i \frac{4}{3}\pi r_i^3\ f_N(r_i), \tag{7}$$

where f_v is the volume fraction and $f_N(r_i)$ is the respective particle density. After calculating Mie's solution for all particle sizes r_i, the optical properties of the polydisperse system for a normalized phase function P(θ, r_i) consequently result as (Modest, 2003)

$$\mu_s = \sum_i C_{\text{sca}}(r_i)\, f_N(r_i), \quad \mu_a = \sum_i C_{\text{abs}}(r_i)\, f_N(r_i), \tag{8}$$

$$P(\theta) = \frac{\sum_i C_{\text{sca}}(r_i)\; P(\theta, r_i)\, f_N(r_i)}{\mu_s}, \tag{9}$$

$$g = \frac{\sum_i C_{\text{sca}}(r_i)\; g(r_i)\, f_N(r_i)}{\mu_s}. \tag{10}$$

The choice of a suitable discretization plays an important role since the number of size intervals influences, on the one hand, the accuracy, and on the other hand, the computation time, if a large wavelength range is examined (Aernouts et al., 2014). As a compromise, 200–400 size intervals were mostly considered for the following calculations.

2.1.2. *Mie model for biological tissue*

Due to its complex composition and structure, biological tissue cannot be regarded without restriction as a suspension of spherical particles in the sense of Mie's solution. In reality, for example, non-spherical particles, strong absorption of the surrounding medium or a high volume concentration of the particles cause considerable deviations compared to the theory. Nevertheless, Mie's theory is regularly used to solve the inverse problem based on experimental data, e.g. to determine the effective diameter or the size distribution of different cell types in human tissue (Wilson and Foster, 2005; Wang et al., 2005; Hammer et al., 1998). Forward calculations for the prediction of optical properties based on Mie simulation considering the microstructure of the investigated samples have also been successfully performed. In addition to Mie models for milk (Frisvad et al., 2007), seawater and sea ice (Zhang et al., 2007; Hamre et al., 2004), more complex models for human skin or other tissue types (Schmitt and Kumar, 1998; Bhandari et al., 2011; Wang et al., 2013) should be mentioned.

The deviations from the Mie model caused by a non-spherical shape of the particles or rough surfaces are particularly well studied in the field of atmospheric science. Using ice crystals as an example, Grenfell and Warren (1999) have shown that approximating cylinders, hexagons, or plates by spheres with an equivalent volume-to-surface ratio leads to very accurate results, with deviations usually below 5 % for the scattering and extinction coefficients, but larger deviations for the phase function. Similarly, for elliptical or Chebychev-shaped particles, the scattering and absorption cross sections can be approximated assuming a sphere in many cases, while the phase function can have large deviations in individual cases (Gronarz et al., 2017; Chýlek, 1977; Mugnai and Wiscombe, 1986). For high volume fractions and correspondingly densely packed particles, there is an overall decrease in μ_s due to the interaction of their near fields, which is referred to as dependent scattering. While this effect can occur for particles with small size parameters ($x \approx 1$) even at volume concentrations below 10 %, particles with large size parameters ($x \approx 100$) can often be considered independent at volume concentrations up to 70 % (Brewster and Tien, 1982).

From these results it follows that apple tissue can also be described in principle by Mie's theory. For air pores with large size parameters from 200 to 5000 and volume concentrations up to 25 %, mainly independent scattering can be expected. In general, Mie's theory approaches geometrical optics in this size range. Although the assumption of spherical air pores is a severe simplification, a sufficiently accurate description of the scattering properties can be expected if the correct volume or better volume–surface ratio is taken into account (Grenfell and Warren, 1999). In contrast, starch granules with size parameters below 100 are significantly smaller and have a spherical shape by nature. With volume fractions of maximum 3 %, mainly independent scattering can be expected here as well.

3. Materials and methods

3.1. *Spatial frequency domain imaging*

The spatially resolved optical properties of different apple samples were determined using a setup for SFDI, which has already been presented in detail in the first part of this work (Lohner et al., 2021). The setup provided sequential illumination at eight switchable wavelengths between 447 and 945 nm, each with a narrow bandwidth of approximately 10 nm. To prepare the apple samples, the skin and outer 3 mm of underlying tissue were removed with a sharp slicer. The underlying cortex tissue was carefully dried to avoid reflections from juice droplets and measured immediately, i.e. before oxidative browning occurred. During the measurement, a digital light projector (DLP LightCrafter 6500, Texas Instruments, USA) projected sinusoidal patterns with different spatial frequencies obliquely onto the sample, and the diffusely reflected light was measured with an sCMOS camera (Zyla 4.2 sCMOS, Andor, UK). By recording three phase-shifted patterns each at spatial frequencies between 0 and 0.5 mm^{-1}, the characteristic amplitude and phase modulation could be determined using demodulation algorithms. During post-processing, the raw data were corrected for location-dependent deviations in intensity or spatial frequency, which are characterized by a one-time calibration of the system. During evaluation, a light propagation model was fitted to the raw data based on an analytical solution of the RTE for semi-infinite geometries (Liemert and Kienle, 2012a, b, 2013). This provides the optical properties for each pixel, in particular μ_s', μ_a and optionally the surface scattering parameter r_s (Nothelfer et al., 2018), taking into account further parameters such as the refractive index or the anisotropy factor.

3.2. *Integrating sphere measurements*

As a further method for the measurement of the optical properties, an integrating sphere setup was used, which was recently designed and developed by Foschum et al. (2020) and Bergmann et al. (2020) in combination with an evaluation method based on Monte Carlo simulations. Essentially, it consists of a 3D-printed and barium sulfate-coated sphere with an inner diameter of 150 mm, a halogen light source and two spectrometers: one for the predominantly VIS from 200 to 1100 nm (Maya2000Pro, Ocean Optics, USA) and one for the NIR from 900 to 1700 nm (NIRQuest512-1.7, Ocean Optics, USA). A 100 W halogen lamp (Halostar Starlite, Osram, Germany) in combination with an open-frame power supply served as a light source. For sample preparation, the skin and outer coarse-pored layers of the apple were first removed and then a 2–3 mm thick slice of the cortex was cut using a vegetable slicer. Since the sample thickness is included in the evaluation, care was taken to ensure that the slices were as uniform as possible. To suppress surface effects, the samples were measured between two glass slides. The leaking juice filled the interface between the tissue and the glass, which prevented the formation of air inclusions and thus undesirable refractive index differences. To obtain better statistics, each sample was measured twice on one side in the direction of the integrating sphere and twice after turning the sample over. Based on the recorded reflectance and transmittance spectra, μ_s' and μ_a were determined for each measurement using a look-up table calculated by the Monte Carlo method, specifying the thickness, refractive index, and anisotropy factor. Finally, the arithmetic mean of the optical properties was calculated from the four measurements for each sample.

3.3. Apple samples

The apple samples examined for comparison purposes are identical to those presented in the first part of this paper (Lohner et al., 2021). They were collected from the research orchard of the Kompetenzzentrum Obstbau Bodensee (47°46′01.8″N 9°33′30.3″E) during the 2019 harvest season between July and November. In this work, the cultivar 'Jonagold' (Novajo) was studied in particular.

4. Results and discussion

4.1. Mie model for the temporal development of the scattering properties during maturation

During maturation, a number of physiological processes occur simultaneously which can influence the morphology and microstructure and thus also the scattering properties of apple tissue. In this context, the temporal development of the intercellular space and the build-up and degradation of starch granules are of particular importance. Several studies based on micro-CT measurements are available to investigate the intercellular space from a microscopic perspective. Specifically, Herremans et al. (2015) documented the temporal variation of average pore size and absolute porosity in 'Jonagold' apples over a period of 7–22 weeks after full bloom. For a quantitative description of the air pores size, they give a cumulative distribution of equivalent sphere diameters, which correspondingly describes the pores as spheres with the same volume. Since the distribution was explicitly given for only six weeks, it was interpolated for the remaining weeks and extrapolated for weeks 23 and 24. The size distributions shown in Fig. 1(A) for different weeks were determined by fitting a log-norm distribution to the cumulative distribution functions according to Eq. (5). The mean pore diameters increased from approximately 100 µm at week 7 to 410 µm at week 22 with corresponding standard deviations of 40 and 120 µm. For better comparability, the area under the curves was weighted to the corresponding volume fraction of the air pores, which indicates the porosity. It increased from 10 % to 26 % over the same period.

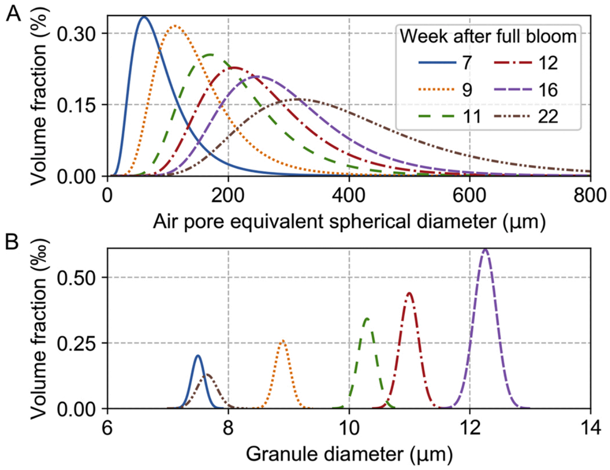

Fig. 1. Temporal variation of the size distribution for (A) the equivalent spherical diameter of air pores as reported by Herremans et al. (2015) and (B) the starch granules as reported by Ohmiya and Kakiuchi (1990) for 'Jonagold' apples during maturation. In both cases, a log-norm distribution was assumed based on the mean diameters and standard deviations reported in the literature. For better illustration, the areas under the curves were weighted to their respective volume fractions.

For the Mie model, the air pores with a refractive index of 1.0 were considered as scattering particles embedded in a homogeneous and highly aqueous environment. This assumption is based on the fact that, due to the strong cell-to-cell adhesion associated with the middle lamella, the cortex tissue represents a relatively densely packed cell structure, especially in the early stages of fruit development (Harker and Hallett, 1992; Allan-Wojtas et al., 2003). In addition, apples generally have comparatively few but large air pores (Rojas-Candelas et al., 2021; Mebatsion et al., 2009). Consequently, the model does not take into account refractive index differences of the surrounding medium, whose mean refractive index was estimated to be 1.37 (Choi et al., 2007).

Furthermore, the build-up and degradation of starch granules were considered. In Ohmiya and Kakiuchi (1990), absolute starch content and mean granule size were reported for 'Jonagold' apples over a period of 3–22 weeks after full bloom. Based on the reported mean granule diameters from four different weeks and the associated standard deviations, a log-normal distribution function was again assumed, as shown in Fig. 1(B). The mean particle diameters range from 7 to 12.5 µm with corresponding standard deviations between 0.1 and 0.2 µm. The starch volume fraction f_V was calculated from the known mass fractions f_M assuming a density of $\rho_T = 0.9\,\mathrm{g/cm^3}$ for apple tissue (Vincent, 1989) and $\rho_S = 1.5\,\mathrm{g/cm^3}$ for starch granules (Dengate et al., 1978) according to

$$f_V = \frac{f_W}{f_W + (1 - f_W)\frac{\rho_S}{\rho_T}}. \tag{11}$$

The area under the curves in Fig. 1(B) was weighted according to the corresponding starch volume fraction, which initially increases steadily to about 1.50 % (corresponding to a mass fraction of 2.48 %) until week 18 and then drops almost completely in the last weeks of maturation.

Since no reference values for the refractive index of starch granules are known specifically for apples, data from other starch-containing crops were used. For example, Wolf et al. (1962) report a refractive index of 1.53 for isolated wheat starch granules and Borch et al. (1972) report a refractive index between 1.50 and 1.54 for isolated tapioca starch granules. Therefore, the choice of an average refractive index of 1.52 for starch granules in apples seems reasonable. Since the starch granules are located inside the chromoplasts, the refractive index of the surrounding medium was assumed to be 1.37 in this case.

Fig. 2(A–C) shows the spectrally resolved μ_s calculated with the Mie model considering the intercellular space, the starch granules and the sum of both. In the case of the starch granules, a maximum of about 5 mm^{-1} is reached at week 18, while μ_s is nearly zero at week 24. Due to the small particle size dispersion, μ_s shows wavelength-dependent oscillations. For the intercellular space, a decrease from 7 to 2.5 mm^{-1} can be observed, especially in the first weeks, but it hardly changes after week 11. In this case, almost no spectral dependence is visible. Taking both components into account, μ_s decreases from about 10 to 2.5 mm^{-1} within less than 20 weeks. Fig. 2(D) shows the corresponding anisotropy factors. In the case of the air pores, the values range between 0.85 and 0.70, with a decrease observed with increasing maturity. In addition, the anisotropy factors tend to slightly increase with increasing wavelength. For the starch granules, the anisotropy factors range between 0.90 and 0.95, with no pronounced dependence on the wavelength. The resulting anisotropy factor from the sum of both components ranges from 0.9 at the beginning of maturation period to 0.8 at the end. Fig. 3(A) shows the resulting change in μ_s' during maturation evaluated at a wavelength of 600 nm again for the intercellular space (blue), starch granules (red), and their sum (black). The error bars indicate the mean square deviation for a variation of the mean particle diameter by ±10 % and the volume fraction by ±2 %. For the intercellular space, a significant decrease in μ_s' from 1.08 to 0.64 mm^{-1} at week 12 was observed, followed by a small decrease to approximately 0.6 mm^{-1} by week 24. Scattering due to the starch granules increased slightly from 0.21 mm^{-1} at the beginning and reaches a maximum of 0.30 mm^{-1} in week 18. In the last six weeks, a

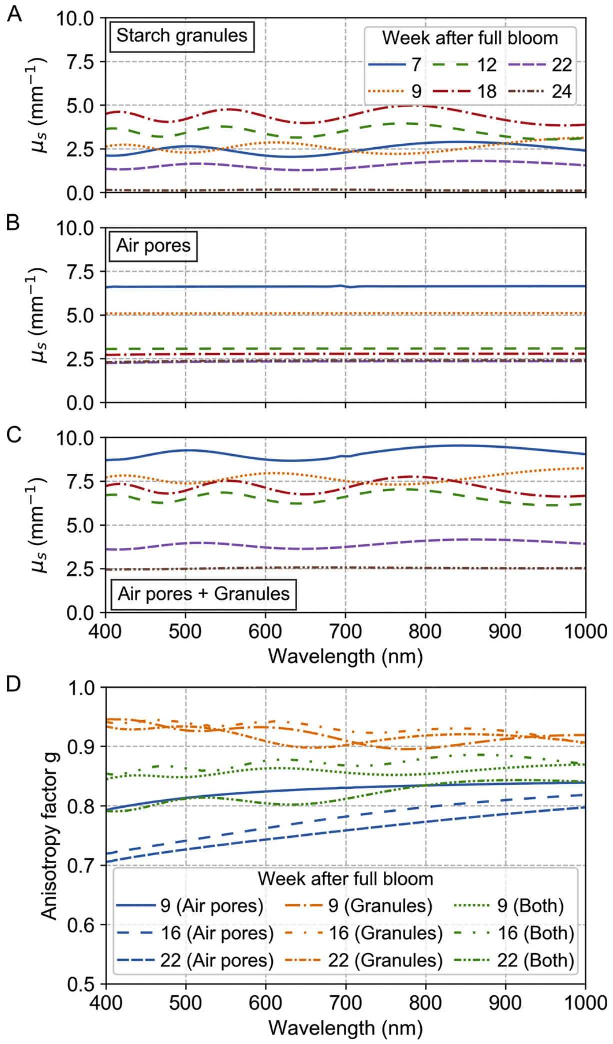

Fig. 2. Modeled scattering coefficients μ_s of starch granules (A), air pores (B) and their sum (C) for different weeks after full bloom and their corresponding anisotropy factors g (D).

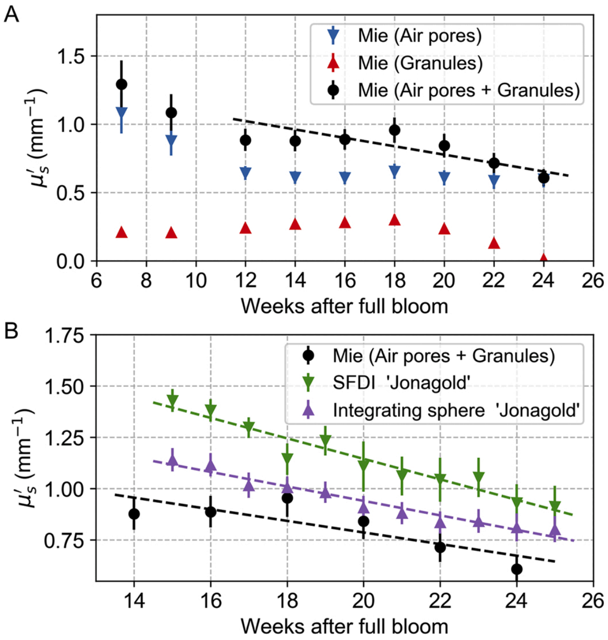

Fig. 3. (A) Changes in modeled effective scattering coefficients μ_s' for air pores and starch granules from 7 to 24 weeks after full bloom for 'Jonagold' apples, with the error bars indicating the uncertainty for 10 % variation in mean particle diameter and 2 % variation in volume content. (B) Comparison of μ_s' obtained with the Mie model and weekly measured with SFDI and integrating sphere for six 'Jonagold' apples over a period of 15–25 weeks after full bloom. The error bars indicate the total standard deviation, for the integrating sphere based on four measurement repetitions and for SFDI based on averaging the optical properties over the entire image area, for both at two measurement positions per apple. A linear regression was performed for each data set (dashed lines) with the functional parameters summarized in Table 1. (For interpretation of the references to color in this figure citation, the reader is referred to the web version of this article).

rapid decrease to almost 0 can be observed. Combining both components results in an overall decrease in μ_s' from 1.29 to 0.61 mm^{-1} during the studied period. A linear regression illustrates this trend between weeks 12 and 24. In Fig. 3(B), the period between end of July (14 weeks after full bloom) and begin of October (24 weeks after full bloom) was selected for which experimental data were available for μ_s' of cortex tissue from 'Jonagold' apples. These were measured and analyzed weekly on six identical apple samples using a SFDI and an integrating sphere setup. For the integrating sphere measurement, two samples were taken from the sun and shade sides of each apple and four measurement repetitions were performed in each case. With the SFDI setup, the apples were also measured on both sides and the optical properties were averaged over the entire image area. In both cases, the mean value of μ_s' was then calculated by averaging over all samples per week, taking into account error propagation. In both cases, an anisotropy factor of 0.9 and the refractive index of water plus a wavelength-independent constant of 0.04 were used for the evaluation, resulting in an exemplary value of 1.37 at a wavelength of 650 nm. Comparison shows that the relative change of μ_s' in the range of about 30 % agrees well for both experimental data and the simulation results. In detail, the decreases obtained by linear regression during the studied period are 30 % for the Mie model, 32 % for the integrating sphere measurements and 36 % for the SFDI measurements. The absolute changes range between 0.31 and 0.50 mm^{-1} over ten weeks. Table 1 shows the individual regression parameters.

In addition, the experimental data show overall larger values of μ_s' between 15 % (integrating sphere) and 30 % (SFDI) compared to the simulation. Thus, the Mie model only approximates the scattering properties and certainly does not take into account all effects that can occur that would explain the deviation from the absolute values. The differences between the two experimental methods could be explained by the different sample preparation. In the case of the integrating sphere, thin slices of apple tissue were cut and positioned between two glass plates. Inevitably, juice escapes and fills part of the air pores, especially at the interfaces. This corresponds to a reduction of the relative refractive index and causes on average a lower μ_s'. In the SFDI

Table 1
Parameters obtained from linear regression of the effective scattering coefficients μ_s' over the weeks after full bloom, shown in Fig. 3(B). R^2 indicates the coefficient of determination.

Data set	Offset	Slope	R^2
Mie model	1.389	−0.031	0.678
SFDI	2.143	−0.050	0.930
Integrating sphere	1.645	−0.035	0.950

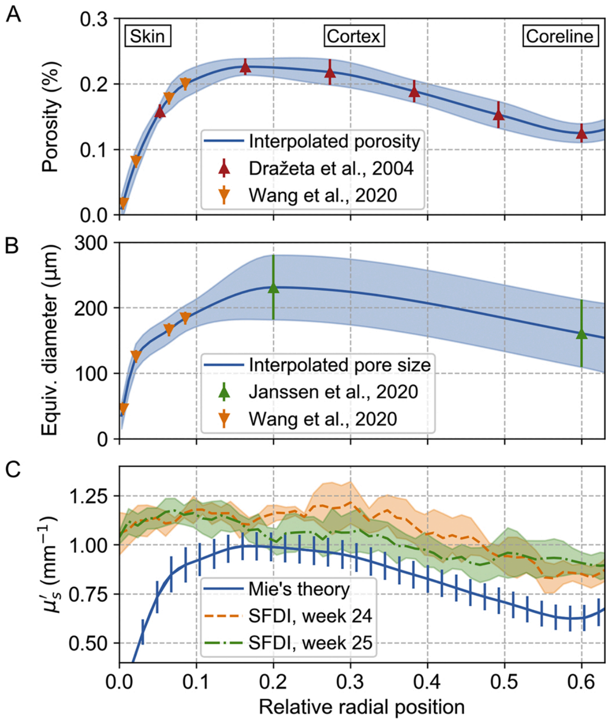

Fig. 4. Spatial change in porosity (A) and mean air pore diameter (B) between the skin and coreline of 'Jonagold' apples, interpolations based on literature data with standard deviations given as shaded area. The radial positions are given relative to the skin, the coreline is in the range of 0.6. (C) Effective scattering coefficient μ_s' calculated using a Mie model based on the data in (A) and (B). Error bars show the uncertainty for 10 % variation in mean air pore diameter and 2 % variation in porosity. For comparison, the scattering profiles of 'Jonagold' apples measured with SFDI are shown with the shaded area indicating the standard deviation of measurements on six different apples per week. The profiles were averaged within a range of 2 mm.

measurements, this effect certainly also occurs in the area of the cut surface, but here the light can generally penetrate deeper into the tissue and interact accordingly with intact tissue. This suggests that the SFDI measurements reflect the absolute scattering properties more realistically. However, the good agreement of the relative changes in all these cases is an indication that the temporal change of μ_s' can be understood primarily by changes in the air pores and starch granules.

The results are in good agreement with experimental studies by other researchers. For the anisotropy factor g, specifically for apple tissue using integrating sphere measurements, values between approximately 0.70 and 0.92 have been reported (Van Beers et al., 2017; Saeys et al., 2008). The relative decrease in μ_s' was also observed in other apple cultivars during maturation, although in some cases less pronounced (Van Beers et al., 2017; Seifert et al., 2015; Lohner et al., 2021). The Mie model predicted a strong influence of at least 70 % of intercellular space on total μ_s' which is in good agreement with the results of Wang et al. (2020). However, especially for the influence of starch, there are hardly any experimental comparative data available, but a maximum contribution of 0.3 mm^{-1} corresponds very well to the differences of about 0.4 mm^{-1} for cortex tissues with high and low starch content found in the first part of this work (Lohner et al., 2021).

4.2. *Mie model for the spatial change of the scattering properties*

In addition to temporal changes, literature data are also available to show lateral changes in intercellular space within the apple fruit. Therefore, the Mie model was used in the same way to estimate the scattering properties of the tissue between the core and the skin area. Both the porosity and the size distribution of air pores in ripe 'Jonagold' apples are reported in Janssen et al. (2020), Wang et al. (2020) and Dražeta et al. (2004) for different distances within fruit tissue relative to the skin, as shown in Fig. 4(A) and (B). For the remaining positions, the mean data were interpolated and based on the standard deviations indicated by the error bars, a corresponding log-norm distribution was calculated according to Eq. (5). The interpolated values considered in the Mie model are shown as blue lines, with the shaded area indicating the standard deviation. For the data taken from Wang et al. (2020) near the skin area, a slightly higher standard deviation than specified was assumed to ensure better agreement with the significantly higher standard deviation in Janssen et al. (2020). Overall, literature values are available ranging from the skin at a relative radial position of 0 throughout the cortex to the coreline, which is localized at a relative radial position of about 0.6. Since no quantitative data on the local starch distribution are known, the additional influence of the starch granules was not considered in detail. Its influence will be addressed in the discussion based on our previous results. The effective scattering coefficient resulting from the Mie model is shown in Fig. 4(C). The error bars indicate the mean square deviation for a variation of the mean pore diameter by ±10 % and the porosity by ±2 %. After reaching a local minimum of 0.62 mm^{-1} at the core line, μ_s' increases towards the outer cortex. The maximum of 1.0 mm^{-1} is reached at a relative radial position of approximately 0.2, with μ_s' decreasing rapidly thereafter towards the skin. Thus, relative to the maximum, the radial decrease in the inner cortex is around 35 %. For comparison, the results of SFDI measurements on 'Jonagold' apples from two different weeks at the end of the maturation period are shown. The individual profiles were first averaged laterally over a range of 2 mm and then these results were averaged again for six different apples per week. In both cases, the absolute μ_s' is about 25 % higher compared to the simulation, the relative radial change is in the range of less than 20 %. Larger deviations are particularly noticeable in the skin area, where μ_s' shows only a slight decrease in the measured data. As shown in Lohner et al. (2021), an underestimation is to be expected in this area due to the underlying semi-infinite model. It should also be taken into account that small pores in the skin area lie below the resolution limit of about 5 µm of the micro-CT measurements (Janssen et al., 2020; Wang et al., 2020). Due to their small size, a considerable influence on light scattering can be assumed, which could explain the differences to the measured data despite lower porosity.

Overall, the Mie model can correctly reproduce the radial change of μ_s' over large parts of the apple tissue. The higher absolute values of the experimental data can be attributed to the neglected influence of other components on μ_s'. In reality, scattering properties also depend strongly on local structures such as vascular bundles, which can lead to larger deviations between modeled and experimental data. In principle, other components, such as the starch granules, also have an influence on the scattering profiles, since their concentration can exhibit a considerable radial dependence. During starch degradation, the granules in the inner cortex are often already completely degraded, while considerable amounts can still be found in the outer cortex (Doerflinger et al., 2015; Brookfield et al., 1997). In this case, additional light scattering of the granules in the outer cortex would presumably lead to an overall larger gradient of the scattering profile.

4.3. *Consideration of cell walls based on layered particles*

To estimate the influence of the cell walls on the scattering properties, the Mie model was extended to include layered particles. For quantitative comparison, single apple cells were studied in four different configurations as shown in Fig. 5(C): cells in air (i), cells with cell walls in air (ii), cells with cell walls in tissue (iii), and cells with cell walls and a thin air gap in tissue (iv). For direct comparison, the same log-normal

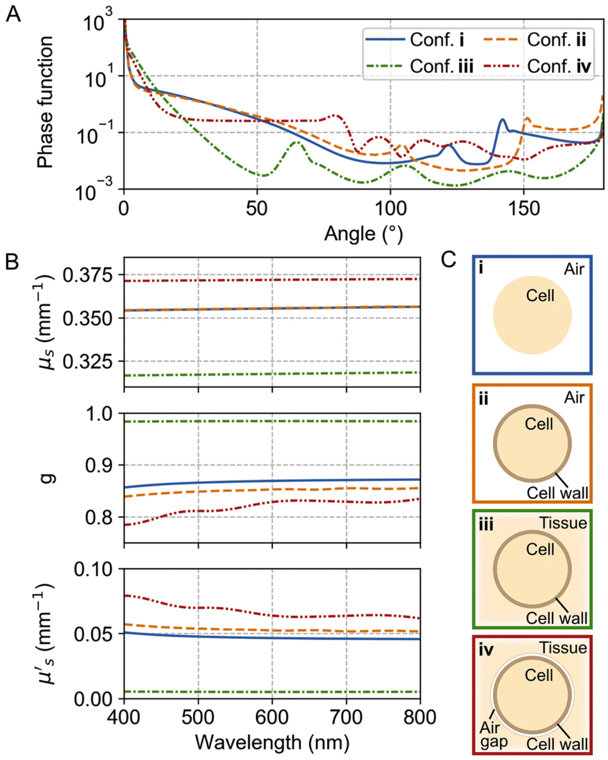

Fig. 5. (A) Phase functions for different layered particles at a wavelength of 600 nm obtained in the context of simplified cell model for the configurations shown in (C). For direct comparison of the results, a log-norm size distribution with a mean size of 100 µm and a standard deviation of 40 µm was chosen for all particles with a volume fraction of 1 %. (B) shows the resulting scattering coefficient μ_s, the anisotropy factor g derived from the phase function, and the combined effective scattering coefficient μ'_s in the visual spectral range.

size distribution with a mean size of 100 µm, a standard deviation of 40 µm and a volume fraction of 1 % was chosen for all cells. Configurations (i) and (ii) are based on isolated cells in air to directly compare the influence of the cell wall on light scattering. The refractive indices were assumed to be 1.37 for the cells and 1.0 for the surrounding air. In configuration (ii), a cell wall with a thickness of 2 % of the mean diameter and a refractive index of 1.425 was added, based on experimental results reported by Mebatsion et al. (2009), Woolley (1975) and Gausman et al. (1974) respectively, without changing the outer cell diameter. Relative to an average mean diameter of 100 µm, the average cell wall thickness of 2 µm is relatively small. The resulting scattering properties are shown in Fig. 5(A) and (B). While μ_s shows little difference for both configurations, the anisotropy factor is slightly smaller and thus μ'_s is slightly larger for configuration (ii). The differences are primarily caused by the phase function, as the comparison in Fig. 5(A) shows. In configurations (iii) and (iv), the cells were placed in surrounding tissue having the same mean refractive index as the cells themselves. This corresponds to the assumption of a dense and homogeneous cell structure with strongly pronounced cell-to-cell adhesion. Light scattering in configuration (iii) is thus completely attributable to the influence of the cell wall due to its higher refractive index. In configuration (iv), a thin air gap with a thickness of 1 µm was added around the cell as a third layer to simulate a cell detached from the cell compound. The results in Fig. 5(A) and (B) for these two cases show large differences in their phase functions and less pronounced also in μ_s. For configuration (iii), pronounced forward scattering with g of almost 1 leads to a very small μ'_s, while in configuration (iv) a smaller anisotropy factor and thus a significant increase in μ'_s are observed.

Overall, two main conclusions can be drawn from these results. In the case of a dense and relatively homogeneous cell structure, the direct influence of cell walls on light scattering is rather small with an increase of about 5 % compared to a homogeneous cell. This is in good agreement with the results of Wang et al. (2020), who reported a subordinate influence of cell organelles on light scattering. When the adhesion between cells decreases during ripening and storage or the cells lose volume, small air gaps may form between the cells as reported by Varela et al. (2007) and Harker and Hallett (1992). This process is accompanied by an increasing change in the composition and texture of the cell wall in terms of pectin, hemicellulose, and cellulose, with the pectin-rich middle lamella in particular increasingly dissoluting (Goulao and Oliveira, 2008). In this case, the increased light scattering would only be indirectly related to the properties of the cell walls and specifically the middle lamella, but as a result this could explain the increase in μ'_s already observed experimentally. As further evidence, Vanoli et al. (2009) reported, based on the study of ‘Jonagored’ apples by time-resolved spectroscopy, that the increase in μ'_s during storage was related to pectin content and composition.

4.4. *SSC influences the scattering properties*

During maturation, starch granules stored in the cells are converted by enzymatic processes into various sugars, leading to an increase in SSC. Yamaki and Ino (1992) showed that about 90 % of the sugar content is present in vacuoles, which in turn account for most of the cell volume (Shiratake and Martinoia, 2007). Depending on cultivar and growth conditions, SSC increases from about 5 % in immature apples to as much as 15 % in mature apples (Yamaki and Ino, 1992; Lu et al., 2000; Wei et al., 2020). This is associated with a change in the refractive index of the vacuoles and thus of the entire cell. Based on measurements of invert sugar solutions with different concentrations by Weast (1986) and Snyder and Hattenburg (1963), an increase in the refractive index from 1.340 to 1.355 can be estimated. To determine the effect of this change on μ'_s, the refractive index of the cell compound in the Mie Model was adjusted for different SSCs. Fig. 6(A) shows, as an example for week

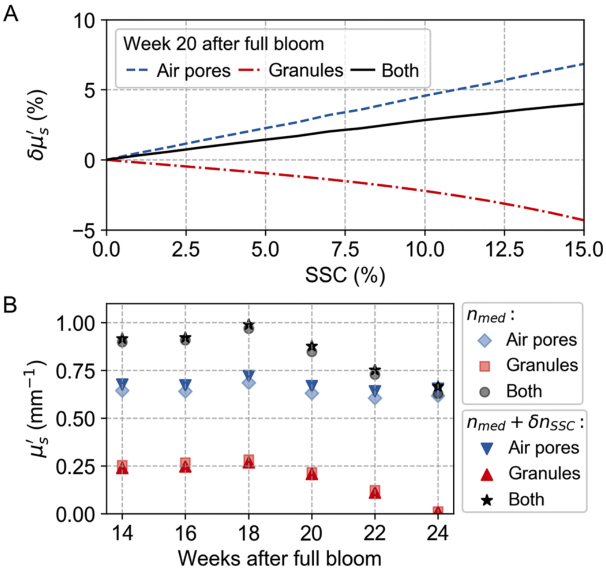

Fig. 6. (A) Modeled changes in relative scattering properties of air pores and starch granules at week 20 after full bloom as a result of increasing SSC, based on literature data. (B) Comparison between the previously presented effective scattering coefficient μ'_s assuming a constant refractive index (n_{med}) during maturation and an extended model considering the experimentally determined changes in SSC ($n_{med} + \delta n_{SSC}$).

20 after full bloom, the change in μ_s' for an SSC ranging from 0 to 15 % separately for the intercellular space and starch granules. The SSC increases the refractive index difference of the cells relative to the air pores, resulting in an increase of μ_s' by almost 7 % for 15 % SSC. At the same time, within the cells, the relative refractive index difference relative to the granules decreases, resulting in a decrease of μ_s' by about 4 %. The sum of both components predicts an increase of about 4 %. In Fig. 6(B), the simulation of μ_s' with and without consideration of the refractive index change was compared for different weeks. SSC was determined by refractometer measurements of 'Jonagold' apples during the corresponding period, ranging from 10.0 % at week 14 to 13.7 % at week 24. Overall, it was observed that the increase in the refractive index of the cells resulted in an increase in μ_s' of about 3 %. However, it must be taken into account that the refractive index of other cell components, such as the granules themselves, may also change over the same period.

5. Discussion

A Mie model was presented to estimate the scattering properties of apple tissue based on its microstructure. The intercellular space, i.e. the air pores, were assumed to be scattering particles located in a relatively homogeneous and dense cell structure. In reality, of course, this is only an approximation, since the refractive index of individual cell components varies to a certain degree (Drezek et al., 2000; Dunn and Richards-Kortum, 1996): 1.36–1.39 (nuclei, cytoplasm, nucleoli) (Choi et al., 2007), 1.40–1.42 (cell walls, mitochondria) (Haseda et al., 2015), and 1.52 (starch granules) (Wolf et al., 1962). Specifically, in plant cells, vacuoles, and cytoplasm alone account for nearly 70 % of cell volume (Yamaki and Ino, 1992). Thus, a mean refractive index of cells in the range of 1.37 seems plausible. As shown by the increase in SSC, the refractive indices of individual components can also change during maturation. Another example is the enzymatic degradation of starch granules, whose refractive index presumably also depends on the progress of hydrolysis (Oates, 1997). Since a quantitative estimation of such processes is hardly possible, this was not considered in the present model. For the cell walls, as another important component, the simulations showed a very small direct influence on scattering. Even with a fresh weight cell wall mass content of up to 3 % (Lapsley et al., 1992), which is comparable to the maximum starch content (Stevenson et al., 2006), this seems plausible because of the much smaller refractive index difference relative to the surrounding tissue. Less important for the cortex, but still conceivable, is the influence of chloroplasts and especially chlorophyll-containing grana on light propagation. Especially in high concentrations, as found in apple skin, they can lead to interesting effects due to their strong absorption (Capretti et al., 2019). Overall, the results of the investigated Mie model compared with experimental results suggest that air pores and starch granules are responsible for about 70–80 % of the total light scattering in the apple cortex and other components have a correspondingly small influence.

The intercellular space, as the presumably dominant component, is also subject to changes during maturation and storage. While the air pores are relatively isolated, especially at the beginning of fruit development with a volume content of about 10 %, their connectivity increases further on and their number decreases accordingly (Herremans et al., 2015). With a sphericity in the range of 0.7, they can be considered relatively spherical. As the fruit ripens, the average size of the air pores and their degree of cross-linking increases. This leads to the conclusion that the approximation of spherical air pores in late stages of fruit development does not fit well with reality. With decreasing cell-to-cell adhesion during storage, the initially dense cell structure increasingly dissolves until finally there are no more strictly localized air pores. In the hypothetical case of a complete dissolution of the middle lamella, the cells themselves would have to be regarded as densely packed scattering particles surrounded by air. With a cell volume fraction of 70 % and the accompanying dominant dependent scattering effect, the Mie theory would no longer be suitable for a realistic description of light scattering under this assumption. Thus, up to which point the presented Mie model retains its validity during storage depends strongly on the cell structure.

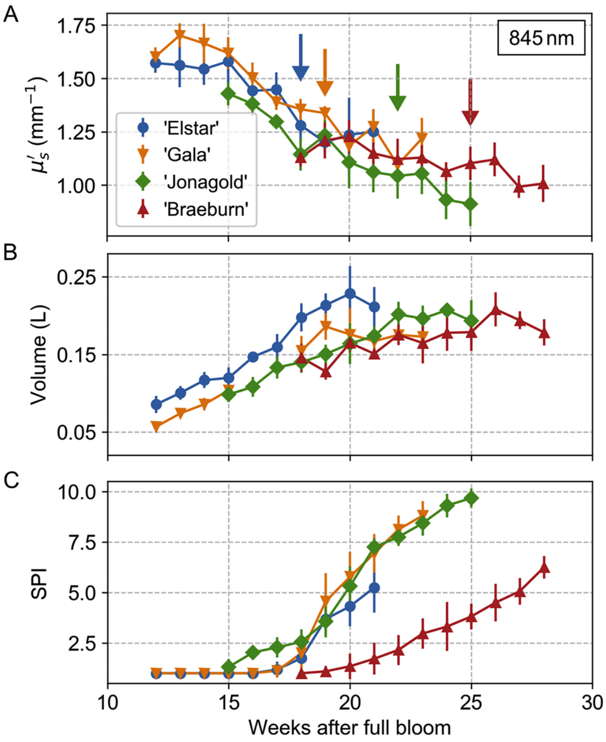

Fig. 7. (A) Temporal evolution of the mean effective scattering coefficient μ_s' compared for different apple cultivars measured with SFDI. The colored arrows mark the recommended harvest dates for each cultivar based on the Streif indices. (B) Temporal evolution of the mean volume estimated from the fruit size of six apples each week with an ellipsoid model. (C) Temporal evolution of the starch pattern index (SPI, ordinal score 1–10) with error bars indicating the standard deviations for a weekly sample set of six apples. (For interpretation of the references to color in this figure legend, the reader is referred to the web version of this article).

On a qualitative level, the results allow a general assessment of the importance of μ_s' in relation to fruit development. Although the microstructural properties used for this study were all determined using 'Jonagold' apples, some variability is to be expected due to different growing seasons and production regions. Therefore, the results can only represent the temporal development of the optical properties in an idealized way. Nevertheless, the model clearly shows that the relative change of μ_s' is strongly related to the influence of individual components, whose respective share is subject to fruit development. A large influence of the intercellular space was evident especially in the early stages between 6 and 16 weeks after full bloom, which is probably related to the cell enlargement occurring during this period (Bain and Robertson, 1951; Ruess and Stösser, 1993). The influence of starch degradation, on the other hand, was important at late stages of maturation, where intercellular space hardly changed. This relationship is also evident from the temporal evolution of μ_s' determined with SFDI from the first part of this work, shown in Fig. 7(A) (Lohner et al., 2021). In Fig. 7(B), the volume of the examined fruit increases steadily within a first period until about week 20 after full bloom. The mean volume was estimated from fruit size based on an elliptical model as shown in Iqbal et al. (2011). In the following second period, the volume change stagnates, but at the same time starch degradation progresses rapidly, as indicated by the increase in the starch pattern index (SPI) in Fig. 7(C). It is noticeable that in early maturing cultivars such as 'Elstar' and 'Gala', which were examined in the first period, the change in μ_s' is much more pronounced ($\Delta\mu'_s \approx 30\%$) than in late maturing cultivars such as 'Braeburn', which were mainly examined in the second period ($\Delta\mu'_s \approx 20\%$). In the case of 'Jonagold', whose maturation period covers both periods, the largest $\Delta\mu'_s \approx 35\%$ was observed in addition to a large volume increase and almost complete starch degradation. Generally, this could mean that a large relative change in μ_s' can be assumed for early maturing cultivars, while it is less pronounced for late maturing cultivars. In addition, the fruit growth itself and the progress of starch degradation play a major role, which in turn depend on the respective cultivar or climatic influences. For the absolute comparison of μ_s' and its relative changes, these parameters must therefore always be taken into account. The extent to which a correlation of μ_s' with individual macroscopic quantities such as firmness is applicable, e.g. for quality control, requires further investigation accordingly. For example, Rojas-Candelas et al. (2021) have recently shown that firmness at the microstructural level depends not only on air pore density, but in particular on cell diameter and cell density, which according to our results are related to μ_s' only to a minor extent. Apart from this, μ_s' nevertheless provides complex but important information about the structure of the tissue, which in combination with other optical parameters, such as absorption at different wavelengths, could well provide the possibility of defining a parameter for determining the degree of maturity or quality.

6. Conclusions

Part 2 of this study showed that a Mie model basically allows the estimation of scattering properties of apple tissue based on its microstructure. It was found that intercellular space, and in particular porosity, has a dominant influence on μ_s'. When simulating the temporal change of μ_s' during maturation, it was found that light scattering from starch granules can contribute to up to 25 % of total scattering. Overall, the predicted relative decrease in μ_s' agrees well with experimental results based on integrating sphere and SFDI measurements. It is noteworthy that μ_s' is differentially influenced by certain morphological components depending on the stage of maturation, which probably makes direct correlation with individual macroscopic quantities difficult. Furthermore, the Mie model predicted a radial increase in μ_s' of up to 35 % from the core to the skin, which is also largely consistent with experimental SFDI results. It was shown that the change in refractive index associated with the increase in SSC in cells leads to an increase in μ_s' of up to 5 %. By extending the Mie model to layered particles in the context of a simplified cell model, we found that the cell walls do not have a large influence on light scattering under the assumption of a relatively homogeneous cell structure. In the presence of an additional thin layer of air, as expected with reduced cell-to-cell adhesion due to dissolution of the middle lamella, a significant increase in light scattering was predicted. This offers an explanation for the increase in μ_s' already observed experimentally during storage.

In summary, the combined application of experimental SFDI measurements and a realistic Mie model provided many new insights into the complex relationships between optical properties, fruit morphology, and physiological processes during maturation.

Credit author statement

Stefan A. Lohner: conceptualization, methodology, investigation, data curation, formal analysis, validation, writing – original draft, writing – review & editing.

Konni Biegert: conceptualization, investigation, project administration, resources, data curation, formal analysis, writing – original draft, writing – review & editing.

Steffen Nothelfer: investigation, software, validation, writing – review & editing.

Ansgar Hohmann: investigation, project administration, writing – review & editing.

Roy McCormick: investigation, resources, formal analysis, writing – review & editing.

Alwin Kienle: supervision, writing – review & editing.

Conflict of interest

The authors declare no conflict of interest.

Acknowledgements

This research was funded in part by 'Zentrales Innovationsprogramm Mittelstand' (ZIM) of the 'Bundesministerium für Wirtschaft und Energie' (BMWi).

References

Aernouts, B., Watté, R., Van Beers, R., Delport, F., Merchiers, M., De Block, J., Lammertyn, J., Saeys, W., 2014. Flexible tool for simulating the bulk optical properties of polydisperse spherical particles in an absorbing host: experimental validation. Opt. Express 22, 20223.

Allan-Wojtas, P., Sanford, K., McRae, K., Carbyn, S., 2003. An integrated microstructural and sensory approach to describe apple texture. J. Am. Soc. Hortic. Sci. 128, 381–390.

Askoura, M., Vaudelle, F., L'Huillier, J.P., 2015. Numerical study of light transport in apple models based on Monte Carlo simulations. Photonics 3, 2.

Bain, J.M., Robertson, R., 1951. The physiology of growth in apple fruits I. Cell size, cell number, and fruit development. Aust. J. Biol. Sci. 4, 75.

Bergmann, F., Foschum, F., Zuber, R., Kienle, A., 2020. Precise determination of the optical properties of turbid media using an optimized integrating sphere and advanced Monte Carlo simulations. Part 2: experiments. Appl. Opt. 59, 3216.

Bhandari, A., Hamre, B., Frette, Ø., Stamnes, K., Stamnes, J.J., 2011. Modeling optical properties of human skin using Mie theory for particles with different size distributions and refractive indices. Opt. Express 19, 14549.

Bohren, C.F., Huffman, D.R., 1983. Absorption and Scattering of Light by Small Particles. John Wiley, New York.

Borch, J., Sarko, A., Marchessault, R., 1972. Light scattering analysis of starch granules. J. Colloid Interface Sci. 41, 574–587.

Brewster, M.Q., Tien, C.L., 1982. Radiative transfer in packed fluidized beds: dependent versus independent scattering. J. Heat Transfer 104, 573–579.

Brookfield, P., Murphy, P., Harker, R., MacRae, E., 1997. Starch degradation and starch pattern indices; interpretation and relationship to maturity. Postharvest Biol. Technol. 11, 23–30.

Capretti, A., Ringsmuth, A.K., van Velzen, J.F., Rosnik, A., Croce, R., Gregorkiewicz, T., 2019. Nanophotonics of higher-plant photosynthetic membranes. Light Sci. Appl. 8, 5.

Choi, W., Fang-Yen, C., Badizadegan, K., Oh, S., Lue, N., Dasari, R.R., Feld, M.S., 2007. Tomographic phase microscopy. Nat. Methods 4, 717–719.

Chýlek, P., 1977. Extinction cross sections of arbitrarily shaped randomly oriented nonspherical particles. J. Opt. Soc. Am. 67, 1348.

Dengate, H.N., Baruch, D.W., Meredith, P., 1978. The density of wheat starch granules: a tracer dilution procedure for determining the density of an immiscible dispersed phase. Starch – Stärke 30, 80–84.

Doerflinger, F.C., Miller, W.B., Nock, J.F., Watkins, C.B., 2015. Variations in zonal fruit starch concentrations of apples – a developmental phenomenon or an indication of ripening? Hortic. Res. 2, 15047.

Dražeta, L., Lang, A., Hall, A.J., Volz, R.K., Jameson, P.E., 2004. Air volume measurement of 'Braeburn' apple fruit. J. Exp. Bot. 55, 1061–1069.

Drezek, R., Dunn, A., Richards-Kortum, R., 2000. A pulsed finite-difference time-domain (FDTD) method for calculating light scattering from biological cells over broad wavelength ranges. Opt. Express 6, 147–157.

Dunn, A., Richards-Kortum, R., 1996. Three-dimensional computation of light scattering from cells. IEEE J. Sel. Top. Quantum Electron. 2, 898–905.

Farrell, T.J., Patterson, M.S., Wilson, B., 1992. A diffusion theory model of spatially resolved, steady-state diffuse reflectance for the noninvasive determination of tissue optical properties in vivo. Med. Phys. 19, 879–888.

Foschum, F., Bergmann, F., Kienle, A., 2020. Precise determination of the optical properties of turbid media using an optimized integrating sphere and advanced Monte Carlo simulations. Part 1: theory. Appl. Opt. 59, 3203.

Frisvad, J.R., Christensen, N.J., Jensen, H.W., 2007. Computing the scattering properties of participating media using Lorenz–Mie theory. ACM Trans. Graph. 26, 60.

Gausman, H.W., Allen, W.A., Escobar, D.E., 1974. Refractive index of plant cell walls. Appl. Opt. 13, 109.

Goulao, L.F., Oliveira, C.M., 2008. Cell wall modifications during fruit ripening: when a fruit is not the fruit. Trends Food Sci. Technol. 19, 4–25.

Grenfell, T.C., Warren, S.G., 1999. Representation of a nonspherical ice particle by a collection of independent spheres for scattering and absorption of radiation. J. Geophys. Res. Atmos. 104, 31697–31709.

Gronarz, T., Schnell, M., Siewert, C., Schneiders, L., Schröder, W., Kneer, R., 2017. Comparison of scattering behaviour for spherical and non-spherical particles in pulverized coal combustion. Int. J. Therm. Sci. 111, 116–128.

Hammer, M., Schweitzer, D., Michel, B., Thamm, E., Kolb, A., 1998. Single scattering by red blood cells. Appl. Opt. 37, 7410.

Hamre, B., Winther, J.G., Gerland, S., Stamnes, J.J., Stamnes, K., 2004. Modeled and measured optical transmittance of snow-covered first-year sea ice in Kongsfjorden. Svalbard. J. Geophys. Res. C Ocean. 109, 1–14.

Harker, F., Hallett, I., 1992. Physiological changes associated with development of mealiness of apple fruit during cool storage. HortScience 27, 1291–1294.

Haseda, K., Kanematsu, K., Noguchi, K., Saito, H., Umeda, N., Ohta, Y., 2015. Significant correlation between refractive index and activity of mitochondria: single mitochondrion study. Biomed. Opt. Express 6, 859.

Hergert, W., Wriedt, T. (Eds.), 2012. The Mie Theory – Basics and Applications, 2nd ed. Springer, Berlin Heidelberg.

Herremans, E., Verboven, P., Bongaers, E., Estrade, P., Verlinden, B.E., Wevers, M., Hertog, M.L., Nicolaï, B.M., 2013. Characterisation of 'Braeburn' browning disorder by means of X-ray micro-CT. Postharvest Biol. Technol. 75, 114–124.

Herremans, E., Verboven, P., Hertog, M.L.A.T.M., Cantre, D., van Dael, M., De Schryver, T., Van Hoorebeke, L., Nicolaï, B.M., 2015. Spatial development of transport structures in apple (Malus × domestica Borkh.) fruit. Front. Plant Sci. 6, 1–14.

van de Hulst, H.C., 1957. Light Scattering by Small Particles, 1st ed. John Wiley & Sons, New York.

Iqbal, S.M., Gopal, A., Sarma, A.S.V., 2011. Volume estimation of apple fruits using image processing. 2011 Int. Conf. Image Inf. Process. 1–6.

Jackèl, D., Walter, B., 1997. Modeling and rendering of the atmosphere using Mie-scattering. Comput. Graph. Forum 16, 201–210.

Janssen, S., Verboven, P., Nugraha, B., Wang, Z., Boone, M., Josipovic, I., Nicolaï, B.M., 2020. 3D pore structure analysis of intact 'Braeburn' apples using X-ray micro-CT. Postharvest Biol. Technol. 159, 111014.

Kai, L., Massoli, P., D'Alessio, A., 1994. Some far-field scattering characteristics of radially inhomogeneous particles. Part. Part. Syst. Charact. 11, 385–390.

Koch, A.L., 1966. The logarithm in biology 1. Mechanisms generating the log-normal distribution exactly. J. Theor. Biol. 12, 276–290.

Lapsley, K.G., Escher, F.E., Hoehn, E., 1992. The cellular structure of selected apple varieties. Food Struct. 11, 339–349.

Liemert, A., Kienle, A., 2012a. Analytical approach for solving the radiative transfer equation in two-dimensional layered media. J. Quant. Spectrosc. Radiat. Transf. 113, 559–564.

Liemert, A., Kienle, A., 2012b. Spatially modulated light source obliquely incident on a semi-infinite scattering medium. Opt. Lett. 37, 4158.

Liemert, A., Kienle, A., 2013. Exact and efficient solution of the radiative transport equation for the semi-infinite medium. Sci. Rep. 3, 2018.

Liemert, A., Reitzle, D., Kienle, A., 2017. Analytical solutions of the radiative transport equation for turbid and fluorescent layered media. Sci. Rep. 7, 1–9.

Lohner, S.A., Biegert, K., Nothelfer, S., Hohmann, A., McCormick, R., Kienle, A., 2021. Determining the optical properties of apple tissue and their dependence on physiological and morphological characteristics during maturation. Part 1: spatial frequency domain imaging. Postharvest Biol. Technol. 181, 111647 https://doi.org/10.1016/j.postharvbio.2021.111647.

Lu, R., Guyer, D.E., Beaudry, R.M., 2000. Determination of sugar content and firmness of apples using near-infrared diffuse reflectance. 2000 ASAE Annu. Int. Meet. Tech. Pap. Eng. Solut. a New Century 2, 1285–1301.

Mebatsion, H.K., Verboven, P., Melese Endalew, A., Billen, J., Ho, Q.T., Nicolaï, B.M., 2009. A novel method for 3-D microstructure modeling of pome fruit tissue using synchrotron radiation tomography images. J. Food Eng. 93, 141–148.

Modest, M.F., 2003. Radiative Heat Transfer, 2nd ed. Academic Press, Boston.

Mugnai, A., Wiscombe, W.J., 1986. Scattering from nonspherical Chebyshev particles I: cross sections, single-scattering albedo, asymmetry factor, and backscattered fraction. Appl. Opt. 25, 1235.

Mundy, W.C., Roux, J.A., Smith, A.M., 1974. Mie scattering by spheres in an absorbing medium. J. Opt. Soc. Am. 64, 1593.

Nothelfer, S., Bergmann, F., Liemert, A., Reitzle, D., Kienle, A., 2018. Spatial frequency domain imaging using an analytical model for separation of surface and volume scattering. J. Biomed. Opt. 24, 1.

Oates, C.G., 1997. Towards an understanding of starch granule structure and hydrolysis. Trends Food Sci. Technol. 8, 375–382.

Ohmiya, A., Kakiuchi, N., 1990. Quantitative and morphological studies on starch of apple fruit during development. J. Jpn. Soc. Hortic. Sci. 59, 417–423.

Qin, J., Lu, R., 2009. Monte Carlo simulation for quantification of light transport features in apples. Comput. Electron. Agric. 68, 44–51.

Rojas-Candelas, L., Chanona-Pérez, J., Méndez Méndez, J., Perea-Flores, M., Cervantes-Sodi, F., Hernández-Hernández, H., Marin-Bustamante, M., 2021. Physicochemical, structural and nanomechanical study elucidating the differences in firmness among four apple cultivars. Postharvest Biol. Technol. 171, 111342.

Rowe, P.I., Künnemeyer, R., McGlone, A., Talele, S., Martinsen, P., Seelye, R., 2014. Relationship between tissue firmness and optical properties of 'Royal Gala' apples from 400 to 1050nm. Postharvest Biol. Technol. 94, 89–96.

Ruess, F., Stösser, R., 1993. Untersuchungen über das Interzellularsystem bei Apfelfrüchten mit Methoden der digitalen Bildverarbeitung/Investigations on the intercellular system of apple fruit by digital image processing methods. Die Gartenbauwiss. 58, 197–205.

Saeys, W., Trong, N.N.D., Watté, R., Tsuta, M., Ramon, H., Nicolaï, B.M., 2010. Optical characterization of biological material: a multiscale approach. Am. Soc. Agric. Biol. Eng. Annu. Int. Meet. 2010, ASABE, 2010 1, 119–130.

Saeys, W., Velazco-Roa, M.A., Thennadil, S.N., Ramon, H., Nicolaï, B.M., 2008. Optical properties of apple skin and flesh in the wavelength range from 350 to 2200 nm. Appl. Opt. 47, 908.

Schäfer, J., 2016. MatScat V1.4.0.0. MATLAB Central File Exchange. https://www.mathworks.com/matlabcentral/fileexchange/36831-matscat.

Schäfer, J., Lee, S.C., Kienle, A., 2012. Calculation of the near fields for the scattering of electromagnetic waves by multiple infinite cylinders at perpendicular incidence. J. Quant. Spectrosc. Radiat. Transf. 113, 2113–2123.

Schmitt, J.M., Kumar, G., 1998. Optical scattering properties of soft tissue: a discrete particle model. Appl. Opt. 37, 2788.

Seifert, B., Zude, M., Spinelli, L., Torricelli, A., 2015. Optical properties of developing pip and stone fruit reveal underlying structural changes. Physiol. Plant. 153, 327–336.

Shiratake, K., Martinoia, E., 2007. Transporters in fruit vacuoles. Plant Biotechnol. 24, 127–133.

Snyder, C.F., Hattenburg, A.T., 1963. Refractive Indices and Densities of Aqueous Solutions of Invert Sugar. National Bureau of Standards Monograph 64, U. S. Department of Commerce.

Stevenson, D., Domoto, P., Jane, J., 2006. Structures and functional properties of apple (Malus domestica Borkh) fruit starch. Carbohydr. Polym. 63, 432–441.

Ulicný, J., 1992. Lorenz-Mie light scattering in cellular biology. Gen. Physiol. Biophys. 11, 133–151.

Van Beers, R., Aernouts, B., Watté, R., Schenk, A., Nicolaï, B., Saeys, W., 2017. Effect of maturation on the bulk optical properties of apple skin and cortex in the 500-1850 nm wavelength range. J. Food Eng. 214, 79–89.

Vanoli, M., Rizzolo, A., Grassi, M., Farina, A., Pifferi, A., Spinelli, L., Torricelli, A., 2011. Time-resolved reflectance spectroscopy nondestructively reveals structural changes in 'Pink Lady®' apples during storage. Proc. Food Sci. 1, 81–89.

Vanoli, M., Van Beers, R., Sadar, N., Rizzolo, A., Buccheri, M., Grassi, M., Lovati, F., Nicolaï, B., Aernouts, B., Watté, R., Torricelli, A., Spinelli, L., Saeys, W., Zanella, A., 2020. Time- and spatially-resolved spectroscopy to determine the bulk optical properties of 'Braeburn' apples after ripening in shelf life. Postharvest Biol. Technol. 168, 111233.

Vanoli, M., Zerbini, P.E., Spinelli, L., Torricelli, A., Rizzolo, A., 2009. Polyuronide content and correlation to optical properties measured by time-resolved reflectance spectroscopy in 'Jonagored' apples stored in normal and controlled atmosphere. Food Chem. 115, 1450–1457.

Varela, P., Salvador, A., Fiszman, S., 2007. Changes in apple tissue with storage time: rheological, textural and microstructural analyses. J. Food Eng. 78, 622–629.

Vaudelle, F., L'Huillier, J.P., 2015. Influence of the size and skin thickness of apple varieties on the retrieval of internal optical properties using Vis/NIR spectroscopy: a Monte Carlo-based study. Comput. Electron. Agric. 116, 137–149.

Vincent, J.F., 1989. Relationship between density and stiffness of apple flesh. J. Sci. Food Agric. 47, 443–462.

Wang, M., Cao, M., Guo, Z.R., Gu, N., 2013. Generalized multiparticle Mie modeling of light scattering by cells. Chin. Sci. Bull. 58, 2663–2666.

Wang, X., Pogue, B.W., Jiang, S., Song, X., Paulsen, K.D., Kogel, C., Poplack, S.P., Wells, W.A., 2005. Approximation of Mie scattering parameters in near-infrared tomography of normal breast tissue in vivo. J. Biomed. Opt. 10, 051704.

Wang, Z., Van Beers, R., Aernouts, B., Watté, R., Verboven, P., Nicolaï, B., Saeys, W., 2020. Microstructure affects light scattering in apples. Postharvest Biol. Technol. 159, 110996.

Weast, R.C., 1986. CRC Handbook of Chemistry and Physics, 67th ed. CRC Press Inc., Boca Raton (USA).

Wei, K., Ma, C., Sun, K., Liu, Q., Zhao, N., Sun, Y., Tu, K., Pan, L., 2020. Relationship between optical properties and soluble sugar contents of apple flesh during storage. Postharvest Biol. Technol. 159, 111021.

Wilson, J.D., Foster, T.H., 2005. Mie theory interpretations of light scattering from intact cells. Opt. Lett. 30, 2442.

Wiscombe, W.J., 1980. Improved Mie scattering algorithms. Appl. Opt. 19, 1505.

Wolf, M., Ruggles, V.J., MacMasters, M.M., 1962. Refractive indices of wheat starch granules at various moisture levels determined with an interference microscope. Biochim. Biophys. Acta 57, 135–142.

Woolley, J.T., 1975. Refractive index of soybean leaf cell walls. Plant Physiol. 55, 172–174.

Yamaki, S., Ino, M., 1992. Alteration of cellular compartmentation and membrane permeability to sugars in immature and mature apple fruit. J. Am. Soc. Hortic. Sci. 117, 951–954.

Zhang, K., Li, W., Eide, H., Stamnes, K., 2007. A bio-optical model suitable for use in forward and inverse coupled atmosphere-ocean radiative transfer models. J. Quant. Spectrosc. Radiat. Transf. 103, 411–423.

Non-destructive Vis/NIR time-series to model apple fruit maturation on the tree

R. McCormick[1,a] and K. Biegert[1,2]

[1]Postharvest Workgroup, Kompetenzzentrum Obstbau-Bodensee, Ravensburg, Germany; [2]Production Physiology Workgroup, Kompetenzzentrum Obstbau-Bodensee, Ravensburg, Germany.

Abstract

Apple growers make harvest decisions based on a few simple destructive tests e.g. soluble solids and starch content, and fruit firmness. However, non-destructive technologies also offer possibilities to monitor fruit maturation and ripening and to build prediction models for an optimum harvest date (OHD) for fruit intended for long-term storage. Technological developments now enable point spectroscopy Vis/NIR spectral scans to be made on fruit in the orchard using portable hand-held devices. In fruit crops like mango, prediction models process spectral information in real-time and provide information about when to pick fruit. A standard type hand-held spectrophotometer (F750, Felix Instruments, USA) was used to collect spectral time-series data from 2016 to 2018 for 'Braeburn' apples during fruit development, growing at the Kompetenzzentrum Obstbau Bodensee in Southwest Germany. Decreasing chlorophyll levels were closely associated with apple maturation, in particular the parameter rededge was consistently close to 689 nm at the OHD for 'Braeburn' over all three study years and was less variable than a normalized difference vegetation index (NDVI). Predictions of an OHD using partial least squares regression models based on all available spectral information were not robust enough to define an OHD with a narrow harvest window. Future efforts to model an OHD for a bicolored apple cultivar like 'Braeburn' should try to untangle changes in the visible spectrum from the carotenoid, anthocyanin and chlorophyll pigments.

Keywords: Streif index, chlorophyll, anthocyanins, carotenoids, rededge

INTRODUCTION

Monitoring fruit maturity is critical to predict an optimum harvest date (OHD) of apples intended for long-term storage. The apple industry relies largely on simple destructive methods for maturity testing e.g. total soluble solids (TSS), fruit firmness (FF) and starch (iodine staining) pattern index (SPI) that are usually expressed as a harvest index (FF/TSS × SPI) with cultivar specific threshold values to define a start and close of a harvest window (Streif, 1996).

From a practical viewpoint, fruit maturation should be considered more an on-tree preharvest process and clearly differentiated from fruit ripening. Fruit can be considered 'physiologically mature' when they develop the ability to ripen adequately (i.e. obtain acceptable consumer eating quality free from physiological disorders) at some future time after picking, usually after long-term storage, postharvest handling and shelf-life.

Destructive harvest maturity testing is multifaceted, as information is combined from different physiological ripening processes in the apple. The destructive tests (FF & SPI) measure aspects of fruit that are difficult to determine non-destructively. But even so, non-destructive methods still show potential to monitor fruit maturation. New spectrophotometers, chemometric software and data communication now enable visible/near-infrared (Vis/NIR) spectra (as point spectroscopy versus hyperspectral imaging) to be collected in the orchard with portable hand-held devices, with the field data processed and the results made available in real-time, e.g. mango harvesting based on dry matter (DM)

---

[a]E-mail: mccormick@kob-bavendorf.de

Acta Hortic. 1311. ISHS 2021. DOI 10.17660/ActaHortic.2021.1311.17
Proc. VI Int. Symp. on Applications of Modelling as an Innovative Technology in the Horticultural Supply Chain - Model-IT 2019
Eds.: M.L. Amodio and G. Colelli

content (Nicolai et al., 2007; Subedi, et al., 2013; Walsh, 2016).

In the apple industry spectral devices for skin green color (DA-Meter, Turoni, IT) are in use and spectrophotometers that sample a wider range of multiple wavelengths as reported in this work are under trial (Walsh, 2016; Musacchi and Serra, 2018). Furthermore, with more advanced spectral methods like time resolved spectroscopy (still laboratory based), changes in the fruit flesh color (chlorophyll) can be related to fruit maturity (Tijskens et al., 2007).

After harvest and storage outturn, the OHD can be confirmed as providing fruit of a suitable consumer quality. Furthermore, any Vis/NIR time-series data collected from maturing apples on the tree during the preharvest period can now be regressed in PLSR (partial least square regression) models against the known OHD and destructive maturity values. Such a modelling approach can provide a simple estimate of the how suitable spectral information is at OHD prediction. Researchers have obtained SEPs (standard error of prediction) of ~6 to 9 d from spectral scans of individual fruit from a range of apple cultivars using wavelength ranges of 300-1100 nm and/or 380 to 1680/2000 nm (Zude-Sasse et al., 2002; Peirs et al., 2005; Van Beers et al., 2014). The PLS regression coefficients can also show which spectral regions are providing most information to the model e.g. the chlorophyll peak at ~670 nm and from the OH bond peaks of water and carbohydrates at 970, 1450 and 1940 nm (Peirs et al., 2005).

Changes in chlorophylls and carotenoids in the visible spectrum are related to fruit maturation, But there are numerous pigments all with overlapping spectral signatures; thus multicollinearity is a problem. Also, apparent absorbance from standard reflectance spectra (RS) is a combination of both light scattering and absorbance and light scattering can change at a different rate to absorbance as fruit ripen. Thus, absolute pigments concentrations are often not related to the RS in a linear manner (Merzlyak et al., 2003). Absolute chlorophyll concentration may not be a reliable indicator of fruit maturity (McGlone et al., 2002), while Knee (1988) proposed xanthophylls in the extra-thylakoid pool as an accurate parameter for apple ripeness.

Apples have four physiologically different pigment pools (Merzlyak, 2006). The peel chloroplasts contain most of the chlorophyll and together with carotenoids are tightly associated with the thylakoid membrane, during ripening chlorophyll gradually decreases and carotenoids accumulate. Xanthophylls also accumulate in the peel during ripening in an extra-thylakoid pool (Knee, 1972, 1988). Phenolics compounds are present in the cuticle and vacuoles, and absorb UV and some blue light. A fourth pool consists of anthocyanins in the peel cell vacuoles, although anthocyanins are not as closely related to fruit maturation as chlorophyll or carotenoids.

Fruit ripeness seems best to be predicted by following changes in pigment patterns (McGlone et al., 2002), in particular the carotenoid/chlorophyll ratio (Merzlyak, 2006). A range of spectral indices with potential application on apple can be found in the literature (Acharya et al., 2016 and references within). Gitelson et al. (2006) proposed three-wavelength band models to estimate fruit pigment concentrations and to minimise multicollinearity. Other multivariate modelling approaches to separate pigment spectra exist but require wet chemistry reference values (Pflanz, 2014). The presence of high anthocyanin concentrations makes it difficult to accurately estimate carotenoids and chlorophyll. Even so the plant senescence reflectance index (PSRI) can show changes in the carotenoid/chlorophyll ratio in ripening of apples and correlations with internal ethylene concentrations (Merzlyak et al., 1999).

Depending on the optical geometry, NIR spectra can be used in PLS models to predict TSS and DM in the fruit flesh (McGlone et al., 2002; Subedi et al., 2013). As well, a better treatment of biological variation has shown clear benefits to improve ripening models in a range of fruit (Rizzolo et al., 2009).

This work discusses the potential of Vis/NIR spectral data that could be used as a basis for non-destructive apple maturity prediction models.

MATERIALS AND METHODS

At the Kompetenzzentrum Obstbau Bodensee in Southwest Germany, as part of a larger project ('BigApple', see McCormick et al., 2017), Vis/NIR spectral scans (310-1100 nm, spectral sampling 3 nm, spectral resolution, 8-13 nm) with an F750 hand-held fruit quality meter (Felix Instruments, Camas, USA) were repeatedly collected from the same position on the sunlit blush face of a population of 'Braeburn' apples still attached to the tree during fruit maturation. The F750 internally calibrates each scan, to remove the influence of sunlight and adjust the integration time. Fruit temperature is not taken into account during scanning in the field as spectral responses to changes of 4-30°C in the 600-750 nm region have been found to be minimal (Zude-Sasse et al., 2002). On the other side, there is a strong effect of temperature in the SWNIR region that can partly be taken into account in the laboratory when building wet chemistry based PLSR models, by scanning the same reference fruit samples at different temperatures (for changes in TSS and/or DM). Time-series data were obtained for 3 seasons from early August (2016, 2017) and from June in 2018 until harvest on 17, 18 and 3 October in 2016 to 2018, respectively [with harvest decisions based on destructive maturity tests following Streif, (1996)]. Fruit were scanned at 3 tree heights; bottom, middle and top thirds. Dropped fruit (~5% of total) were replaced with a similar fruit nearby.

The 'Braeburn' trees were planted in 2006 and trained as splendour spindles (3.2×0.8 m×~3.8 m high). Trees were hand thinned to 3 different cropload levels of 30-40 (light), 100-120 (standard) and 180-200 (heavy) fruit per tree (2016 and 2018). In 2017, fruitset was severely affected by frost, overall trees had the required croploads, but fruit distribution from the top to bottom was uneven. Cropload treatments were replicated 3 times. Trees received no ground applied nitrogen fertiliser or calcium sprays during the entire study period.

Raw F750.dat scan files were extracted as absorbance spectra (AS) using Dataviewer software (Felix Instruments, Camas, USA). AS were converted to RS values [RS=1/10^(AS)] and pigment indices calculated with 'R' software (R Core Team, 2018). A normalized difference vegetation index for chlorophyll [NDVI=(R750-R705)/(R750+R705 nm)] (Zude, 2003), an anthocyanin index [AI=(R801/R549)-(R801-R699 nm)] (Acharya et al., 2016) and a plant senescence reflectance index [PSRI=678-501)/(801 nm)] (Merzlyak et al., 1999) were calculated. The rededge inflection point in the chlorophyll reflectance curve (Zude and Herold., 2002; Geyer et al., 2007) was calculated from the 2nd derivative AS between 678 and 717 nm. The NIR 2nd derivative AS from 729 to 975 nm were used in Modelbuilder software (Felix Instruments, Camas, USA) to build local PLS models for TSS and DM in each year, calibrated with wet chemistry reference values for 30 fruit samples picked regularly over all the scanning periods.

PLSR models to estimate the potential information available in the 'Braeburn' AS (429-1110 nm) from 70 d preharvest up until the OHD (as determined by destructive testing i.e. Streif Index) were built with the 'R' software 'pls' package (Mevik et al., 2018) to predict the days to the OHD. In the 70 d preharvest period there were 9, 11, and 7 scanning dates for 2016, 2017 and 2018, respectively. Scan data were pooled over the 3 years, per calendar week and tree sector using either all individual scans available (846) or mean data for each replication (111). Model cross validation was conducted with the leave one out method, also using groups as complete seasons and with an independent data set from 2018. Four scans were identified as outliers and removed.

RESULTS AND DISCUSSION

Figure 1 shows the changes in the raw AS during fruit development on the tree during 2018. Marked changes within the visible region are due mainly to changes in chlorophyll, anthocyanins and carotenoids, changes in the NIR region (>~750 nm) are less marked.

Estimating the potential amount information available in Vis/NIR field data set to predict an OHD

When all available scans (846) from all years and the middle tree sector were used in a PLSR model to predict the days to the OHD (based on the Streif harvest index values), the RMSECV (leave one out method) was 10.8 d with R^2=0.68 using 5 PCs. When all available scan data (111) where combined as mean scans per plot and calendar week and then used as model input, the resulting RMSECV reduced to 6.3 d, with R^2=0.89 and 5 PCs. Pre-processing the AS data by standardisation and/or multiple scatter correction before PLS did not improve the models. These results broadly correspond with Peirs et al. (2005). However, the models were clearly not robust enough when data from 2 years was used to predict the third year. Here the predicted OHDs differed from the measured by 5, 20 and 40 d when the 2017, 2018 and 2016 years were used as test data, respectively. One independent data set was available from the middle tree sector in 2018 and was used as a test set with the model build from mean values per plot and calendar week from all years. In this case the model RMSEP for days to OHD was 9.0 d with an R^2=0.86 using 5 PCs.

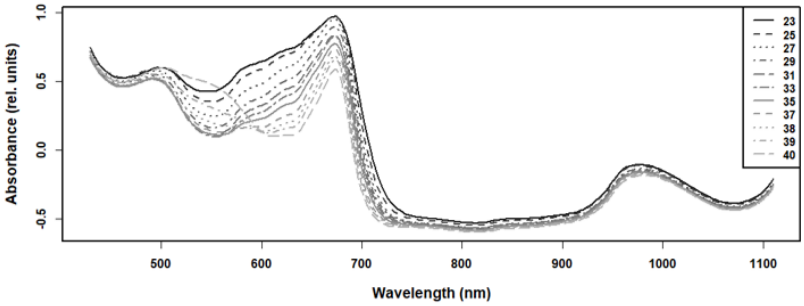

Figure 1. 2018 mean absorbance spectra (AS) from 11 separate dates from the same population of marked apples on the tree between calendar week 23 and 40 (harvest 3 Oct.) *n*=108.

The regression coefficients for the mean models are plotted against wavelength in Figure 2. Strong positive regression coefficients come from the visible spectrum around the blue/ green (501 nm), the red (630 nm) and near red (696 nm) regions just before and after the maximal chlorophyll absorbance and also from the NIR 960 nm region around the water absorbance peak. Regression coefficients for all the other tree sector models using individual scans and/or mean scan data showed similar patterns (data not shown). But to be of practical use, model RMSEPs need to be reduced to around ~3.0 d and in addition provide an increasing level of accuracy in the period from at least two weeks before and up to the expected ODH.

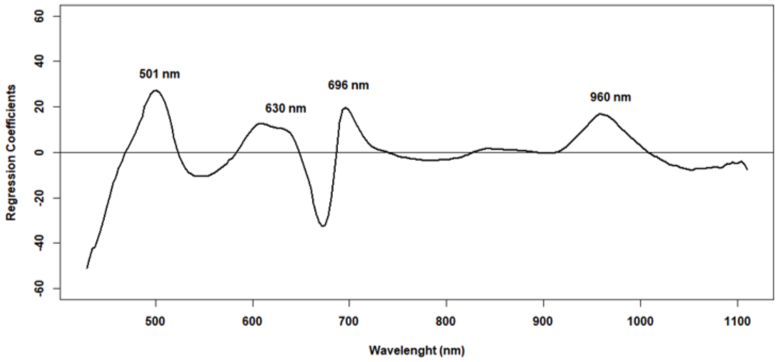

Figure 2. PLS regression coefficients for the 'days to optimum harvest date' model for the middle tree sector using mean values (scans averaged by treatment replicate and calendar week). Peak wavelength positions are shown.

Chlorophyll parameters (NDVI and rededge)

The 2018 year rededge and NDVI data averaged over each tree sector are shown in

Figure 3A and over each cropload level in Figure 3B. Both the NDVI and rededge curves show a similar sigmoidal pattern where the changes in slope separate the curves into 3 periods (steep decrease, then flatter, then steeper) similar to Zude and Herold (2002) although in these 'Braeburn' data, the changes in slope occur earlier. Closer to harvest the rededge curves are more tightly grouped when compared to the NDVI. In Figure 3A, the NDVI indices for the top sector show lower values compared to the middle or bottom tree sectors. In Figure 3B both the NDVI indices and rededge wavelengths for the light cropload show lower values. Fruit from low cropload trees are normally large (which was the case here – data not shown) and as commonly observed especially in early season apple cultivars like 'Gala' or 'Elstar', tend to mature and ripen much faster compared to standard or heavy croploads. However, in all our 'Braeburn' data from 2016 to 2018, we consistently found no differences in the Streif index at-harvest for light croploads treatments compared to standard or heavy croploads and thus all cropload levels were harvested on the same date. Reasons for this lack of cropload effect on harvest date are perhaps a specific late season cultivar effect, 'Braeburn' is a firm cultivar and is slow to soften before ethylene levels really increase and also in all study years the starch levels were high and the starch pattern index slow to change as fruit matured. However, while destructive maturity tests did not distinguish between cropload treatments, the 'Braeburn' apples showed differences in storage behavior (i.e. higher incidence of storage disorders in light cropload treatments, data not shown) and other non-destructive pigment indices could distinguish differences (e.g. see PSRI data below).

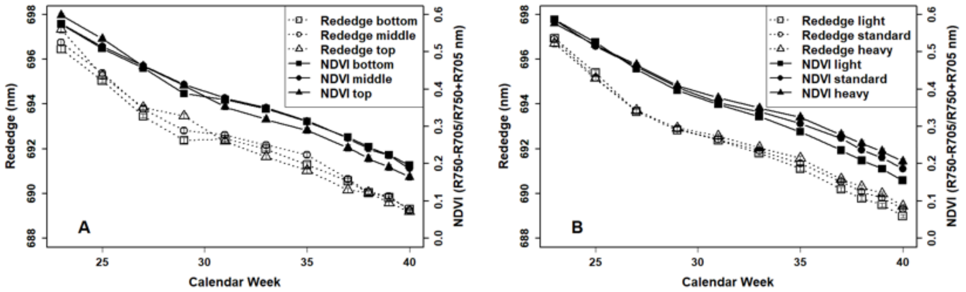

Figure 3. (A) Changes in mean rededge and mean NDVI for 'Braeburn' apples in 2018 from week 23 and week 40 (harvest 3 Oct.) for different tree sectors (top, middle, bottom) and (B) different cropload levels (light, standard and heavy). *n*=36, bars=standard errors.

The rededge data all show very low coefficients of variation (CVs < 1%). There are no rededge 'Braeburn' data in the literature, but our data show lower absolute values and are less variable than reported by Zude and Herold (2002) for 'Elstar' and 'Jonagold'. In addition to cultivar differences, cropload and light exposure there are other factors known to affect apple skin green color, e.g. cultural practices (nitrogen applications), growing location (latitude) and spring temperatures ('BigApple' project unpublished data). Importantly, these rededge data show much lower CVs than the NDVI (~25%) suggesting rededge is the better parameter to use to model changes in chlorophyll. Remarkably, all the rededge values directly before the ODH in all three years were very similar at around ~689 nm (Table 1).

Plant senescence reflectance index (PSRI) to show changes in chlorophyll and carotenoids

Over three seasons, the PSRI remained constant until some 5 or 6 weeks preharvest when both the mean values and the variance began to increase exponentially (Figure 4). This fits with the expected ripening pattern, with a decrease in chlorophyll and increase in carotenoids following Merzlyak et al. (1999) and Knee (1972). Over 3 years the PSRI could consistently distinguish different cropload levels, with fruit from light cropping trees showing a steeper rate of change compared to standard or heavy, see Figure 4A for 2018 data only (2016 and 2017 data not given). Both plots in Figure 4 are adjusted to show biological time using the methodology developed by Pol Tijskens (Rizzolo et al., 2009) to separate the variation and fit trend lines. A negative biological shift factor (here biological time) indicates less mature fruit. Biological time corrects so to speak for the state of development of individual fruit.

Table 1. Mean NDVI and rededge for 'Braeburn' apples from Vis/NIR scans directly on or slightly before the ODH in 2016 (0 d), 2017 (-4 d) and 2018 (-1 d) for standard cropload and 3 different tree sectors. *n*=3, 12-18 & 12 apples for 2016, 2017 & 2018, respectively.

Tree sector	**Mean NDVI at OHD (std dev)**			**Mean Rededge (nm) at ODH (std dev)**		
	2016	**2017**	**2018**	**2016**	**2017**	**2018**
Bottom	0.13 (0.03)	0.15 (0.04)	0.20 (0.05)	688.8 (0.4)	688.8 (0.5)	689.3 (0.5)
Middle	0.10 (0.01)	0.16 (0.04)	0.20 (0.05)	688.8 (0.1)	688.8 (0.4)	689.4 (0.6)
Top	0.09 (0.03)	0.11 (0.04)	0.17 (0.04)	688.6 (0.2)	688.6 (0.3)	689.1 (0.4)

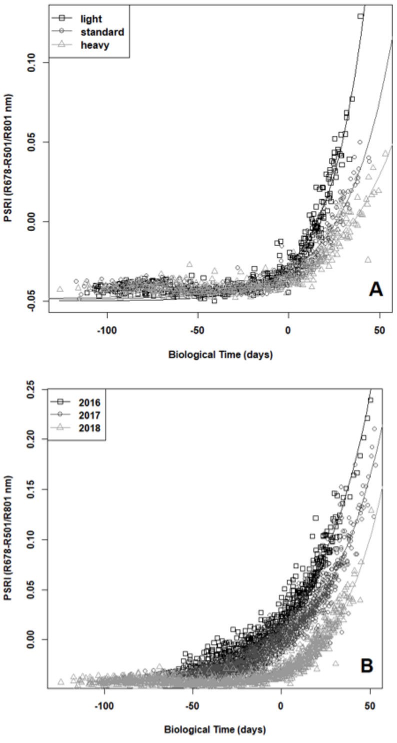

Figure 4. (A) Changes in the plant senescence reflectance index (PSRI) for 'Braeburn' apples from 3 different croploads (light, standard, heavy) in 2018. 36 apples per cropload level, repeatedly scanned 11 times from 6 June and 2 October. (B) Changes in the PSRI in cropload experiments in 2016, 2017 and 2018 with 27, 132 and 108 apples repeatedly scanned 21, 11 and 11 times per year, respectively. Scans from either early June (2018) or August (2016 and 2017) until optimum harvest date in October. The *x*-axis shows biological time, where zero is the model midpoint value and is only synchronised (indirectly related) to the actual harvest time.

In 2017 and 2018, the PSRI could also distinguish between fruit at the top of trees with a faster rate of change compared to the middle or bottom sectors (data not shown). The PSRI data for all study years are compared in Figure 4B. While each year shows a similar rate of change, the changes in PSRI do not match up with the actual maturity pattern observed in the orchard. The OHD in 2016 and 2017 was reached on 17 and 18 October and in 2018 was some two weeks earlier on 3 October. The PSRI patterns for fruit at the top of the tree or from light croploads can be explained partially by higher carotenoids in sun exposed fruit or a faster fruit development on light cropping trees. Understanding why the PSRI does not consistently show the same relationship to the OHD in all years will require further work (i.e. attempt to separate the confounding influence of anthocyanins).

Anthocyanin index (AI), total soluble solids (TSS) and dry matter (DM)

The AI shows a seasonal trend, at first decreasing (young apple fruitlets are known to be high in anthocyanins) and then as temperatures decrease and light conditions change closer to harvest red blush color increases particularly at the top of the trees with higher light exposure (Figure 5A). The seasonal trends for both TSS and DM % are slightly separated by the 3 cropload treatments (Figure 5B). 2018 was a very dry sunny year, differences in both TSS and DM by cropload level were greater in 2016 and 2017 (data not given).

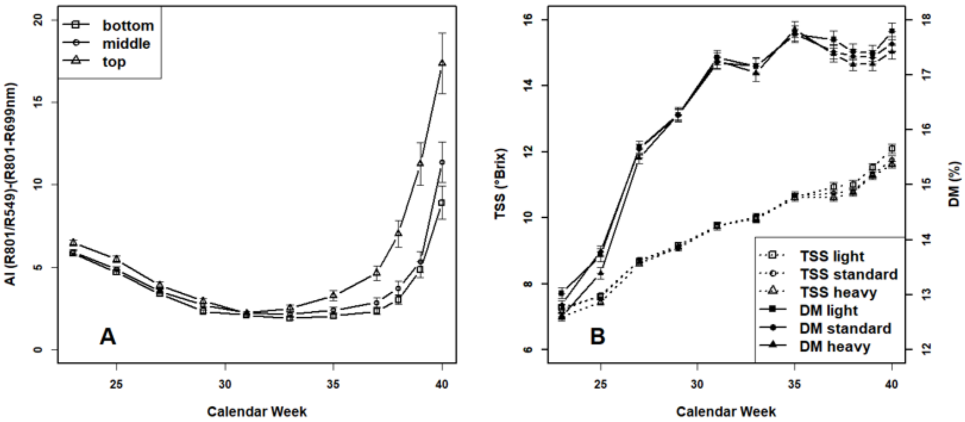

Figure 5. (A) Changes in the anthocyanin index (AI) for ‘Braeburn’ apples in 2018 from 3 different tree sectors (bottom, middle, top). (B) Changes in total soluble solids (TSS) and dry matter (DM) for ‘Braeburn’ apples from 3 different cropload treatments in 2018. *n*=36 apples per sector or cropload level scanned 11 times from 6 June to 02 October Bars=std. error. Harvest date was 3 October (CW 40).

CONCLUSIONS

Standard Vis/NIR time-series data scanned from marked apples on the tree contain multiple information ‘dimensions’ that can be used to model apple maturity. Changes in the visible spectrum, primarily chlorophyll found largely in the fruit skin should be used as a basic model ‘framework’ with other components modulating the relationship. A different experimental approach is required to try and non-destructively separate aspects of the xanthophyll cycle. More information about changes in carbohydrate metabolism from the NIR wavelength region over multiple seasons and growing regions is needed to build better maturity models based on non-destructive data. Moreover it should be considered that the light penetration decreases depth at high wavelengths (1450-1600 nm) reducing the amount of information available from tissues further inside the fruit. Advanced spectral technologies i.e. spatial or time resolved Vis/NIR should be developed for hand-held devices to obtain more non-destructive information from fruit maturing on the tree.

ACKNOWLEDGEMENTS

Pol Tijskens for helpful advice and providing 'R' scripts for rededge and the biological shift factor. Kerry Walsh for improvements to the text. The German Agricultural and Food Ministry (on the basis of a decision by the German Bundestag) and Federal Agency for 'BigApple' project funding.

Literature cited

Acharya, U.K., Subedi, P.P., Walsh, K.B., and McGlasson, W.B. (2016). Estimation of fruit maturation and ripening using spectral indices. Acta Hortic. *1119*, 265–272 https://doi.org/10.17660/ActaHortic.2016.1119.37.

Geyer, M., Herold, B., Zude, M., and Truppel, I. (2007). Non-destructive evaluation of apple fruit maturity on the tree. Vegetable Crops Research Bulletin *66* (*2007*), 161–169 https://doi.org/10.2478/v10032-007-0018-4.

Gitelson, A.A., Keydan, G.P., and Merzlyak, M.N. (2006). Three-band model for non invasive estimation of chlorophyll, carotenoids, and anthocyanin contents in higher plant leaves. Geophys. Res. Lett. *33* (*11*), 11402 https://doi.org/10.1029/2006GL026457.

Knee, M. (1972). Anthocyanin, carotenoid, and chlorophyll changes in the peel of Cox's Orange Pippin apples during ripening on and off the tree. J. Exp. Bot. *23* (*1*), 194–196 https://doi.org/10.1093/jxb/23.1.184.

Knee, M. (1988). Carotenol esters in developing apple fruits. Phytochemistry *27* (*4*), 1005–1009 https://doi.org/10.1016/0031-9422(88)80261-9.

McCormick, R.J., Biegert, K., and Streif, J. (2017). Risk of 'Braeburn' browning disorder based on weather and orchard factors. Paper presented at: XII International Controlled and Modified Research Conference (Warsaw, Poland: ISHS).

McGlone, V.A., Jordan, R.B., and Martinsen, P.J. (2002). Vis/NIR estimation at harvest of pre- and post-storage quality indices for 'Royal Gala' apple. Postharvest Biol. Technol. *25* (*2*), 135–144 https://doi.org/10.1016/S0925-5214(01)00180-6.

Merzlyak, M.N. (2006). Modeling pigment contributions to spectral reflection of apple fruit. Photochem. Photobiol. Sci. *5* (*8*), 748–754 https://doi.org/10.1039/b602160c. PubMed

Merzlyak, M.N., Gitelson, A.A., Chivkunova, O.B., and Rakitin, V.Y. (1999). Non-destructive optical detection of pigment changes during leaf senescence and fruit ripening. Physiol. Plant. *106* (*1*), 135–141 https://doi.org/10.1034/j.1399-3054.1999.106119.x.

Merzlyak, M.N., Solovchenko, A.E., and Gitelson, A.A. (2003). Reflectance spectral features and non-destructive estimation of chlorophyll, carotenoid and anthocyanin content in apple fruit. Postharvest Biol. Technol. *27* (*2*), 88–103 https://doi.org/10.1016/S0925-5214(02)00066-2.

Mevik, B-H., Wehrens, R., and Liland, K. (2018). pls, Partial Least Squares and Principal Component Regression. R package version 2.7–0. https,//CRAN.R-project.org/package=pls.

Musacchi, S., and Serra, S. (2018). Apple fruit quality, Overview on pre-harvest factors. Sci. Hortic. (Amsterdam) *234*, 409–430 https://doi.org/10.1016/j.scienta.2017.12.057.

Nicolai, B.M., Beullens, K., Bobelyn, E., Peirs, A., Saeys, W., Theron, K.I., and Kammertyn, J. (2007). Non destructive measurement of fruit and vegetable quality by means of NIR spectroscopy, A review. Postharvest Biol. Technol. *46* (*2*), 99–118 https://doi.org/10.1016/j.postharvbio.2007.06.024.

Peirs, A., Schenk, A., and Nicolai, B.M. (2005). Effect of natural variability among apples on the accuracy of VIS-NIR calibration models for optimal harvest date predictions. Postharvest Biol. Technol. *35* (*1*), 1–5 https://doi.org/10.1016/j.postharvbio.2004.05.010.

Pflanz, M. (2014). A methodical approach for non-destructive estimation of plant pigments by means of remission spectroscopy applied in fruit and vegetable analyses. PhD dissertation, Humboldt University, Berlin.

R Core Team. (2018). R, a Language and Environment for Statistical Computing (Vienna, Austria: R Foundation for Statistical Computing). https,//www.R-project.org/.

Rizzolo, A., Vanoli, M., Eccher Zerbini, P., Jacob, S., Torricelli, A., Spinelli, L., Schouten, R.E., and Tijskens, L.M.M. (2009). Prediction ability of firmness decay models of nectarines based on the biological shift factor measured by time-resolved reflectance spectroscopy. Postharvest Biol. Technol. *54* (*3*), 131–140 https://doi.org/10.1016/j.postharvbio.2009.05.010.

Streif, J. (1996). Optimum harvest date for different apple cultivars in the 'Bodensee' area. In A. de Jager, D. Johnson, and E. Hohn, eds. (Brussels: COST 94. ECSC-ECEAEC), p.15–20.

Subedi, P., Walsh, K., and Purdy, P. (2013). Determination of optimum maturity stages of mangoes using fruit spectral signatures. Acta Hortic. *992*, 521–528 https://doi.org/10.17660/ActaHortic.2013.992.64.

Tijskens, L.M.M., Eccher Zerbini, P., Schouten, R.E., Vanoli, M., Jacob, S., Grassi, M., Cubeddu, R., Spinelli, L., and Torricelli, A. (2007). Assessing harvest maturity in nectarines. Postharvest Biol. Technol. *45* (*2*), 204–213 https://doi.org/10.1016/j.postharvbio.2007.01.014.

Van Beers, R., León Gutiérrez, L., Schenk, A., Nicolai, B., Kayacan, E., and Saeys, W. (2014). Optical measurement techniques for the ripeness determination of Braeburn apples. Int. Conf. Agri. Eng. (Zurich, Switzerland).

Walsh, K.B. (2016). The evolution of spectrophotometers used in fruit quality assessment. Acta Hortic. *1119*, 203–208 https://doi.org/10.17660/ActaHortic.2016.1119.28.

Zude, M. (2003). Comparison of indices and multivariate models to non-destructively predict the fruit chlorophyll by means of visible spectrometry in apple fruit. Anal. Chim. Acta *481* (*1*), 119–126 https://doi.org/10.1016/S0003-2670(03)00070-9.

Zude, M., and Herold, B. (2002). Optimum harvest date determination for apples using spectral analysis. Eur. J. Hortic. Sci. *67*, 199–204.

Zude-Sasse, M., Truppel, I., and Herold, B. (2002). An Approach to non-destructive apple chlorophyll determination. Postharvest Biol. Technol. *25* (*2*), 123–133 https://doi.org/10.1016/S0925-5214(01)00173-9.

Photochemical & Photobiological Sciences
https://doi.org/10.1007/s43630-021-00164-1

ORIGINAL PAPERS

Chlorophyll- and anthocyanin-rich cell organelles affect light scattering in apple skin

Stefan A. Lohner[1] · Konni Biegert[2] · Ansgar Hohmann[1] · Roy McCormick[2] · Alwin Kienle[1]

Received: 28 September 2021 / Accepted: 21 December 2021

Abstract

Apple skin contains several groups of strongly absorbing cell organelles with pigments that change dynamically in type and concentration during fruit maturation. Chlorophylls and carotenoids, both primarily involved in photosynthesis, are found in the grana of chloroplasts, while anthocyanin vacuolar inclusions (AVIs) accumulate for light protection in red-skinned cultivars. A Mie model describing light scattering by absorbing spherical particles in a non-absorbing medium allowed to theoretically investigate the explicit influence of grana and AVIs on the effective scattering coefficient μ_s' and the absorption coefficient μ_a. The reconstruction of the complex refractive indices of the organelles predicted anomalous dispersion, i.e., a local increase in the real part of the refractive index in the spectral regions with high chlorophyll and anthocyanin absorption, in agreement with the Kramers–Kronig relations. As a result, peaks in μ_s' were predicted to be shifted to longer wavelengths compared to the corresponding μ_a bands. This selective scattering effect was confirmed experimentally with integrating sphere measurements for red- or green-skinned apple samples of the cultivars 'Elstar', 'Gala' or 'Jonagold'. Comparison between simulations and measurements indicated that the Soret bands of chlorophyll *a* and chlorophyll *b* are at 435 nm and 469 nm, respectively, and overlap with the absorption of carotenoids, whose red-most edge is at 488 nm. For anthocyanin absorption, a pronounced blue shift from 550 to 520 nm was observed, indicating structural or chemical changes of AVIs.

Graphical abstract

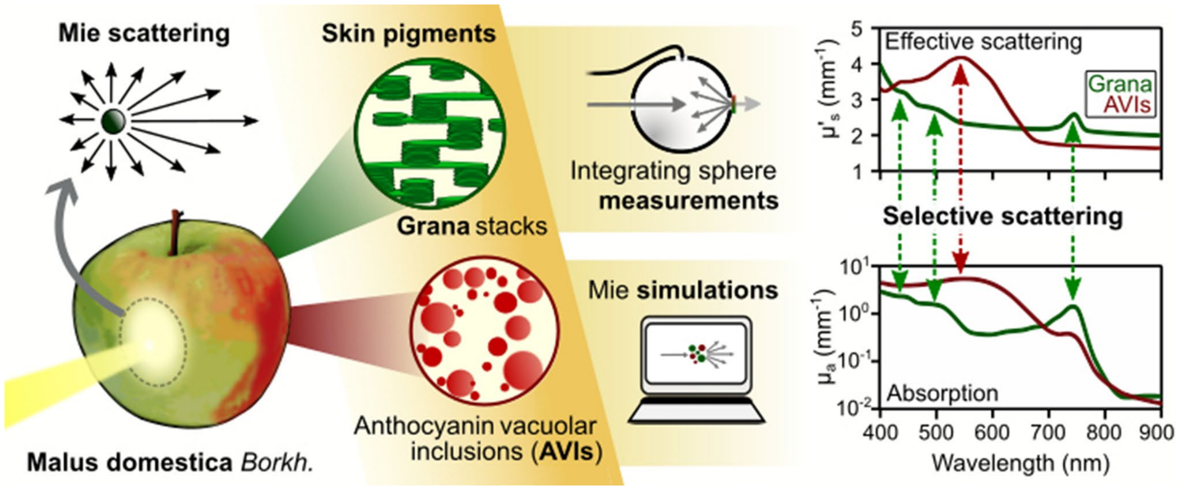

Keywords Selective scattering · Mie's theory · Grana · Anthocyanin · Carotenoids

---

✉ Stefan A. Lohner
stefan.lohner@ilm-ulm.de

Extended author information available on the last page of the article

1 Introduction

Some of the most obvious changes during apple maturation concerns the pigmentation of the apple skin. Depending on the cultivar, the background coloration changes from green to yellow and the red blush color increases. The overall color impression is the combined result of several pigment types, which absorb the incident sunlight in one or more specific spectral bands. As in all higher plants, the chlorophylls in particular play an important role in photosynthesis by converting sunlight into chemical energy. Chlorophyll *a* and chlorophyll *b* have two distinct absorption bands, the more pronounced in the blue wavelength region (Soret band) and the second in the red wavelength region (Q band), while the green components of the incident light are almost completely reflected [1]. The light reactions of photosynthesis take place in special cell organelles, the chloroplasts, whose thylakoid membrane contains various light-collecting protein complexes. Local stratification of the membrane results in the formation of disc-shaped structures called granules (grana) with a typical diameter of around 500 nm [2]. In addition to chlorophylls, various carotenoids, including carotenes (e.g., β-carotene) and xanthophylls (e.g., lutein), are involved in the light reaction in the thylakoid membrane [3]. The yellow coloration of apple skin, however, is determined by carotenoids independent of the photosynthetic system, e.g., xanthophylls such as lutein, neoxanthin and violaxanthin, which are esterified with fatty acids [4]. The third important pigment class is phenolic compounds, e.g., flavonoids and anthocyanins, which accumulate in cell vacuoles especially at the end of maturation [5]. They have a number of different functions, including photo-protection against harmful radiation in the ultraviolet (UV) and visible (Vis) spectral range or scavenging free radicals [6, 7]. Cyanidin 3-*O*-galactoside ('idaein') is the predominant anthocyanin found in apples, it absorbs light in the green spectral range and causes the intense red coloration of many apple cultivars [5]. In vacuoles, anthocyanins, together with other copigments, form complexes [8], now being referred to as AVIs, that are separated from the surrounding cell fluid but presumably have no membrane or distinct internal structure. All of these plant pigment types exhibit complex light interactions depending on their occurrence in particular cell organelles, although the specific effects on macroscopic absorption and scattering properties are still largely unknown.

In cell suspensions of green algae with high chlorophyll content, an early observed effect was selective scattering [9, 10] with a substantial increase in the effective scattering coefficient μ_s' for the prominent absorption bands as associated with chlorophyll. Using Mie's theory and assuming simultaneously absorbing and scattering particles, indications of a correlation between the spectral course of absorption and scattering parameters with the structural properties of chloroplasts were found [11, 12]. In this context, determining the complex refractive index for the pigment-containing organelles plays an important role. The complex refractive index is generally composed of a wavelength dependent real part (ratio between the speed of light in vacuum to the speed of light in a medium) and an imaginary part, which is directly linked to the absorption properties. Both parts are physically dependent on each other, so that in case of strong absorption, i.e., an increase of the imaginary part, the real part of the refractive index also changes in a certain wavelength range [13, 14]. For the chlorophyll-containing grana stacks in chloroplast, recent studies have reconstructed the complex refractive index by considering their molecular structure and their influence on light propagation [15]. In particular, the influence of plant pigments on the bulk optical properties of apple has so far mainly been the result of experimental investigations, based on integrating sphere measurements. For example, Saeys et al. [16] and Rowe et al. [17] reported an increase in μ_s' at spectral bands corresponding to high pigment and water absorption and attributed this to the increase in the imaginary part of the refractive index [18]. However, Zamora-Rojas et al. [19] proposed in a similar study examining animal tissue that the effect was more likely the result of a faulty separation between absorption and scattering and that increasing the imaginary part should not result in pronounced peaks in μ_s'. Thus, the influence of pigment-containing structures on the optical properties is still actively under discussion.

At the microscopic level, the interaction of light with grana and AVIs can be described approximately by scattering of spherical and absorbing particles within a non-absorbing surrounding medium. For this case, Mie's theory provides an analytical solution to Maxwell's equations, which gives exact results for arbitrary particle sizes and refractive index differences [20]. Model simulations recently described by Lohner et al. [21], developed to study the influence of air pores and starch granules on scattering in apple core and cortex tissues, could be adapted for pigment structures.

The aim of this work was to investigate the influence of pigment-containing organelles such as grana and AVIs on the optical properties of apple skin. Both an experimental and a theoretical approach were chosen each with the objective to determine μ_a and μ_s' in the Vis spectral range. The application of Mie's theory for grana and AVIs required the reconstruction of their complex refractive indices, which was considered as an essential part of the modeling process. Additional measurements with an integrating sphere were intended to verify from an experimental point of view the extent to which differences in the optical properties of apple skin with either high chlorophyll or high anthocyanin content can be determined.

2 Theoretical background

2.1 Mie's theory

Mie's theory (also called Lorenz–Mie theory) is an analytical solution to Maxwell's equations and describes electromagnetic scattering by a homogeneous and isotropic sphere in a non-absorbing medium. The calculation is based on the size parameter $x = \pi d/\lambda$, as the ratio between sphere diameter d and light wavelength λ, and the ratio m between the complex refractive index n_{sph} of the sphere and the real refractive index n_{med} of the surrounding non-absorbing medium. Mie's theory provides exact solutions for the scattering coefficient μ_s, the phase function $P(\theta, \phi)$, which describes the scattered light intensity in spherical coordinates, the anisotropy factor g, the effective scattering coefficient $\mu_s' = (1-g)\mu_s$ and the absorption coefficient μ_a [20]. Since biological particles are usually subject to a broad size distribution, a polydisperse Mie model must be developed, in which the optical properties are averaged over different particle sizes, taking into account their volume fraction [22]. A detailed overview for the implementation using the *MatScat* function library [23] was recently presented by Lohner et al. [21]. It must be noted that for air and water, the absorption in the Vis is negligible, which means that in these cases the real part of the complex refractive index is sufficient for calculating the scattering properties. For pigment-containing particles, however, significant absorption has to be expected in this spectral range, which requires consideration of the complex refractive index.

2.2 Reconstruction of the complex refractive index

The refractive index plays an important role for light propagation in scattering media. In general, it is defined as complex number

$$n_{\text{sph}} = \eta + i\kappa, \tag{1}$$

with a real part η and an imaginary part κ. While the real part describes the ratio between the speed of light in vacuum and the speed of light in a medium, κ, also called extinction coefficient, defines the attenuation. The two parts are not completely independent of each other, but rather connected by Hilbert transforms, which are mathematically described by the Kramers–Kronig relations [24]. These are of particular importance for the investigation of biological tissue, since η and κ are usually only partially known or even not at all. In many cases, the real part can be determined experimentally, e.g. based on dispersion and refraction properties of a medium. The imaginary part is related to the absorption coefficient μ_a and the molar extinction coefficient ϵ_M according to

$$\kappa(\lambda) = \frac{\mu_a(\lambda)\,\lambda}{4\pi} = \frac{\ln 10\,\epsilon_M(\lambda)\,c_M\,\lambda}{4\pi}, \tag{2}$$

with wavelength λ and the molar concentration c_M [25]. Even though estimates can be made independently for the real and imaginary parts, they must be linked via the Kramers–Kronig relations to maintain self-consistency. Especially in the wavelength range where strong absorption prevails, they lead to a physically reasonable adaptation of both parts. In this work, the function library presented by Lucarini et al. [24] was used with a numerical implementation of the Kramers–Kronig relations that provides the complex refractive index based on an estimate for κ over the full spectral range from UV to IR and a single estimate for η.

2.3 Chloroplasts and grana

Apple skin has a mean thickness of about 100–150 µm and can be divided into three different layers: the epidermis with cuticle on top and the hypodermis underneath [28]. With diameters in the range of 20–50 µm, the cell size of the epidermis and hypodermis is significantly smaller than that of the cortex tissue [29]. Their relatively dense cell structure is interrupted by many small air pores, which are important for gas exchange [30]. Photosynthesis takes place in certain cell organelles, the chloroplasts, which are found in large concentrations in apple skin [31, 32]. Chloroplasts essentially contain an aqueous phase, the stroma, interspersed with thylakoid membranes. These form local layered structures called grana, which are connected by individual membrane layers of stromal thylakoids. Figure 1A shows schematically the structure of grana and their composition, which in reality can vary largely in shape and size. In higher plants, mostly cylindrical grana stacks of 10–20 membrane layers and dimensions of about 500 nm × 300 nm are reported [2, 33]. An enlarged view of two superimposed thylakoid layers and their substructure with dimensions reported by Daum et al. [26] is shown in Fig. 1B. The membranes enclose a further cavity of aqueous phase, the so-called lumen. The membrane itself contains 20% lipids and 80% photoactive proteins, notably photosystem II (PSII) and light-harvesting complex II (LHCII) [34]. Together, these proteins form the supercomplex PSII/LHCII, which is essential for photosynthesis. Both the size and molecular composition of this protein complex have been extensively studied [35, 36]. According to Wei et al. [27] for spinach leaves, it has a size of 26 nm × 11 nm × 14 nm and contains 80 chlorophyll *a*, 25 chlorophyll *b* and 28 carotenoid

Fig. 1 **A** Schematic illustration of a chloroplast consisting of aqueous phase (stroma) and thylakoid membranes forming cylindrical stacked structures (grana) with typical sizes of 500 nm × 300 nm. **B** The thylakoid membrane encloses the lumen, also aqueous phase, and contains 20% lipids and 80% photoactive proteins. In particular, photosystem II (PSII) and the light-harvesting complex II (LHCII) are significantly involved in photosynthesis. The dimensions are taken from Daum et al. [26]. In **C**, the volume fractions of the individual components are shown in an overview, for the PSII/LHCII complex indicating the number of molecules *N* of chlorophyll *a*, chlorophyll *b*, and carotenoids [27]

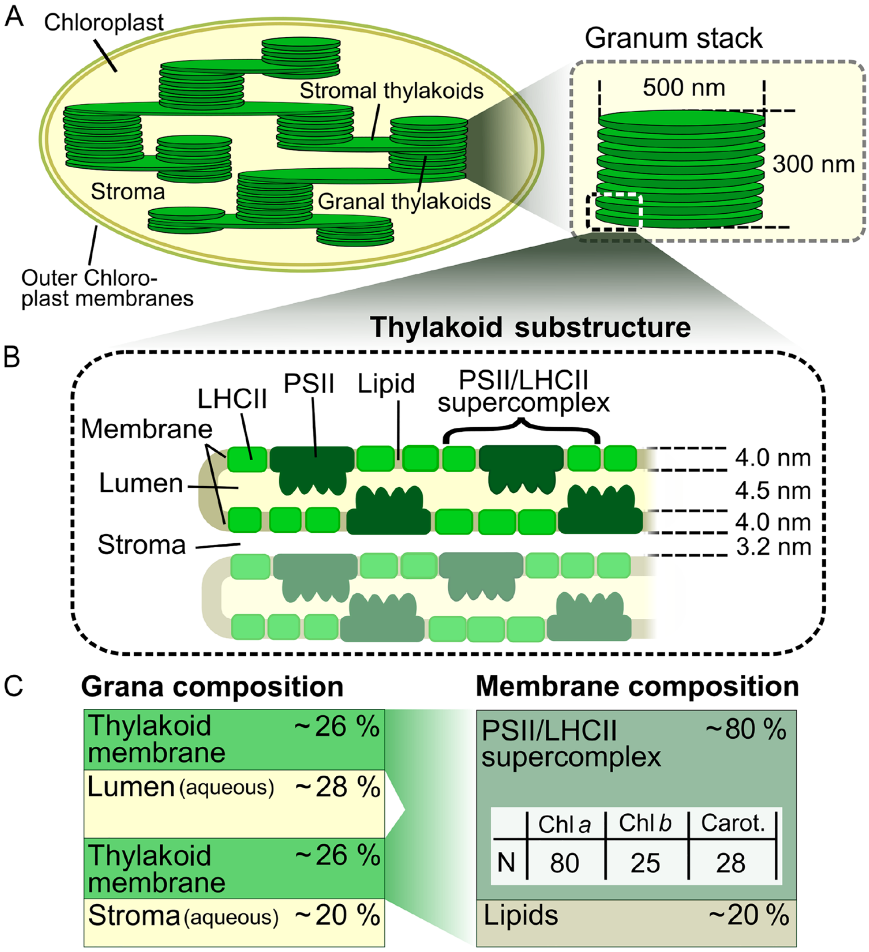

molecules, resulting in molar concentrations of 0.063 mol/l, 0.020 mol/l and 0.022 mol/l, respectively. As shown in an overview in Fig. 1C, approximately 48% of the grana volume is accounted for by the aqueous phase and 52% by the thylakoid membrane, which in turn consists of 80% pigment-containing protein complex and 20% lipids.

2.4 Anthocyanic vacuolar inclusions (AVIs)

In contrast to the rather well known structure of chloroplasts and grana, relatively little is known about anthocyanin-containing structures in apple skin. These can be found in the aqueous vacuoles along with various sugars, organic acids, amino acids and other phenolic constituents [37]. Flavonols such as quercetin-3-*O*-galactoside ('hyperoside') or quercetin-3-*O*-rutinoside ('rutin') with absorption in the near UV range are among the most abundant phenolics ahead of anthocyanins, in particular idaein, with an absorption maximum in the green spectral range [38]. Anthocyanins have the ability to form molecular non-covalent bonds depending on various external factors, which allows the formation of anthocyanin complexes. Of particular importance are π-stacking interactions of aromatic rings underlying the mechanisms of self-association, i.e., binding between anthocyanin molecules, and co-pigmentation, i.e., binding of anthocyanin molecules with other phenols [39]. Complex formation is often favored in an acidic pH environment, resulting in significant differences in molar extinction bands, both spectrally and in absolute terms, between free and bound pigments [39]. Depending on the pigment type and pH, both bathochromic and hypsochromic shifts of the absorption bands are observed, which explains the importance of these processes for color variation [39]. In cell vacuoles of apple skin, similar to other plants tending to have low pH in the vacuoles, the formation of so-called AVIs is reported [40], which can probably be regarded as a local accumulation of these anthocyanin complexes. According to Bae et al. [8], their diameter ranges from about 0.5

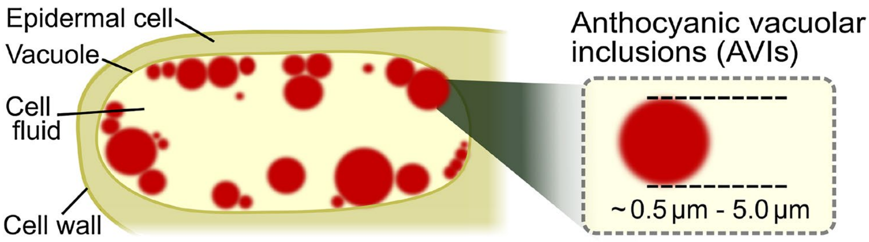

Fig. 2 Schematic illustration of an epidermal cell vacuole with AVIs having an average size between 0.5 and 5.0 µm

to 5.0 µm for apple skin, with generally high variability in shape and size, as schematically shown in Fig. 2. The observation that AVIs appear to have no outer membrane [8] also supports the interpretation of pigment complexes bound by intra- and intermolecular interactions. The dynamic formation of AVIs appears very complex, for example, Kallam et al. [41] found that the formation of AVIs is related to pH, with the acidic environment in the pH range of 4–5 likely changing during maturation [42]. In addition, the influence of flavonols and interactions with other biopolymers such as pectin and glycosides, whose concentrations in the vacuole are subject to considerable changes during maturation, are also conceivable [39].

3 Materials and methods

3.1 Integrating sphere setup

To determine the optical properties of apple skin over a wide spectral range in the Vis, an integrating sphere setup recently described by Foschum et al. [43] and Bergmann et al. [44] was used. It consists of a 3D-printed and barium sulfate-coated sphere with an inner diameter of 150 mm, combined with a halogen light source and two spectrometers: one for the VIS from 200 to 1100 nm (Maya2000Pro, Ocean Optics, USA) and one for the near-infrared (NIR) from 900 to 1700 nm (NIRQuest512-1.7, Ocean Optics, USA). The light source is a 100 W halogen lamp (Halostar Starlite, Osram, Germany). During the measurement process, the absolute reflectance and transmittance spectra of a sample with known thickness is recorded over a wide spectral range. The evaluation is based on Monte Carlo simulations taking into account sample geometry, refractive index, and anisotropy factor, and provides a lookup table to determine the corresponding μ_s' and μ_a. For sample preparation, a peeler was used to remove pieces of skin from both the sun and shade sides of the apples, and the remaining pulp was carefully removed completely with a scalpel. The thickness of the skin samples was determined individually with a micrometer screw and taken into account in the following evaluation, the arithmetic mean value was 0.22 ± 0.07 mm. Both skin pieces were measured in a cuvette between two N-BK7 glass slides (34-427, Edmund Optics, USA), taking care to completely cover the sample port, which has a diameter of 25 mm. The addition of a few drops of water prevented the formation of air bubbles between the slides, which would lead to undesirable influences on the measurement process. The sample cuvette was measured from each side at two positions rotated by 180°, and the optical properties were then calculated as the arithmetic mean with the corresponding standard deviation from four individual measurements. The spectrally resolved refractive index and the geometry of the glass sides were taken into account accordingly in the evaluation.

3.2 Fruit samples

The examined apple samples are identical to those investigated by Lohner et al. [21, 45]. They were collected from the research orchard of the Kompetenzzentrum Obstbau Bodensee (47° 46′ 01.8″ N 9° 33′ 30.3″ E) during the 2019 harvest season between July and November. The cultivars were *Malus domestica* ‘Gala’ (Simmons/Buckeye), ‘Elstar’ (P.C.P.), and ‘Jonagold’ (Novajo). The selection of cultivars and the measurement period covered the early to late harvest period with different ripening characteristics and thus variable pigment content. Six apples were picked weekly and measured with a laboratory setup on the sun and shade side of each apple with four repetitions.

4 Results and discussion

4.1 Complex refractive indices of grana and AVIs

The reconstruction of the complex refractive index of the grana and AVIs required an estimation of their absorption properties over a wide spectral range from UV to NIR. As an approach, the individual components and their volume fractions were estimated on the basis of literature data. The full absorption spectra were then calculated as a linear combination of corresponding reference absorption spectra, as shown in Fig. 3A, B.

According to Fig. 1C, about 48% of the grana consists of aqueous phase, for which the absorption of water was

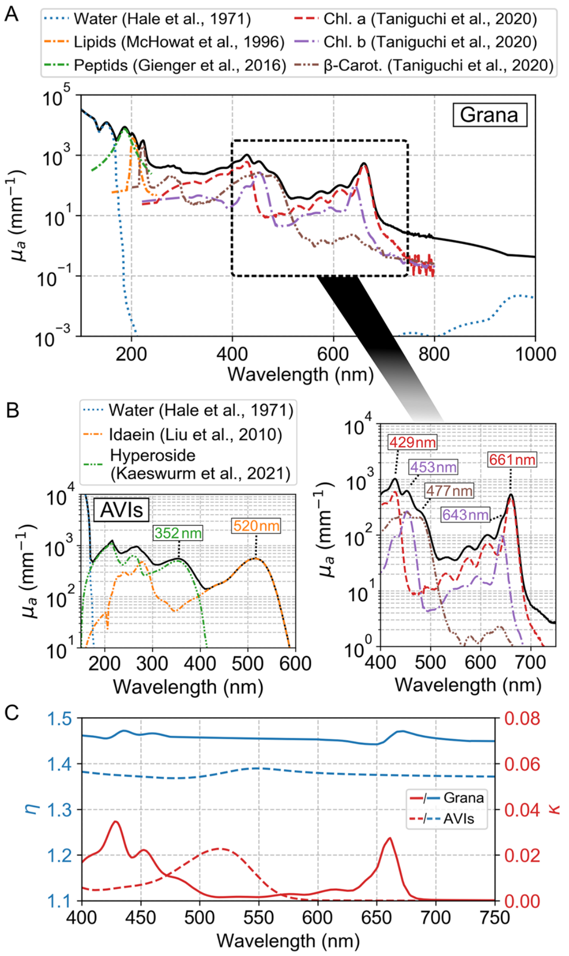

Fig. 3 **A** Reconstructed absorption coefficient μ_a of grana in the UV to Vis spectral region obtained by linear combination of weighted reference spectra considering aqueous phase, the thylakoid membrane composed of lipids, and the pigment-containing PSII/LHCII protein complex. The enlarged image section on the right below shows the Vis spectral region in detail with the Soret bands of chlorophyll *a* and chlorophyll *b* at 429 nm and 453 nm, their Q bands at 643 nm and 661 nm, overlaid by the absorption maxima of *β*-carotene with maximum at 453 nm and shoulder at 477 nm. **B** Reconstructed μ_a of AVIs composed of water, hyperoside, and idaein with dominant absorption bands at 352 nm and 520 nm, respectively. **C** Reconstructed complex refractive indices of grana and AVIs with real part η (blue, upper curves) and imaginary part κ (red, lower curves)

assumed [46]. Due to the excitation of electronic transitions, it absorbs light in the UV at wavelengths below 180 nm, while in the Vis the absorption is negligible and increases in the NIR beyond a wavelength of 900 nm. The remaining 52% of the grana volume is occupied by the thylakoid membrane, which contains the pigment-containing protein complexes and lipids. The absorption spectrum of the lipids was adapted from McHowat et al. [47], who reported an absorption peak at a wavelength of 203 nm with a molar extinction $\epsilon_M = 2 \cdot 10^4\ \text{M}^{-1}\,\text{cm}^{-1}$ for phospholipids commonly found in cell membranes. Another absorption band in the UV at 187 nm can be attributed to the excitation of peptide bonds, which are present in large numbers in the protein complex of the membrane [48]. It was adapted from Gienger et al. [25] with $\epsilon_M = 4 \cdot 10^4\ \text{M}^{-1}\,\text{cm}^{-1}$. The pigments contained in the protein complex begin to absorb at about 200 nm, with maxima known to be mainly located in the Vis. In addition to chlorophyll *a* and chlorophyll *b*, *β*-carotene was chosen as an example for carotenoids because a molar extinction spectrum in diethyl ether was also available from Taniguchi and Lindsey [49, 50]. In general, the absorption properties of the carotenoids are quite similar, at least from a qualitative point of view [51]. Chlorophyll *a* and *b* exhibit absorption bands at wavelengths of 429 nm and 453 nm with $\epsilon_M = 1.1 \cdot 10^5\ \text{M}^{-1}\,\text{cm}^{-1}$ and $\epsilon_M = 2 \cdot 10^4\ \text{M}^{-1}\,\text{cm}^{-1}$ (Soret bands), and at 661 nm and 644 nm with $\epsilon_M = 8.6 \cdot 10^5\ \text{M}^{-1}\,\text{cm}^{-1}$ and $\epsilon_M = 5.6 \cdot 10^5\ \text{M}^{-1}\,\text{cm}^{-1}$ (Q bands), respectively. The absorption spectrum of *β*-carotene solubilized in hexane shows three adjacent absorption bands at wavelengths of 429 nm, 451 nm, 477 nm, where the maximum extinction is given as $\epsilon_M = 1.4 \cdot 10^5\ \text{M}^{-1}\,\text{cm}^{-1}$ [50]. It should be noted that the absorption bands of these pigments behave differently in the solvent than in the protein environment, both in absolute values and in their spectral position. As shown in Fig. 3A, the absorption spectrum of grana was calculated as the sum of the weighted reference spectra, where μ_a was calculated from the indicated molar extinction coefficients according to Eq. (2). The enlarged figure in the wavelength range from 400 to 750 nm allows the assignment between characteristic absorption bands to the individual pigments in more detail.

Figure 3B shows the analogous procedure for modeling the absorption spectrum of the AVIs. It was assumed that the anthocyanin complexes in the case of copigmentation can be approximately described by an aqueous solution of 50 mm idaein and 100 mm hyperoside. The ratio of 2:1 for flavonols and anthocynanins was assumed regarding the results of Huber et al. [38] at the end of the maturation period. The absorption spectrum of idaein was taken from Liu et al. [52] and shows a broad absorption band with a maximum at a wavelength of 520 nm. Following Fuleki and Francis [53], the absorption maximum was assumed to be $\epsilon_M = 4.8 \cdot 10^4\ \text{M}^{-1}\,\text{cm}^{-1}$. The absorption spectrum of hyperoside was taken from Kaeswurm et al. [54] and shows two smaller absorption bands with maximum wavelengths around 260 nm and 352 nm, respectively. The spectrum was scaled to $\epsilon_M = 2.2 \cdot 10^4\ \text{M}^{-1}\,\text{cm}^{-1}$ at 352 nm [54]. It is noted that, contrary to this simplified assumption, in reality both the molar extinction and the spectral position of the absorption bands probably change during complex formation.

Based on the reconstructed absorption spectra, the imaginary parts κ of the complex refractive indices were calculated using Eq. (2). The real parts η were then computed using the function library provided by Lucarini et al. [24]. To compensate for the unavoidable errors caused by uncertainties in the estimation of the imaginary part, it proved useful to provide an estimate for the real part. For grana, a refractive index of 1.42 was chosen according to Margalit et al. [55]. Since AVIs do not have a distinct structure, a lower refractive index of 1.38 seems plausible. The results for self-consistent real and imaginary parts according to Kramers–Kronig relations are shown in Fig. 3C. Whereas κ widely corresponds to the modeled absorption properties, the real part η shows anomalous dispersion in the region of high absorption, i.e., the refractive index increases in these regions with increasing wavelength. This behavior leads simultaneously to a local increase of η by about 3% with the spectral maximum shifted to longer wavelengths relative to the absorption band. In the case of grana, κ shows a maximum at 429 nm with 0.035 and at 661 nm with 0.028, while η is in the range of 1.45. In the case of AVIs, κ reaches a maximum of 0.023 at 520 nm, while η lies in the range of 1.38.

For comparison, the results of Capretti et al. [15] were considered, who similarly modeled the complex refractive index of grana. For the Q band of chlorophyll *a* they reported also anomalous dispersion with $\kappa = 0.014$ combined with a local change of η by up to 5%. Despite differences in the assumed composition and reference spectra used for modeling, the magnitude of the obtained complex refractive index could thus be confirmed. The correct application of the Kramers–Kronig relations, which are certainly subject to considerable uncertainty in the case of heterogeneous structures and only partly known absorption properties, has a major influence on the results. This is particular evident in a less pronounced anomalous dispersion in our results despite the comparatively higher extinction. Generally, it must be taken into account that the assumptions are based on results of different studies and therefore correspond only to a limited extent to the conditions for real chloroplasts in apple skin. The composition and content of different chlorophyll and carotenoids as well as the structure of the grana itself may differ. Since quantitative absorption spectra of the investigated pigments are only available for different types of solvents, the characteristic absorption bands are spectrally shifted compared to the natural protein environment. Nevertheless, the modeled absorption spectra provide a good overview of the influence of the individual components and allow a qualitative assignment of characteristic absorption bands. In the case of grana in particular, it becomes clear that, in contrast to the widely known Q bands of chlorophyll in the red spectral range, several broad bands overlap at wavelengths below 500 nm, whose local maxima can be assigned to the Soret bands of chlorophyll *a* and *b* and β-carotene with increasing wavelengths.

4.2 Simulated optical properties of grana and AVIs using a Mie model

Based on the reconstructed complex refractive indices, a polydisperse Mie model was used to simulate the optical properties of grana and AVIs. In both cases, a log-normal size distribution was assumed, with a mean diameter for grana of 0.5 µm and for AVIs of 2.5 µm with a standard deviation of 0.1 µm and 0.5 µm, respectively. The surrounding medium in both cases was assumed to be water with the refractive index reported by Hale and Querry [56]. In the absence of literature data on the volume concentrations of grana and AVIs in apple skin, these were estimated to be 0.5% and 5%, respectively, which was considered as a realistic chlorophyll and anthocyanin content. For example, this volume concentration would correspond to 1.1 mg of idaein per 1 g fresh weight apple skin. In view of the subsequent comparison with real measurements, it was taken into account that the scattering properties of the apple skin are influenced not only by the grana and AVIs but also by other scattering particles, such as small air pores of the intercellular space. These typically lead to a steady decrease in μ_s' with increasing wavelength, which can be described by a power law. For the simulation of these additional scattering particles, air pores with an average size of 3 µm and a porosity of 5% were assumed, considering microscopic and micro-CT measurements [28, 57].

The results of the simulations for μ_s, g, μ_s' and μ_a are shown in Fig. 4 compared for grana, AVIs, and air pores. For grana and AVIs, μ_s lies in the range of 2-6 mm^{-1}, whereas for air pores it is about 20 mm^{-1} due to the much higher refractive index difference. Larger differences can also be observed for the anisotropy factor g, which ranges from 0.9 to 0.8 for grana, from 0.95 to 0.90 for AVIs, and from 0.90 to 0.94 for air pores. In Fig. 4C, μ_s' is shown for air pores in combination with grana or AVIs to realistically reproduce scattering in red and green apple skin. For comparison, scattering of solely air pores is also shown and follows a power law $\propto \lambda^{-0.58}$. In spectral regions with high absorption, several corresponding peaks also occur in μ_s'. For grana two small peaks at 437 nm and 461 nm correspond to the Soret bands of chlorophyll *a* and *b*, respectively, while the more pronounced peak at 671 nm corresponds to the Q band of chlorophyll *a*. All three are shifted between 8 and 10 nm to longer wavelengths relative to their associated absorption band. For AVIs, a broad increase of μ_s' appears with maximum at 547 nm and a 27 nm red-shift of the central wavelength compared to idaein absorption.

When evaluating these results, it must be taken into account that the application of a Mie model requires different

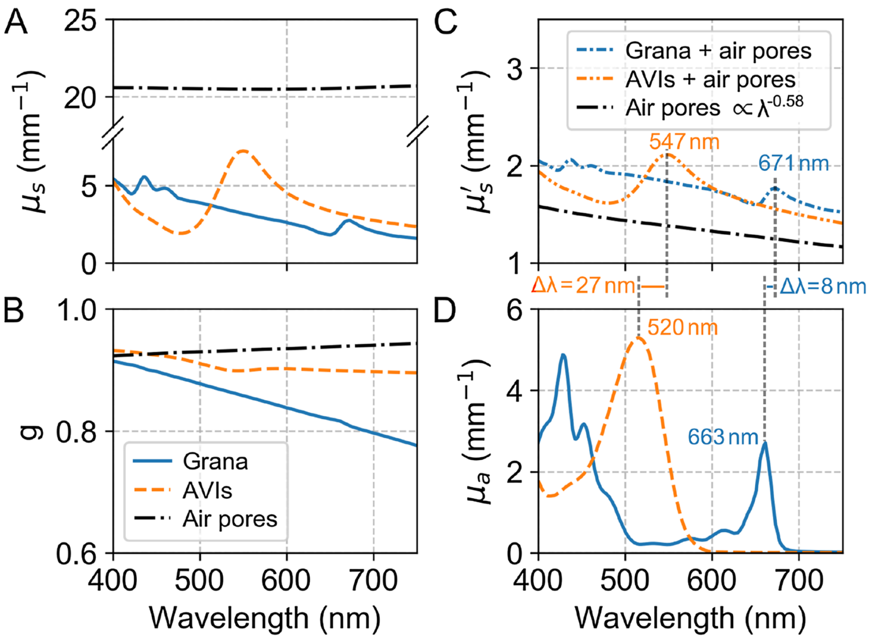

Fig. 4 Modeled scattering coefficients μ_s (**A**), anisotropy factors g (**B**), effective scattering coefficients μ_s' (**C**), and absorption coefficients μ_a (**D**) for grana, AVIs, and air pores with a mean size of 3 µm in apple skin

assumptions. The approximation of cell organelles as spherical particles seems evident in the case of the AVIs, whereas the grana have a more cylindrical shape. The expected deviations, however, are rather small at around 5%, as shown by Grenfell et al. [58] using the example of cylindrical ice crystals with an unchanged volume-to-surface ratio. The assumed size distributions and volume concentrations of AVIs and grana, for which only sparse data are available, probably have a larger influence. For example, studies of Phan et al. [59, 60] showed that besides to small granules in apple skin, chloroplasts with few or even single, but larger granules are present in the pulp. Other microscopic studies of apple skin indicated an overall large variability in shape, size, volume concentration, and molecular composition of all types of organelles [8, 32]. The Mie model further assumes a homogeneous refractive index for the particles in the sense of an effective medium approximation, whereby changes in the refractive index due to the microstructure are not taken into account. Although this approximation is often used for biological tissue, its range of validity is difficult to estimate, especially for only roughly studied structures such as AVIs.

4.3 Integrating sphere measurements to determine the optical properties of apple skin

To experimentally investigate the influence of strongly absorbing pigments on the optical properties of apple skin, three different apple cultivars were measured with an integrating sphere during maturation. Over a period of ten weeks, a sample set of six apples with four measurement repetitions was examined weekly using samples from the sun side. The mean μ_s' and μ_a and their standard deviation were determined by averaging both the results of the repetitions and all apples of the same cultivar on a weekly basis. The results are shown in Fig. 5 for the cultivars 'Elstar', with high chlorophyll content at the beginning of maturation, and 'Gala' with a high anthocyanin content at the end of maturation. The insets show images of the skin color from the first and last week of the studied period.

For 'Elstar' in Fig. 5A, μ_s' largely follows a power law of the form $\mu_s'(\lambda) \propto \lambda^{-\alpha}$, i.e., μ_s' decreases with increasing wavelength. In the first week, $\alpha = 1.60$ was determined based on a regression. In the following weeks, μ_s' shows a continuous decrease, e.g., at a wavelength of 600 nm from about 2.0 mm^{-1} in week 11 to 1.0 mm^{-1} in week 21. Especially in week 11, μ_s' shows several peaks in the wavelength range between 400 and 500 nm as well as at 678 nm. These peaks appear to correspond to the absorption bands in μ_a, with a peak at 678 nm known to be associated with chlorophyll a. It decreases from 1.38 mm^{-1} in week 11 to 0.36 mm^{-1} in week 21. In the spectral range below 500 nm, several smaller peaks stand out, with relatively high absorption between 1.0 and 3.0 mm^{-1}. At the end of maturation in week 21, μ_a increases in the range of about 520 nm, which can be associated with anthocyanins and the corresponding slight red coloration.

Figure 5B shows the optical properties for the skin of 'Gala' apples, which exhibit a much more intense red coloration compared to 'Elstar'. Also in this case μ_s' follows a

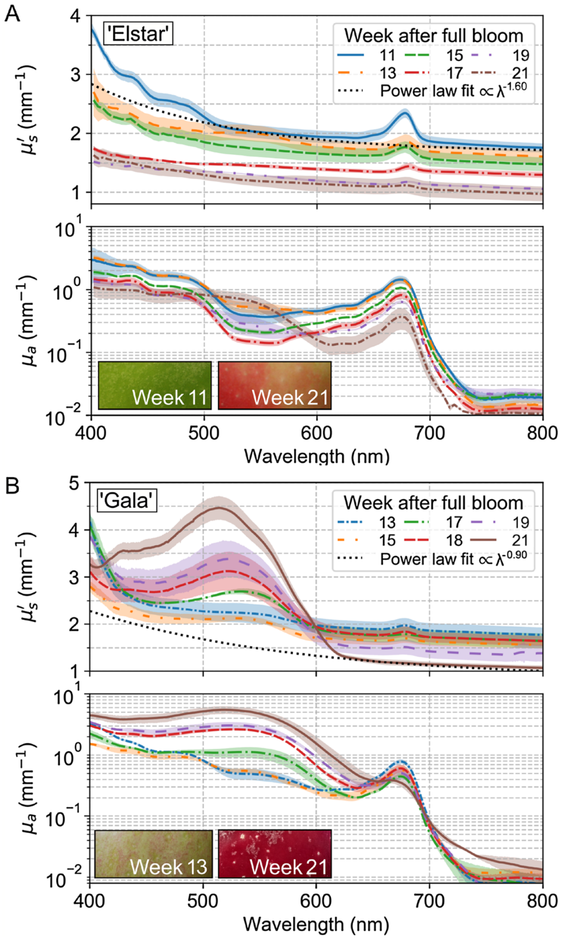

Fig. 5 Spectrally resolved effective scattering coefficient μ_s' and absorption coefficient μ_a of apple skin measured for the cultivars 'Elstar' (**A**) and 'Gala' (**B**) during maturation. The shaded areas indicate the standard deviation based on a sample set of six apples per week with four measurement repetitions each. To determine the scattering not directly related to pigments, e.g., caused by air pores, a power law was fitted in spectral regions with negligible pigment absorption in **A** at week 11 and in **B** at week 21 after full bloom. The insets show color images of apple skin taken with an SLR camera from the first and last week of the maturation period studied to illustrate the cultivar-dependent change in coloration

power law in all weeks, with $\alpha = 0.90$ determined in week 21. In addition, μ_s' decreases from 2.1 mm^{-1} at week 13 to 1.1 mm^{-1} at week 21 at 650 nm. Beginning at week 15, a broad increase occurs at a wavelength of 530 nm, which increases steadily until the end of maturation. The difference between μ_s' at 520 nm with 4.5 mm^{-1} and at 700 nm with 1.1 mm^{-1} at week 21 reaches about a factor of four. At the same time, μ_a also increases from 0.53 to 5.46 mm^{-1}, which is due to the absorption of anthocyanins and causes dark red coloration. At 678 nm, a small peak in μ_s' is visible only in the first weeks of maturation with a corresponding decrease of μ_a from 0.76 to 0.33 mm^{-1}.

To investigate the peaks in μ_s' associated with either high chlorophyll or anthocyanin content, the optical properties for 'Elstar' from week 11 and 'Gala' from week 21 are shown in Fig. 6 in more detail. In both cases, the obtained power laws shown in Fig. 5 were subtracted from μ_s'. Without this background scattering, which is presumably caused by small air pores, the remaining fraction of μ_s' can be attributed mainly to the influence of pigment-containing organelles. For apple skin with high chlorophyll content in Fig. 6A, four peaks can be identified at 435 nm, 469 nm, 488 nm, and 678 nm, whose central wavelengths were determined by regression of a Gaussian curve each. The two neighboring peaks at 469 nm and 488 nm can be distinguished only vaguely by a small dip. The height of the peaks relative to background is between 0.25 and 0.5 mm^{-1}. The corresponding absorption spectrum shows increases of μ_a at corresponding spectral positions, but slightly shifted by about 4 nm to shorter wavelengths. It must be taken into account that apart from the carotenoids bound in the grana, other xanthophylls with almost the same absorption properties are present in the skin [4]. However, their concrete influence on the height and spectral position of the absorption bands is difficult to estimate and requires further investigation. For apple skin with high anthocyanin content in Fig. 6B, a single peak in μ_s' with a height of up to 3 mm^{-1} relative to the subtracted background occurs. The corresponding absorption peak has a maximum of 6 mm^{-1} and no spectral shift was observed in this case.

In a comparable study using integrating sphere measurements, Van Beers et al. [61] observed a strong increase in μ_s' at 550 nm during maturation from 1 to 5 mm^{-1} for two red-skinned cultivars, while no change was observed in 'Granny Smith' apples which are known to form almost no anthocyanins in the skin. This observation clearly confirms our results and thus the significant impact of AVIs on μ_s'. Naqvi et al. [62] presented a method to calculate the scattering and absorption properties based on extinction spectra of chloroplasts or LHCII solutions taking advantage of the Kramers–Kronig relations. In both cases, the results show qualitatively very similar characteristics compared to our measurement results, in particular pronounced selective scattering effects and a spectral offset between the absorption and scattering peaks.

Further comparison between these experimental results and our Mie simulations allows a more differentiated evaluation of the influence of grana and AVIs on the optical properties of apple skin. Both approaches independently demonstrated the occurrence of selective scattering effects in the spectral range of high chlorophyll and anthocyanin absorption. In contrast to the simulation results, in the experiment the peaks in μ_s' are more pronounced relative to their

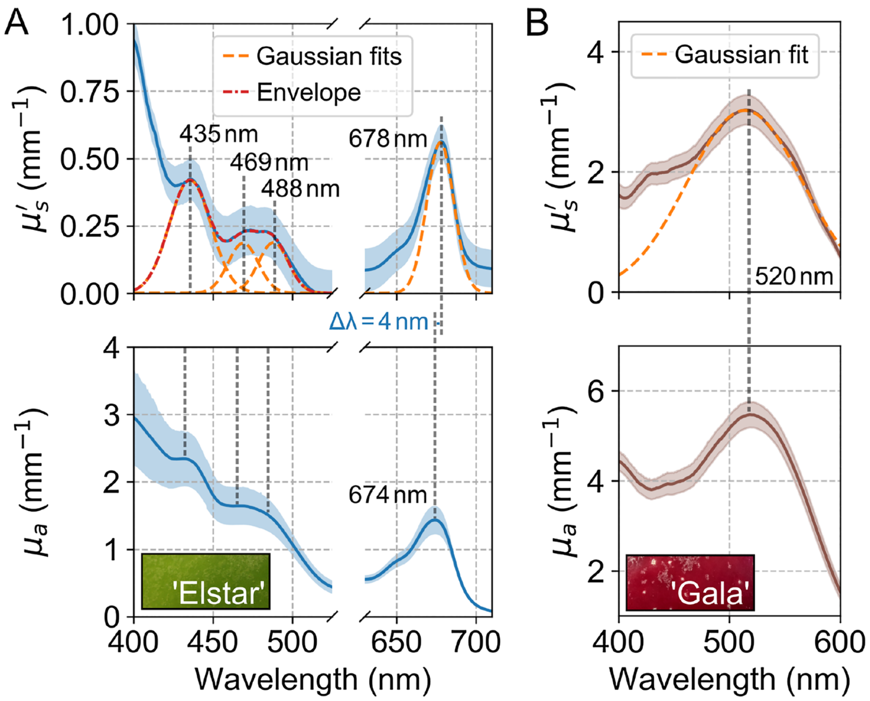

Fig. 6 Spectrally resolved optical properties of apple skin measured for 'Elstar' in week 11 (**A**) and 'Gala' in week 21 (**B**). In both μ_s' spectra, the background was subtracted by means of the obtained power laws shown as black-dotted lines in Fig. 5. The indicated central wavelengths of the peaks as well as their spectral shift $\Delta\lambda$ were determined by regression of gaussian curves for μ_s' and μ_a

corresponding μ_a band, and both are additionally spectrally shifted. Renge and Mauring [63] reported that chlorophyll absorption in protein environments is red-shifted by up to 20 nm compared to reference spectra in a solvent due to exciton interaction between closely spaced chromophores, which agrees well with our results for grana. The shift of the peaks in μ_s' to longer wavelengths relative to μ_a is smaller than predicted, but confirms the presence of anomalous dispersion. Considering the explicit reconstruction of the complex refractive index, for grana the change in μ_s' thus can be interpreted as the combined result of high extinction and local increase in the real part of the refractive index. Despite the spectral shift, the number and relative position of the peaks in μ_s' agrees quite well with the model. Besides to the known Q band of chlorophyll *a* at 678 nm, by direct comparison between experiment and simulation the maxima at 435 nm and 469 nm can be assigned to the Soret bands of chlorophyll *a* and *b* and the maximum at 488 nm to the red-most absorption band of carotenoids. This assignment is well confirmed by the results of Croce et al. [64], who reported for the LHCII supercomplex the Soret bands of chlorophyll *a* and *b* at 439 nm and 467 nm and the red-most absorption bands of three predominant carotenoids, namely lutein, neoxanthin, and violaxanthin, at 489 nm, 488 nm, and 492 nm, respectively. The comparable μ_a for the maxima at 469 nm and 488 nm suggests a larger influence of carotenoids than the model predicts, either due to a higher molar extinction or, more likely, due to a higher molar concentration compared to the chlorophylls than assumed.

In the case of the AVIs, the increase in μ_s' is almost an order of magnitude higher than predicted by the model, while the expected spectral shift between μ_s' and μ_a is completely absent. Since only sparse information is available on the structure and chemical composition of AVIs, the reason for this cannot be conclusively determined. However, the absence of the spectral shift indicates that there is probably no abnormal dispersion and, accordingly, the reconstruction of the complex refractive index is not close to reality.

4.4 Anthocyanin absorption shifts blue

For the two cultivars 'Gala' and 'Jonagold' with intense red blush color at the end of maturation the anthocyanin absorption was investigated in more detail. In both cases, skin samples were taken weekly from the sun side of six apples and measured using the integrating sphere setup as previously presented. As shown in Fig. 7, their μ_a spectra show a dominant absorption peak that increases from about 1 to 6 mm^{-1} in less than 10 weeks. The central wavelength of the peaks, determined by regression of a Gaussian curve, shifts from an initial wavelength of about 550–520 nm, over the same period. It is noticeable that both the absolute absorption and the shift are very similar when comparing the results of the two cultivars.

Fig. 7 Temporal evolution of the absorption coefficient μ_a in the Vis spectral range measured for the skin of **A** 'Gala' and **B** 'Jonagold' apples during maturation. The shaded area indicates the standard deviation of measurements on six different apples per week. On the right side, the central wavelength of the absorption band is plotted against the respective week after full bloom with error bars indicating the uncertainty of the underlying regression of a Gaussian curve

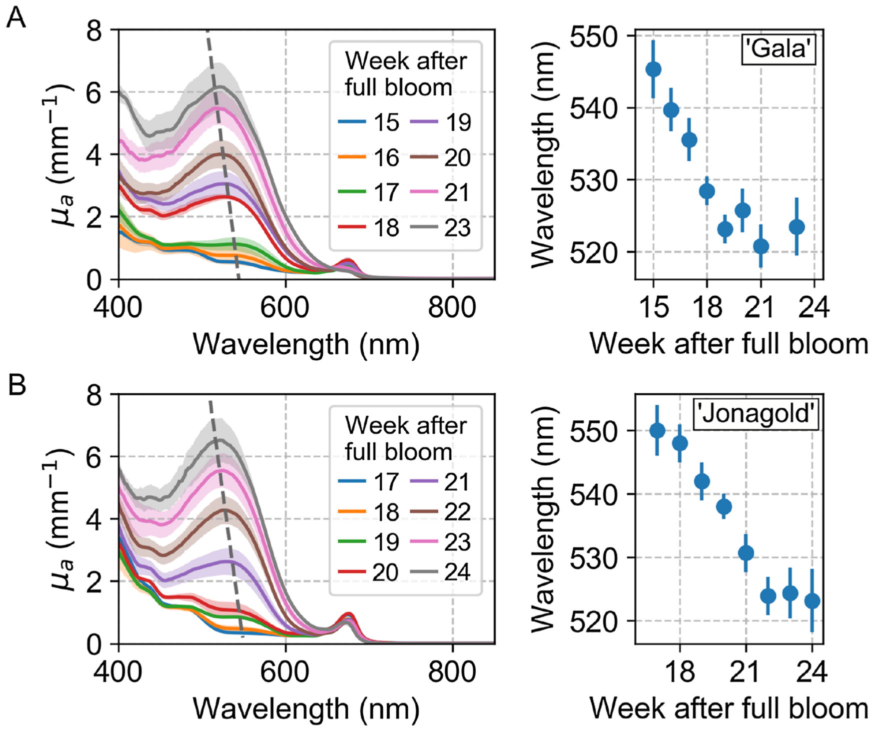

There are essentially two different explanations for the observed effect. On the one hand, the observed changes could be the result of an overlap with absorption bands of other pigments, which in principle could explain both the shift of the central wavelength and an apparent increase of μ_a. Carotenoids in particular come into consideration, since for them an increase of μ_a in the spectral range up to about 500 nm at the end of maturation is documented [21, 65]. On the other hand, it must be taken into account that anthocyanins are generally chemically reactive due to their molecular structure, resulting in a large number of possible complex interactions. In particular, copigmentation plays an important role, meaning that anthocyanins form non-covalent bonds with other anthocyanins, other phenols such as flavonoids or even metal ions [66]. Under the influence of additional external factors, e.g., pH and temperature, both a bathochromic shift (red shift) and a hypsochromic shift (blue shift) in the central wavelength of the anthocyanin absorption as well as changes in the molar extinction coefficient can be observed [67]. According to Dangles et al. [39], the formation of AVIs can be understood as agglomeration of acylated anthocyanins. Thus, the observed blue shift would be a direct consequence of a chemical restructuring of the anthocyanins, which could possibly provide more detailed information about the structure of the AVIs or the pH in the cell vacuole.

5 Conclusions

Based on a combined theoretical and experimental study using apple skin as an example, the influence of grana and AVIs on the optical properties of biological tissue was described for the first time using quantitative quantities such as μ_s' and μ_a. The reconstruction of the absorption spectra showed that grana has characteristic absorption bands in the blue and red wavelength regions, which can be assigned to chlorophylls and carotenoids. In contrast, the AVIs showed a broad absorption band between 520 and 550 nm. Consideration of the complex refractive indices based on the Kramers–Kronig relations together with a polydisperse Mie model allowed in an innovative way the prediction of multiple peaks in μ_s' associated with the main absorption bands but shifted by 8–27 nm to longer wavelengths. This effect, known as selective scattering, was confirmed experimentally by measurements of apple skin samples with an integrating sphere, although differences in the height and spectral position of the peaks in μ_a and μ_s' were found. By direct comparison, the Soret bands of chlorophyll *a* and chlorophyll *b* at 435 nm and 469 nm, respectively, and at 488 nm the red-most edge of carotenoid absorption could be located. Especially for anthocyanin absorption, red-skinned apples showed a strong blue shift from 550 to 520 nm associated with an increase in absorption. While a spectral shift of about 4 nm between the peaks in μ_a and μ_s' was found for grana in agreement with the Mie model, this was not the case for AVIs, raising further questions about their chemical structure and composition.

Overall, it was shown that simultaneously determining μ_s' and μ_a provides complementary information about the chemical composition as well as structural parameters such as the size distribution of pigment-containing cell organelles or their refractive index difference relative to their surroundings. Due to the limited literature data specifically for apple skin, numerous assumptions had to be made in the modeling, which means that the comparison between experiment and theory in the context of this work is largely on a qualitative level. Nevertheless, it is conceivable to use the presented model on the basis of measured data also for quantitative evaluation, if individual aspects of the chemical composition or structure can be clarified in the future. For example, a regression model based on spectrally resolved μ_s' and μ_a could be used to determine the size distribution of cell organelles for a given complex refractive index or vice versa. Facing the strong influence of AVIs on the optical properties, this approach could be useful to better understand the complex formation of anthocyanins, which are increasingly in focus due to their multiple physiological properties. In addition, the results are of interest in the growing field of applying optical properties for quality assurance of agricultural products, since high pigment concentrations in the skin and flesh of tomato, kiwi, or mango, for example, suggest comparable effects. In the long term, the development of microscopic light propagation models, e.g., based on numerical solutions to Maxwell's equations, would be desirable to obtain even more accurate and realistic results, especially with respect to heterogeneous cell organelles such as grana.

Acknowledgements This research was funded in part by 'Zentrales Innovationsprogramm Mittelstand' (ZIM) of the 'Bundesministerium für Wirtschaft und Energie' (BMWi).

Declarations

Conflict of interest On behalf of all authors, the corresponding author states that there is no conflict of interest.

References

1. Milne, B. F., Toker, Y., Rubio, A., & Nielsen, S. B. (2015). Unraveling the intrinsic color of chlorophyll. *Angewandte Chemie, 127*(7), 2198–2201. https://doi.org/10.1002/ange.201410899
2. Mullineaux, C. W. (2005). Function and evolution of grana. *Trends in Plant Science, 10*(11), 521–525. https://doi.org/10.1016/j.tplants.2005.09.001
3. Hashimoto, H., Sugai, Y., Uragami, C., Gardiner, A. T., & Cogdell, R. J. (2015). Natural and artificial light-harvesting systems utilizing the functions of carotenoids. *Journal of Photochemistry and Photobiology C: Photochemistry Reviews, 25*, 46–70. https://doi.org/10.1016/j.jphotochemrev.2015.07.004
4. Knee, M. (1988). Carotenol esters in developing apple fruits. *Phytochemistry, 27*(4), 1005–1009. https://doi.org/10.1016/0031-9422(88)80261-9
5. Lancaster, J. E., Grant, J. E., Lister, C. E., & Taylor, M. C. (1994). Skin color in apples - influence of copigmentation and plastid pigments on shade and darkness of red color in five genotypes. *Journal of the American Society for Horticultural Science, 119*(1), 63–69. https://doi.org/10.21273/JASHS.119.1.63
6. Merzlyak, M. N., & Chivkunova, O. B. (2000). Light-stress-induced pigment changes and evidence for anthocyanin photoprotection in apples. *Journal of Photochemistry and Photobiology B: Biology, 55*(2–3), 155–163. https://doi.org/10.1016/S1011-1344(00)00042-7
7. Solovchenko, A., & Schmitz-Eiberger, M. (2003). Significance of skin flavonoids for UV-B-protection in apple fruits. *Journal of Experimental Botany, 54*(389), 1977–1984. https://doi.org/10.1093/jxb/erg199
8. Bae, R.-N., Kim, K.-W., Kim, T.-C., & Lee, S.-K. (2006). Anatomical observations of anthocyanin rich cells in apple skins. *HortScience, 41*(3), 733–736. https://doi.org/10.21273/HORTSCI.41.3.733
9. Latimer, P., & Rabinowitch, E. (1959). Selective scattering of light by pigments in vivo. *Archives of Biochemistry and Biophysics, 84*(2), 428–441. https://doi.org/10.1016/0003-9861(59)90605-8
10. Merzlyak, M. N., et al. (2008). Light absorption and scattering by cell suspensions of some cyanobacteria and microalgae. *Russian Journal of Plant Physiology, 55*(3), 420–425. https://doi.org/10.1134/S1021443708030199
11. Bialek, G. E., Horvath, G., Garab, G. I., Mustardy, L. A., & Faludi-Daniel, A. (1977). Selective scattering spectra as an approach to internal structure of granal and agranal chloroplasts. *Proceedings of the National Academy of Sciences, 74*(4), 1455–1457. https://doi.org/10.1073/pnas.74.4.1455
12. Charney, E., & Brackett, F. S. (1961). The spectral dependence of scattering from a spherical alga and its implications for the state of organization of the light-accepting pigments. *Archives of Biochemistry and Biophysics, 92*(1), 1–12. https://doi.org/10.1016/0003-9861(61)90210-7
13. Chen, M., & Weng, F. (2012). Kramers-Kronig analysis of leaf refractive index with the PROSPECT leaf optical property model. *Journal of Geophysical Research: Atmospheres, 117*(17), 1–9. https://doi.org/10.1029/2012JD017477
14. Sai, T., Saba, M., Dufresne, E. R., Steiner, U., & Wilts, B. D. (2020). Designing refractive index fluids using the Kramers-Kronig relations. *Faraday Discussions, 223*, 136–144. https://doi.org/10.1039/d0fd00027b
15. Capretti, A., et al. (2019). Nanophotonics of higher-plant photosynthetic membranes. *Light: Science and Applications, 8*, 5. https://doi.org/10.1038/s41377-018-0116-8
16. Saeys, W., Velazco-Roa, M. A., Thennadil, S. N., Ramon, H., & Nicolaï, B. M. (2008). Optical properties of apple skin and flesh in the wavelength range from 350 to 2200 nm. *Applied Optics, 47*(7), 908. https://doi.org/10.1364/AO.47.000908
17. Rowe, P. I., et al. (2014). Relationship between tissue firmness and optical properties of 'Royal Gala' apples from 400 to 1050nm. *Postharvest Biology and Technology, 94*, 89–96. https://doi.org/10.1016/j.postharvbio.2014.03.007
18. Bashkatov, A. N., Genina, E. A., Kochubey, V. I., & Tuchin, V. V. (2005). Optical properties of human skin, subcutaneous and mucous tissues in the wavelength range from 400 to 2000

nm. *Journal of Physics D: Applied Physics, 38*(15), 2543–2555. https://doi.org/10.1088/0022-3727/38/15/004

19. Zamora-Rojas, E., et al. (2013). Double integrating sphere measurements for estimating optical properties of pig subcutaneous adipose tissue. *Innovative Food Science and Emerging Technologies, 19*, 218–226. https://doi.org/10.1016/j.ifset.2013.04.015
20. Bohren, C. F., & Huffman, D. R. (1983). *Absorption and scattering of light by small particles*. New York: John Wiley.
21. Lohner, S. A., et al. (2021). Determining the optical properties of apple tissue and their dependence on physiological and morphological characteristics during fruit maturation. Part 2: Mie's theory. *Postharvest Biology and Technology, 181,* 111652. https://doi.org/10.1016/j.postharvbio.2021.111652
22. Modest, M. F. (2003). *Radiative heat transfer* (2nd ed.). Boston: Academic Press. https://doi.org/10.1016/B978-0-12-503163-9.X5000-0
23. Schäfer, J. (2016). *MatScat V1.4.0.0*. MATLAB Central File Exchange. https://www.mathworks.com/matlabcentral/fileexchange/36831-matscat
24. Lucarini, V., Saarinen, J. J., Peiponen, K.-E., & Vartiainen, E. M. (2005). *Kramers-Kronig relations in optical materials research*, vol. 110 of *Springer Series in Optical Sciences*. Berlin: Springer-Verlag. https://doi.org/10.1007/b138913
25. Gienger, J., Gross, H., Neukammer, J., & Bär, M. (2016). Determining the refractive index of human hemoglobin solutions by Kramers-Kronig relations with an improved absorption model. *Applied Optics, 55*(31), 8951–8961. https://doi.org/10.1364/ao.55.008951
26. Daum, B., Nicastro, D., Austin, J., Richard McIntosh, J., & Kühlbrandt, W. (2010). Arrangement of photosystem II and ATP synthase in chloroplast membranes of spinach and pea. *The Plant Cell, 22*(4), 1299–1312. https://doi.org/10.1105/tpc.109.071431
27. Wei, X., et al. (2016). Structure of spinach photosystem II-LHCII supercomplex at 3.2 Å resolution. *Nature, 534*(7605), 69–74. https://doi.org/10.1038/nature18020
28. Verboven, P., et al. (2013). Optical coherence tomography visualizes microstructure of apple peel. *Postharvest Biology and Technology, 78*, 123–132. https://doi.org/10.1016/j.postharvbio.2012.12.020
29. Tukey, H. B., & Young, J. O. (1942). Gross morphology and histology of developing fruit of the apple. *Botanical Gazette, 104*(1), 3–25. https://doi.org/10.1086/335103
30. Verboven, P., et al. (2008). Three-dimensional gas exchange pathways in pome fruit characterized by synchrotron X-ray computed tomography. *Plant Physiology, 147*(2), 518–527. https://doi.org/10.1104/pp.108.118935
31. Delgado-Pelayo, R., Gallardo-Guerrero, L., & Hornero-Méndez, D. (2014). Chlorophyll and carotenoid pigments in the peel and flesh of commercial apple fruit varieties. *Food Research International, 65*, 272–281. https://doi.org/10.1016/j.foodres.2014.03.025
32. S. M, Schaeffer, et al. (2017). Comparative ultrastructure of fruit plastids in three genetically diverse genotypes of apple (Malus × domestica Borkh.) during development. *Plant Cell Reports, 36*(10), 1627–1640. https://doi.org/10.1007/s00299-017-2179-z
33. Mustárdy, L., & Garab, G. (2003). Granum revisited. A three-dimensional model - Where things fall into place. *Trends in Plant Science, 8*(3), 117–122. https://doi.org/10.1016/S1360-1385(03)00015-3
34. Kirchhoff, H. (2008). Molecular crowding and order in photosynthetic membranes. *Trends in Plant Science, 13*(5), 201–207. https://doi.org/10.1016/j.tplants.2008.03.001
35. Nield, J., & Barber, J. (2006). Refinement of the structural model for the photosystem II supercomplex of higher plants. *Biochimica et Biophysica Acta - Bioenergetics, 1757*(5–6), 353–361. https://doi.org/10.1016/j.bbabio.2006.03.019
36. Dekker, J. P., & Boekema, E. J. (2005). Supramolecular organization of thylakoid membrane proteins in green plants. *Biochimica et Biophysica Acta - Bioenergetics, 1706*(1–2), 12–39. https://doi.org/10.1016/j.bbabio.2004.09.009
37. Yamaki, S. (1984). Isolation of vacuoles from immature apple fruit flesh and compartmentation of sugars, organic acids, phenolic compounds and amino acids. *Plant and Cell Physiology, 25*(1), 151–166. https://doi.org/10.1093/oxfordjournals.pcp.a076688
38. Huber, G. M., & Rupasinghe, H. P. (2009). Phenolic profiles and antioxidant properties of apple skin extracts. *Journal of Food Science, 74*(9), 693–700. https://doi.org/10.1111/j.1750-3841.2009.01356.x
39. Dangles, O., & Fenger, J. A. (2018). The chemical reactivity of anthocyanins and its consequences in food science and nutrition. *Molecules*. https://doi.org/10.3390/molecules23081970
40. Zhang, H., Wang, L., Deroles, S., Bennett, R., & Davies, K. (2006). New insight into the structures and formation of anthocyanic vacuolar inclusions in flower petals. *BMC Plant Biology, 6*, 1–14. https://doi.org/10.1186/1471-2229-6-29
41. Kallam, K., et al. (2017). Aromatic decoration determines the formation of anthocyanic vacuolar inclusions. *Current Biology, 27*(7), 945–957. https://doi.org/10.1016/j.cub.2017.02.027
42. Richmond, A. E., Dilley, D. R., & Dewey, D. H. (1964). Cation, organic acid, and pH relationships in peel tissue of apple fruits affected with Jonathan spot. *Plant Physiology, 39*(6), 1056–1060. https://doi.org/10.1104/pp.39.6.1056
43. Foschum, F., Bergmann, F., & Kienle, A. (2020). Precise determination of the optical properties of turbid media using an optimized integrating sphere and advanced Monte Carlo simulations. Part 1: theory. *Applied Optics, 59*(10), 3203. https://doi.org/10.1364/AO.386011
44. Bergmann, F., Foschum, F., Zuber, R., & Kienle, A. (2020). Precise determination of the optical properties of turbid media using an optimized integrating sphere and advanced Monte Carlo simulations. Part 2: experiments. *Applied Optics, 59*(10), 3216. https://doi.org/10.1364/AO.385939
45. Lohner, S. A., et al. (2021). Determining the optical properties of apple tissue and their dependence on physiological and morphological characteristics during maturation. Part 1: spatial frequency domain imaging. *Postharvest Biology and Technology, 181*, 111647. https://doi.org/10.1016/j.postharvbio.2021.111647
46. Segelstein, D. J. (1981). *The complex refractive index of water*. Ph.d. thesis, University of Missouri - Kansas City.
47. McHowat, J., Jones, J. H., & Creer, M. H. (1996). Quantitation of individual phospholipid molecular species by UV absorption measurements. *Journal of Lipid Research, 37*(11), 2450–2460. https://doi.org/10.1016/S0022-2275(20)37493-9
48. Woods, A. H., & O'Bar, P. R. (1970). Absorption of proteins and peptides in the far ultraviolet. *Science, 167*(3915), 179–181. https://doi.org/10.1126/science.167.3915.179
49. Taniguchi, M., & Lindsey, J. S. (2021). Absorption and fluorescence spectral database of chlorophylls and analogues. *Photochemistry and Photobiology, 97*(1), 136–165. https://doi.org/10.1111/php.13319
50. Taniguchi, M., & Lindsey, J. S. (2018). Database of absorption and fluorescence spectra of >300 common compounds for use in photochem CAD. *Photochemistry and Photobiology, 94*(2), 290–327. https://doi.org/10.1111/php.12860
51. Solovchenko, A. (2010). *Screening pigments: general questions*. In: Photoprotection plants. Springer Ser. Biophys. vol 14. Berlin: Springer. https://doi.org/10.1007/978-3-642-13887-4_2
52. Liu, P., Yang, B., & Kallio, H. (2010). Characterization of phenolic compounds in Chinese hawthorn (*Crataegus pinnatifida* Bge. var. major) fruit by high performance liquid chromatography-electrospray ionization mass spectrometry. *Food Chemistry,*

121(4), 1188–1197. https://doi.org/10.1016/j.foodchem.2010.02.002

53. Fuleki, T. ., & Francis, F. .J. (1968). Quantitative methods for anthocyanins. 2. Determination of total anthocyanin and degradation index for cranberry juice. *Journal of Food Science, 33*(1), 78–83. https://doi.org/10.1111/j.1365-2621.1968.tb00888.x
54. Kaeswurm, J. A., Scharinger, A., Teipel, J., & Buchweitz, M. (2021). Absorption coefficients of phenolic structures in different solvents routinely used for experiments. *Molecules, 26*(15), 1–15. https://doi.org/10.3390/molecules26154656
55. Margalit, O., Sarafis, V., & Zalevsky, Z. (2010). The effect of grana and inter-grana components of chloroplasts on green light transmission: a preliminary study. *Optik, 121*(16), 1439–1442. https://doi.org/10.1016/j.ijleo.2009.02.007
56. Hale, G. M., & Querry, M. R. (1973). Optical constants of water in the 200-nm to 200-μm wavelength region. *Applied Optics, 12*(3), 555. https://doi.org/10.1364/AO.12.000555
57. Janssen, S., et al. (2020). 3D pore structure analysis of intact 'Braeburn' apples using X-ray micro-CT. *Postharvest Biology and Technology, 159,* 111014. https://doi.org/10.1016/j.postharvbio.2019.111014
58. Grenfell, T. C., & Warren, S. G. (1999). Representation of a nonspherical ice particle by a collection of independent spheres for scattering and absorption of radiation. *Journal of Geophysical Research: Atmospheres, 104*(D24), 31697–31709. https://doi.org/10.1029/1999JD900496
59. Phan, C. T. (1973). Chloroplasts in the peel and internal apple tissue. *Experientia, 29*, 1555–1557.
60. Phan, C. T. (1984). All-granal chloroplasts of apple-fruit. *Advances in Photosynthesis Research, III*, 63–66. https://doi.org/10.1007/978-94-017-4973-2_14
61. Van Beers, R., et al. (2017). Effect of maturation on the bulk optical properties of apple skin and cortex in the 500–1850 nm wavelength range. *Journal of Food Engineering, 214*, 79–89. https://doi.org/10.1016/j.jfoodeng.2017.06.013
62. Naqvi, K. R., Merzlyak, M. N., & Melø, T. B. (2004). Absorption and scattering of light by suspensions of cells and subcellular particles: an analysis in terms of Kramers-Kronig relations. *Photochemical and Photobiological Sciences, 3*(1), 132–137. https://doi.org/10.1039/b304781d
63. Renge, I., & Mauring, K. (2013). Spectral shift mechanisms of chlorophylls in liquids and proteins. *Spectrochimica Acta Part A: Molecular and Biomolecular Spectroscopy, 102*, 301–313. https://doi.org/10.1016/j.saa.2012.10.034
64. Croce, R., Cinque, G., Holzwarth, A. R., & Bassi, R. (2000). The Soret absorption properties of carotenoids and chlorophylls in antenna complexes of higher plants. *Photosynthesis Research, 64*(2–3), 221–231. https://doi.org/10.1023/A:1006455230379
65. Ampomah-Dwamena, C., et al. (2012). Metabolic and gene expression analysis of apple (Malus × domestica) carotenogenesis. *Journal of Experimental Botany, 63*(12), 4497–4511. https://doi.org/10.1093/jxb/ers134
66. Pina, F., Melo, M. J., Laia, C. A., Parola, A. J., & Lima, J. C. (2012). Chemistry and applications of flavylium compounds: a handful of colours. *Chemical Society Reviews, 41*(2), 869–908. https://doi.org/10.1039/c1cs15126f
67. Giusti, M. M., Rodríguez-Saona, L. E., & Wrolstad, R. E. (1999). Molar absorptivity and color characteristics of acylated and non-acylated pelargonidin-based anthocyanins. *Journal of Agricultural and Food Chemistry, 47*(11), 4631–4637. https://doi.org/10.1021/jf981271k

Authors and Affiliations

Stefan A. Lohner[1] · Konni Biegert[2] · Ansgar Hohmann[1] · Roy McCormick[2] · Alwin Kienle[1]

[1] Institut für Lasertechnologien in der Medizin und Meßtechnik an der Universität Ulm, Helmholtzstr. 12, 89081 Ulm, Germany

[2] Kompetenzzentrum Obstbau Bodensee, Schuhmacherhof 6, 88213 Ravensburg, Germany

7.2 Acknowledgments

I would like to express my particular gratitude to the following who always supported and challenged me to finish this work:

Roy J. McCormick, Josef Streif, Prof. Peter Braun, Stefan A. Lohner, Prof. Alwin Kienle, Prof. Christian Zörb

Kompetenzzentrum Obstbau Bodensee: The outdoor team, the "flower counting team" and interns managed the orchard at the best with counting, weighing, collecting data and my indoor colleagues at the lively coffee break.

La familia

Spuhlertec, Andreas Riehle, Niklas and Sharon Schneider, Simon Bitterwolf.
Endless, fruitful, great discussions.

To my friends, riding with me the wave at the breakwater and staying at my side at the wave troughs.

Thank you.

7.3 Funding

Several promotors contributed to the success of the dissertation.

The projects ’BigApple’ (2016-2019) and ’Apfel4.NULL’ (2020-2023) were supported by funds of the Federal Ministry of Food and Agriculture (BMEL) based on a decision of the Parliament of the Federal Republic of Germany via the Federal Office for Agriculture and Food (BLE) under the innovation support program.

The ’Melon’ project (2018-2020) was funded by ‘Zentrales Innovationsprogramm Mittelstand’ (ZIM) of the Bundesministerium für Wirtschaft und Energie (BMWi).

Kompetenzzentrum Obstbau Bodensee.

7.4 Statuory declaration

Name: Konni Biegert

I declare that I have prepared the submitted thesis independently and without unauthorised third-party help and that no other than the in the thesis listed facilities have been used. All text passages that are quoted literally or analogously from other published papers and all information that are based on verbal statements are identified as such. I have observed the principles of good scientific practice as defined in the statutes of the Hochschule Geisenheim University for safeguarding good scientific practice when carrying out the analyses of my research mentioned in the thesis.

Geisenheim, ...

Konni Biegert